SAND2018-12124R

Evaluation of Engineered Barrier Systems in the Disposition of Spent Nuclear Fuel

Spent Fuel and Waste Disposition

Prepared for US Department of Energy
Spent Fuel and Waste Science and Technology

Edward N. Matteo and Teklu Hadgu, Sandia National Laboratories

Liange Zheng, Hao Xu, Patricia Fox, Peter Nico, Jens Birkholzer
Lawrence Berkeley National Laboratory

Florie A. Caporuscio, Kirsten B. Sauer, M. J. Rock, L. M. Houser
Los Alamos National Laboratory

September 24, 2018
M2SF-18SN010308042
SAND#:

Prepared by:
Sandia National Laboratories
Albuquerque, New Mexico 87185

Sandia National Laboratories is a multimission laboratory managed and operated by National Technology & Engineering Solutions of Sandia, LLC, a wholly owned subsidiary of Honeywell International Inc., for the U.S. Department of Energy's National Nuclear Security Administration under contract DE-NA0003525.

U.S. DEPARTMENT OF ENERGY

Sandia National Laboratories

Revision 4
07/05/2017

APPENDIX E
NTRD DOCUMENT COVER SHEET[1]

Name/Title of Deliverable/Revision No. Evaluation of Engineered Barrier Systems in the Disposition of Spent Nuclear Fuel,Rev.0

Work Package Title and Number: Engineered Barrier System R&D – SNL (Rev. 2)

Work Package WBS Number SF-18SN01030804 / 1.08.01.03.08

Responsible Work Package Manager Edward Matteo / E. Matteo
(Name/Signature)

Date Submitted

Quality Rigor Level for Deliverable/Milestone[2]	☐ QRL-1 ☐ Nuclear Data	☐ QRL-2	☒ QRL-3	☐ QRL-4 Lab- Specific

This deliverable was prepared in accordance with Sandia National Laboratories
(Participant/National Laboratory Name)

QA program which meets the requirements of
☒ DOE Order 414.1 ☐ NQA-1 ☐ Other

This Deliverable was subjected to:

☒ Technical Review ☐ Peer Review

Technical Review (TR)
Review Documentation Provided
☐ Signed TR Report or,
☐ Signed TR Concurrence Sheet or,
☒ Signature of TR Reviewer(s) below

Peer Review (PR)
Review Documentation Provided
☐ Signed PR Report or,
☐ Signed PR Concurrence Sheet or,
☐ Signature of PR Reviewer(s) below

Name and Signature of Reviewers

Mark Rigali / Mark Rigali

NOTE 1: *Appendix E should be filled out and submitted with the deliverable. Or, if the PICS:NE system permits, completely enter all applicable information in the PICS:NE Deliverable Form. The requirement is to ensure that all applicable information is entered either in the PICS:NE system or by using the NTRD Document Cover Sheet.*

- *In some cases there may be a milestone where an item is being fabricated, maintenance is being performed on a facility, or a document is being issued through a formal document control process where it specifically calls out a formal review of the document. In these cases, documentation (e.g., inspection report, maintenance request, work planning package documentation or the documented review of the issued document through the document control process) of the completion of the activity, along with the Document Cover Sheet, is sufficient to demonstrate achieving the milestone.*

NOTE 2: *If QRL 1, 2, or 3 is not assigned, then the QRL 4 box must be checked, and the work is understood to be performed using laboratory specific QA requirements. This includes any deliverable developed in conformance with the respective National Laboratory / Participant, DOE or NNSA-approved QA Program.*

SUMMARY

This document is a summary of the R&D activities associated with the *Engineered Barrier Systems Work Package.* Multiple facets of Engineered Barrier Systems (EBS) research were examined in the course of FY18 activities. This report is focused on delvering an update on the status and progress of modelling tools and experimental methods, both of which are essential to understanding and predicting long-term repository performance as part of the safety case.

Specifically, the work described herein aims to improve understanding of EBS component evolution and interactions. Utlimately, the EBS Work Package is working towards producing process models for distinct processes that can either be incorporated into performance assessment (PA), or provide critical information for implementing better contraints on barrier performance. The main objective of this work is that the models being developed and refined will either be implemented directly into the Genreric Disposal System Analysis platform (GDSA), or can otherwise be indirectly linked to the performance assessment by providing improved bounding conditions. In either the case, the expectation is that validated modelling tools will be developed that provide critical input to the safety case.

This report covers a range of topics – modelling topics include: thermal-hydrologic-mechnical-chemical coupling (THMC) in buffer materials, comparisons of modelling approaches to optimize computational efficiency, thermal analysis for EBS/repository design, benchmarking of thermal analysis tools, and a preliminary study of buffer re-saturation processess. Experimental work reported, includes: chemical evolution and sorption behavior of clay-based buffer materials and high-pressure, high temperature studies of EBS material interactions.

The work leverages international collaborations to ensure that the DOE program is active and abreast of the latest advances in nuclear waste disposal. This includes participation in the HotBENT Field Test, aimed at understanding near-field effects on EBS materials at temperatures above 100 ºC, and the analysis of data and characterization of samples from the FEBEX Field Test. Both the FEBEX and HotBENT Field Tests utilize/utilized the Grimsel Test Site in Switzerland, which is situated in a granite host rock. These tests offer the opportunity to understand near field evolution of bentonite buffer at *in situ* conditions for either a relatively long timescale (18 years for FEBEX) or temperature above 100 ºC (HotBENT).

Overall, this report provides in depth descriptions of tools and capabilities to investigate near-field performance of EBS materials (esp. bentonite buffer), as well as tools for drift-scale thermal and thermal-hydrologic analysis critical to EBS and repository design. For a more detailed description of work contained herein, please see Section 10 (“Conclusions”) of this document.

This page is intentionally left blank.

ACKNOWLEDGEMENTS

This work was supported by the U.S. Department of Energy Office of Nuclear Energy, through the Office of Spent Fuel and Waste Science and Technology (SFWST) Research and Development Campaign (DOE NE-81) within the Office of Spent Fuel and Waste Disposition.

The authors acknowledge the contributions to this activity from the following: Eric Simo (BGE), Ernie Hardin (SNL), Carlos Jove-Colon, Yifeng Wang, Peter Swift (SNL), Kevin McMahon (SNL), and Robert MacKinnon (SNL) for discussions on technical aspects and integration of this work. In addition, the authors thank Mark Tynan (DOE NE-81), Bill Spezialetti (DOE NE-81), Prasad Nair (DOE NE-81), Tim Gunter (DOE NE-81) and William Boyle (DOE NE-8) for their discussions, oversight and guidance on topics covered in this report.

The authors would like to thank George Perkins for water chemistry analyses. Scanning electron microscopy facilities were provided by Materials Science and Technology group at Los Alamos National Laboratory. Dr. Lindsey Hunt at the University of Oklahoma was instrumental in the obtaining of EMP analyses. XRD analyses were performed by Dr. James Maner at University Texas – Austin.

The authors thank Jeri Crenshaw (SNL) for assistance with formatting and proofing of this document.

Lastly, we thank Mark Rigali (SNL) for providing a careful and thorough technical review of this document.

ACRONYMS

1D, 1-D	One Dimensional
2D, 2-D	Two Dimensional
3D, 3-D	Three Dimensional
AET	Aqueous Extraction Test
ANDRA	Agence Nationale pour la Gestion Des Déchets Radioactifs (France)
ANL	Argonne National Laboratory
BBM	Barcelona Basic Model
BExM	Barcelona Expansive Model
CEC	Cation Exchange Capacity
CFRT	Colloid-Facilitated Radionuclide Transport
CIEMAT	Centro de Investigaciones Energéticas, Medioambientales y Tecnológicas (Spain)
CT	Computerized Tomography
CTD	Closure Test Drift
DECOVALEX	DEvelopment of COupled Models and their VALidation against EXperiments
DFN	Discrete Fracture Network
DOE	Department of Energy
DOE-NE	Department of Energy, Office of Nuclear Energy
DRZ	Disturbed Rock Zone
DSEF	Disposal Systems Evaluation Framework
EBS	Engineered Barrier System
EBS-NS	Engineered Barrier System-Natural System
EC	European Community
EDL	Electric Double Layer
EDS, EDX	Energy dispersive X-ray spectroscopy
EDZ	Excavated Disturbed Zone
EMP(A)	Electron Microprobe (Analysis)
ENRESA	Empresa Nacional de Residuos Radioactivos SA
FCRD	Fuel Cycle Research and Development
FCT	Fuel Cycle Technologies

FCM	Fracture Continuum Model
FE	Full-Scale Emplacement Experiment
FEBEX	Full-scale Engineered Barriers Experiment
FEBEX-DP	Full-scale Engineered Barriers Experiment-Dismantling Project
FEP	Features, Events, and Processes
FY	Fiscal Year
GDSA	Generic Disposal System Analysis
GDSA-PA	Generic Disposal System Analysis – Performance Assessment
GREET	Groundwater REcovery Experiment in Tunnel
GTS	Grimsel Test Site
GW	Gigawatt
GWd	Gigawatt days
GWd/MT	Gigawatt (thermal) - days per Metric Ton
HC	Hydrological and Chemical
HE-E	Half-Scale Heater Test (Mont Terri)
HLW	High-Level nuclear Waste
HM	Heavy Metal
HPLC	High Pressure Liquid Chromatograph
IAEA	International Atomic Energy Association
IC	Ion Chromatography
I-S	Illite-Smectite
JAEA	Japan Atomic Energy Agency
JNC	Japan Nuclear Cycle Development Institute
LANL	Los Alamos National Laboratory
LBNL	Lawrence Berkeley National Laboratory
LC	Loading Collapse
LCS	Low Carbon Steel
LT	Local Thickness
LLNL	Lawrence Livermore National Laboratory
MC	Mechanical-Chemical
MT	Metric Ton
MTHM	Metric Tons Heavy Metal
Micro XRCT	Micro X-ray Computer Tomography

NAGRA	National Cooperative for the Disposal of Radioactive Waste
NBS	Natural Barrier System
NE	DOE-Nuclear Energy
NS	Natural (Barrier) System
NW	Nuclear Waste
OECD	Organization for Economic Co-operation and Development
P	Pressure
PA	Performance Assessment
PNNL	Pacific Northwest National Laboratory
PWR	Pressurized Water Reactor
QXRD	Quantitative X-ray Diffraction
R&D	Research and Development
RH	Relative Humidity
SCM	Surface complexation model
SEM	Scanning Electron Microscopy
SFWST	The Spent Fuel Waste Science and Technology
SIT	Specific Interaction Theory
SNF	Spent Nuclear Fuel
SNL	Sandia National Laboratories
SXR-μCT	Synchrotron X-ray micro-Computer-Tomography
T	Temperature
t	time
TC	Thermal and Chemical
TDB	Thermodynamic Database
TEM	Transmission Electron Microscopy
TH	Thermal and Hydrological
THM	Thermal-Hydrological-Mechanical
THMC	Thermal-Hydrological-Mechanical-Chemical
TM	Thermal-Mechanical
TSPA	Total System Performance Assessment
UFD	Used Fuel Disposition
UFDC	Used Fuel Disposition Campaign

UOX	Uranium Oxide Fuel
UPC	University of Catalonia
URL	Underground Research Laboratory
WP	Waste Package
XRD	X-ray Diffraction
XRF	X-ray Fluorescence

CONTENTS

LIST OF FIGURES

LIST OF TABLES

SPENT FUEL AND WASTE SCIENCE AND TECHNOLOGY/ENGINEERED BARRIER SYSTEM R&D

1. INTRODUCTION

1.1 Context

This report describes Research and Development (R&D) Activities in the Spent Fuel Waste Science and Technology Camapaign, specifically related to the *Engineered Barrier System (EBS) R&D* Work Package. This work package is focused on design and performance prediction of the EBS, and in FY18 includes activities from Sandia National Laboratories, Lawrence Berkley National Laboratories, and Los Alamos National Laboratories.

The FY18 research in *EBS R&D* is focused on understanding EBS component evolution and interactions within the EBS, as well as interactions between the host media and the EBS. Specifically, *EBS R&D* is working towards producing process models for distinct processes that can either be incorporated into performance assessment (PA), or provide critical information for implementing better contraints on barrier performance. The main objective of this work is that the models being developed and refined will either be implemented directly into the Genreric Disposal System Analysis platform (GDSA), or can otherwise be indirectly linked to the performance assessment by providing improved bounding conditions.

1.2 Purpose and Scope

The purpose of this report is to provide a summary of the FY18 activities performed as part of the *EBS R&D* work package.

This report covers a range of topics – modelling topics include: thermal-hydrologic-mechnical-chemical coupling (THMC) in buffer materials, comparisons of modelling approaches to optimize computational efficiency, thermal analysis for EBS/repository design, benchmarking of thermal analysis tools, and a preliminary study of buffer re-saturation processess. Experimental work reported, includes: chemical evolution and sorption behavior of clay-based buffer materials and high-pressure, high temperature studies of EBS material interactions.

The work leverages international collaborations to ensure that the DOE program is active and abreast of the latest advances in nuclear waste disposal. This includes participation in the HotBENT Field Test, aimed at understanding near-field effects on EBS materials at temperatures above 100 ºC, and the analysis of data and characterization of samples from the FEBEX Field Test. Both the FEBEX and HotBENT Field Tests utilize/utilized the Grimsel Test Site in Switzerland, which is situated in a granite host rock. These tests offer the opportunity to understand near field evolution of bentonite buffer at *in situ* conditions for either a relatively long timescale (18 years for FEBEX) or temperature above 100 ºC (HotBENT).

2. THMC MODELING INVESTIGATION OF THE IMPACT OF HIGH TEMPERATURE LIMITS IN CLAY-BASED BUFFER MATERIAL

2.1 Introduction

2.1.1 Background

There is growing interest in the international EBS community to investigate the feasibility of raising the limit of the waste package surface temperature above 100 ºC, and in doing so, ascertain what the overall effect will be on the performance assessment. For EBS designs in granite and argillite, which place a significant reliance on bentonite buffer and/or backfill, rainsing the termal limit above 100 ºC could have significant impact on repository operations (esp. surface storage time), the repository design concept, and/or site selection. A higher temperature limit could, in theory, allow waste packages to be in placed after a shorter surface storage time-period, which may impact operational workflows. A higher thermal limit would also allow waste packages and drift to be spaced more closely, thus decreasing the overall size of the repository footprint. A smaller footprint, in turn, may impact the site selection process, as disposal formation thickness and especially areal extent are critical parameters in site slection.

2.1.2 Overview

This chapter is aimed at the results of simulations using a coupled thermal, hydrological, chemical, and mechanical (THMC) model to evaluate mechanical changes induced by the chemical alteration in EBS (Engineering Barrier System) bentonite and the NS (Natural System) clay formation under various scenarios, which are needed to provide the information for decision-making on temperature limits. Two scenarios were simulated: (1) the maximum temperature in the bentonite near the waste canister was about 200 ^{o}C, and (2) the temperature in the bentonite near waste canister peaks was about 100^{o}C. The comparison of the results of simulations of these two scenarios is used to evaluate the impact of temperature on the HMC-coupled processes in bentonite.

The coupling between chemical and mechanical processes is the key part of THMC model that allow one to evaluate the direct impact of chemical changes on the mechanical behavior. In previous THMC model simulations (e.g., Zheng et al., 2015), the coupling between chemical and mechanical processes was carried out via an extended linear swelling model, which was simple and its key parameters were relatively easy to calibrate. However, such model does not accurately describe the transient state of swelling, neglects the history of mechanical change, and is unable to account for the impact of cation exchange on the swelling. In FY17, the THMC models were improved based on the double structure Barcelona Expansive Model (BExM) (Sánchez *et al.*, 2005) to link the mechanical process with chemistry, and to incorporate simultaneously the effects of exchangeable cations, ionic strength of pore solution and the abundance of swelling clay on the swelling stress of bentonite. In FY18, we recalibrated the parameters of BExM for FEBEX bentonite to account for the effects of chemical reactions and to align with the reference state of *in-situ* bentonite. In this chapter of the report, we first summarize the modeling scenarios and Chemo-Mechanical (C-M) coupling included in the BExM. Then, we discuss the results of coupled THMC model simulations using BExM and the chemical effect on stress.

2.2 Model Development

Because the modeling approach used in this report is similar to that presented in previous reports (Liu *et al.*, 2013; Zheng *et al.*, 2014; Zheng *et al.*, 2015; Zheng *et al.*, 2016; Zheng *et al.*, 2017), we briefly describe each element of the THMC model, focusing on the updates made in FY18. Additional details on the THMC model are presented in Liu *et al.* (2013).

2.2.1 Simulator

A review of numerical simulators that could be used to conduct coupled THMC model simulations was given in Zheng et al., (2016). The problem of numerically simulating THMC processes is very challenging. The numerical simulations in this study have been conducted with TOUGHREACT-FLAC3D, which sequentially couples the multiphase fluid flow and reactive transport simulator TOUGHREACT (Xu *et al.*, 2011) with the finite-difference geomechanical code FLAC3D (Itasca, 2009). The coupling of TOUGHREACT and FLAC3D was initially developed and described in Zheng et al. (2012). Recently, the model was improved by using the dual structural BExM, and will be discussed in more details below in this report.

2.2.2 Modeling Scenarios

The model scenario used in this report is the same as that in Liu *et al.* (2013) and Zheng *et al.* (2014). The model is being applied to a hypothetical bentonite-backfilled nuclear waste repository in clay rock, a repository example involving a horizontal nuclear waste emplacement tunnel at a 500m depth Figure 2-1 (Rutqvist *et al.*, 2014). The model is a pseudo 2D model with the Y-axis aligned parallel to the 1 m thick tunnel. The Z-axis is vertical, and the horizontal X-axis is aligned perpendicular to the emplacement tunnel Figure 2-1. Note that while the canister is modeled as a heat source with mechanical properties of steel, the THC changes in the canister and their interactions with EBS bentonite are not considered in this model for the sake of simplicity. Additionally, neglecting canister-buffer simplicity allows for construction of a base-case buffer response, to isolate those phenmemnon that will be independent of buffer-canister interactions.

An initial stress field was imposed by the self-weight of the rock mass. Zero normal displacements are prescribed on the lateral boundaries of the model. Zero stress is applied to the top, and vertical displacements were prevented at the bottom. Liquid pressure is applied at the open boundary at top and bottom, and the model domain is initially in a hydrostatic state. The initial temperature at the top is about 11 ºC, with a thermal gradient of 27 ºC/km, the initial temperature at the bottom is 38 ºC. The model simulation was conducted in a nonisothermal mode with a time-dependent heat power input (Rutqvist *et al.*, 2014). The power curve in Figure 2-1 was adopted from representative heating data from the U.S. DOE's Used Fuel Disposition campaign for Pressurized Water Reactor (PWR) used fuel. This heat load is then scaled in the 2D model to represent an equivalent line load, which depends on the assumed spacing between individual waste packages along an emplacement tunnel. The heat load for the “low T” case corresponds to an initial thermal power of 3144 W (total power, equal to about 220 W/m along the length of the heater) for a 4-PWR-element waste package after aging for 60 years, a 50-m spacing between emplacement tunnels, and 3-m spacing between the 5-m long packages. The input power was estimated to increase the temperature to 100 ºC at peak inside bentonite buffer. The heat load for the “high T” case represents similar waste package and spacing, except with only 20 years of aging, and will induce 200 ºC at peak in the buffer. Initially, the EBS bentonite has a water saturation of 65% and the clay formation is fully saturated. From time zero, the EBS bentonite undergoes simultaneously re-saturation, heating, chemical alteration, and stress changes.

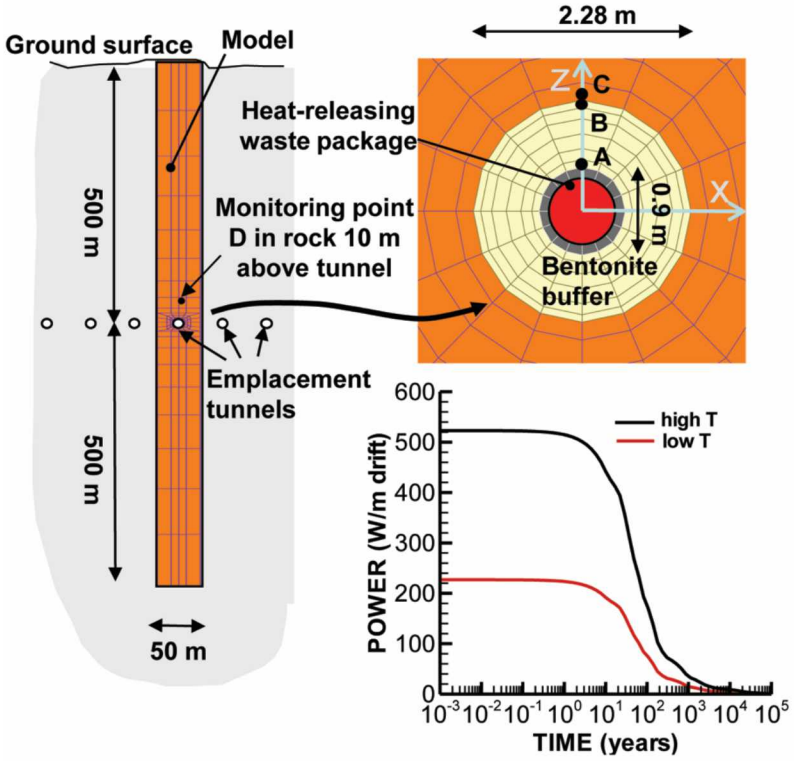

Figure 2-1. Schematic of the domain for the test example of a bentonite back-filled horizontal emplacement drift at 500 m (Rutqvist *et al.*, 2014). Modeling monitoring points: A-inside the bentonite near the canister, B—inside the bentonite and near the EBS-NS interface, C-inside the clay rock formation and near the EBS-NS interface, D—inside the clay rock formation at a distance of 10 m from the canister. Power curves in simulations: "high T" —200 ºC peak temperature in the buffer; "low T" — 100 ºC peak temperature in the buffer.

2.2.3 THC Model

Similar to previous models for generic cases, the host rock properties are assumed to be representative of Opalinus Clay (Bossart, 2011; Lauber et al., 2000), and the EBS backfill is assumed to represent the FEBEX bentonite (ENRESA, 2000). The model considers non-isothermal two-phase (air and water) flow, with each individual phase flux described by a multiphase version of Darcy's Law. For the vapor flow in the air phase, in addition to Darcy flow, mass transport can also occur by diffusion and dispersion according to Fick's law. The model considers both conductive (described by Fourier's law) and convective heat flux. The basic mass and energy balance equations, as well as the equations for fluxes, are given in Pruess et al. (1999). Thermal and hydrological properties are summarized in Table 2-1.
To establish a chemical model, one needs to know aqueous and mineralogical composition of each medium, chemical reactions considered in the model, and the thermodynamic data for each reactions. The model considers aqueous complexation, minerals dissolution/precipitation, cation exchange, and surface complexation. Details of these reaction and parameters needed to define these reactions are given in Zheng et al. (2016). In this report, we list the mineralogical (Table 2-2) and aqueous composition (Table 2-3).

Table 2-1. Thermal and hydrodynamic parameters.

Parameters	Clay formation—Opalinus Clay	EBS Bentonite—FEBEX
Grain density [kg/m^3]	2700	2700
Porosity ϕ	0.162	0.33
Saturated permeability [m^2]	2.0×10^{-20}	2.0×10^{-21}
Relative permeability, k_{rl}	$m = 0.6$, $S_{rl} = 0.01$ (model parameters)	$K_{rl} = S^3$ (model)
Van Genuchten α [1/Pa]	6.8×10^{-7}	3.3×10^{-8}
Van Genuchten m	0.6	0.3
Compressibility, β [1/Pa]	3.2×10^{-9}	5.0×10^{-8}
Thermal expansion coeff., [1/^{o}C]	1.0×10^{-5}	1.5×10^{-4}
Dry specific heat, [J/kg-^{o}C]	860	800
Thermal conductivity [W/m-^{o}C] dry/wet	1.48/1.7	1.1/1.5
Tortuosity for vapor phase	$\phi^{1/3} S_g^{10/3}$ (model)	$\phi^{1/3} S_g^{10/3}$ (model)
Bulk modulus, (GPa)	4.17	0.02
Shear modulus, (GPa)	1.92	0.0067

Source: from https://www.mont-terri.ch/en/geology%20/properties-and-characteristic-values.html

Table 2-2. Mineral volume fraction (dimensionless, ratio of the volume for a mineral to the total volume of medium) of FEBEX bentonite (ENRESA, 2000; Fernández et al., 2004; Ramírez et al., 2002) and Opalinus Clay (Bossart 2011; Lauber et al., 2000).

Mineral	**EBS Bentonite—FEBEX**	**Clay formation—Opalinus Clay**
Calcite	0.0065	0.093
Dolomite	0.0	0.050
Illite	0.0	0.273
Kaolinite	0.0	0.186
Smectite	0.6	0.035
Chlorite	0.0	0.076
Quartz	0.026	0.111
K-Feldspar	0.0065	0.015
Siderite	0.0	0.020
Ankerite	0.0	0.045
Pyrite	0.01	0.000
Greenrust	0.000	0.000
Magnetite	0.000	0.000
Hematite	0.000	0.000
Goethite	0.000	0.000
Fe(oh)3(s)	0.000	0.000
Fe(oh)2	0.000	0.000
Vermiculites	0.000	0.000
Berthierine(Fe^{+2})	0.000	0.000
Berthierine(Fe^{+3})	0.000	0.000
Saponite(Fe, Ca)	0.000	0.000
Saponite(Fe,K)	0.000	0.000
Saponite(Fe, Na)	0.000	0.000
Saponite(Fe, Mg)	0.000	0.000

Table 2-3. Pore-water composition (mol/kg water, except pH) of FEBEX bentonite (Fernández et al., 2001) and Opalinus Clay (Fernández et al., 2007).

	EBS Bentonite—FEBEX	**Clay formation—Opalinus Clay**
pH	7.72	7.40
Cl	1.60E-01	3.32E-01
SO_4^{-2}	3.20E-02	1.86E-02
HCO_3^-	4.1E-04	5.18E-03
Ca^{+2}	2.2E-02	2.26E-02
Mg^{+2}	2.3E-02	2.09E-02
Na^+	1.3E-01	2.76E-01
K^+	1.7E-03	2.16E-03
Fe^{+2}	2.06E-08	3.46E-06
$SiO_2(aq)$	1.1E-04	1.10E-04
AlO_2^-	1.91E-09	3.89E-08
$O_2(aq)$	2.57e-4	1.2E-51

2.2.4 Mechanical Model

2.2.4.1 Double Structure Model

In previous modeling works (e.g., Zheng *et al.*, 2015; 2016), extended linear swelling model was used to describe the mechanical behavior of bentonite. In this section, we primarily used a dual structure model, Barcelona Expansive Model (BExM).

For unsaturated soils, usually only the macrostructure is considered in a constitutive model, such as the Barcelona Basic Model (BBM). The microstructure is incorporated to extend the BBM to a dual structure model, such as BExM, which enables simulating the behavior of expansive soils, such as the dependency of swelling strains and swelling pressures on the initial stress state and on the stress path, strain accumulation upon suction cycles and secondary swelling. Thus, in the dual structure model, the total volume (V), the total void ratio (e), and porosity (ϕ) of the material are divided into a micro-structural part and a macro-structural part. The micro-structure is assumed to swell to invade the macro-porosity, depending on the mechanical confinement and a load level. This is analogous to the process of permeability changes resulting from soil swelling, because fluid flow takes place mostly through the macro-porosity, which is not proportional to the total strain and deformation of the expansive soil. Equations to describe the mechanical behavior of micro-structural and macro-structural domains and their interaction are not expressed here for the sake of simplicity.

We developed a one-way coupling approach, in which chemical changes affect mechanical behaviors of bentonite through the evolution of volume fraction of smectite, exchangeable cation concentrations, and ionic strength (via osmotic suction). In this report, these effects are incorporated into the model using a dual-structure model (BExM). The mathematical formulations for C-M coupling are summarized below.

The original BExM predicts the micro-strains induced by the effective stress for the whole micro-structure, ignoring the effects of the evolution of volume fraction of smectite. When the material is hydrated, instead of the whole micro-structure, only the parts of the smectite within the micro-structure, interacting with the invaded water, swell. Here, we introduce the volume fraction of smectite, f_s, in the micro-structure in BExM for C-M coupling. The swelling capacity of the material should decrease with the reduction of the volume fraction of smectite. Thus, the micro-structural volumetric strains are assumed to depend on the change in the microstructural effective stress as follows:

$$\mathrm{d}\varepsilon_{vm}^{e} = \frac{f_s}{K_m}\mathrm{d}\hat{p} \qquad 2\text{-}1$$

where $\hat{p} = p + s_m$, $\hat{p}$ is the effective mean stress, p is the net mean stress, which is the total mean stress $\bar{\sigma}$ minus gas pressure p_g, and s_m is the microstructural suction. The total suction, s_m, contains two components: matric suction, s, and osmotic suction, s_o, and $s_m = s + s_o$. The effect of ionic strength of the pore water on microstructural strain is transferred via the osmotic suction, and is computed as:

$$s_o = -10^{-6}\frac{RT}{V_w}\ln a_w \qquad 2\text{-}2$$

where V_w is the molar volume of water (in m^3/mol), R is the ideal gas constant, T is temperature (in K), a_w is the activity of water, and a_w is calculated in TOUGHREACT (Xu *et al.*, 2011) as follows:

$$\ln a_w = -\Phi m^* \frac{1}{55.51} \qquad 2\text{-}3$$

where Φ is the osmotic coefficient of the solution, and m^* is the sum of the molalities of all species in solution.

In Equation 2-1, K_m is calculated as:

$$K_m = \frac{e^{\alpha_m \hat{p}}}{\beta_m} \quad 2\text{-}4$$

where α_m is the material parameter. The effect of exchangeable cations is linked to mechanics through the dependence of β_m on exchangeable cation concentration given by (Gens, 2010):

$$\beta_m = \sum_i \beta_m^i x_i \quad 2\text{-}5$$

Gens (2010) and Guimaraes *et al.* (2013) proposed that β_m^i is proportional to the ionic hydrated radius and inversely proportional to its valence. Based on this hypothesis, we will calibrate the values of β_m^i for different cations against laboratory experiments.

2.2.4.2 Calibration of Parameters of BExM for FEBEX Bentonite

A coupled THMC model, using the BExM to link chemistry with mechanics, was first tested in FY16. The parameters of the mechanical model were taken from published literature, and the parameters for the C-M coupling, such as f_s, were taken directly from the chemical model. When the C-M coupling was incorporated into the BExM, the entire set of parameters should be calibrated, so that the BExM can accurately describe the reference state of bentonite. In FY17, we have calibrated the parameters of the BExM based on the swelling pressure experiments to make sure the model results are aligned with the reference state, and the model is able to reasonably predict the material swelling pressure. However, we only accounted for a chemical effect of the smectite volume fraction. In FY18, we incorporated additional experimental laboratory data obtained from testing the FEBEX bentonite, which allowed for inclusion of more realistic chemical effects, including the exchangeable cation concentration and ionic strength.

We launched a series of simulations on the swelling pressure test to investigate the swelling capacity of bentonite and to calibrate the parameters of the BExM for FEBEX bentonite against experiments conducted by Castellanos *et al.* (2008). These swelling pressure tests were operated under constant volume conditions. All samples were subjected to an initial suction of 98 MPa and a low vertical stress. During a wetting process, samples were saturated by different salinity solutions, the time variation of the swelling pressure was recorded, and the suction was reduced to 0 MPa. The numerical model was used to mimic the HMC process, based on the results of measurements of the swelling pressure, including simulations of infiltration of the solutions of different salinity into the partially saturated FEBEX bentonite, the geochemical and mechanical evolution of bentonite, and apparently the MC coupling. The hydrological and chemical parameters of FEBEX bentonite were presented in Section 2.2.3.

In this calibration, our current model was used to investigate three chemical effects (the effects of exchangeable cations, ionic strength of pore solution and the abundance of swelling clay). Four solutions were utilized to saturate the bentonite samples, namely: distilled water (representing the 0 mol NaCl), 0.1 mol NaCl, 2.5 mol NaCl, and 5.5 mol NaCl. The initial smectite volume fraction was determined by the laboratory measurement, and its change over time and space was based on the simulation results. The osmotic suction in the simulation was obtained from the chemical model. The only parameters to be calibrated are the values of each mineral's β_m^i. Using simulations on swelling pressure experiments, parameters of BExM were calibrated and the optimal parameters are listed in Table 2-4. The detailed definition of all parameters can be found in Lloret *et al.* (2003) and Sánchez *et al.* (2005). The void ratios e_{micro} and e_{macro} were recalculated based on the experimental data reported by Lloret *et al.* (2003).

Table 2-4. Parameters of BExM for FEBEX bentonite.

Parameters defining the Barcelona basic model for macrostructural behavior						
$\kappa = 0.030$	$\kappa_s = 0.006$	$\lambda(0) = 0.08$	$p_c = 0.5$ MPa	$r = 0.90$	$\zeta = 1$ MPa^{-1}	$p_0^* = 6.5$ MPa
$\alpha_a = 0.5$	$\alpha_0 = 1\times10^{-5}$°C	$\beta_m^{Na} = 2.574$	$\beta_m^{K} = 0.257$	$\beta_m^{Mg} = 3.346$	$\beta_m^{Ca} = 2.574$	
Parameters defining the law for microstructural behavior						
$\alpha_m = 2.1\times10^{-2}$ MPa^{-1}	$\chi = 1$					
Interaction functions						
$f_{ci} = 1 + 0.9\tanh\left[20\left(\frac{p_r}{p_0} - 0.25\right)\right]$	$f_{si} = 0.8 - 1.1\tanh\left[20\left(\frac{p_r}{p_0} - 0.25\right)\right]$					
Initial conditions						
$e_{macro} = 0.21$	$e_{micro} = 0.48$	$f_s = 0.5428$	$s_o = 0.777$ MPa	$\beta_m = 2.676\times10^{-9}$ MPa^{-1}		

The simulation results of swelling pressure test results are displayed in Figure 2-2.

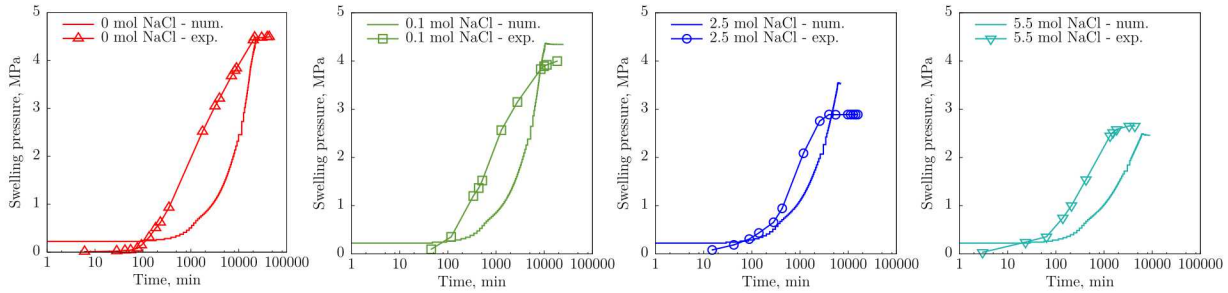

Figure 2-2. Simulation results of swelling pressure with different salinity solutions: a) Distilled water; b) 0.1 mol NaCl; c) 2.5 mol NaCl; d) 5.5 mol NaCl.

During hydration, swelling induces the stress increase in bentonite. The experiment indicated the swelling pressure of FEBEX bentonite saturated with distilled water (0 mol NaCl) was around 4.5 MPa Figure 2-2 a). When the concentration of NaCl increased, the swelling pressure decreased to about 2.5 MPa. Our simulation results provide a good agreement with the pattern of the swelling pressure decrease with respect to salinity changes. The magnitude of the swelling pressure is well captured for solutions with distilled water, 0.1 mol NaCl and 5.5 mol NaCl. The only exception is the simulation with 2.5 mol NaCl, in which our model predicted the pressure of being about 0.7 MPa higher than that in the experiment. Because the BExM requires that the initial stress should be non-zero compressive, our simulations started with the small compressive stress. Moreover, our model predicted a slow growth of the swelling pressure for around 100 minute, but later the stress accumulation became stiffer than experimental measurements.

Castellanos *et al.* (2008) conducted laboratory tests and measured vertical swelling strains of bentonite under the constant vertical stress, when samples were saturated with $CaCl_2$ solutions. However, they did not provide details of experimental records on swelling strain changes with time, but only the final swelling strain results Figure 2-3. Their experiments indicate that the solutions with same concentrations of $CaCl_2$ and NaCl induce almost equal swelling strains. From these observations, we assume that the swelling pressure causued by $CaCl_2$ is practically the same as that caused by the NaCl solution.

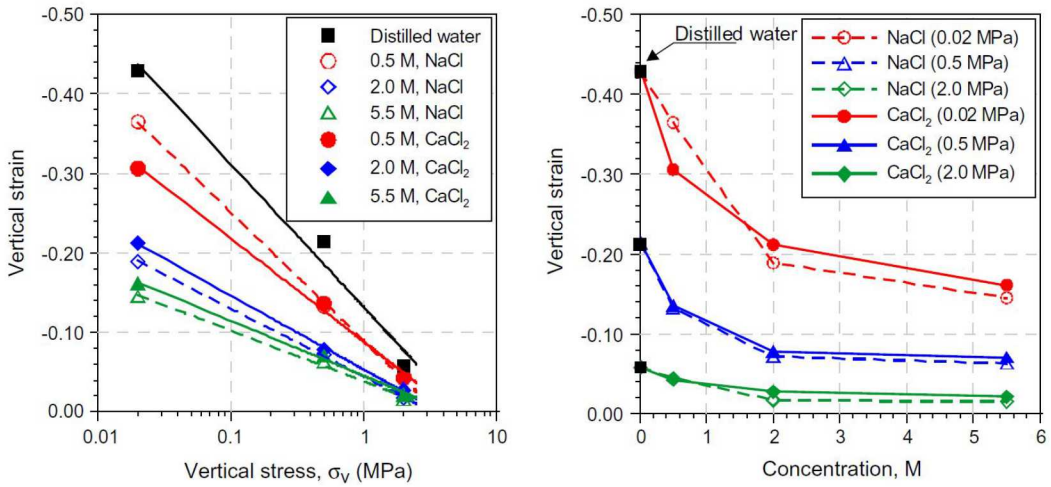

Figure 2-3. Final swelling strains of the FEBEX bentonite compacted at dry density of 1.65 g/cm^3 due to wetting with different solutions under the different vertical stresses (Castellanos *et al.*, 2006).

Using the parameters listed in Table 2-3, we launched simulations of swelling pressure tests with different salinity $CaCl_2$ solutions, and the simulation results, given in terms of final swelling pressure, are presented in Figure 2-4. This figure also provides a comparison of numerical predictions and experimental observations for the NaCl solutions. The figure illustrates that the final swelling pressure due to the $CaCl_2$ saturation is lower when the $CaCl_2$ concentration increases, which is the same as in experiments. However, the swelling pressure induced by $CaCl_2$ is lower than that induced by the NaCl solution.

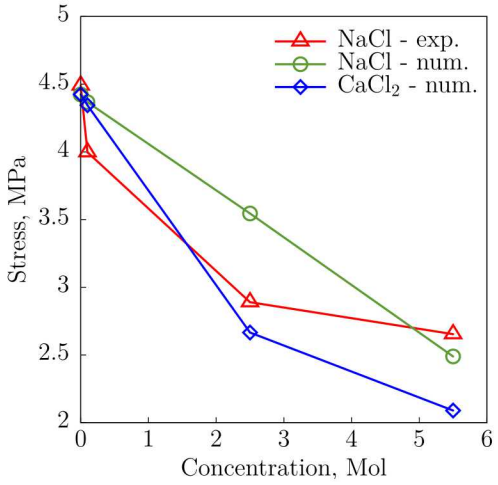

Figure 2-4. Simulation results of final swelling pressure achieved using different NaCl and $CaCl_2$ solutions, and experimental results with NaCl solutions.

Thus, based on the results of simulations of swelling pressure experiments, the BExM parameters were calibrated against laboratory experiments, incorporating the corresponding chemical reactions. Swelling pressure dependence on different salinity solutions was calibrated to account for the effects of smectite volume fraction, exchangeable cation concentration and ionic strength. The simulation results plotted in Figure 2-2 and Figure 2-4 indicate that our model with calibrated parameters can be used to predict, with reasonable accurately, the swelling pressure. Such parameters will be utilized in generic cases to study the long-term behavior of FEBEX bentonite as a buffer in the nuclear waste disposal.

2.3 Model Results

In this multiple years' effort of studying bentonite alteration using coupled THMC model, the simulator was upgraded, more constitutive relationships were tested and more scenarios were analyzed. While the previous model mostly employed an extended linear elastic model for mechanical behavior, models in this report are using the BExM for simulations of the mechanical behavior. In the past year, the BExM was recalibrated against experiments in which with chemical reactions were studied. In this section, we present new model results with newly calibrated parameters from FY18 effort.

2.3.1 THMC Results of "High T" Cases with The Dual-Structure Model

As described in Section 2.2.4, the chemical-mechanical coupling was studied based on simulations using the dual-structure model. It allowed us to evaluate how the chemical changes may affect the mechanical behavior of the EBS bentonite in terms of the effective/net and total stress. The effects considered in the model are caused by the three factors: volume fraction of smectite, exchangeable cation concentration, and osmotic suction.

To illustrate the effects of chemical reactions on stress change, we simulated a series of generic repository cases. We firstly present high temperature ("high T") cases. The results of low temperature ("low T") cases show behavior similar to the "high T" cases, and will be illustrated later. Five types of simulations were conducted to account for the effect of each chemical component shown in Table 2-5. The first is the reference case, marked THM," which is conducted without C-M coupling, and in which the mechanical behavior of bentonite depends only on the TH processes. Since the coupling is one-way, i.e. the mechanical behavior does not affect the fluid, thermal transport or chemical reactions. The evolution of temperature, liquid saturation and pore pressure is the same for THM case and other cases computed with C-M couplings, which helps distinguish the chemical effect on stress, when comparing other cases with the reference one. The second case only accounts for the effect of a volume fraction of smectite through C-M coupling, so it is referred as THMC(f_s). Similarly, the simulation referred as THMC(β_m) only takes into account the effect of exchangeable cations, and the simulation referred as THMC(s_o) only takes into account the effect of the ionic strength via osmotic suction. The simulation considering the effect of all three chemical components is marked as THMC (f_s, β_m, s_o).

Table 2-5. Summary of simulation cases with different C-M couplings.

Cases	C-M coupling		
	smectite volume fraction	exchangeable cations	ionic strength
THM	-	-	-
THMC(f_s)	Yes	-	-
THMC(β_m)	-	Yes	-
THMC(s_o)	-	-	Yes
THMC (f_s, β_m, s_o)	Yes	Yes	Yes

2.3.1.1 Effects of Volume Fraction of Smectite

According to explanation given in the previous section, the THMC(f_s) case is used to simulate the THMC processes with C-M coupling based only the smectite volume fraction. Figure 2-5 shows the evolution of the volume fraction of smectite at Points A and B. The current model predicts the dissolution of smectite, which leads to the decrease in the volume fraction of smectite. Figure 2-5 displays the smectite volume

fraction with time, indicating that f_s decreases from 54.3% to 52% at Point A, while it decreases from 54.3% to 44.5% at Point B (the layout of the Points in shown in Figure 2-1).

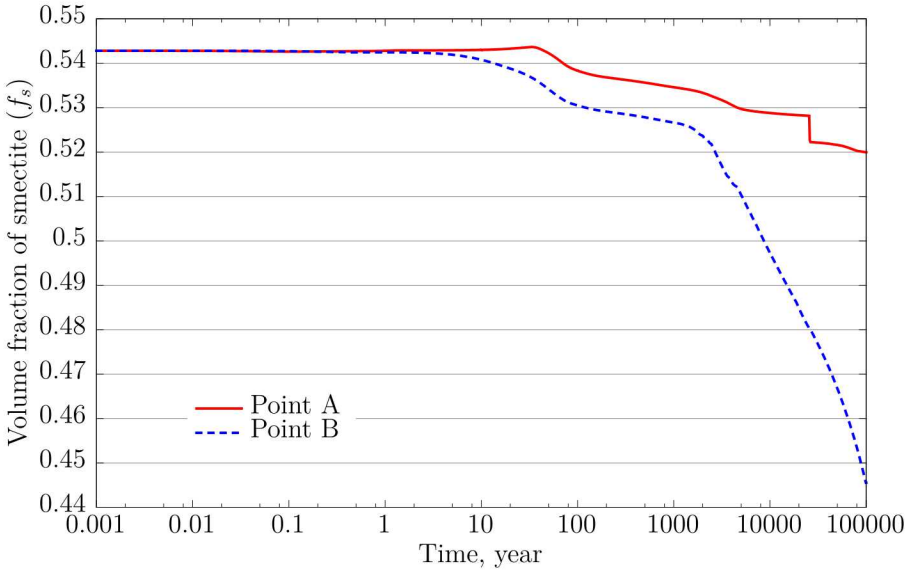

Figure 2-5. Simulation results of the evolution of the volume fraction of smectite at Points A and B with FEBEX bentonite for the "high T" scenario.

The calculated temporal changes of stresses for THMC(f_s) and THM case at Points A and B are plotted in Figure 2-6 and Figure 2-7, respectively. Since smectite is the mineral phase in bentonite to induce swelling due to hydration, the swelling capacity of bentonite tends to decrease as the smectite volume fraction decreases. However, the reduction of total mean stress at Points A and B is negligible when compared THMC(f_s) case with THM case (Figure 2-6 and Figure 2-7). At Point A, the smectite volume fraction change is small—only from 54.3% to 52%. The small stress change at Point B can be explained by the fact that the swelling due to smectite is overshadowed by the thermal pressurization and hydraulic pressurization, which may balance the stress reduction. Therefore, the stress change due to dissolution of smectite is not significant in the current model.

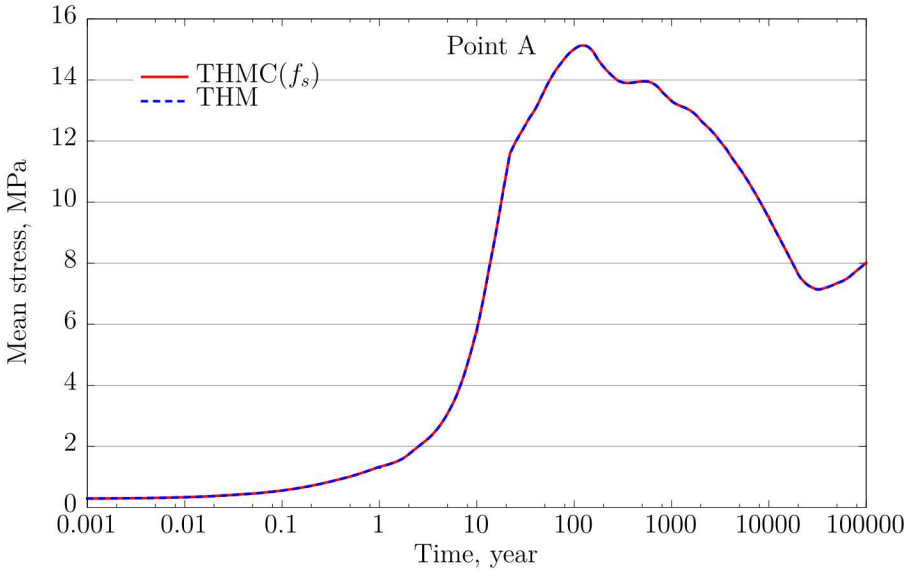

Figure 2-6. Simulation results of mean total stress at Point A with FEBEX bentonite for the THMC(f_s) and THM scenarios in "high T" case, respectively.

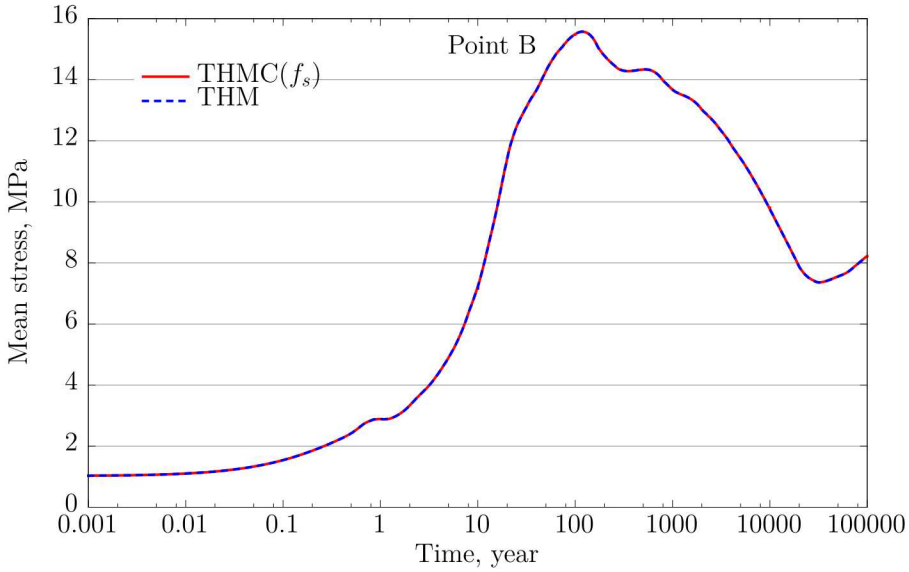

Figure 2-7. Simulation results of mean total stress at Point B with FEBEX bentonite for the THMC(f_s) and THM scenarios in "high T" case, respectively.

2.3.1.2 Effects of Exchangeable Cation Concentration

The THMC(β_m) case was designed to simulate the THMC processes with C-M coupling based only on the effect of the exchangeable cation concentration, which is represented in the model by β_m. Figure 2-8 shows the temporal evolution of β_m at Points A and B. In the current model, β_m depends on the concentration of the exchangeable cations Na, K, Ca and Mg. In FY17, simulations using other published β_m^i values, taken from the work by Sánchez *et al.* (2005), showed that the chemical reactions induce the enrichment of exchangeable sodium in the interlayer, which, in turn, caused the increase β_m. In FY18, we launched simulations with calibrated β_m^i and corrected porosity for the FEBEX bentonite. The current model predicts the initial decrease of β_m, shown in Figure 2-8, with β_m decreasing from 2.665×10^{-9} to 2.48×10^{-9} at Point A for approximately 30 years, while it decreases from 2.665×10^{-9} to 2.55×10^{-9} at Point B for about 3 years and then slightly evolves until it reaches the steady state starting from 100 years. Starting from 100 years, the values of β_m increase to 2.58×10^{-9} for both Points A and B . With the initial drop of β_m, stresses at Points A and B are reduced, then stresses increase since β_m increases.

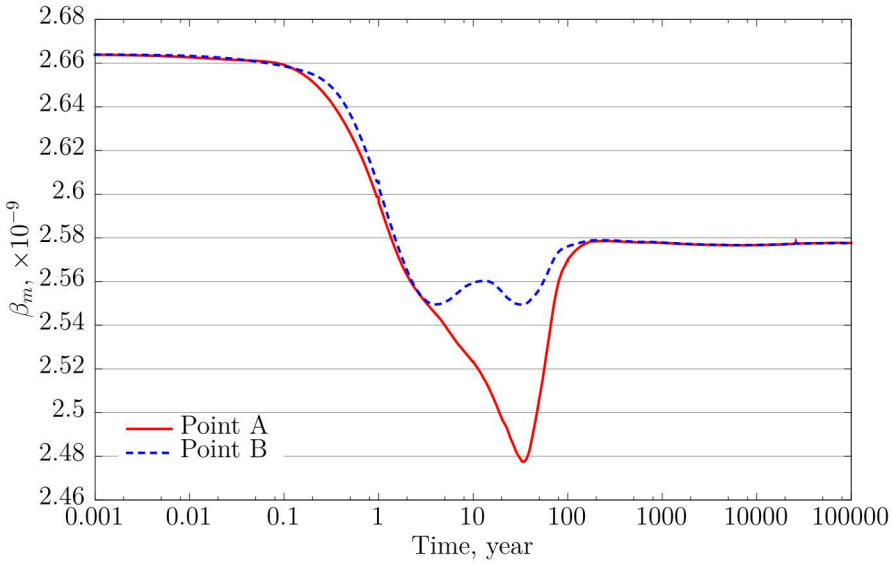

Figure 2-8. Simulation results of the evolution of β_m at Points A and B with FEBEX bentonite for the "high T" scenario.

The calculated stresses for THMC(β_m) and THM cases at Points A and B are plotted in Figure 2-9 and Figure 2-10, respectively. The initial drop of β_m tends to decrease the swelling capacity of bentonite. At Point A, the total mean stress in THMC(β_m) case is slightly lower than the total mean stress in THM case, but the difference is quite small. Around 4000 years, as β_m rises the stress in THMC(β_m) case grows to reach the stress as in the THM case. The similar behavior is not clear at Point B. The difference in stress between THMC(β_m) and THM cases is negligible, which may be due to the high confining stress from host rock in the repository. The difference in stress at Points A and B can be explained by the fact that Point B is located near the boundary between EBS and host rock, so the large modulus of host rock and high magnitude of stress inside the rock suppress the swelling of bentonite. Therefore, the stress change due to alteration of exchangeable cation cannot manifest in current model.

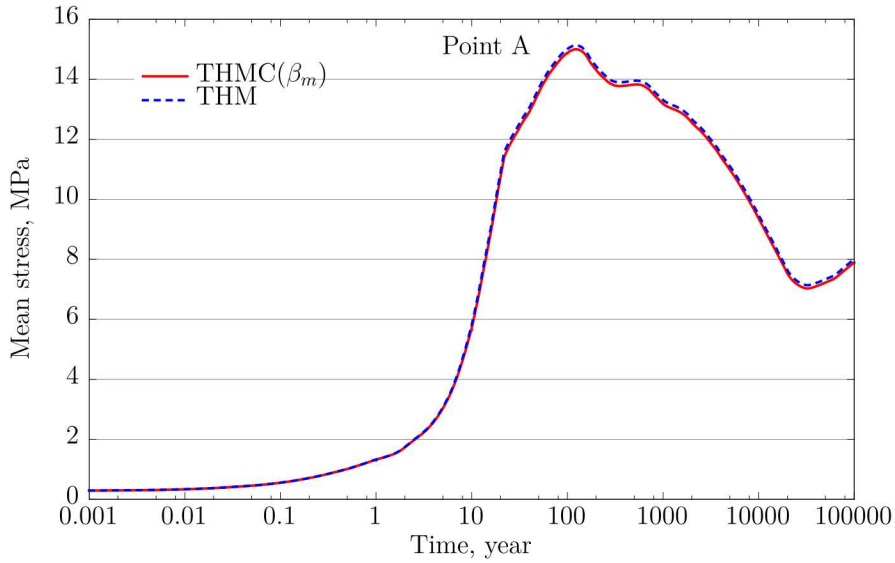

Figure 2-9. Simulation results of mean total stress at Point A with FEBEX bentonite for the THMC(β_m) and THM scenarios in "high T" case, respectively.

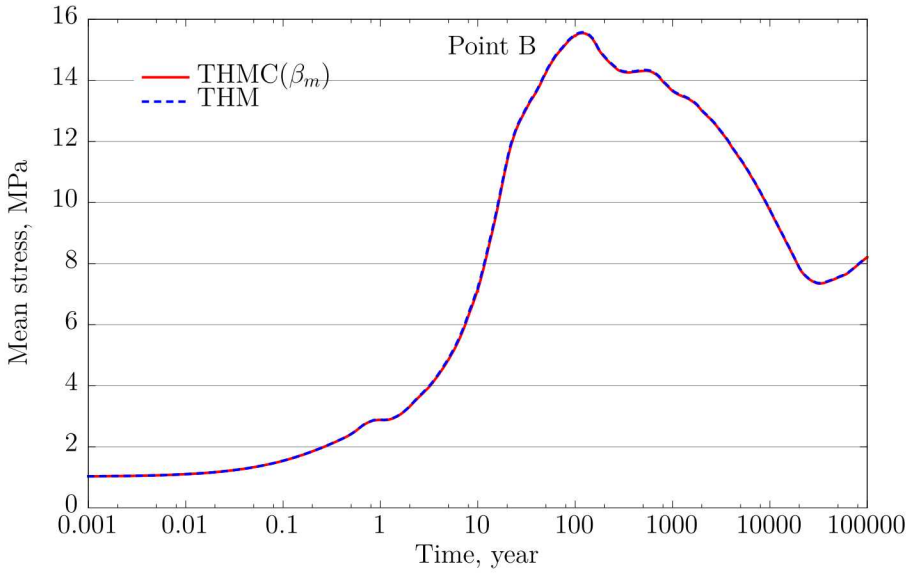

Figure 2-10. Simulation results of mean total stress at Point B with FEBEX bentonite for the THMC(β_m) and THM scenarios in "high T" case, respectively.

2.3.1.3 Effects of Ionic Strength

The THMC(s_o) case computes the THMC processes with the effect of ionic strength via osmotic suction. Figure 2-11 shows the evolution of osmotic suction at Points A and B. For Point A, the osmotic suction increases to two peaks about 2.8 MPa at around 3 years and 80 years, then starts to decrease until the end of simulation. At Point B, the peak magnitude 2.75 MPa is reached at around 100 years. The osmotic suction reduces to 1.75 MPa at both points by the end of the simulation. The increase in osmotic suction tends to suppress the swelling of bentonite whereas the reduction of osmotic suction makes bentonite swell more.

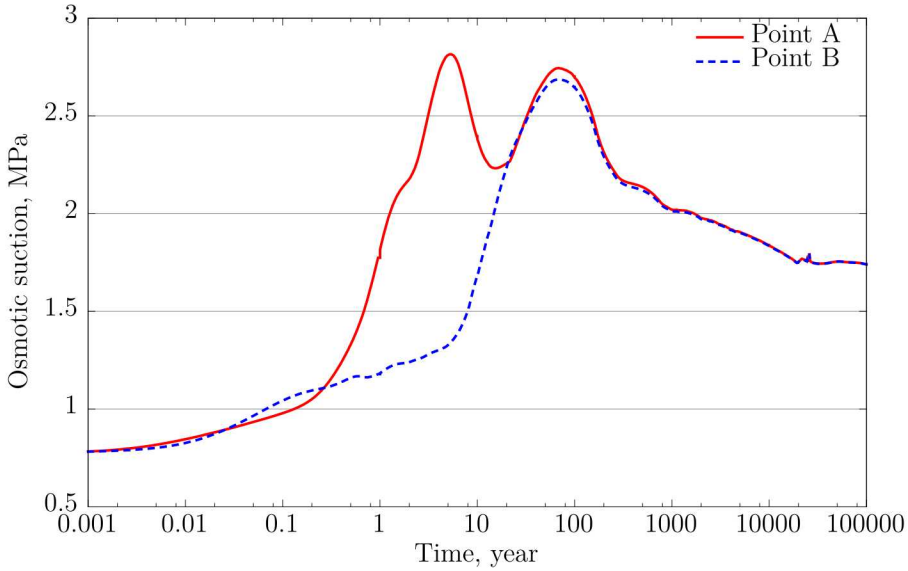

Figure 2-11. Simulation results of osmotic suction evolutions at Points A and B with FEBEX bentonite for the "high T" scenario.

The calculated temporal variations of stresses for THMC(s_o) and THM cases at Points A and B are plotted in Figure 2-12 and Figure 2-13 respectively. The osmotic suction causes the stress at Points A and B both to decrease compared to the THM case. The total mean stress at Point A in the THMC(s_o) case is about 1 MPa lower than that in the THM case at around 100 years. After that, the osmotic suction decreases continuously, so the stress difference between THMC(s_o) and THM cases is reduced. The similar behavior is also observed at Point B (Figure 2-13). The total mean stress at Point B in the THMC(s_o) case is about 0.6 MPa lower than that in the THM case at around 100 years, and the stress in THMC(s_o) is almost the same as the stress in the THM case after 4000 years. It is clear that the increase in osmotic suction leads to the decrease in stress due to the suppression of swelling by osmotic pressure, and vice versa.

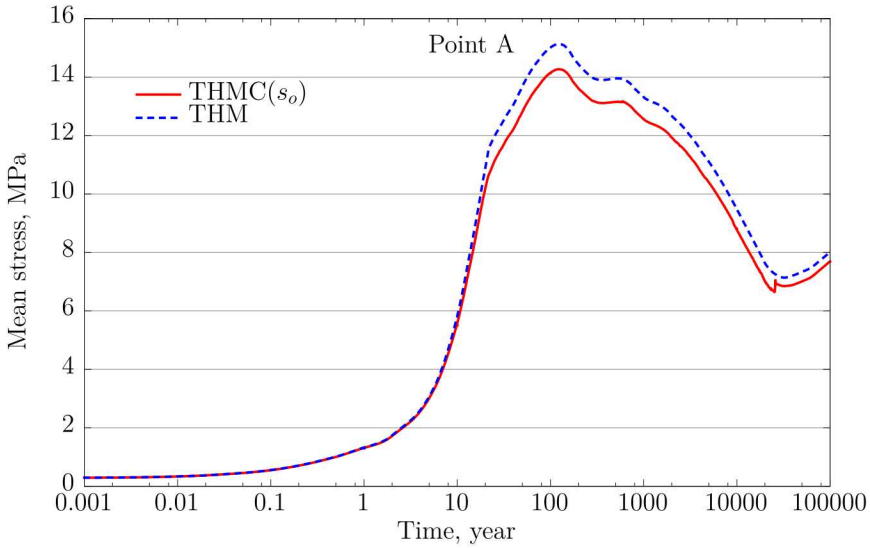

Figure 2-12. Simulation results of mean total stress at Point A with FEBEX bentonite for the THMC(s_o) and THM scenarios in "high T" case, respectively.

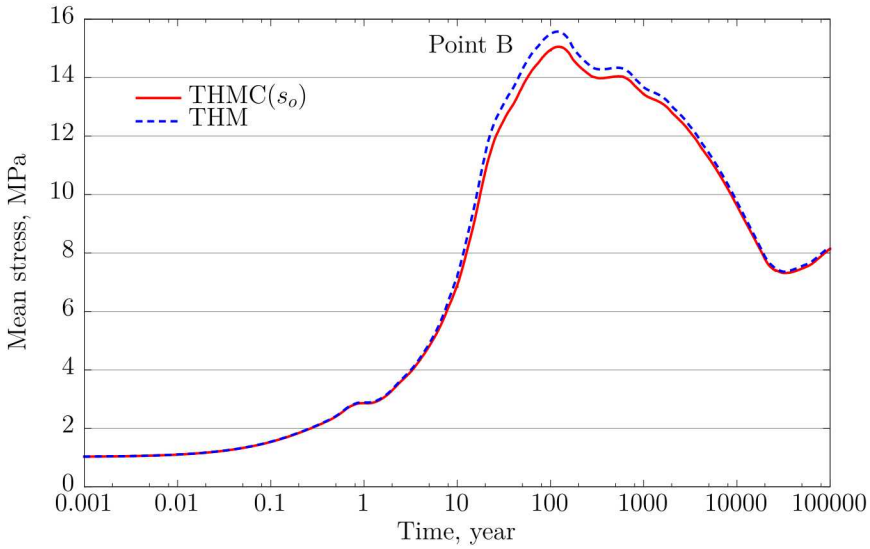

Figure 2-13. Simulation results of mean total stress at Point B with FEBEX bentonite for the THMC(s_o) and THM scenarios in "high T" case, respectively.

2.3.1.4 Combined Effects of Chemical Reactions

The THMC(f_s, β_m, s_o) case takes into account the alteration of mechanical behavior by the three chemical factors: the change in the volume fraction of smectite, change in exchangeable cations, and ionic strength contribution. These simulations are used to assess whether and how the combined effect of chemical changes enhance or suppress the stress.

Figure 2-14 and Figure 2-15 show the temporal evolution of the mean total stress at Points A and B for the THMC(f_s, β_m, s_o) and THM cases, caused by the combined effect of chemical changes on stress. At Point A, the peak stress in bentonite is 14.2 MPa for the THMC(f_s, β_m, s_o) case, and 15.2 MPa for the THM case, and both are at around 100 years. Then, the total stress decreases until 30,000 years, and then the stress increases again to reach the hydrostatic status. The difference in stress between the THM and THMC" cases is 1 MPa at around 100 years, and decreases to 0.5 MPa in the long term. Apparently,

chemical changes in bentonite lead to the lower total stress at Point A, indicating that the swelling capacity of the bentonite is reduced. At Point B, the behavior is similar, with the peak stress in bentonite of 15 MPa for the THMC(f_s, β_m, s_o) case and 15.5 MPa for the THM case at around 100 years. The final stress at Point B in the THMC(f_s, β_m, s_o) case is 0.1 MPa less than that in the THM case.

The dual-structure model cannot be easily used for simulations of the swelling stress, because the micro-swelling strain is calculated directly in the framework of the model. Moreover, the non-linear plasticity induced from both micro- and macro-structures increases the difficulty to distinguish the swelling stress from the total stress. In addition to the total mean stress, $\bar{\sigma}$, we present the mean effective/net stress, noted as $\hat{\sigma}$ (mean net stress for unsaturated bentonite, and mean effective stress for fully saturated bentonite) in Figure 2-14 and Figure 2-15 to illustrate the accumulation of stress in the solid skeleton of bentonite. The difference between mean stress $\bar{\sigma}$ and effective/net stress $\hat{\sigma}$ ($\hat{\sigma}$ stands for mean effective stress $\hat{p}$ after bentonite is fully saturated or mean net stress p when bentonite is unsaturated) is the pore pressure. The condition for the simulation is unsaturated bentonite. During unsaturated phase, $\hat{\sigma}$ is net stress and it goes up to the peak stress at around 20 years until the bentonite becomes fully saturated, and then $\hat{\sigma}$ become effective stress for the saturated phase. At Point A, mean effective/net stresses peak at about 6.3 MPa in THMC(f_s, β_m, s_o) case, and 7.4 MPa in the THM case at around 20 years, then decreasing to 4.5 MPa and 5 MPa, respectively. For the THMC(f_s, β_m, s_o) case, the stress is always lower than that for the THM case. Similar stress behavior is at Point B, where the mean effective/net stress reaches the highest value of 6.2 MPa in THMC(f_s, β_m, s_o) case, and 5.5 MPa in the THM case. Then, after the bentonite is fully saturated, the effective/net stress at Point B decreases to 5.2 MPa in the THMC(f_s, β_m, s_o) case ,and 5.3 MPa in the THM case.

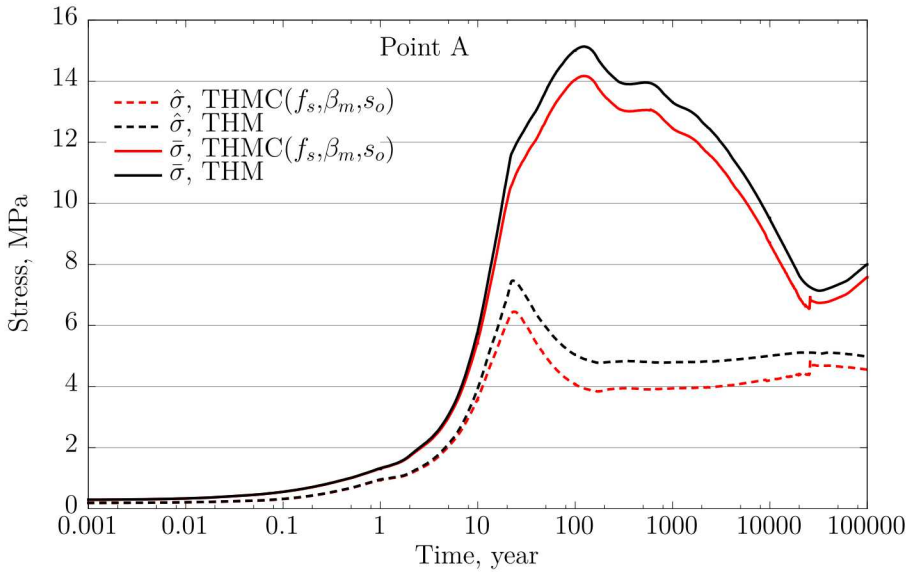

Figure 2-14. Simulation results of mean effective/net stress, $\hat{\sigma}$, and total mean stress, $\bar{\sigma}$, at Point A with FEBEX bentonite for the THMC(f_s,β_m,s_o) and THM scenarios in "high T" case, respectively.

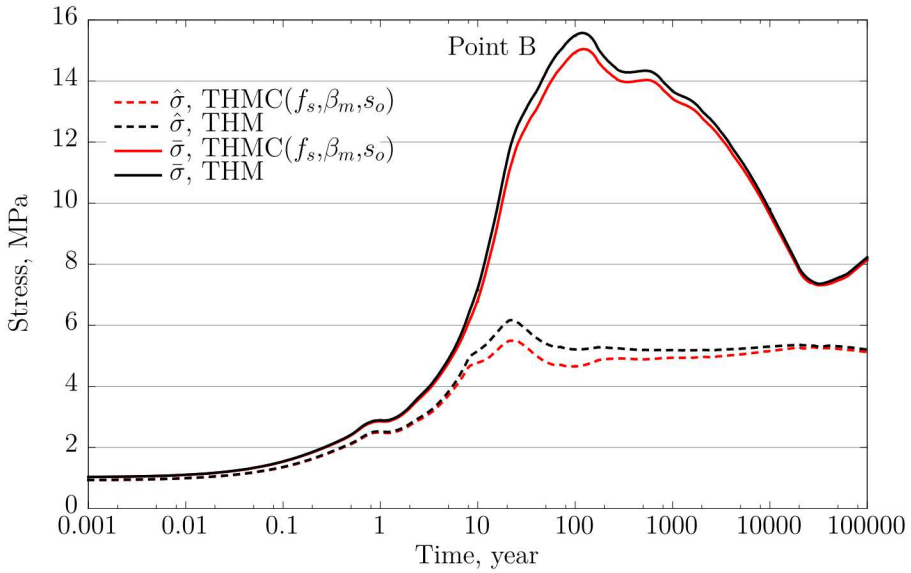

Figure 2-15. Simulation results of stress evolutions at Point B with FEBEX bentonite for the THMC(f_s,β_m,s_o) and THM scenarios in "high T" case, respectively.

Figure 2-16 shows the total stress evolution at Point A for the "high T" cases with different C-M coupling schemes. Overall, the chemical effect leads to the lower stress. The stress calculated without any C-M coupling (THM) almost the same as in the THMC(f_s) scenario used to evaluate the effect of the volume fraction of smectite, indicating that changes in volume fraction of smectite have only minimal effect on stress. In FY17, the stress computed with only exchanged cation concentration (THMC(β_m)) was higher than the THM case, which revealed that exchanged cations increased the stress. However, in FY18, with the calibrated β_m^i, the stress computed with only exchanged cation concentration (THMC(β_m)) is slightly lower than that in the THM case, which reveals that exchanged cations decreased the stress. Overall, the difference between results of simulations for the THM, THMC(f_s) and THMC(β_m) scenarios is negligible. The water infiltration from the host rock leads to an increase of ionic strength of pore water in the bentonite barrier, which, in turn, causes the increase in osmotic suction. As a result, the swelling capacity of bentonite decreases, which is manifested by the reduction of the total stress for the case of THMC(s_o)." Eventually, the reduction effect of ionic strength via osmotic suction on stress outplays the increase effect of exchanged cations on stress, and consequently chemical changes result in lower stress overall. The combined effect of chemical factors leads to the lower stress compared to the THM model, which can be explained by the dominating impact of osmotic suction, whereas the effects induced by f_s and β_m are smaller. The stress evolutions for all cases at Point B are plotted in Figure 2-17, showing the similar curves. The results of simulations of the THMC(f_s,β_m,s_o) case are close to those for the THMC(s_o) case at Point B. The combined chemical effect at Points A and B is practically the same, showing the lower stress than that for the THM scenario.

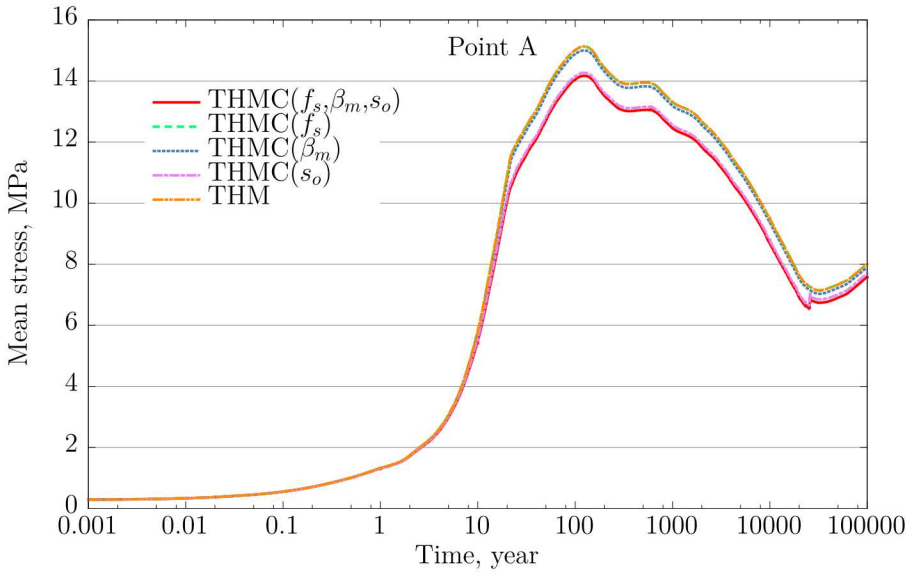

Figure 2-16. Simulation results of mean total stress at Point A with FEBEX bentonite in "high T" case. Different C-M couplings are considered and computed.

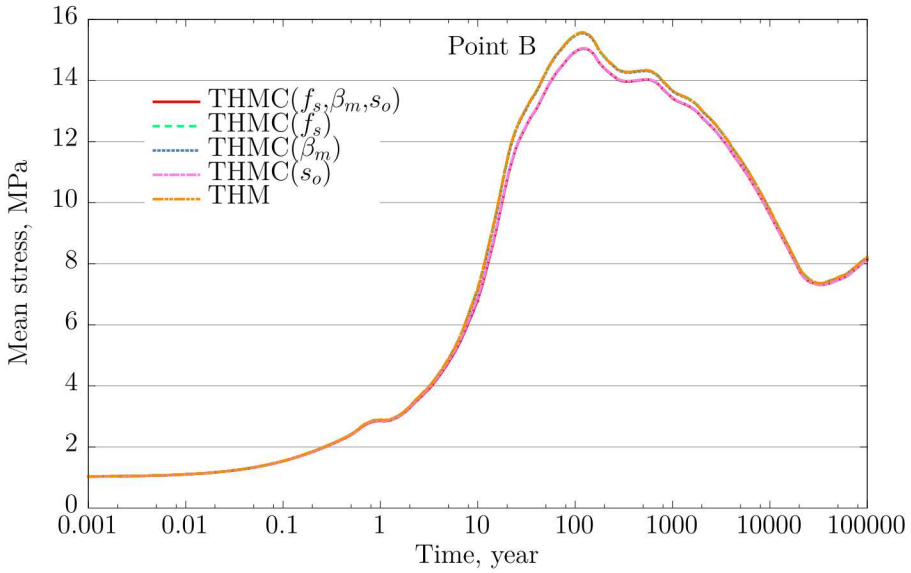

Figure 2-17. Simulation results of mean total stress at Point B with FEBEX bentonite in "high T" case. Different C-M couplings are considered and computed.

2.3.2 THMC Results of "Low T" Cases with the Dual-Structure Model

In this section, we present the results of simulations for the low temperature ("low T") cases. The same as the "high T" case, five different simulations were conducted to account for the effect of each chemical component. The results of "low T" cases show the behavior is similar to that for the "high T" cases. The changes of smectite volume fraction, exchangeable cation concentration and ionic strength follow the same trends as for "high T" cases, but with smaller magnitude evolution. Since the applied temperature is lower, chemical changes at Point A almost have the same magnitude as those at Point B. For the sake of

simplicity, we do not illustrate the simulation results case by case, but present all effects together compared with THM case without any C-M coupling.

2.3.2.1 Combined Effects of Chemical Reactions

Figure 2-18 and Figure 2-19 show the evolution of the mean total stress at Points A and B for THMC(f_s, β_m, s_o) and THM cases, and clearly demonstrate the effect of chemical changes on the stress for the "low T" case. At Point A, the peak stress in bentonite is 8.5 MPa for the THMC(f_s, β_m, s_o) case and 9.5 MPa for the THM case, both at around 100 years. Then the total stresses decrease until 30,000 years, after which the stresses increase again to reach the hydrostatic status. The difference in stresses between THM and THMC" cases is 1 MPa at around 100 years, and decrease to 0.7 MPa in the long term. The same as for the "high T" case, chemical changes in bentonite lead to lower total stresses at Point A, and the swelling capacity of the bentonite is reduced. At Point B, the behavior is similar. The peak stress in bentonite at Point B is 9 MPa for the THMC(f_s, β_m, s_o) case, and 10 MPa for the THM case at around 100 years. The final stress at Point B in the THMC(f_s, β_m, s_o) case is 0.8 MPa less than that in the THM case.

Figure 2-18 and Figure 2-19 also illustrate the accumulation of stress in the solid skeleton of bentonite in term of mean effective/net stress, $\hat{\sigma}$, which is the mean stress $\bar{\sigma}$ minus the pore pressure. At the beginning of the simulation, bentonite is unsaturated. During the unsaturated phase, $\hat{\sigma}$ is net stress, which increases to reach the peak stress at around 20 years until the bentonite becomes fully saturated, and then $\hat{\sigma}$ becomes the effective stress for the saturated phase. At Point A, the mean effective/net stresses peaks at about 6.2 MPa in the THMC(f_s, β_m, s_o) case, and at 7 MPa in THM case at around 20 years, then the stresses decrease to 5.3 MPa and 6.2 MPa, respectively. The THMC(f_s, β_m, s_o) case always has lower stress than the THM case. Point B is characterized by the similar behavior, and the mean effective/net stresses reach the highest values of 6.4 MPa in the THMC(f_s, β_m, s_o) case and 7.2 MPa in the THM case. Then, when the bentonite is fully saturated, the effective/net stress at Point B decreases to 5.7 MPa in the THMC(f_s, β_m, s_o) case and 6.5 MPa in the THM case.

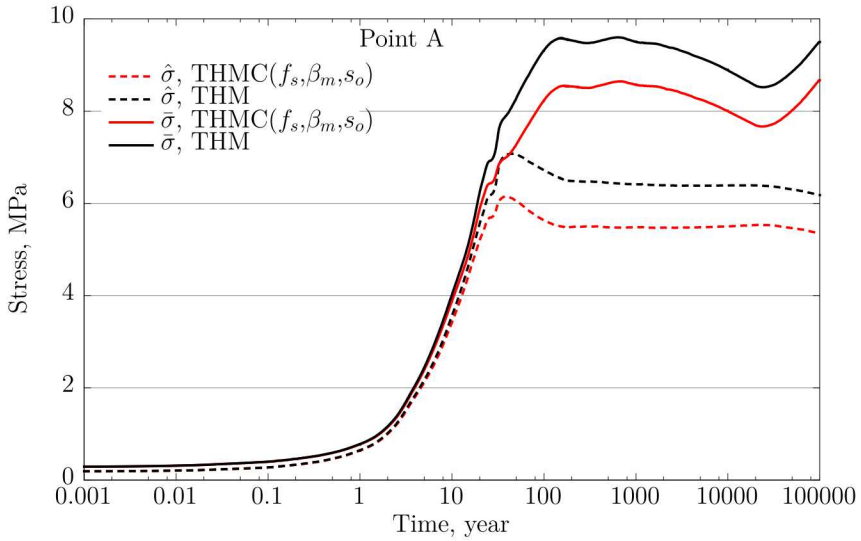

Figure 2-18. Simulation results of mean effective/net stress, $\hat{\sigma}$, and total mean stress, $\bar{\sigma}$, at Point A with FEBEX bentonite for the THMC(f_s,β_m,s_o) and THM scenarios in "low T" case, respectively.

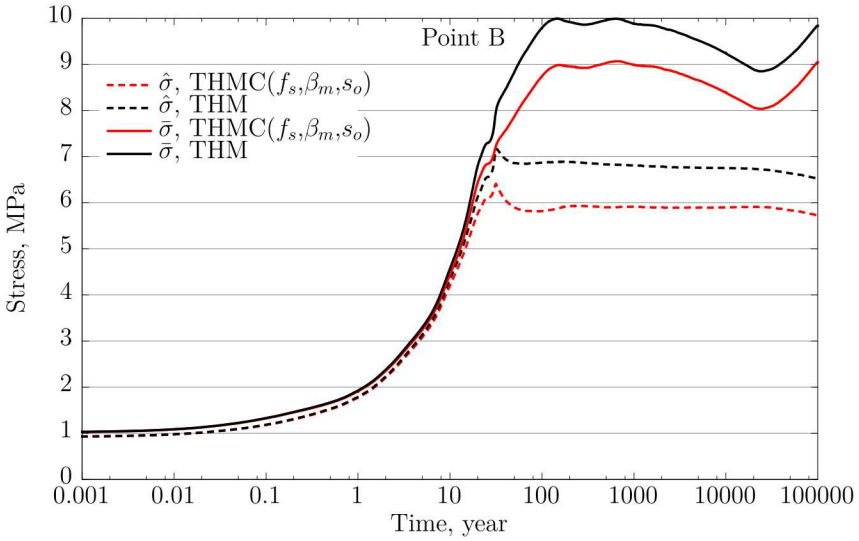

Figure 2-19. Simulation results of stress evolutions at Point B with FEBEX bentonite for the THMC(f_s,β_m,s_o) and THM scenarios in "low T" case, respectively.

Figure 2-20 shows the total stress evolution at Point A for "low T" cases with different C-M coupling schemes. Overall, the chemical effect lowers the stress. The same conclusion can be drawn for the "high T" case regarding simulations of changes in the volume fraction of smectite, which have only minimal effect on the stress. Overall, exchanged cations have a negative effect on the stress. As a result of osmotic suction changes, the swelling capacity of bentonite decreases, which is revealed by the reduction of the total stress for the case of THMC(s_o). The negative effect of ionic strength via osmotic suction on the stress outplays the positive effect of exchanged cations on stress, and, consequently, the combined chemical effect leads to a lower stress overall. The overall chemical effects lead to the lower stress compared to that of the THM model, since the dominating effect of the osmotic suction. The stress evolutions for all cases at Point B are plotted in Figure 2-21, in which similar observations were obtained.

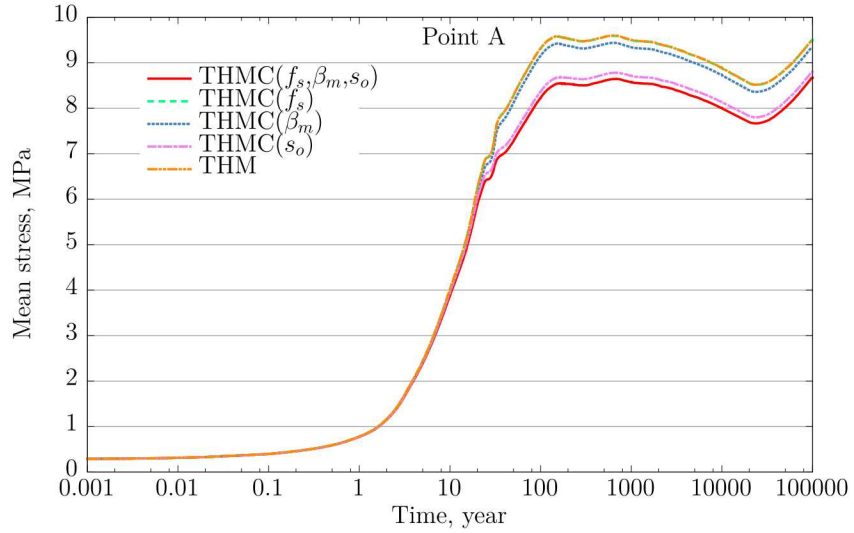

Figure 2-20. Simulation results of mean total stress at Point A with FEBEX bentonite in "low T" case. Different C-M couplings are considered and computed.

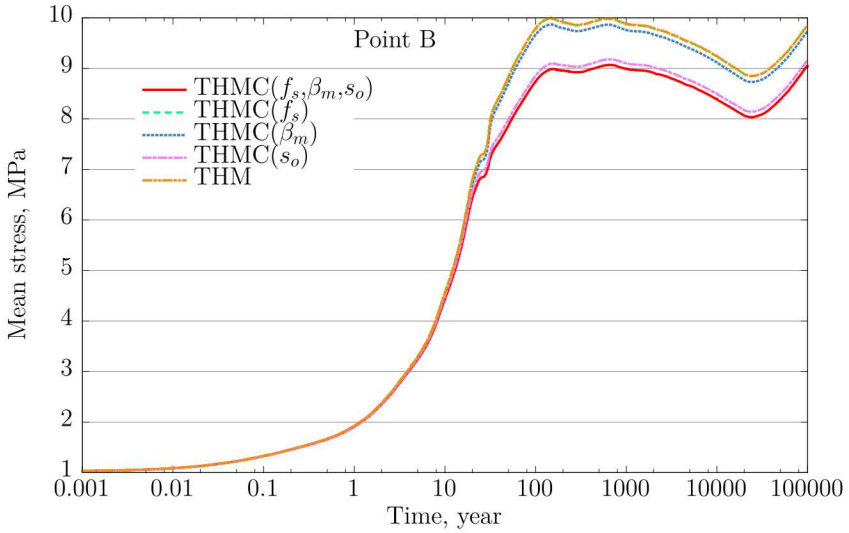

Figure 2-21. Simulation results of mean total stress at Point B with FEBEX bentonite in "low T" case. Different C-M couplings are considered and computed.

2.3.3 Comparison Between THMC Results of "Low T" and "High T" Cases

Figure 2-22 and Figure 2-23 show the mean total stress changes at Points A and B for both "low T" and "high T" cases. At the beginning of the simulation, stresses in "high T" cases are higher than the stresses in "low T" cases, due to the temperature increase and pore pressure build-up from the heat expected to emanate from the disposed waste. Since a higher bentonite pore pressure is developed in "high T" cases, the mean total stress is higher than that for "low T", the corresponding peak stress is higher for the "high T" cases, too. However, before the bentonite is fully saturated, the high stress induces a micro-structure that penetrates into the macro-structure, causing the strength degradation of the macro-structure. As a result, when the system finally reaches a hydrostatic equilibrium, the final stress in the "high T" cases is lower than that in the corresponding "low T" cases, as demonstrated in Figure 2-22 and Figure 2-23.

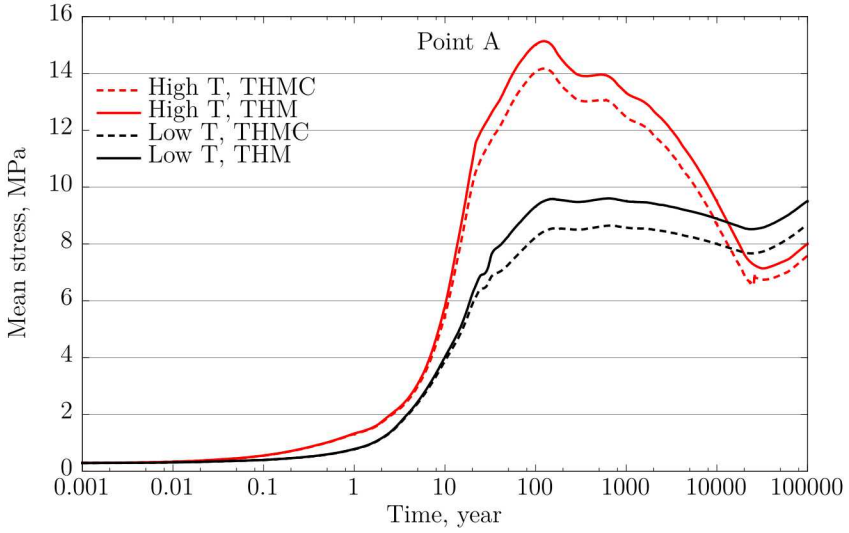

Figure 2-22. Simulation results of mean total stress at Point A with FEBEX bentonite for the "low T" and "high T" scenarios, respectively.

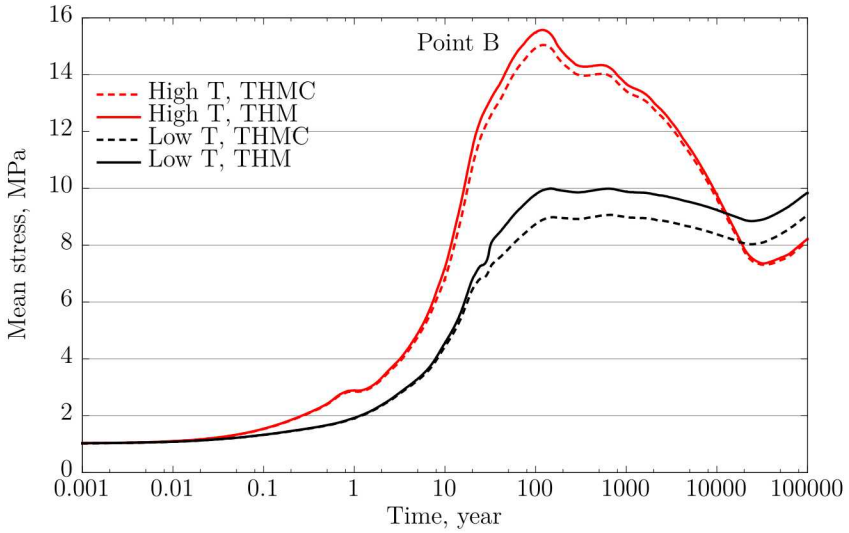

Figure 2-23. Simulation results of mean total stress at Point B with FEBEX bentonite for the "low T" and "high T" scenarios, respectively.

The macro-structural modulus is another way to indicate the stress reduction in "high T" cases. Subjected to hydration, bentonite swells, inducing the stress increase in bentonite. Figure 2-24 shows that at the beginning, the "high T" cases display the larger macro-structural stiffness than the "low T" cases, which can be explained by the presence of high energy generated from the heater. When approaching 20 years, both "high T" and "low T" cases reach the peak of macro bulk moduli, and after 20 years the macro-structural moduli in "high T" cases drop much more than the "low T" cases. Since the high stress induces a micro-structure that penetrates into macro-structure, it causes the strength degradation of macro-structure. In "high T" cases, the invasion by micro-structure is more than the "low T" cases, inducing more "collapse" in macro-structure. Because of that, the stiffness reduces more than the ones in "low T" cases.

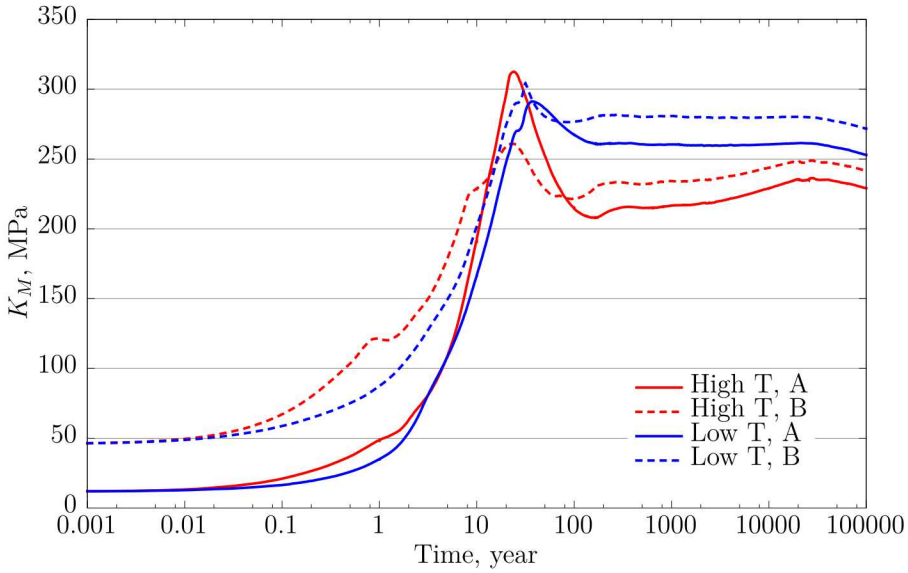

Figure 2-24. Simulation results of macro-structural bulk moduli at Points A and B with FEBEX bentonite for the "low T" and "high T" scenarios, respectively.

2.4 Summary and Future Work

2.4.1 Summary of Current Modeling Work

Investigations of the thermal limit of a clay repository are very important for the design of a nuclear waste repository. A reliable evaluation of the impact of a long-term geochemical on mechanical behavior, using a coupled THMC model, is critical for studying whether a clay repository can sustain high (>100 °C) temperature. To increase the model reliability, we first implemented a more mechanistic constitutive relationship for C-M coupling, the BExM, then calibrated the key parameters based on the results of the laboratory test, which were used for a large scale generic model. In FY 18, we simulated a series of swelling pressure tests, in which partially saturated FEBEX bentonite was saturated with various salinity solutions. By using simulations to reproduce the measured swelling pressure, we were able to calibrate the parameters related to the C-M coupling, which affect the smectite volume fraction, and exchangeable cations and the effect of the ionic strength on the stress were taken into account. Eventually, the THMC model, with calibrated C-M coupling parameters, was used to perform simulations for the generic case of nuclear waste disposal. The following conclusions have been drawn from the modeling results:

- Dissolution of smectite leads to the decrease in the volume fraction of smectite, which, in turn, decreases the stress. The new model predicts the reduction of exchangeable sodium in the interlayer, which is different from what was found in FY17. The change in exchangeable cations also causes the decrease in stress. Infiltration of higher salinity water from the surrounding clay formation to the EBS bentonite leads to the increase in osmotic suction and subsequently lowers the stress. The combination of these three effects as a whole reduces both the total stress and the effective/net stress in the bentonite buffer in the “high T” cases. The difference between the computed stress in bentonite with C-M coupling (THMC”) and without C-M coupling (THM) ranges within 1 MPa.
- The THMC model, using BExM, showed less influence of the chemical effect on the stress compared to the previous THMC model with the extended linear swelling model (Zheng *et al.*, 2015). The primary reason is that a previous extended linear swelling model computed the swelling pressure as a linear state function of material’s saturation, which predicted a higher stress accumulation than the elasto-plastical model, such as BExM. The BExM model generates more plastical strain to resist the increased swelling stress, and the stress is redistributed in the material. The other reasons are: the mechanical-chemical coupling via BExM and the dissolution of smectite were factored in directly into the model via the volume fraction of smectite by means of modifying the bulk modulus for micro-structure, and the bulk modulus is a function of stress and changed significantly in the model. Moreover, the bulk modulus changes by smectite dissolution were overshadowed by the stress change.

2.4.2 Future Work

The developed coupled THMC model has greatly improved our understanding of the coupled processes contributing to chemical and mechanical alteration in the EBS bentonite and NS argillite formations, which helped answer questions regarding the thermal limit of EBS bentonite in the clay repository. Nevertheless, the simulator for conducting modeling of coupled THMC processes causing the alteration of bentonite and clay formations needs to be further improved. In the remaining time of FY18 and in FY19 we are planning:

- To investigate chemical controls on montmorillonite structure and swelling pressure. After implementing C-M in TOUGHREACT-FLAC via BExM, we are going to evaluate how the chemical change controls the montmorillonite structure and swelling pressure. We are planning to investigate how exchangeable cations affect swelling of montmorillonite, to improve an empirical

relationship describing this process, and to implement it in our simulator. Research will be conducted to calibrate model parameters. We also propose to conduct complementary experimental and simulation studies to evaluate the swelling clay structure as a function of the solution composition, and to derive an improved constitutional model to describe variations of the swelling pressure in compacted clay barriers.

- To derive a reduced order model that can be integrated into the performance assessment model GDSA. The importance of bentonite alteration and its impact on mechanical behavior needs to be integrated to PA model to assess its relevance to the safety of a repository. Specifically, we will first implement the bentonite swelling models, such as linear swelling, state surface, BBM, and BExM into a parallel THMC simulator TREACTMECH, and will then derive a reduced order model based on the large number of THMC simulations.

We will also conduct other exploratory modeling studies, including the following activities:

- Numerical verification of the applicability of BExM with C-M coupling based on laboratory and field tests with bentonite other than FEBEX bentonite, and simulations of *in-situ* experiments. Model for Kunigel-V1 bentonite, which was used in the previous modeling study (e.g., Zheng et al., 2015) will be improved and the robustness of x C-M coupling via BExM will be tested.
- Comparing BExM simulations with computations by other available constitutive models to investigate the material behavior under the same environmental conditions and to better understand a possibility of using BExM for other materials.

3. COUPLED THMC MODELING OF THE EVOLUTION OF BENTONITE IN FEBEX-DP

3.1 Introduction

The design of clay and crystalline radioactive waste repository typically involves investigations of a multi-barrier system. In addition to the investigations of a natural barrier system (NBS), i.e. the host rock and its surrounding subsurface environment, a multi-barrier system is also expected to include an engineered barrier system (EBS). The EBS represents the man-made, engineered materials placed within a repository, including the waste form, waste canisters, buffer materials, backfill, and seals.

The most common buffer material for EBS is compacted bentonite, which features low permeability and high retardation of radionuclide transport. The safety functions of EBS bentonite should include limiting transport in the near field, damping the shear movement of the host rock, preventing the sinking of canisters (if emplaced in the center of the tunnel), limiting pressure on the canister and rock, and reducing the effect of microbial activity. To assess whether EBS bentonite can maintain these desirable features, when undergoing heating from the waste package and hydration from the host rock, we need a thorough understanding of the thermal, hydrological, mechanical, and chemical evolution of bentonite under disposal conditions. While numerous laboratory experiments, field tests, and numerical models have been conducted to improve the understanding of individual processes or coupled THC/THM processes, there is a lack of studies on coupled THMC processes due to the challenges of conducting experiments and developing models that could be used to evaluate the THMC processes. Recently in the Spend Fuel and Waste Science and Technology (SFWST) program, coupled THMC models have been developed for a generic disposal system in clayey host rock with EBS bentonite (Liu et al., 2013; Zheng et al., 2014; Zheng et al., 2015b). However, model validation was difficult for lack of THMC data from long-term, large-scale experiments. The FEBEX (Full-scale Engineered Barrier EXperiment) *in situ* test (ENRESA, 2000), which has been operated for 18 years, provides a unique opportunity for validating coupled THMC models.

The FEBEX-DP project is comprised of extensive THMC and biological characterization of bentonite, and includes the development of numerical models. In the FEBEX *in situ* test, two heaters surrounded by bentonite blocks about 0.7 m thick were emplaced in a tunnel excavated in granite. The heaters were switched on in 1997. In 2002, Heater #1 was dismantled; in 2015, the Heater #2 was dismantled. LBNL/DOE joined the FEBEX-DP project in FY15. The ultimate goal of the project is to use the THMC data from FEBEX-DP to validate THMC models, and therefore to enhance our understanding of coupled THMC processes. From 2015 to 2017, extensive THMC characterization of bentonite samples, collected during the dismantling of the Heater #2, were carried out by partners of FEBEX-DP. Ion concentrations in the pore-water of bentonite were obtained via an indirect method, aqueous extract. The results of this analysis were used to initially constrain the chemical model. In FY18, we first used the geochemical model to accurately infer the ion concentrations in pore-water for one of the bentonite sampling sections. After that, we critically analyzed the project reports (e.g. Villar et al., 2017) to deduce available geochemical data other than ion concentrations in pore-water of bentonite. Finally, extensive calibration was conducted to determine the factual combination of parameter values and reactions, attempting to explain the available geochemical data, as well as the THM data with the THMC model. In this Section of the report, a discussion of investigations on the chemical evolution of bentonite barrier is presented based on the experimental data and results of numerical modeling.

3.2 A Brief Description of FEBEX Experiments

3.2.1 Test Description

FEBEX (**F**ull-scale **E**ngineered **B**arrier **Ex**periment in crystalline host rock) is a research and demonstration project that was initiated by ENRESA (Spain). Its objective was to demonstrate the feasibility of constructing an engineered barrier system and to study the behavior of components in the near-field for a high-level radioactive waste (HLW) repository in crystalline rock. Specifically, the project aimed to demonstrate the feasibility of fabricating and assembling the EBS and developing methodologies and models for the evaluation of the thermo-hydro-mechanical (THM) and thermo-hydro-chemical (THC) behavior of the near-field (ENRESA, 2000). These objectives are to be achieved through the combination of *in situ* and mock-up tests, numerous small-scale laboratory tests, and THC/THM modeling.

The centerpiece of the FEBEX experiments is, of course, the *in situ* test conducted at the Grimsel Underground Laboratory, Switzerland. The test consists of five basic components: the drift, the heating system, the bentonite barrier, the instrumentation, and the monitoring and control system (Figure 4-2). The drift is 70.4 m long and 2.28 m in diameter. The test area, which was sealed with a concrete plug, is located at the last 17.4 m of the drift where heaters, bentonite and instrumentation were installed. The main elements of the heating system are two heaters (#1 and #2), 1 m apart, which simulate full-sized canisters. Heaters were placed inside a cylindrical steel liner. Each heater is made of carbon steel, measures 4.54 m in length and 0.9 m in diameter, and has a wall thickness of 0.1 m. Heaters were operated at a constant power output of 1200 W/heater during the first 20 days and 2000 W/heater for the following 33 days. Afterwards, the heaters were switched to a constant-temperature control mode to maintain a maximum temperature of 100 ºC at the steel liner/bentonite interface.
The bentonite barrier is made of blocks of highly compacted bentonite, arranged in vertical sections normal to the axis of the tunnel. There were gaps between blocks, but the volume of gaps has not been reliably estimated. Although the dismantling of bentonite barrier revealed that all gaps were sealed, these gaps might affect the initial hydration of bentonite, but such an effect is difficult to incorporate into models. The average values of the initial dry density and the water content of compacted bentonite blocks are 1.7 g/cm^3 and 14.4%, respectively.

The *in situ* test began on February 27, 1997. Heater #1 was switched off in February 2002 and dismantled from May to September in 2002. The buffer and all components were removed up to a distance of 2 meters from Heater #2 to minimize disturbance of the non-dismantled area. A dummy steel cylinder with a length of 1 m was inserted in the void remained in the center of the buffer (Figure 3-2). The description of the partial dismantling operation is given by Bárcena et al. (2003). A comprehensive post-mortem bentonite sampling and analysis program was performed on the solid and liquid phases to evaluate the physical and chemical changes induced by the combined effect of heating and hydration and to test THM and THC model predictions (ENRESA 2006a; b).

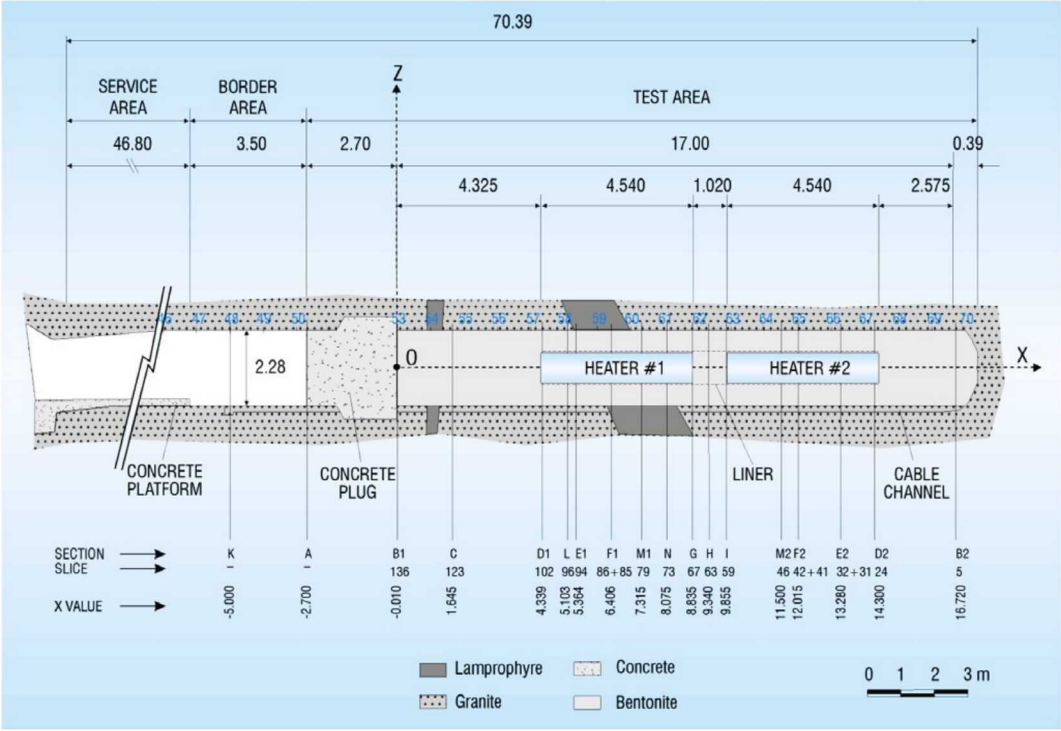

Figure 3-1. The initial configuration of the FEBEX *in situ* test at the Grimsel underground laboratory (Switzerland) (ENRESA, 2000).

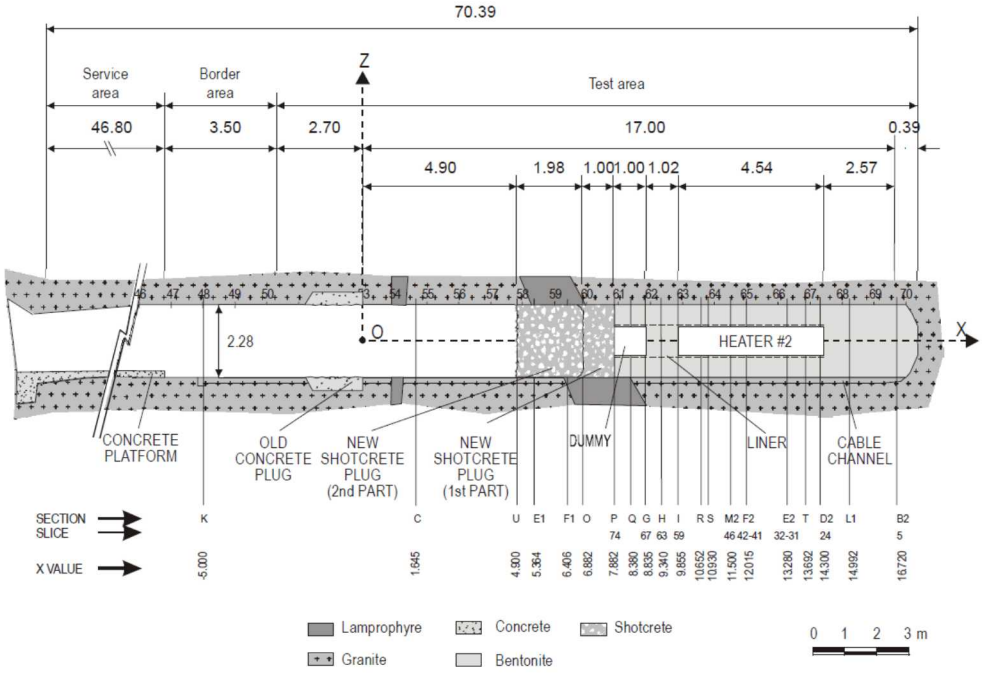

Figure 3-2. *In situ* test configuration following dismantling of Heater #1 (Huertas et al., 2005)

After the dismantling of Heater #1, the tunnel was plugged with shotcrete (Figure 3-2), and Heater #2 was kept working under normal conditions to maintain a constant 100 °C at the steel liner/bentonite interface. In 2014, considering that changes in the state of bentonite buffer were very slow and it was unlikely for bentonite to fully reach saturation in the project lifetime, the decision was made to turn off and dismantle Heater #2. The objective of the second dismantling operation, carried out throughout 2015, was to dismantle all the remaining parts of the *in situ* test, including Heater #2. This operation included carrying out a complete sampling of the bentonite, rock, relevant interfaces, sensors, metallic components and tracers to allow the analysis of the barriers' condition after ~18 years of heating and natural hydration. On April 24, 2015, Heater #2 was switched off. After a short cool-off time period, dismantling was carried out from the shotcrete towards the bentonite section by sections (see Figure 3-3) and samples were taken for THMC and microbiological characterization. Details about the dismantling of Heater #2 are given in Garcia-Sineriz et al. (2016). THM characterization revealed that the bentonite away from the heater is fully saturated, but the bentonite at the vicinity of Heater #2 has not been fully saturated yet.

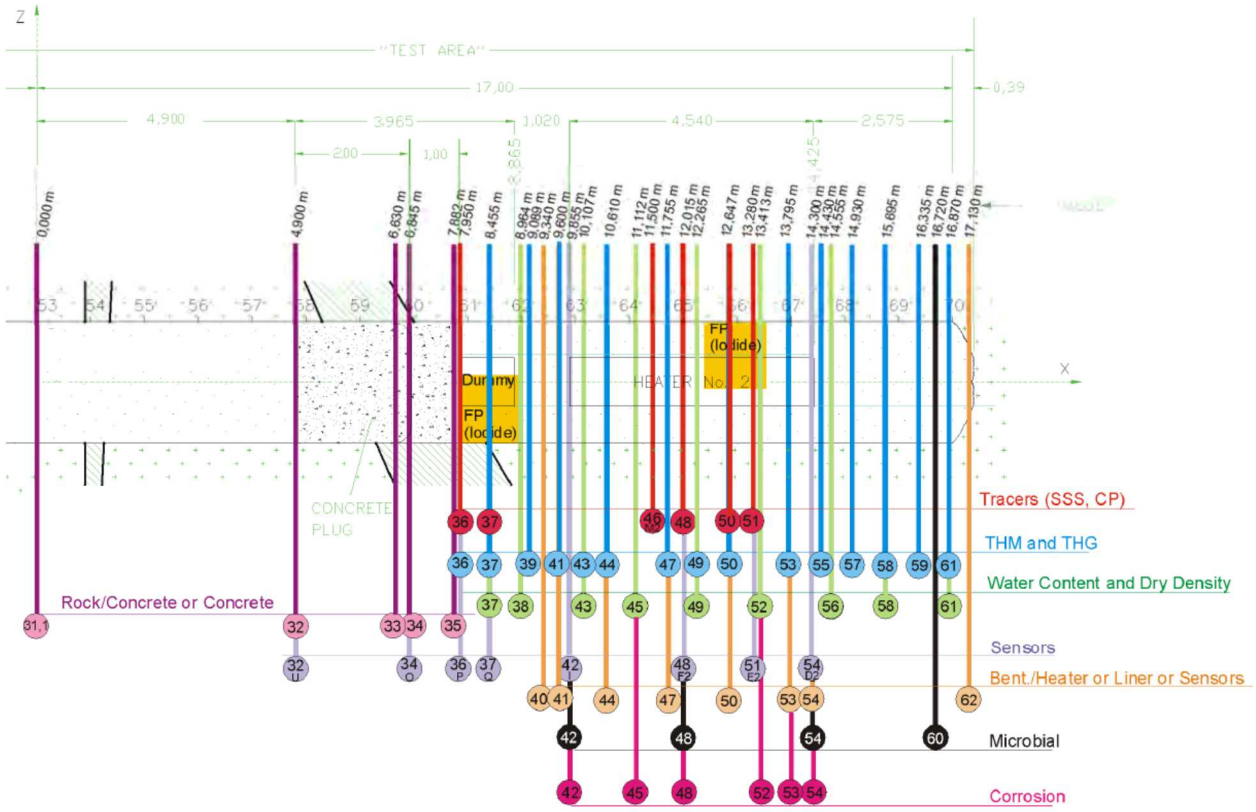

Figure 3-3. Section layout during the dismantling operation of Heater #2 (Detzner and Kober, 2015)

The long-term FEBEX *in situ* test generated comprehensive datasets of THMC data, which provide a unique opportunity to validate coupled THMC models and strengthen our understanding of coupled processes in bentonite. In addition, experiments at different scales with the same type of bentonite are also very useful to evaluate the key parameters obtained at different scales, and to study the scaling effect based on modeling of THMC processes. Up to present, several THM/THC models have been developed to interpret the FEBEX experiments, including the THM model for the mock-up test (Sánchez et al., 2005; 2012a) and *in situ* test (Sánchez et al., 2012b), and THC models for the small scale heating and hydration experiment (Zheng et al., 2010), mock-up test (Zheng and Samper, 2008), and *in situ* tests (Samper et al., 2008a; Zheng et al., 2011; Zheng et al., 2015b).

3.2.2 Available THM Data

In the FEBEX *in situ* test, some data were collected real time by the sensors installed in the bentonite block, such as temperature, relative humidity and stress, and some of them were measured in the laboratory, using the bentonite samples, that were taken after dismantling of test sections, including water content and dry density. The dismantling of Heater #1 in 2002 and Heater #2 in 2015 (Table 3-1) provides two snapshots of measured water content and dry density, which are very valuable for understanding the temporal evolution of these key data, as shown later in the report. Details of these data will be presented when model results are discussed in Section 3.4.

Table 3-1. Timeline of FEBEX *in situ* test.

Event	Date	Time	
		Days	Years
Commencement of heating	2/27/1997	0	0.0
Shutdown of Heater #1	2/2/2002	1827	5.0
Sampling after Heater #1 was dismantled	5/2/2002	1930	5.3
Shutdown of Heater #2	4/24/2015	6630	18.2
Sampling after Heater #2 was dismantled	7/3/2015	6700	18.3

3.2.3 Chemical Data for Bentonite

3.2.3.1 Ion Concentrations in Pore Water

Bentonite samples were taken after dismantling of Heater #1 in 2002 and Heater #2 in 2015, and ion concentrations in pore water of bentonite were measured. They provided data on spatial distribution of ion concentrations at two time points, which are very valuable to constrain the chemical model and understand the geochemical evolution of bentonite in the test. The chemical results from the THMC model are primarily tested against data of ion concentrations.

The bentonite samples collected after the final dismantling were preserved and pore water concentration were measured by two methods: squeezing and aqueous extract tests (AET).

The squeezing process involved the expulsion of interstitial fluid from the saturated argillaceous material being compressed (Entwisle and Reeder, 1993). In these squeezing experiments, the volume of water extracted depends on the following factors: the water content of the rock sample, the rock properties (e.g., dry density, the relative contents of easily-squeezed clays and of stiffer materials like quartz and calcite), and the experimental conditions, such as, the pressure applied, the duration time of squeezing, and size of the squeezing cell (Fernández et al., 2003). Fernández et al. (2017) conducted squeezing tests for three samples at section 36, three at section 47 and five at section 59 (see Figure 3-3 for the locations of sections). Because our model only represents the “hot” sections (sections around the middle of heater), we will only use the data from section 47, which is shown in Table 3-2. Sample BB-47-7 was taken from outer rings of bentonite, with a radial distance from the tunnel axis of 1.02 m, sample BB-47-8 is from the middle ring with a radial distance of 0.79 m and sample BB-47-9 is from the inner rings (near the heater) with a radial distance of 0.56 m.

Table 3-2. Chemical composition of the pore water collected from the BB-47-7, BB-47-8 and BB-47-9 bentonite blocks at different pressures (Fernández et al., 2017).

Sample			BB-47-7	BB-47-8	BB-47-8	BB-47-9	BB-47-9
Pressure		MPa	20	30	40	70	85
Extracted water		g	11.2	1.5	4.0	0.58	2.58
Sensoric Parameter Lab							
Color / Turbidity			No	No	No	No	No
Physical-Chemical Parameter Lab							
pH value (20 °C) Lab. (Glove box / lab)	pH		7.9	7.8	7.6	6.8	7.8
Redox potential	Eh (SHE)	mV	n.d.	n.d.	n.d.	n.d.	n.d.
Spec. electr. conductivity (25 °C) Lab.	Cond.	µS/cm					
Alkalinity (pH 4.3) Lab.	Alk.4.3	mmol/L	4.63	2.58	2.53	<5	2.59
Main Ions							
Sodium	Na^+	mg/L	710	2300	1500	4161	3210
Potassium	K^+	mg/L	9.2	24	13	23	23
Calcium	Ca^{2+}	mg/L	32	380	210	1700	2000
Magnesium	Mg^{2+}	mg/L	20	260	150	1400	1000
Chloride	Cl^-	mg/L	481	1600	976	12000	10700
Sulfate	SO_4^{2-}	mg/L	779	4300	2900	2300	1400
Nitrate	NO_3^-	mg/L	1.9	15	8.3	124	114
Nitrite	NO_2^-	mg/L	<d.l	<d.l	<d.l	<0.2	<2
Phosfate	PO_4^{3-}	mg/L	< 1	< 1	< 1	<0.1	<2
Bromide	Br^-	mg/L	1.1	2.5	0.74	12.7	11.9
Fluoride	F^-	mg/L	<d.l.	<d.l.	<d.l.	<1	<2
Thiosulfate	$S_2O_3^{2-}$	mg/L	< 0.5	< 1	< 1	<0.5	20
Trace Compounds							
Aluminium	Al	mg/L	< 0.1	< 0.3	< 0.3	<2.9	<0.3
Silicon	Si	mg/L	23	22	24	15	14
Iron	Fe (II/III)	mg/L	< 0.1	< 0.3	< 0.3	<2.9	<0.3
Strontium	Sr	mg/L	0.59	6.7	4.0	29	30
Copper	Cu	mg/L	0.15	1.4	0.3	<2.9	0.5
Boron	B	mg/L	1.5	1.8	1.3	<2.9	1.4
Manganese	Mn	mg/L	0.15	0.70	0.3	5.6	4.6
Nickel	Ni	mg/L	0.09	0.41	< 0.3	<2.9	0.6
Lead	Pb	mg/L	0.18	< 0.3	< 0.3	<2.9	<0.3
Zinc	Zn	mg/L	0.08	0.59	< 0.3	<2.9	<0.3
Organic Parameter							
Total organic carbon	TOC	mg/L	38	--	83	n.d.	n.d.
Acetate	CH_3-COO^-	mg/L	< 0.1	86	45	142	141
Formiate	$HCOO^-$	mg/L	0.36	25	12	1.3	13
Oxalate	$(COO)_2^{2-}$	mg/L	--	--	--	17.7	23

AET is a method to quantify the total content of soluble salts of a clay sample. An *1:R* AET consists on adding to a mass M_s of powdered clay sample a mass of distilled water equal to R times M_s. Clay sample and water are stirred during a period of time of usually 2 days during which equilibration of water and clay sample is allowed. Chemical analyses are performed on supernatant solution after phase separation by centrifugation (Sacchi et al., 2001). In addition to dilution, several chemical reactions take place during pore-water extraction from clay samples, which change the concentrations of dissolved species in a complex nonlinear manner. This makes it difficult to derive the chemical composition of the original (before aqueous extraction) clay pore-water from aqueous extract data (Bradbury and Baeyens, 2003; Sacchi et al. 2001). The inference of dissolved concentration for reactive species requires geochemical modeling based on mineralogical data (Bradbury and Baeyens, 2003; Zheng et al., 2008).

For the sample collected at the final dismantling of the FEBEX *in situ* test, Fernández et al. (2017) conducted 1:4 AET for 154 samples, and among them, 36 were for section 47 and 36 for section 53. The procedure of AET is shown in Figure 3-4. Clearly the concentrations of ions (C_{aq} in Figure 3-4) measured in AET do not represent the pore water concentration. In addition to dilution, chemical reactions also occur, which requires geochemical modeling to reconstitute the concentration of ions in the original pore water concentrations (C_{pore}) that corresponds to a sample with original water content (θ_i). We therefore developed a geochemical model to reverse the procedure of AET. In this model, a water+bentonite system with known water content (θ_f) and concentration (C_{aq}) undergoes an "evaporation" and eventually reaches the water content of θ_i (the water content of bentonite sample before conducting AET) and C_{pore} values are obtained and are compared with model results from THMC models in Section 3.4.

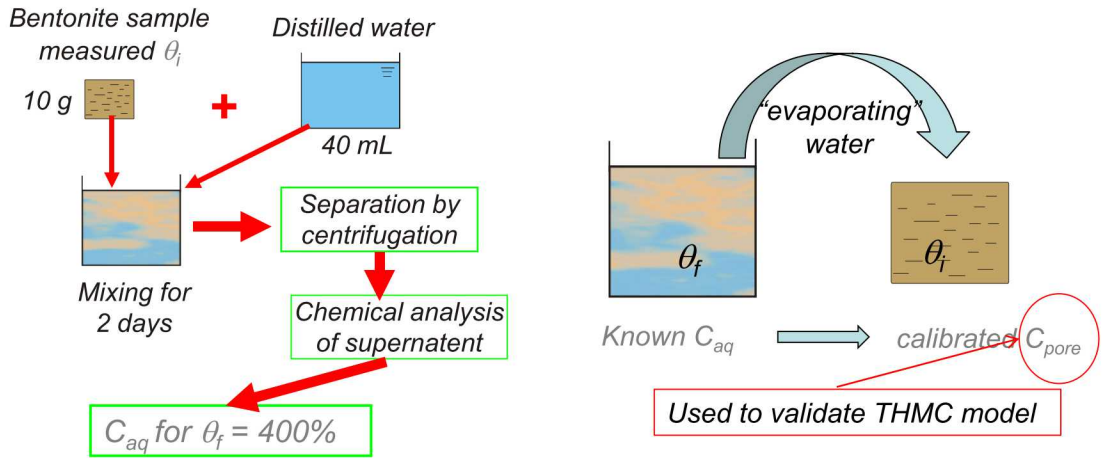

Figure 3-4. The aqueous extract test (AET) procedure (left) used for measuring pore water concentration for samples collected at the final dismantling of FEBEX *in situ* test, and the geochemical model (right) that reverses the AET procedure to calibrate the ion concentration for the original pore water.

3.2.3.2 Geochemical Data of the Solid Matrix

In FEBEX-DP, mineralogical and geochemical characterization were conducted by four groups for samples in Section S36 (near the shotcrete), S42, S45, S48, S50 and S53 (BGR, Federal Institute for Geosciences and Natural Resources,Germany), S47 and S53 (CIEMAT, Centro de Investigaciones Energéticas, Medioambientales y Tecnológicas, Spain), S45 (UAM, Univesidad Autonoma De Madrid, Spain), S46 and S47 (ETH, Swiss Federal Institute of Technology Zurich) and S36 (SÚRAO, Radioactive Waste Repository Authority, Czech Republic). Among them, S42-S53 surrounds the heater and is located in the "Hot" section. Characterization results are documented in Villar et al. (2017) and a summary is given below:

Smectite phases and the illite/smectite mixed layers in ground bulk materials were analyzed by CIEMAT, UAM and ETH using X-ray diffraction (XRD). The smectite content ranges from 82-96% (Figure 3-5), depending on sample and laboratory, and is the same as the reference bentonite (92±4%). The smectite phases were made up of a R0 smectite-illite mixed-layer (R0 meaning that the layering was disordered), with 5-23% of illite layers, although most samples had between 5 and 13%. Given the large variation of illite fraction in the illite/smectite mixed layer between samples, it is impossible to delineate if there is any increase or decrease in illite mass fraction compared with the reference bentonite. The crystal thickness of the smectite particles ranged between 7.65 and 10.31 nm, the number of TOT layers in the

quasi-crystals being 5-6. This is in agreement with previous analyses of the reference FEBEX bentonite (Fernández et al. 2004; ENRESA 2006). This would indicate that no structural changes took place in the montmorillonite during the experiment.

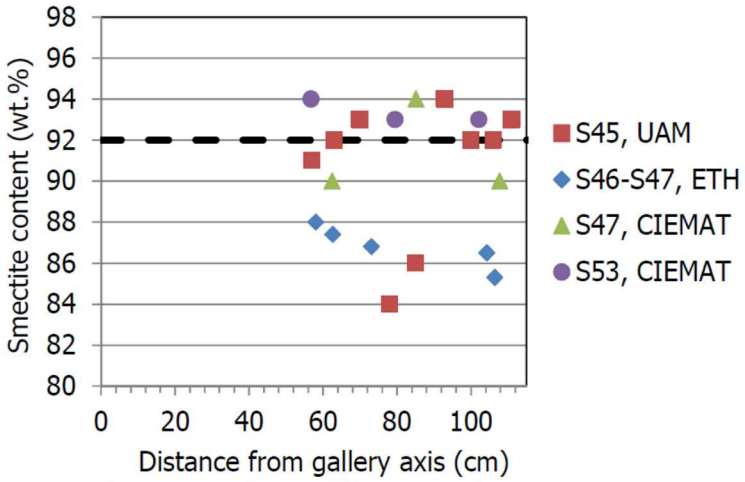

Figure 3-5. Smectite content in samples from different sections around the heater determined by X-ray diffraction by different laboratories. The dashed line indicates the content in the reference sample as determined by CIEMAT (Villar et al., 2017).

One important characteristic of clay minerals is the layer charge, which is the result of ionic substitutions in the structure of clay minerals is balanced by the exchangeable cations in the interlayer space. It not only determines cation retention and specific adsorption of water and organic polar molecules (Lagaly & Mermut 2001), but also plays an important role over the course of illitization. Although illite and smectite are both 2:1 structure clay minerals, smectite swells but illite does not. One of the reasons is that illite has higher layer charge than smectite. Change in the layer charge of smectite could be a good precursor of illitization. CIEMAT, UAM and ETH determined the MLC by means of the simplified method of alkylammonium cations established by Olis et al. (1990). Because the layer charge may be different for each layer, both in terms of charge location (tetrahedral or octahedral) and charge magnitude, and the mean layer charges (MLC) which represent only the statistical average of the charge classes in the layers (Olis et al. 1990) were measured. For the reference bentonite, CIEMAT and UAM found a value of 0.37 MLC/hfu (hfu=half unit cell). For the retrieved samples, MLC are between 0.36 and 0.38 MLC/hfu, which shows (1) the smectite particles prior and after the FEBEX in situ test can be classified as low charge smectites and (2) there is no change in layer charge in bentonite prior and after the FEBEX in situ test.

CIEMAT analyzed the material of less than 2 μm fraction for samples from sections S36, S47, S53 and 59 and determined the structural formulae for the smectite in three samples along a radius in sections S36, S47 and S53 and in five samples along a radius in section S59. The structural formulae are given in Table 3-3. No significant changes were observed among the different retrieved samples and the reference bentonite. All smectites showed substantial substitution in the octahedral sheet (85-95%), whereas the substitution of the tetrahedral charge was much lower (between 5 to 15%). In the octahedral sheet, magnesium substituted mainly for aluminum, the amount of iron being low. All the samples displayed an octahedral filling below 2.05 mol/fu, matching the dioctahedral character of the smectite. Furthermore,

since the layer charge was <0.42 MLC/hfu and the percentage of tetrahedral charge <15%, the smectites can be classified as Wyoming-type montmorillonites (Villar et al., 2017).

Table 3-3. Structural formulae calculated by CIEMAT from the chemical analyses of the < 2 µm of the Ba-homoionized samples(Villar et al., 2017).

Sample	Structural formula
FEBEX ref[a]	$(Si_{3.94}Al_{0.06})^{IV}\ (Al_{1.35}Fe^{3+}_{0.21}Mg_{0.49}Ti_{0.01})^{VI}\ O_{10}(OH)_2\ X_{0.38}$
Average retrieved (16)	$(Si_{3.96\pm0.01}Al_{0.04\pm0.01})^{IV}\ (Al_{1.35\pm0.01}Fe^{3+}_{0.20\pm0.01}Mg_{0.48\pm0.01}Ti_{0.01})^{VI}\ O_{10}(OH)_2\ X_{0.37}$

[a]not homoionised

Table 3-4. Structural formulae calculated by UAM from the analyses of the < 2 µm of the samples Ca-homoionized performed by EDX.

Sample	Structural formula
FEBEX ref	$(Si_{3.94}Al_{0.05})^{IV}\ (Al_{1.41}Fe^{3+}_{0.09}Mg_{0.50})^{VI}\ O_{10}(OH)_2Ca_{0.24}K_{0.04}$
Average retrieved (11)	$(Si_{3.96\pm0.02}Al_{0.04\pm0.02})^{IV}\ (Al_{1.41\pm0.02}Fe^{3+}_{0.09\pm0.01}Mg_{0.50\pm0.02})^{VI}\ O_{10}(OH)_2Ca_{0.25\pm0.02}K_{0.04\pm0.01}$

The only noticeable change that might suggest that illitization processes are occurring, is the increase of calcium atoms and decrease of irreversibly fixed potassium towards the heater relative the reference bentonite, obtained by UAM.

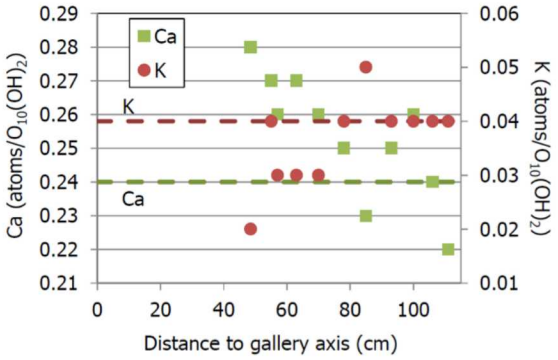

Figure 3-6. Calcium and potassium atoms in the structural formula of the Ca-homoionized montmorillonite as determined by UAM.

Minerals in the ground bulk materials other than illite/smectite were also quantified by XRD. Scanning Electron Microscopy (SEM) was also used by CIEMAT to define the microstructural morphology of clay minerals, possible alteration products and accessory minerals for samples from Sections S36, S47, S53 and S59. Regarding minerals other than illite/smectite, we have the following findings:

- Minerals appearing systematically in all the samples were K-feldspars, quartz, cristobalite, calcite and plagioclase, all of them in proportions lower than 5%. SEM found that smectite, quartz and K-feldpar are major ones, with trace amounts of carbonates, sulphates, zircon, monazite, biotite, muscovite, ilmenite and apatite are found, just as in reference bentonite.

- The total inorganic carbon (TIC) percentage in the bulk material (>2 μm fractions) would correspond to an average calcite content about 0.9%, which agrees with the value obtained for the reference bentonite based on XRD analysis (Kaufhold et al., 2016). The total carbon content for the three analyses of the < 2 μm size fraction was 0.14%, which is only slightly above the value for the reference bentonite. Most of the carbon measured was inorganic, and the content of organic carbon was always below 0.06% in the analyses by ETH and below 0.10% in the analyses by BGR.
- Albite was found near the heater.
- In a few samples, dolomite and iron-sulfide was found in the fraction< 2 μm, and there is no clear pattern. The sulphur content was very low (lower than 0.06%), and in many of the samples analyzed by CIEMAT even below the detection limit. However, CIEMAT found also a significant overall sulphur increase in the bulk material (>2 μm) in the samples retrieved with respect to the reference bentonite, although this was not found by BGR.
- Microorganisms and organic matter (deduced from the carbon content) were found in samples from the external and middle rings in sections S36, S47, and S59, i.e., in the wettest part of the barrier. Colonies of microorganisms had systematically been found in the wettest samples from the thermo-hydraulic tests.
- In section S36, just at the contact with the shotcrete plug, portlandite and ettringite were found, along with increases of K and Mg in the structure and changes in the Al/Si ratio in the tetrahedral sheets.
- The spatial distribution of the elements in the bulk solid phase did not follow any particular trend for most elements. Nevertheless, the content of magnesium increased from the granite towards the axis of the gallery, both in the sections around the heater and in the cool sections (Figure 3-6).
- The calcium and sodium contents increased from the internal part of the barrier towards the gallery wall (Figure 3-7 and 3-8). In the case of calcium this increase was particularly clear in the cool sections analyzed by CIEMAT (S36 and S59). It is important to note that these trends were not found in the analyses of the less than 2 μm fractions, which would indicate that they do not respond to changes in the smectite, but in other secondary minerals.

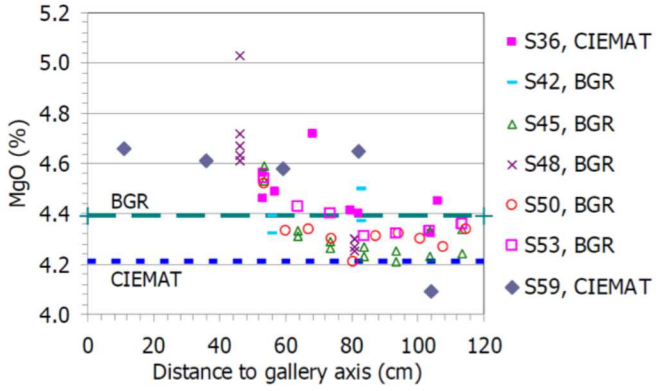

Figure 3-7. Magnesium content in bulk samples from different sections analyzed by BGR and CIEMAT (the horizontal dashed lines indicate the reference values).

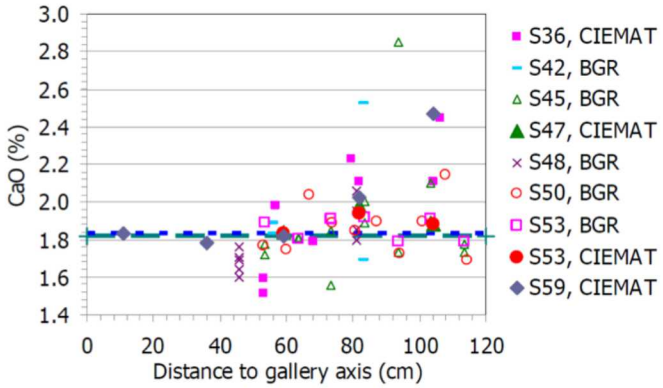

Figure 3-8. Calcium content in bulk samples from different sections analyzed by BGR and CIEMAT (the horizontal dashed lines indicate the reference values).

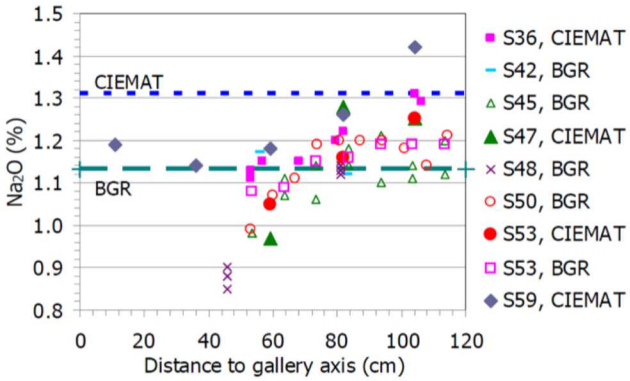

Figure 3-9. Sodium content in bulk samples from different sections analyzed by BGR and CIEMAT (the horizontal dashed lines indicate the reference values).

Regarding cation exchange capacity (CEC), the first impression is that data vary a great deal depending on the measuring method. Second, there is no clear spatial trend no matter what method had been employed. The biggest problem with CEC is probably that soluble cations were not separated from the exchangeable cations. We therefore do not use CEC data to constrain our model in this report.

3.2.4 Chemical Analysis of the Granitic Pore Water

Groundwater geochemistry was measured over the course of the FEBEX *in situ* test to study the solute transport from bentonite to granite. Two boreholes for hydrogeochemical investigation (FU-1, FU-2) were drilled at the end of 2005 in the FEBEX drift (Figure 3-11) in order to carry out *in-situ* studies of the geochemical processes related to the migration of solutes in crystalline rocks (Pérez-Estaún et al., 2006). FU-1 (17.8 m long) is parallel to the axis of the drift and relatively close to the bentonite interface (20 cm) and intersects some hydraulically active structures. FU-2 is 17.6 m long and presents a vertical deviation 2º in relation to the axis of the gallery and 1º parallel to the gallery. It lies approximately 60 cm away from the bentonite interface (Pérez-Estaún et al., 2006). The FU-1 and FU-2 boreholes were separated into several intervals. A total of 157 water samples were collected from FU-1 and FU-2 from 2006 to 2016. The samples were preserved and analysed for major and trace elements whereas pH, temperature, and specific electrical conductivity (EC) were measured inside the flow cell through electrodes connected to a multi-parametric probe. Data for sample collected from interval FU1-3 (Figure 3-11) and FU2-2 (Figure 3-12) are relevant to the models in this report. Because most ions in pore-water in bentonite have

higher concentrations than those of the pore-water of granite, diffusion from bentonite to granite is expected to increase the ion concentrations in granite.

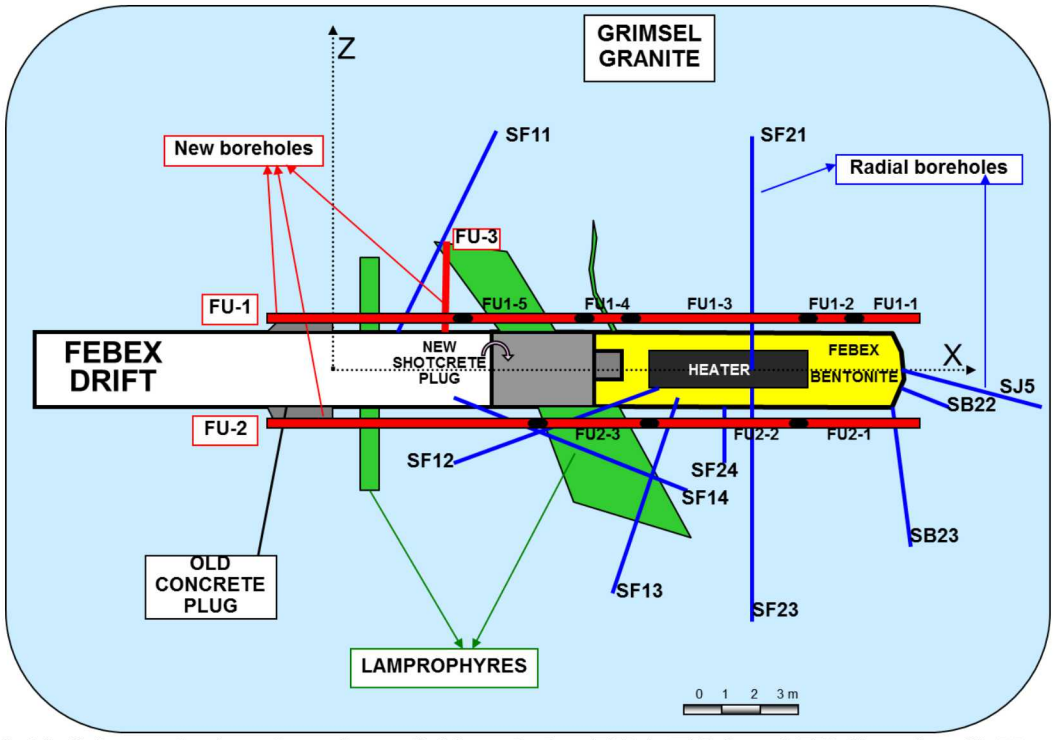

Figure 3-10. Schematic situation of parallel boreholes (FU-1, FU-2 and FU-3) and radial boreholes, plain view.

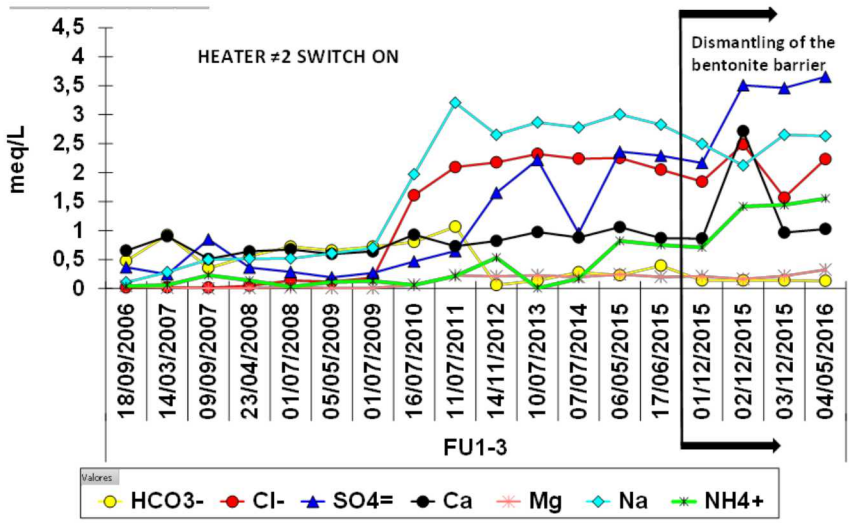

Figure 3-11. Chemical composition evolution of the packed-off interval FU1-3 in the borehole FU-1.

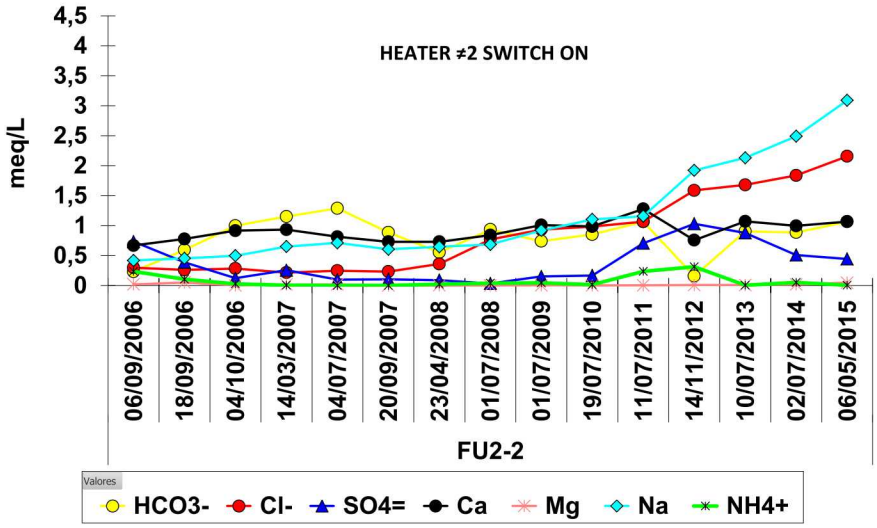

Figure 3-12. Chemical composition evolution of the packed-off interval FU2-2 in the borehole FU-2.

3.3 Model Development

Since FY15, the model interpretation of the FEBEX in situ test started from a simple TH model and gradually increased the level of complexity until a coupled THMC model was developed in FY17 that can match all of the THM data and the concentration profile of chloride at 5.3 years. In FY18, the model effort focuses on the interpretation of the concentration profiles at 18.3 years obtained from the dismantling of Heater #2 in 2015. The updates of the model are largely about the chemical model whereas the THM model remains similar with some adjustments of mechanical models and parameters. The model setup is therefore similar to the previous model in Zheng et al. (2016, 2017). In this section, we briefly present the model setup: more details about the model development can be found in Zheng et al. (2016; 2017).

3.3.1 Simulator

The numerical simulations in Zheng et al. (2016, 2017) were conducted with TOUGHREACT-FLAC3D, which sequentially couples the multiphase fluid flow and reactive transport simulator, TOUGHREACT V2 (Xu et al., 2011), with the finite-difference geomechanical code FLAC3D (Itasca, 2009). The coupling of TOUGHREACT and FLAC was initially developed by Zheng et al. (2012) to provide the necessary numerical framework for modeling fully coupled THMC processes. It was equipped with a linear elastic swelling model (Zheng et al., 2012; Rutqvist et al., 2013) to account for swelling as a result of changes in saturation and pore-water composition and the abundance of swelling clay (Liu et al., 2013; Zheng et al., 2014). A recent addition to the code is the capability of simulating Non-Darcian flow (Zheng et al. 2015b) and thermal osmosis. In FY18, the code has been through a major upgrade — TOUGHREACT V2 (Xu et al., 2011) was replaced with TOUGHREACT V3.0-OMP (Xu et al., 2014). In comparison with TOUGHREACT V2 (Xu et al., 2011), TOUGHREACT V3.0-OMP (Xu et al., 2014) has the several major improvements (see http://esd1.lbl.gov/research/projects/tough/software/toughreact.html), one of the them is the OpenMP parallelization of chemical routines on multi-core shared memory computers, which significantly decreases the computation time.

3.3.2 Modeling Setup

Because the hydration of bentonite is fairly symmetrical, we use an axi-symmetrical mesh (Figure 3-4) to save computation time so that we can focus on the key coupling processes. However, such a model can only be used to interpret and predict the THMC behavior in the "hot sections," i.e., sections of bentonite block surrounding the heater including sections 41-54 (or more typically section 49) shown in Figure 3-4.

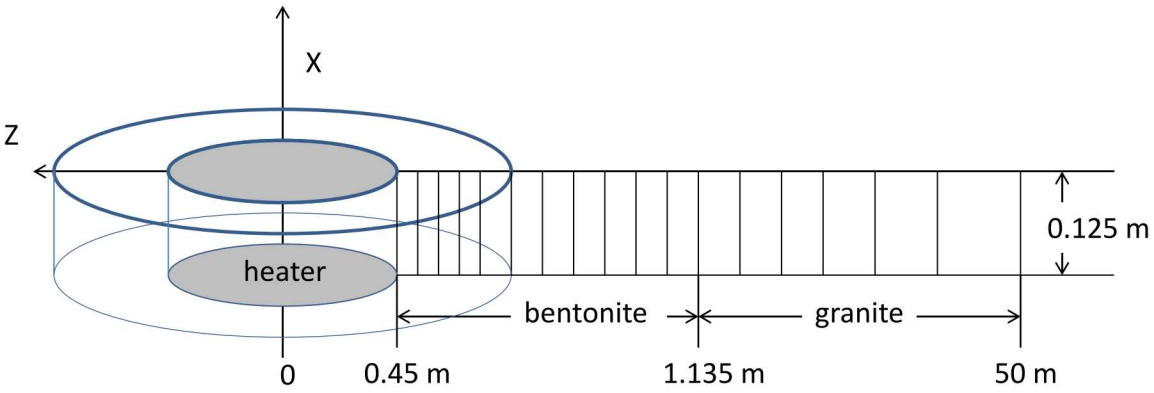

Figure 3-13. Mesh used for the model, not to the scale.

The model considers two material zones: one for the bentonite and the other for the granite. The first two nodes (1 and 2) are located on the external wall of the heater (r = 0.45-0.46 m). Bentonite is located within 0.45 m < r < 1.135 m. The remaining domain up to 50 m is used to simulate the granite. The simulation time starts on February 27, 1997 and ends on July 1, 2015, a total of 6,698 days (18.3 years).

The initial temperature is uniform and equal to 12 ºC. A constant temperature of 100 ºC is prescribed at the heater/bentonite interface (r = 0.45 m) while temperature is assumed to remain constant at its initial value of 12 ºC at the external boundary (r = 50 m) because the thermal perturbation induced by the heaters over the time frame of the experiment does not extend to this boundary.

The bentonite has initially a gravimetric water content of 14%, which corresponds to a saturation degree of 55% and a suction of 1.11×10^5 kPa. The boundary conditions for flow include: 1) no flow at r = 0.45 m and 2) a prescribed liquid pressure of 7 bars at r = 50 m.

3.3.3 The TH Model

The model considers non-isothermal two phase (air and water) flow, with each individual phase fluxes given by a multiphase version of Darcy's Law. For the vapor flow in the air phase, in addition to Darcy flow, mass transport can also occur by diffusion and dispersion according to Fick's law. Thermal behavior is relatively well understood because it is less affected by coupled processes in comparison with hydrological and chemical processes and the relevant parameters can be reliably measured. In current model, both conductive (Fourier's law) and convective heat flux are considered in the model and thermal conductivity is the key parameter.

Because over the span of water saturation that FEBEX bentonite went through (from an initial degree of water saturation 55-59% to 100%), the thermal conductivity/water saturation relationship can sufficiently be represented by a linear relationship; we use a linear relationship implemented in TOUGH2 (Pruess et al., 1999):

$$K_{th} = K_{wet} + S_l(K_{wet} - K_{dry}) \quad 3\text{-}1$$

where K_{wet} is the thermal conductivity under fully saturated conditions, K_{dry} is the thermal conductivity under dry conditions, and S_l is the liquid saturation degree. K_{wet} and K_{dry} are given in Table 3-2.

The key parameters affecting the hydration of bentonite are permeability of granite, relative permeability and retention curves of bentonite, the vapor diffusion coefficient and permeability of bentonite. In Zheng et al. (2015b), the most plausible values for these parameters were discussed and illustrated based on the results of the sensitivity analysis.

Granite is fractured media and should ideally be represented by fractures and matrix. Just as previous models for *in situ* tests (Samper et al., 2008a; Sánchez et al., 2012b), the current model also assumes granite is a homogeneous porous medium, which requires us to use an equivalent permeability. Based on the total water flow from tunnel wall at the entire length of test zone (17.4 m, see Figure 3-1) (ENRESA, 2000), the permeability of fractured granite is around 5×10^{-18} to 8×10^{-18} m^2. ENRESA (2000) also reports that the most frequent permeability is 1×10^{-18} but deems it is more representative of rock matrix. Zheng et al. (2011) used 8×10^{-18} m^2, Kuhlman and Gaus (2014) estimated permeability of 6.8×10^{-19} m^2, and Sánchez et al. (2012b) used a small value of 8.18×10^{-21} m^2. Based on the published values, it seems that a permeability value between 7×10^{-19} to 8×10^{-18} m^2 is plausible. Based on the evaluation in Zheng et al. (2015b), a permeability of 2×10^{-18} m^2 is used (Table 3-5).

The capillary pressure is calculated by van Genuchten function (retention curve) as:

$$P_{cap} = -\frac{1}{\alpha}\left(\left[S^*\right]^{-1/m} - 1\right)^{1-m} \quad 3\text{-}2$$

where P_{cap} is the capillary pressure (Pa), $S^* = (S_l - S_{lr})/(1 - S_{lr})$ and S_l is the water saturation, S_{lr} is the residual water saturation. S_{lr} is 0.1 for bentonite and 0.01 for granite. The values of α and m are given in Table 3-5. The retention curve has been fairly well studied for FEBEX bentonite. For example, ENRESA (2000) presented the retention curve for both the drying and wetting path and van Genuchten function (van Genuchten, 1980) for both were derived with an m ranging from 0.3 to 0.6. Kuhlman and Gaus (2014) estimated an m of 0.3 and Zheng et al. (2011) and Sánchez et al. (2012b) use an m of 0.18, which is slightly lower.

Table 3-5. Thermal and hydrodynamic parameters.

Parameter	Granite	Bentonite
Grain density [kg/m^3]	2700	2780
Porosity ϕ	0.01	0.41
Saturated permeability [m^2]	2.0×10^{-18}	2.15×10^{-21}
Relative permeability function, k_{rl}	$k_{rl} = S$	$k_{rl} = S^3$
Van Genuchten $1/\alpha$ [1/Pa]	4.76×10^{-4}	1.1×10^{-8}
Van Genuchten m	0.7	0.45
Compressibility, β [1/Pa]	3.2×10^{-9}	5.0×10^{-8}
Thermal expansion coeff. [1/^{o}C]	1.0×10^{-5}	1.5×10^{-4}
Dry specific heat [J/kg- ^{o}C]	793	1091
Thermal conductivity [W/m-^{o}C] dry/wet	3.2/3.3	0.47/1.15
Effective vapor diffusion coefficient (m^2/s)	1.03×10^{-4}	1.03×10^{-4}

**Note: in the relative permeability function, S is water saturation

The effective permeability of bentonite has been under scrutiny by modelers (e.g. Zheng et al., 2011) due to its critical role in determining the hydration of bentonite. It is the product of intrinsic permeability (k) (or saturated permeability, absolute permeability) and relative permeability (k_r). Relative permeability using $k_r=S_l^3$ (where S_l is water saturation degree) has been consistently used by different models (Zheng et al., 2011; Sánchez et al., 2012b; Kuhlman and Gaus, 2014) and we use the same function here. The plausible saturated permeability for FEBEX bentonite in the initial state could range from 1×10^{-21} to 9×10^{-21} m^2 based on various sources (Zheng et al., 2011; Sánchez et al., 2012b; Kuhlman and Gaus, 2014; Chen et al., 2009) and we use 2.15×10^{-21} m^2 in the model. However, as demonstrated by Zheng et al. (2015b), a constant intrinsic permeability for bentonite could not explain the relative humidity data over the entire thickness of the bentonite barrier. The stress-dependence of permeability for low-permeability sedimentary rock is fairly well known and has been studied extensively (e.g. Ghabezloo et al., 2009; Kwon et al., 2001). Many empirical relationships have been put forward to describe the permeability changes with effective stress. In this report, we ultimately used an empirical relationship obtained by fitting the permeability-dry density data (ENRESA, 2000) as shown in Equation 3-3:

$$\log k = -2.96\rho_d - 8.57 \qquad 3\text{-}3$$

where ρ_d is dry density. Then a scaling factor α of 1.882, was added to equation 3-3, as shown in Equation 3-4, such that initial permeability is 2.15×10^{-21} m^2 :

$$\log k = (-2.96\rho_d - 8.57)/\alpha \qquad 3\text{-}4$$

According to coupled transport phenomena, thermal, hydraulic and chemical gradients all have effects on the heat, liquid and solute fluxes. Thermal osmosis is a coupled process that can produce a fluid flux. Zhou et al. (1999) showed that additional coupled flow terms due to a temperature gradient had significant effects on the distribution of capillary pressure and saturation degree in a THM model of a

thick cylinder heating test. The flux of fluid caused by thermal osmosis v_{to} can be written as (Dirksen, 1969):

$$v_{to} = -k_T \nabla T \tag{3-5}$$

where T is temperature and k_T is the thermo-osmotic permeability ($m^2/K/s$). Liquid flux caused by thermal osmosis term can be added to Darcian terms (Ghassemi and Diek, 2002; Zhou et al., 1999). In current model, k_T of 1.2×10^{-12} $m^2/K/s$ is used.

3.3.4 Mechanical Model

In Zheng et al. (2016), we tested two mechanical models for bentonite: a linear swelling model and dual structure Barcelona expansive clay model (BExM), and found out that both models led to similar fits to measured THM data. Both methods have pros and cons: BExM provide a mechanistic description of the swelling of bentonite, but it is more computationally expensive and parameters are difficult to calibrate, whereas linear swelling models has simple parameterization and parameters can be easily calibrated, but it does not describe correctly the transient state of swelling. Eventually for the THMC model for the FEBEX in situ test, we use a method what is somewhat in between --- the state surface approach.

Clay materials are usually porous media, forming the channels the multiphase flows can pass through. The adoption of one single state variable, such as effective stress, has shortcomings, since non-recoverable strain or collapse of unsaturated soil due to wetting-drying could not be simulated (Rutqvist et al., 2011). To overcome this disadvantage, a state surface model for geomaterials is developed based on the classical Biot's poro-elastic approach and extended to partially saturated materials. The model's equation, as experimentally derived from suction-controlled oedometric tests, was used to express the nonlinear behavior of poro-elasticity as functions of the void ratio and the applied load. The model was used to simulate laboratory experiments on the FEBEX bentonite, and now for the interpretation of the FEBEX in-situ experiment. In FY 2018, we have implemented this state surface model for bentonite in our simulator, TOUGHREACT-FLAC.

Within the theoretical framework of poromechanics (Coussy, 2004), the constitutive equation of solid skeleton includes thermal effects and partial saturation and the total stress, σ_{ij}, can be written in incremental form as follows

$$\mathrm{d}\sigma_{ij} = 2G\mathrm{d}\varepsilon_{ij} + \delta_{ij}\lambda\mathrm{d}\varepsilon_{kk} - \alpha_m K_D \delta_{ij}\mathrm{d}T - \delta_{ij}\alpha S\mathrm{d}p \tag{3-6}$$

where G, λ is the Lame's constant; δ_{ij} is the second order identity tensor; α is the pseudo-Biot's coefficient; S is the degree of saturation; p is the liquid pressure; α_m is the volumetric thermal dilation coefficient; K_D is the bulk modulus of the soil; T is the temperature; and ε_{ij} is the small strain tensor.

To take into account the nonlinear behavior, the poro-elastic coefficients of the equation are expressed as functions of suction (s) and net stress (σ_m'') by adopting the concept of a state surface equation (Matyas and Radhakrishna, 1968). Based on results of oedometric tests, Lloret and Alonso (1995) proposed the equation of void ratio on the state surface:

$$e = A + B\ln(-\sigma_m'') + C\ln(s + p_a) + D\ln(-\sigma_m'')\ln(s + p_a) \tag{3-7}$$

where e is the void ratio; p_a is atmospheric pressure; A, B, C and D are empirical constants; $\sigma_m'' = \left(\frac{\sigma_{kk}}{3}\right) - p_g$ is the mean net stress and $s = p - p_g$ is the suction, where p_g is the gas pressure. With this equation, the state of the material can be drawn in σ_m''-s-e space as Figure 3-14 shows. The figure displays, in general, that with the increase of mean net stress σ_m'' or the increase of the suction s, the void ratio decreases, indicating the volume of the material is reduced.

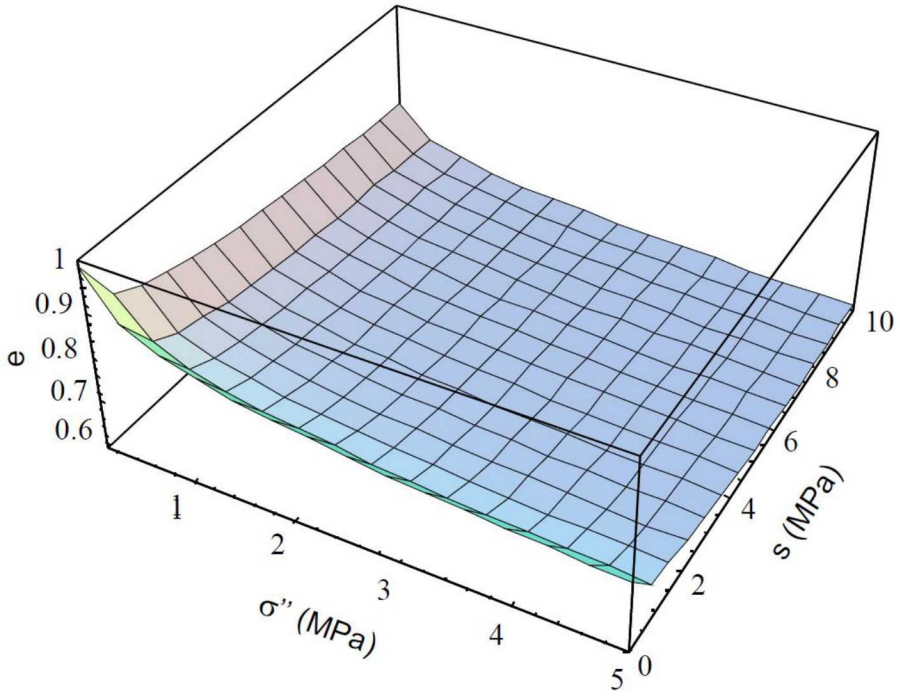

Figure 3-14. State surface for the FEBEX bentonite (Nguyen *et al.*, 2005).

For simplicity, the gas pressure is assumed to be small compared with fluid pressure. Thus, we can obtain

$$\mathrm{d}\sigma_m = \mathrm{d}\sigma_m'' \text{ and } \mathrm{d}p = \mathrm{d}s \qquad 3\text{-}8$$

When the temperature change is small, the problem is reduced to an isothermal case, so the change of mean total stress is derived based on Equation (3-9):

$$\mathrm{d}\sigma_m = K_D \mathrm{d}\varepsilon_v - \alpha S \mathrm{d}s \qquad 3\text{-}9$$

The increment of the volumetric strain can be calculated by the change of the void ratio:

$$\mathrm{d}\varepsilon_v = \frac{\mathrm{d}e}{1+e} \qquad 3\text{-}10$$

Comparing Equation (3-10) with (3-7), we can compute the updated bulk modulus K_D based on the partial derivative as

$$K_D = \frac{1+e}{\frac{\partial e}{\partial \sigma_m''}} = \frac{(1+e)\sigma_m''}{B + D\ln(s+p_a)} \qquad 3\text{-}11$$

Using the same strategy, we can obtain the pseudo-Biot's coefficient α as well:

$$\alpha = \frac{K_D}{S(1+e)}\frac{\partial e}{\partial s} = \frac{1}{S}\frac{\sigma_m''}{B + D\ln(s+p_a)}\frac{C + D\ln(-\sigma_m'')}{s+p_a} \qquad 3\text{-}12$$

Note that the pseudo-Biot's coefficient should range between 0 and 1 as Figure 3-15 shows.

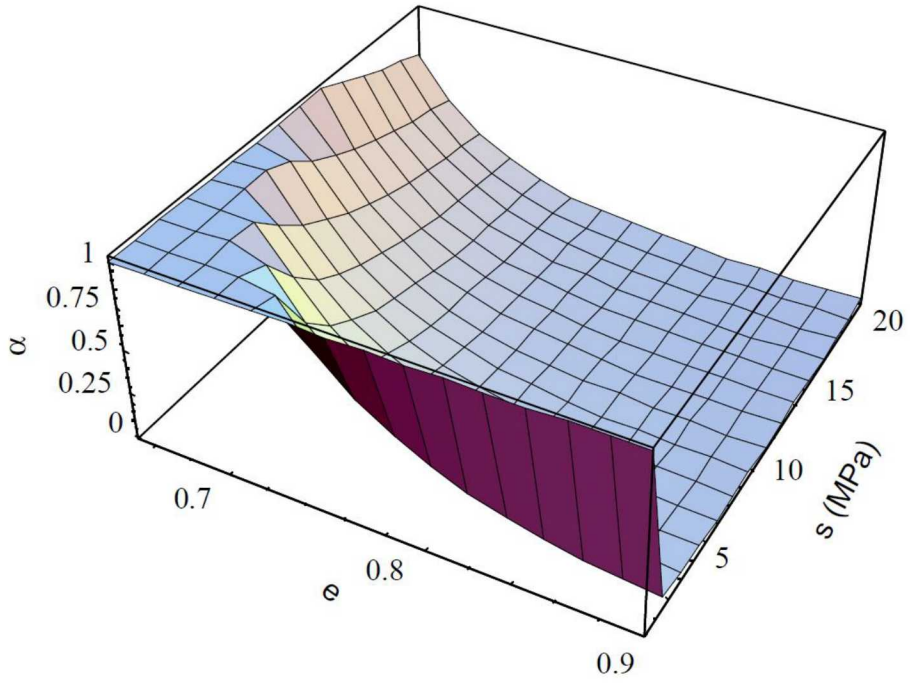

Figure 3-15. Pseudo-Biot's coefficient (Nguyen et al., 2005).

The state surface model is implemented through the FISH language, which is embedded within FLAC3D that enables the user to define new variables and functions. In the input parameters, A, B, C and D are the only material parameters needed to calibrate for the model on the specific material. For the FEBEX compacted bentonite these parameters are equal to A = 0.91, B = - 0.0552, C = - 0.0606413 and D = 0.00479977. During each time increment, the mean net stress σ_m'' is calculated first based on the current pore pressure obtained from TOUGHREACT and previous total stress from FLAC3D, then the pseudo-Biot's coefficient α and the void ratio are computed following Equation (3-12) and Equation (3-7) respectively. With the updated void ratio, the bulk modulus is modified as well as Equation (3-11) expresses. The equivalent hydraulic stress due to suction change contributes to each grid's unbalanced force, which is redistributed to the associated nodes in each grid. Then the geomechanical simulator FLAC3D solves the momentum balance equation based on poromechanical constitutive laws.

3.3.5 Chemical Model

The development of a chemical model requires first the knowledge of initial chemical conditions in bentonite and granite, i.e., the initial mineralogical and pore water compositions. During the operation of the FEBEX *in situ* test, extensive mineralogical characterization was conducted, based on the results presented in ENRESA (2000), Fernández et al. (2004), Ramírez et al. (2002), which were the basis for establishing the mineral compositions in the previous models (e.g. Zheng et al., 2016). After the final dismantling of the FEBEX *in situ* test, characterization of mineral phases was conducted (Villar et al., 2017). In this report, the mineral phases and their volume fraction (Table 3-6) are based on the results given in ENRESA (2000), Fernández et al. (2004), Ramírez et al. (2002) and Villar et al. (2017). Trace amounts of zircon, monazite, biotite, muscovite, ilmenite and apatite have been reported in Villar et al. (2017), but zircon, monazite and apatite not included in the model because there are no water chemistry data for Zr, Ce and phosphate. Biotite, muscovite and ilmenite are trace rock-forming minerals and unlikely have tangible interactions with the aqueous phase, and, therefore, are not considered in the model. Note that all these publications used mass fraction which is transformed to volume fraction (ratio of the volume for a mineral to the total volume of medium) using a porosity of 0.41 (see Table 3-6). Note the minerals that have zero initial volume fractions are the secondary minerals that could be formed. Detailed mineralogical composition of the Grimsel granite was given in Garralon et al. (2017). Previous THC models for the *in situ* test (Samper et al., 2008a; Zheng et al., 2011) only include quartz in the mineral assemblage in granite. Siitari-Kauppi et al. (2007) reported that Grimsel granite is composed of quartz, K-feldspar, plagioclase and a small amount of "dark material" and Garralon et al. (2017) gave a detailed list. In the current model, we consider quartz, K-feldspar, plagioclase in granite with their volume fractions listed in Table 3-6.

Table 3-6. Mineral volume fraction (dimensionless, ratio of the volume for a mineral to the total volume of medium) FEBEX bentonite (ENRESA, 2000; Fernández et al., 2004; Ramírez et al., 2002) and granite (Zheng et al., 2011).

Mineral	**FEBEX Bentonite**	**Granite**
Calcite	0.00472	0
Smectite	0.546	0
Gypsum	0.00059	0
Quartz	0.018	0.37
Cristobalite	0.0059	0.00
K-Feldspar	0.0059	0.35
Plagioclase	0.0059	0.27
Dolomite	0.0	0
Illite	0.0	0
Kaolinite	0.0	0
Siderite	0.0	0
Ankerite	0.0	0
Anhydrite	0.0	0
Chlorite	0.0	0

FEBEX bentonite blocks have an initial gravimetric water content of 13.5–14% (ENRESA 2000). The model presented in this report uses the pore water composition (see Table 3-7) inferred by Fernández et al. (2001) from aqueous extract data. The pore water composition for granite (Table 3-7) is taken from Zheng et al. (2011).

Table 3-7. Pore-water composition (mol/kg water except for pH) of FEBEX bentonite (Fernández et al., 2001) and granite (Zheng et al., 2011).

	EBS Bentonite: FEBEX	Granite
pH	7.72	8.35
Cl	1.60E-01	1.31E-05
SO_4^{-2}	3.20E-02	7.86E-05
HCO_3^-	4.1E-04	3.97E-04
Ca^{+2}	2.2E-02	1.81E-04
Mg^{+2}	2.3E-02	1.32E-06
Na^+	1.3E-01	3.76E-04
K^+	1.7E-03	7.80E-06
Fe^{+2}	2.06E-08	2.06E-08
$SiO_2(aq)$	1.1E-04	6.07E-04
AlO_2^-	1.91E-09	3.89E-08

In the chemical model, we consider aqueous complexation, cation exchange, surface complexation and mineral dissolution/precipitation. Aqueous complexes and their disassociation constants for reactions that are written in terms of the primary species in Table 3-7 are listed in Table 3-8. These thermodynamic data were taken from Data0.dat.YMPv4.0, an EQ3/6 (Wolery, 1993) database qualified by the U.S. DOE for the Yucca Mountain project. Surface protonation reactions are given in Table 3-9 and cation exchange reactions are given in Table 3-10.

Table 3-8. Aqueous complexes and their dissociation constants

Species	Log K (25°C)	Species	Log K (25°C)
OH^-	13.99	$MgHCO_3^+$	-1.03
Al^{+3}	-22.88	$CO_2(aq)$	-6.34
$HAlO_2(aq)$	-6.45	CO_3^{-2}	10.33
$NaAlO_2(aq)$	0.75	$CaCO_3(aq)$	7.01
$AlOH^{+2}$	-17.87	KCl(aq)	1.50
$Al(OH)_2^+$	-12.78	$MgCl^+$	0.14
$Al(OH)_3(aq)$	-6.72	$MgSO_4(aq)$	-2.38
$CaCl^+$	0.70	$NaSO_4^-$	-0.81
$CaCl_2(aq)$	0.65	KSO_4^-	-0.88
$CaSO_4(aq)$	-2.10	$NaHSiO_3(aq)$	8.30
NaCl(aq)	0.78	$CaOH^+$	12.85
$FeCl^+$	0.17	NaOH(aq)	14.15
$FeHCO_3^+$	-2.04	$NaCO_3^-$	9.82
$FeCO_3(aq)$	4.88	$NaHCO_3(aq)$	-0.17
$FeCl_4^{-2}$	1.94	$CaHCO_3^+$	-1.04

Table 3-9. Surface protonation reactions on montmorillonite (Bradbury and Baeyens, 2005)

Surface complexation	Log K
mon_sOH$_2^+$ = mon _sOH + H$^+$	-4.5
mon_sO$^-$ + H$^+$ = mon _sOH	7.9
mon_w1OH$_2^+$ = mon_w1OH + H$^+$	-4.5
mon_w1O$^-$ + H$^+$ = mon_w1OH	7.9
mon_w2OH$_2^+$ = mon_w2OH + H$^+$	-6
mon_w2O$^-$ + H$^+$ = mon_w2OH	10.5

Table 3-10. Cation exchange reactions on montmorillonite and illite (Bradbury and Baeyens, 2005)

Cation exchange reaction	$K_{Na/M}$
Na$^+$ + mon-H = mon -Na + H$^+$	1
Na$^+$ + mon -K = mon -Na + K$^+$	0.0775
Na$^+$ + 0.5 mon -Ca = mon -Na + 0.5Ca^{+2}	0.302
Na$^+$ + 0.5 mon -Mg = mon -Na + 0.5Mg^{+2}	0.302

Table 3-11. Equilibrium constants for mineral precipitation/dissolution at 25 °C

Primary Mineral	log(*K*)	Secondary Mineral	log(*K*)
Calcite	1.85	Siderite	1.543
Smectite-Na	-34.62	Dolomite	2.524
Quartz	-3.75	Ankerite	-1.035
K-feldspar	-22.91	Illite	-47.33
Albite	-20.133	Chlorite	4.298
Anorthite	-19.19	Kaolinite	-39.9
Gypsum	-4.472	Anhydrite	-4.297

The equilibrium constants for precipitation/dissolution of primary minerals (minerals that are present initially) and secondary minerals are listed in Table 3-11. Note that plagioclase is a solid solution with albite and anorthite as its end members. In the current model, we assume plagioclase in both bentonite and granite contains 20% anorthite and 80% albite (named ab80an20) so that there is a quasi-equilibrium between pore water and plagioclase.

Mineral dissolution/precipitation is kinetically controlled. The kinetic law for mineral dissolution/precipitation is given in Xu et al. (2011). The kinetic rates and surface areas for the minerals considered in the model were taken mostly from Xu et al. (2006) (Table 3-12). However, the illitization rate (the rate of illite precipitation and smectite dissolution) was calibrated (Liu et al., 2013) based on the measured illite percentage in an illite/smectite (I/S) mixed layer from the Kinnekulle bentonite, Sweden (Pusch and Madsen, 1995).

Table 3-12. Kinetic properties for minerals considered in the model (Xu et al., 2006).

Mineral	A (cm^2/g)	Parameters for Kinetic Rate Law							
		Neutral Mechanism		Acid Mechanism			Base Mechanism		
		k_{25} (mol/m^2-s)	E_a (kJ/mol)	k_{25} (mol/m^2-s)	E_a (kJ/mol)	$n(H^+)$	k_{25} (mol/m^2-s)	E_a (kJ/mol)	$n(H^+)$
Quartz	9.8	1.023×10^{-14}	87.7						
K-feldspar	9.8	3.89×10^{-13}	38	8.71×10^{-11}	51.7	0.5	6.31×10^{-12}	94.1	-0.823
Kaolinite	151.6	6.91×10^{-14}	22.2	4.89×10^{-12}	65.9	0.777	8.91×10^{-18}	17.9	-0.472
Illite	1.18×10^{4} (1)	1.66×10^{-13}	105 (2)						
Chlorite	9.8	3.02×10^{-13}	88	7.76×10^{-12}	88	0.5			
Calcite	3.5	1.63×10^{-7}	23.5						
Dolomite	12.9	2.52×10^{-12}	62.76	2.34×10^{-7}	43.54	1			
Ankerite	9.8	1.26×10^{-9}	62.76	6.46×10^{-4}	36.1	0.5			
Smectite	1.18×10^{4} (1)	1.66×10^{-13}	105 (2)						
Cristobalite	9.8	1.023×10^{-14}	87.7						
ab80an20	9.8	1.023×10^{-14}	87.7						

(1) calibrated based on the field illitization data (Liu et al., 2013)
(2) from Pusch and Madsen (1995)

3.4 Model Results

The ultimate goal of using coupled THMC model to interpret the data collected in the FEBEX *in situ* test is to understand the THMC evolution of bentonite under simulated repository conditions, so that we can use most plausible processes and parameters to describe the behavior of bentonite. Once the coupled THMC model can simultaneously match the measured temperature, relative humidity, water content, stress, aqueous concentrations, and mineral phase changes, we can further use it to predict the long term (e.g. 100,000 years as required by most performance assessment) under different conditions, such as under higher temperature as was done by Zheng et al. (2015a).

3.4.1 Processes Controlling the Hydration of Bentonite

The safety functions of EBS bentonite include limiting transport in the near field including water infiltration from host granite into bentonite and migration of radionuclides from canister to host rock; damping the shear movement of the host rock; preventing the sinking of canisters (if emplaced in the center of the tunnel), limiting pressure on the canister and rock, and reducing microbial activity. The significance of thorough understanding of hydration dynamics of bentonite is that the unsaturated phase of bentonite coincides with the high temperature period of bentonite; the combination of these two conditions might result in some irreversible change of bentonite, which will affect the ability of bentonite retarding the migration of radionuclides once the canister is fully corroded, presumably1000-10,000 years after the emplacement of radioactive waste. In this section, we present the key processes that control the hydration of bentonite revealed by the THMC model of the FEBEX *in situ* test and also the processes that we think are not relevant to the hydration of bentonite.

3.4.1.1 Non-Darcian Flow

When a TH model was developed for the FEBEX in situ test (Zheng et al., 2015), it was clear that the TH model was not able to match the measure temporal evolution of relative humidity at several radial distances. In fact, THM/THC models for mock-up tests (Zheng and Samper, 2008; Sánchez et al., 2012b) clearly showed that the typical Darcy flow model overestimated the hydration of FEBEX bentonite. While summarizing the main findings from 15 years of operation of the mock-up and *in situ* tests, Lanyon et al. (2013) identified three second-order processes that may be relevant: thermal osmosis, threshold gradient for flow (i.e. Non-Darcian flow) within bentonite, and the evolution of pore structure during hydration. We therefore added Non-Darcian flow to the TH model, aiming to resolve the discrepancy

between model and relative humidity data to some extent knowing that Non-Darcian flow won't solve all the problem as other processes might also be at play, especially HM coupling.

After implementing the model of Non-Darcian flow into the simulator, according to Liu and Birkholzer (2012), we calibrated the most important parameter for Non-Darcian flow, the threshold gradient, based on a permeability test (Samper et al., 2008b). The calibration process was given in Zheng et al. (2015). A Non-Darcian flow in the TH model was developed for the FEBEX *in situ* test. Comparison between relative humidity data and model results from the Darcy and Non-Darcian flow TH models at several radial distances were checked. The Non-Darcian flow models significantly underestimated the relative humidity data (Figure 3-16), even in bentonite near the bentonite/granite interface.

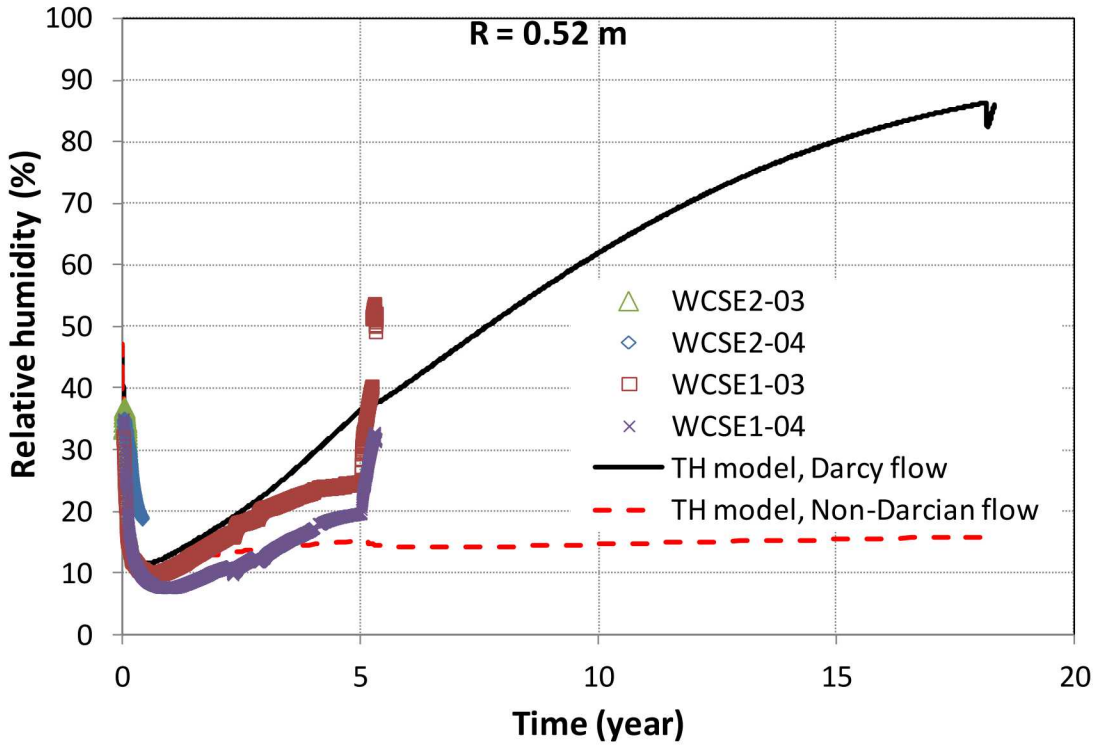

Figure 3-16. Measured relative humidity by sensors located at a radial distance of 0.52 m in sections E2 and E1 (see Figure 3-2 for their locations) and model results from the Darcy flow TH model and the Non-Darcian Flow TH model.

The relevance of Non-Darcian behaviour is clear for saturated flow in clay rock (Liu and Birkholzer, 2012 and references cited therein), and intuitively one would try to evaluate whether Non-Darcian behaviour would be relevant to unsaturated flow in clay rock. However, when the numerical model was used to evaluate such relevance, there are a couple of issues that might prevent us from clearly delineating the contribution of Non-Darcian flow to unsaturated clay or bentonite. First and foremost, the calibration of relative permeability and retention curves overshadows the effect of Non-Darcian flow. The non-linear relationship between water flux and hydraulic gradient, which motivates the relevance of Non-Darcian behavior to water flow, is already accounted for, at least partially, by the relative permeability (which, in turn, is a function of the retention curve) in the flux-gradient relationship for unsaturated flow. In other words, the non-linear relationship between water flux and hydraulic gradient for unsaturated flow might be affected by two features: Non-Darcian flow and relative permeability. However, in most modelling

exercises, relative permeability is calibrated based on a Darcy-type flow model. As a result, the calibration of the parameters associated with relative permeability overshadows the contribution of Non-Darcian flow— the parameters for relative permeability might be "over-calibrated," so that the effect of Non-Darcian flow appears irrelevant. For FEBEX bentonite, the relative permeability and water retention functions were calibrated based on the Darcy type flow model (ENRESA, 2000), which essentially obviates Non-Darcian flow for unsaturated bentonite. Thus, if the Non-Darcian flow model is added in addition to the relative permeability function calibrated based on Darcy flow, as in the model presented in this section, we may miscalculate the non-linear function between flux and gradient, and consequently the model would significantly underestimate the water inflow from granite to bentonite, as shown in Figure 3-16. This is essentially an issue of process uncertainty versus parameter uncertainty, which is faced by many complex models. Second, Cui et al. (2008) reported that threshold gradients are different for different capillary pressure. In this report, we used the equation proposed in Liu and Birkholzer (2012), in which threshold gradient is solely a function of saturated permeability. Further research is needed to incorporate the effect of capillary pressure, when a threshold gradient is calculated. However, even though we can improve our threshold gradient calculation by incorporating the capillary pressure, it is unlikely to eliminate the aforementioned issue of process uncertainties versus parameter uncertainties.

3.4.1.2 The Quasi-Final THMC Model

In FY16, after extensive calibration simulations, we finally obtained a THMC model (Zheng et al., 2016), and the results of simulations practically matched measured temporal evolution of temperature, relative humidity and stress at several radial distances, and measured spatial distribution of water content and dry density at 5.3 and 18.3 years, namely all the THM data available in our possession. To distinguish this from the final THMC model presented in the report, we named this model the "quasi-final THMC model." In comparison with the TH model, this quasi-final THMC model includes the mechanical process and calculated the change of void ratio according to a state surface approach:

$$e = A + B\ln\sigma' + C\ln(\psi + p^a) + D\ln\sigma'\ln(\psi + p^a) \qquad 3\text{-}13$$

Regarding the change of permeability, the quasi-final THMC model used an exponential law (David et al., 1996):

$$k = k_0 \exp[-\gamma(\sigma - \sigma_0)] \qquad 3\text{-}14$$

where k is the permeability at the effective stress σ, k_0 is the permeability at initial stress σ_0 and is equal to 2.15E-21 m^2; γ is the stress sensitivity coefficient and equal to 1E-7 Pa^{-1} in the current model based on the calibration against THM data. The stress-dependence of permeability for low-permeability sedimentary rocks is well-known and has been studied extensively (e.g. Ghabezloo et al., 2009; Kwon et al., 2001). Many empirical relationships have been put forward to describe the permeability changes with effective stress. Equation 3-14 is one approach to describing permeability.

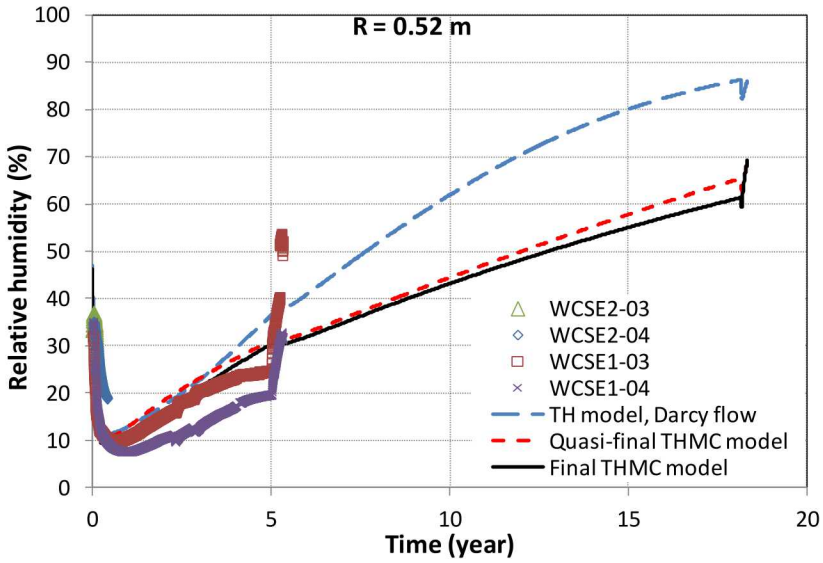

Figure 3-17. Measured relative humidity by sensors located at a radial distance of 0.52 m and results from the TH model, the quasi-final THMC model and final THMC model.

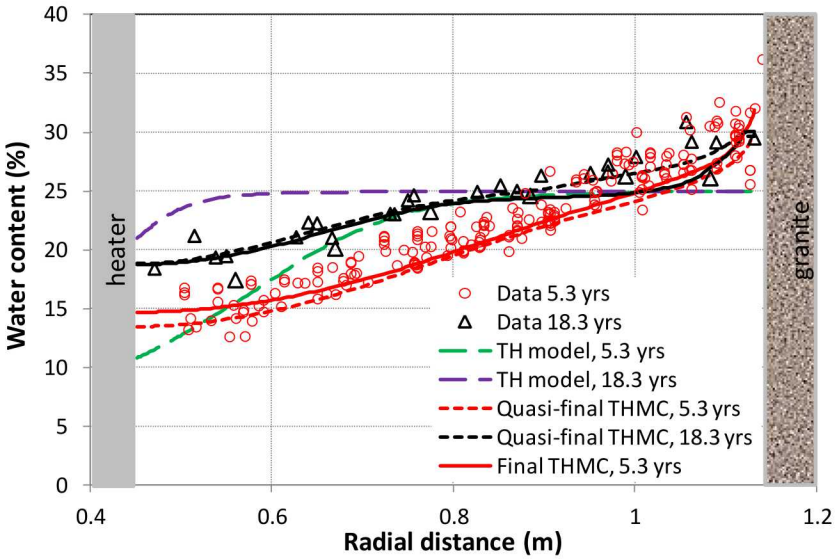

Figure 3-18. Measured water content at 5.3 and 18.3 years, and results from the TH model, the quasi-final THMC model and final THMC model.

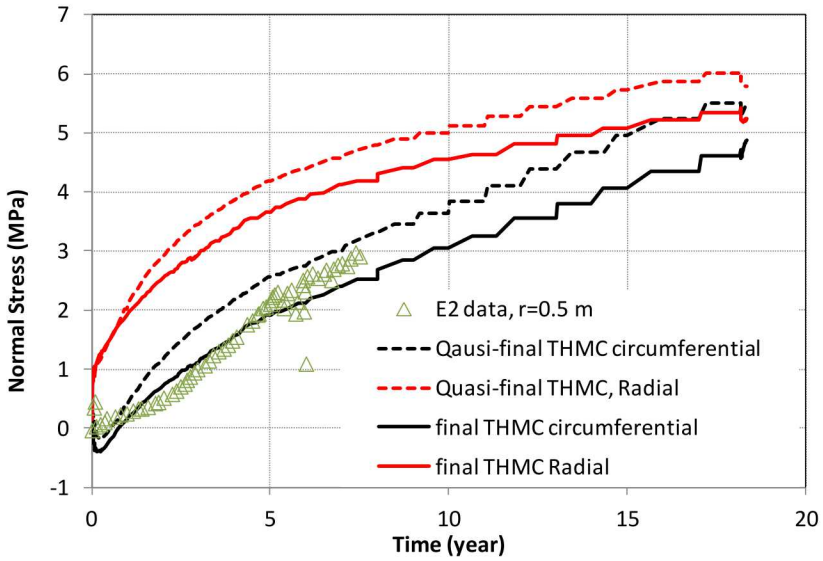

Figure 3-19. Measured stress by sensors located at a radial distance of ~0.5 m in section E2 and results from the quasi-final THMC model and final THMC model.

The quasi-final THMC model matches nicely all available THM data, including temporal evolution of temperature, relative humidity and stress at several radial distances and water content data at two time snapshots, as exemplified in Figures 3-17 to 3-19. Considering that the transport of conservative chemical species (e.g. chloride) is largely controlled by water movement, one would expect that the quasi-final THMC model should be able to match the concentration profile of chloride. However, as shown in Figure 3-20, the quasi-final THMC model overestimates significantly the measured chloride concentration in bentonite near the granite and underestimates the measured chloride concentration near the heater, and adjusting the diffusion coefficient did not improve the match (Zheng et al., 2016). Therefore, in the final THMC model (details are given in Section 3.3), two changes were introduced to the THMC model. First, a coupling process, thermal osmosis, was added to the model, with a calibrated thermal osmotic permeability. Second, the permeability changes as a function of swelling were revised — instead of relating permeability to stress (see Equation 3-14), permeability is related to dry density (which is a function of porosity) based on the measured permeability at different dry density (ENRESA, 2000) as in Equation 3-4. The final THMC model can achieve a match similar to that of the THM data, as exemplified by the relative humidity data (Figure 3-17), water content data (Figure 3-18) and stress data (Figure 3-19) and unlike the quasi-final THMC model, the final THMC model matches the chloride concentrations measured at 5.3 years and 18.3 years well. The lessons learned here is that chemical data provide an important additional piece of information for calibrating a THM model.

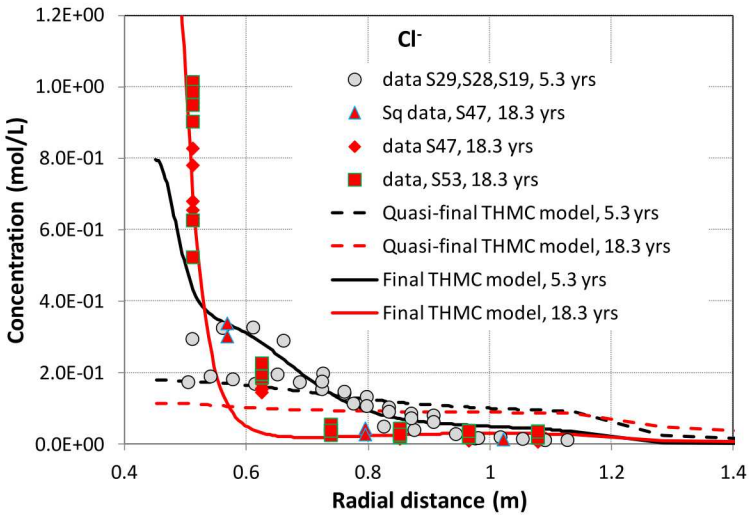

Figure 3-20. Calibrated chloride concentration data at 5.3 years from aqueous extract test for sections 29, 28, and 19 (Zheng et al., 2011), calibrated chloride concentration data at 18.3 years from aqueous extract test for section 47 (data S47, 18.3 yrs) and section 53 (data S53, 18.3 yrs), chloride concentration data from squeezing test for section 47 (Sq data, S47, 18.3 yrs) and model results from the THMC model.

3.4.2 Geochemical Evolution in the Test

As presented in Section 3.2, two types of geochemical data are available for the FEBEX in situ test: ion concentration in the pore water of bentonite and granite, compositions of solid phase including minerals phases and exchangeable cations. While both types of data help us understand the geochemical evolution in the in situ test, model interpretation has to heavily focus on the ion concentration in pore water of bentonite and granite. The solid phases underwent relatively small changes and their spatial and temporal evolution are overshadowed by the measurement variation. For example, measured mass fraction of smectite ranges from 85% to 96%, depending on laboratory and sample; such variation is much larger than expected the change in smectite mass fraction, and have no clear spatial trend, and therefore the measured mass fractions of smectite are of little use for constraining the model. Some geochemical data, such as the content of calcium in solid phases, shows clear trends, and can be used to qualitatively constrain the model because such data are not comparable to the model results unless additional information, e.g. for this case a complete list of mass fraction of all minerals, is known. In this section, we primarily use the comparison of model and data for ion concentrations in pore-water of bentonite to guide the discussion, with data from solid phases providing supplementary information. However, attention is called that the ion concentrations in pore-water of bentonite are measured through an indirect method, aqueous extract, and geochemical modeling was conducted to infer the “true” ion concentration in pore-water from aqueous extract data, thus adding another layer of uncertainties to understand the chemical evolution in bentonite.

Geochemical evolution is the consequence of coupled THMC processes. THM processes strongly affect the geochemical evolution but usually not vice versa, which is why from FY15 to FY17, a great deal of effort was dedicated to have a sound THM model that can match the THM data. Once the THM processes are relatively well established, before we study the possible chemical reactions, we need to constrain the transport process. While the advection of chemical species is fixed in the THM model, diffusion has to be calibrated in the chemical model.

Because chloride is only controlled by transport processes, its temporal and spatial evolution is a good indicator of the transport processes. The final calibrated effective diffusion coefficient for Cl is the $\emptyset^{1/3}S^{10/3}\times 2\times 10^{-10} m^2/s$, where $\emptyset$ is porosity and S is water saturation. Depending on the time and location, the effective diffusion coefficient ranges from 8×10^{-14} m^2/s to 1.4×10^{-12} m^2/s, with effective diffusion coefficient for most time and locations around $(0.4 – 1.4)\times10^{-12}$ m^2/s. Figure 3-20 shows the comparison of chloride concentration data and model results. The THMC model nicely fit the data near the heater, indicating that the chloride concentration could be fairly high at the canister-bentonite interface. If such a trend persists for an extended time period until the canister is fully corroded, the high chloride concentration might significantly affect the degradation of waste. As granite pore water (which has much lower chloride concentration than bentonite pore water) infiltrates into the bentonite, it dilutes the bentonite pore water significantly as shown by the very low chloride concentration near the granite (radial distance between 0.8 and 1.1 m). Meanwhile, bentonite pore water was pushed further near the heater and evaporation caused an increase in chloride concentration, as manifested by the high chloride concentration near the heater.

Another mass exchange process between bentonite and granite is the diffusion of Cl from the bentonite to the granite, which leads to a higher Cl concentration in granite pore water. As mentioned in Section 3.2.4, granite pore water samples were collected in two tunnels, FU1 and FU2, 0.2 and 0.6 m away from the tunnel wall (bentonite/granite interface), respectively. We therefore check the comparison of model results and data (Figure 3-21). Reasonable fit was achieved, which support the parameterization of the transport process in bentonite.

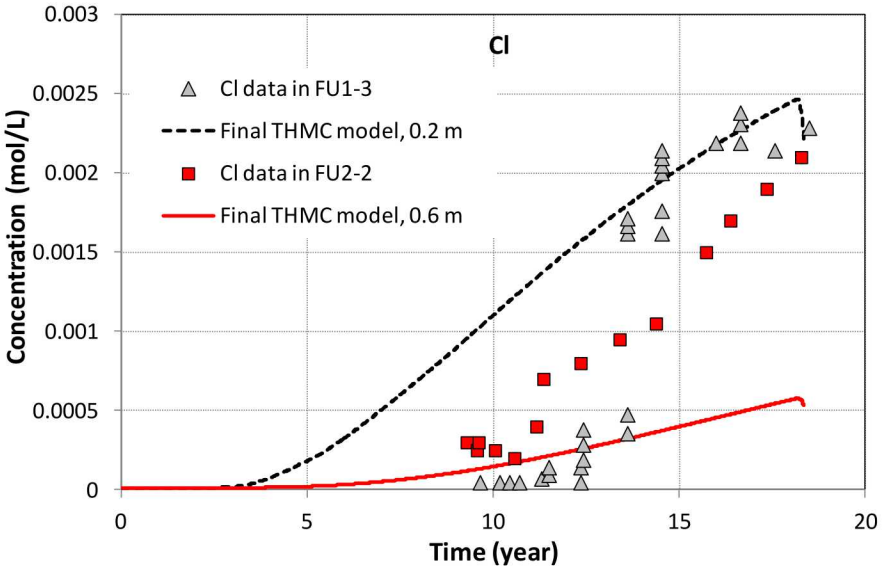

Figure 3-21. Model results and chloride concentration data in granite. Data in FU1-3 are collected from a tunnel at 0.2 m away from the bentonite/granite interface; Data in FU2-2 are data from tunnel 0.6 m away from the bentonite/granite interface.

Measured sulfate data (Figure 3-22) show a spatial profile that is different from the profile for chloride, indicating that chemical reactions play significant role in shaping the spatial and temporal evolution of sulfate in addition to transport processes. The final calibrated effective diffusion coefficient for sulfate is the same as Cl, ranging from 8×10^{-14} m^2/s to 1.4×10^{-12} m^2/s, and at most times and locations the effective diffusion coefficient is around $(0.4 – 1.4)\times$10-12 m^2/s. A good match between model results and sulfate concentration measured at the two tunnels in granite (Figure 3-23) seems support the calibrated effective diffusion coefficient for sulfate. However, model and data for the spatial profiles in bentonite faced a

great challenge in matching each other for both small scale heating and hydration tests (Zheng et al., 2010) or the *in situ* test after dismantling of Heater #1 (Zheng et al., 2011). The challenge problems are (1) the data are not directly measured but rather inferred from the aqueous extract (see section 3.2.1.1), using a geochemical model, in which the initial amount of gypsum is critical, (2) initially FEBEX bentonite (ENRESA, 2000) contains small amount of gypsum, but the bentonite samples contain gypsum, and (3) the layout of collected bentonite samples after dismantling the heaters is uncertain due to the spatial heterogeneity of bentonite. The current model assumes the initial content of 0.3% of gypsum. Once the heating started, gypsum dissolves (Figure 3-24), forming anhydrite ($CaSO_4.2H_2O$), which has lower solubility than gypsum at temperatures higher 43 °C (Figure 3-25). As granite pore water infiltrates into the bentonite, anhydrite dissolves, which raises the concentration of sulfate. Later, as more granite pore water infiltrates into the bentonite, dilution leads to a decrease in sulfate concentration and apparently bentonite in the area near the granite undergoes more dilution, lowering the concentration. Meanwhile, evaporation near the heater leads to higher sulfate concentration and more precipitation of anhydrite therein (Figure 3-28). The simulated concentration profiles at 5.3 and 18.3 years are basically a reflection of these processes. The model results match well the inferred data at 5.3 years, but not at 18.3 years. It is noteworthy that model results match the data measured by squeezing well, which do not require model inference like aqueous extract data. Another possibility is that pyrite oxidation occurs at the early stage of the *in situ* test and sulfate reduction takes place when the bentonite becomes more reducing at the latter stage of the test. However, Fernández et al. (2017) showed a high amount of dissolved O_2 in the initial pore water of bentonite, 0.2 mmol/L, which makes the water highly under-saturated with respect to pyrite and essentially rules out the possibility of the existence of pyrite. Moreover, if pyrite is initially present, it will be quickly oxidized and would lead to high Fe concentration in the bentonite pore water, which has not been observed in the FEBEX in situ test. However, as we are synthesizing the measured pore water concentration, gas, biological and mineralogical data, other possibilities could exist for better interpretation of the sulfate data. The precipitation of anhydrite is consistent with the high sulfur content in some samples.

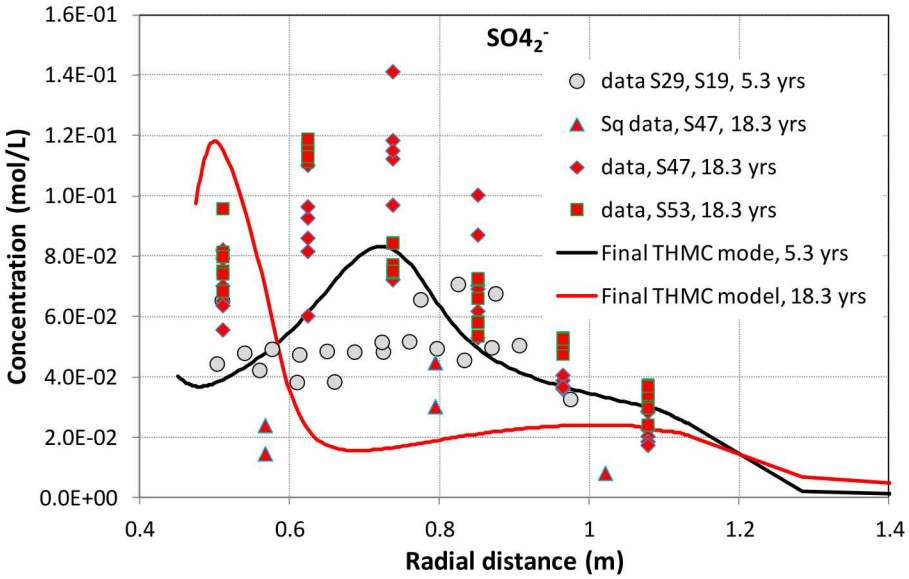

Figure 3-22. Calibrated sulfate concentration data at 5.3 years from aqueous extract test for sections 29, 28, and 19 (Zheng et al., 2011), calibrated chloride concentration data at 18.3 years from aqueous extract test for section 47 (data S47, 18.3 yrs), sulfate concentration data from squeezing test for section 47 (Sq data, S47, 18.3 yrs) and model results from the THMC model.

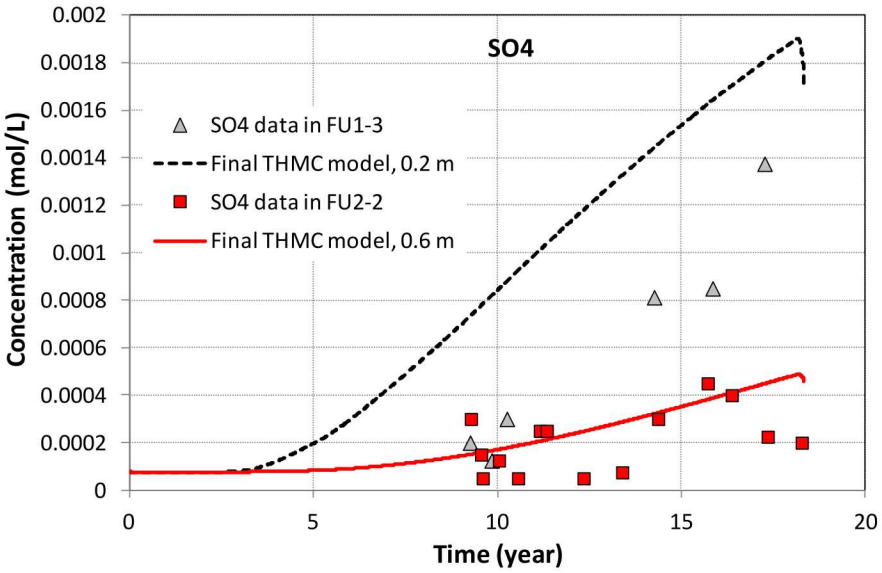

Figure 3-23. Model results and sulfate concentration data in granite. Data in FU1-3 are collected from a tunnel at 0.2 m away from the bentonite/granite interface; Data in FU2-2 are data from tunnel 0.6 m away from the bentonite/granite interface.

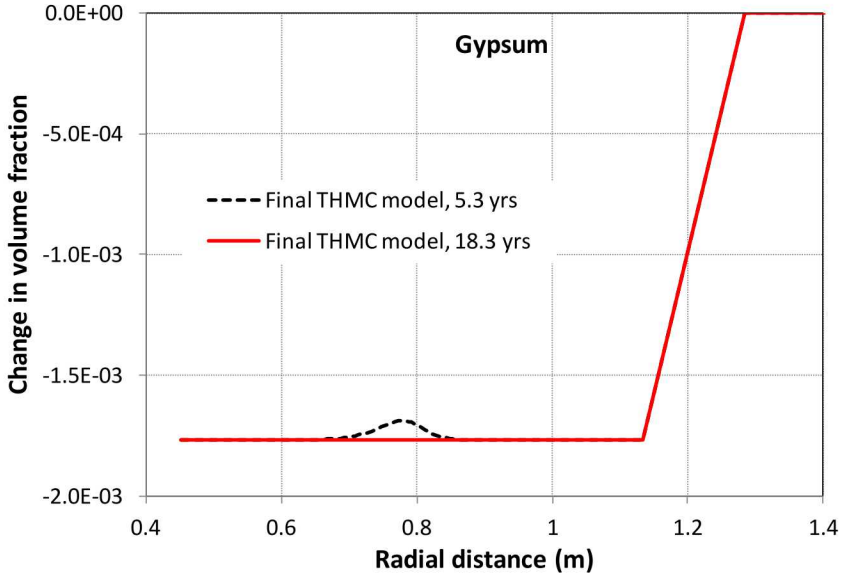

Figure 3-24. Model results of gypsum volume fraction change at 5.3 and 18.3 years. Negative value means dissolution and positive value means precipitation.

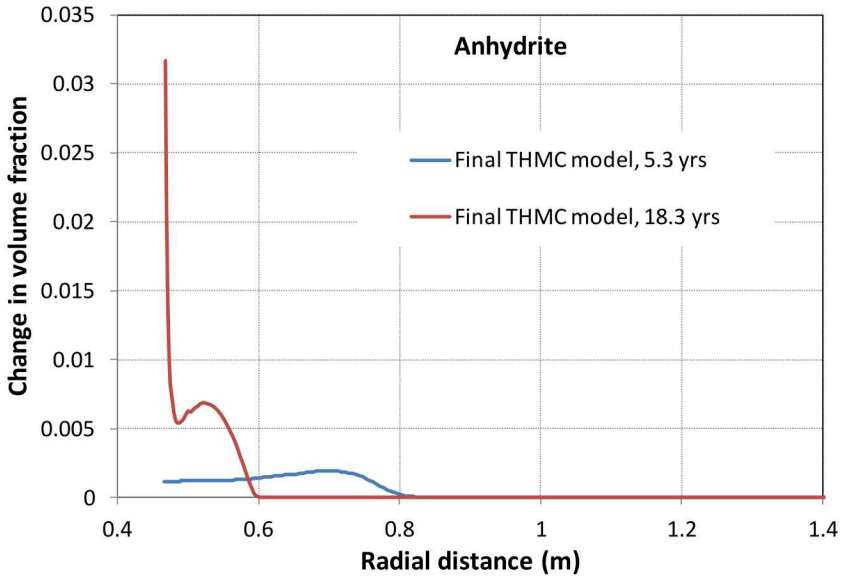

Figure 3-25. Model results of anhydrite volume fraction change at 5.3 and 18.3 years. Negative value means dissolution and positive value means precipitation.

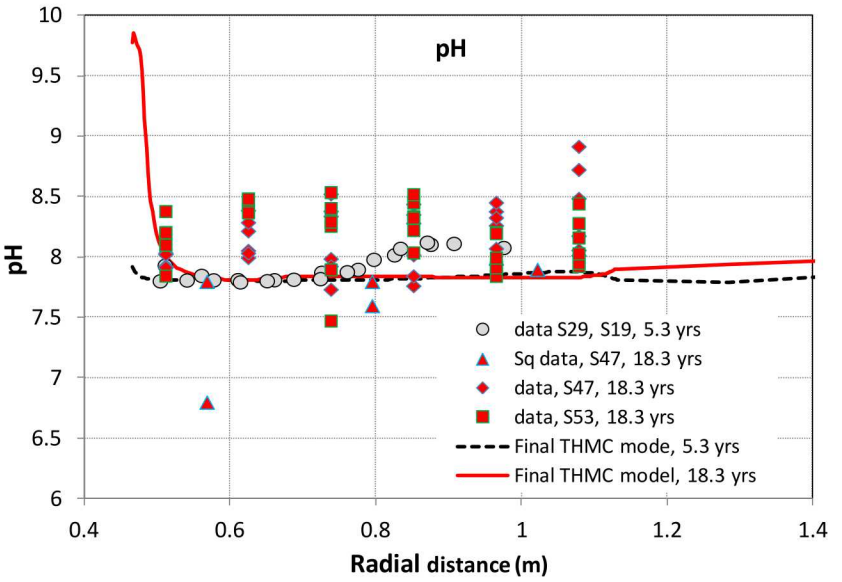

Figure 3-26. Calibrated pH data at 5.3 years from aqueous extract test for sections 29, 28, and 19 (Zheng et al., 2011), pH data at 18.3 years from aqueous extract test for section 47 (data S47, 18.3 yrs) and section 53 (data S53, 18.3 yrs), pH data from squeezing test for section 47 (Sq data, S47, 18.3 yrs) and model results from the THMC model.

It was found out by previous modeling (e.g., Zheng et al., 2011; Zheng et al., 2015) that pH is buffered by surface protonation and maintained at the initial level. As shown in Figure 3-26, from 5.3 years to 18.3 years, pH does not change significantly in most areas. The spatial profile of pH is also fairly flat, except in the areas near the granite and the heater. The increase in pH in bentonite pore water at the vicinity of heater is related to the dissolution of montmorillonite (Figure 3-36). The current model confirms that surface protonation buffers pH. In the *in situ* test, granite water has a pH just slightly higher than

bentonite pore water, surface protonation seems to be able to maintain pH at a stable level in most area. Model also indicates that the pH buffer by surface protonation is limited — when there is significant mineral dissolution or precipitation, pH could go up or down significantly. It remains to be seen whether surface protonation is able to maintain a stable pH in bentonite when it is in contact with concrete, whose pore water is highly alkaline.

Bicarbonate concentration data have been very difficult to match by modeling because of the uncertainties in both the CO_2 gas evolution in the bentonite barrier in the *in situ* test and the inference of bicarbonate concentration data from aqueous extract. As shown in Figure 3-27, inferred aqueous extract data vary two orders of magnitude for the samples at the same location. Data measured by squeezing do not show any clear spatial trend, but the inferred aqueous extract data show a roughly decreasing trend from granite towards the heater. The current model, which accounts for the CO_2 gas evolution and carbonate minerals, has the same trend except the area near the heater. Even though organic reactions, i.e. bacteria-mediated reactions, are considered, the model results might be not be very different.

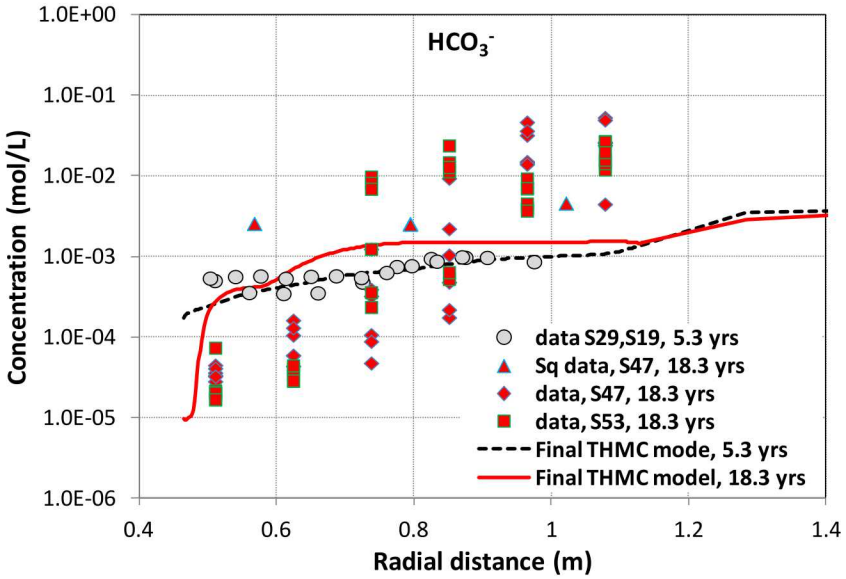

Figure 3-27. Calibrated bicarbonate concentration data at 5.3 years from aqueous extract test for sections 29, 28, and 19 (Zheng et al., 2011), calibrated bicarbonate concentration data at 18.3 years from aqueous extract test for section 47 (data S47, 18.3 yrs) and section 53(data S53, 18.3 yrs), bicarbonate concentration data from squeezing test for section 47 (Sq data, S47, 18.3 yrs) and model results from the THMC model.

Sodium concentration in the bentonite barrier goes through similar transport processes that control chloride concentration profiles in bentonite, which leads to higher sodium concentrations near the heater and lower concentrations near the granite (Figure 3-28). However, chemical reactions such as cation exchange mitigate the concentration change such that the concentration of sodium is not as low as that of chloride near the granite and not as high as that of chloride near the heater. The final calibrated effective diffusion coefficient for sodium is the $\emptyset^{1/3}S^{10/3}\times3\times10^{-10}[\frac{m^2}{s}]$, ranging from 1.2×10^{-13} m^2/s to 2.1×10^{-12} m^2/s, and at most times and locations the effective diffusion coefficient is around (0.6 – 2.1)×10-12 m^2/s. Model results and sodium concentration data in granite show similar trend (Figure 3-29), which weakly confirms the mass exchange between bentonite and granite calculated by the model is roughly in the ballpark and provide a supplementary support of the parameters for sodium transport. Exchangeable sodium data are not used here because they are unreliable. The measured sodium contents in solid phases increased from the internal part of the barrier towards the gallery wall (see Section 3.2), which cannot be

explained by the current model. No sodium-bearing mineral precipitates in the current model. Further investigation of both model and data is needed.

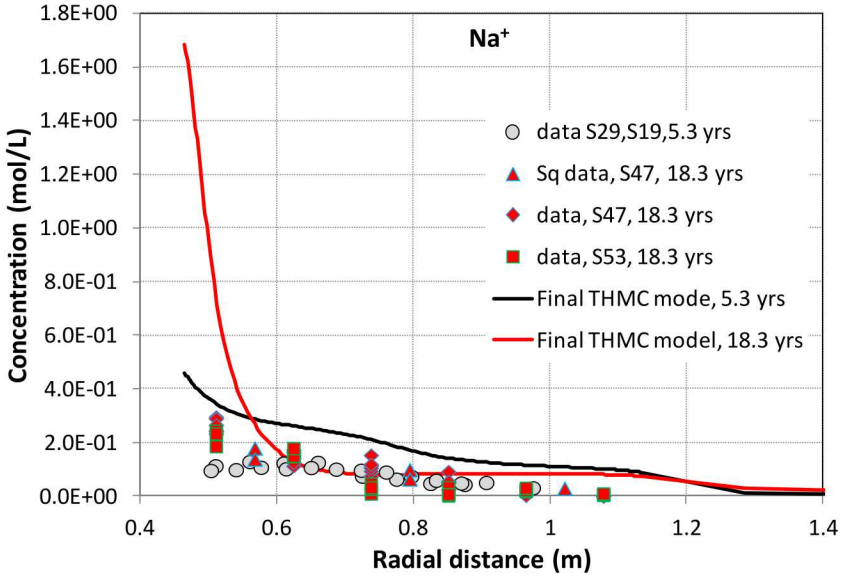

Figure 3-28. Calibrated sodium concentration data at 5.3 years from aqueous extract test for sections 29, 28, and 19 (Zheng et al., 2011), calibrated sodium concentration data at 18.3 years from aqueous extract test for section 47 (data S47, 18.3 yrs) and section 53 (data S53, 18.3 yrs), sodium concentration data from squeezing test for section 47 (Sq data, S47, 18.3 yrs) and model results from the THMC model.

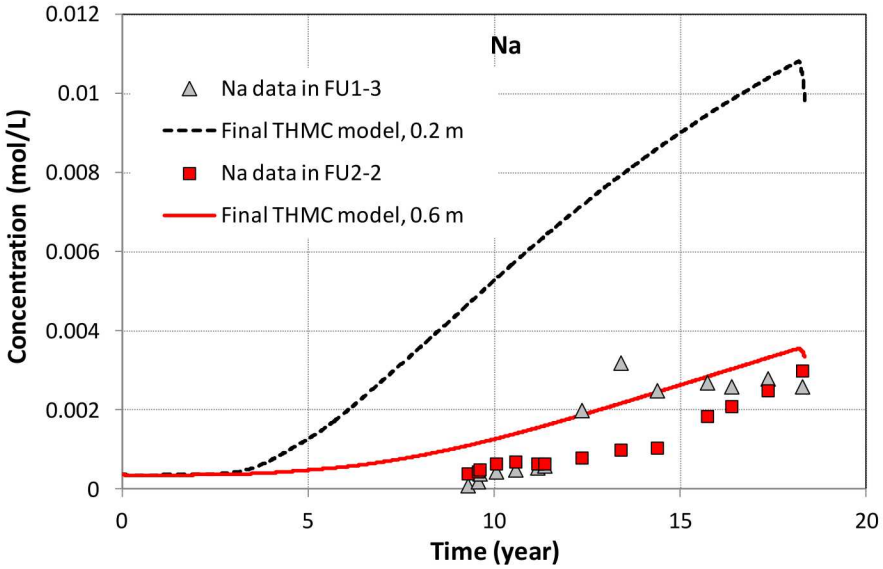

Figure 3-29. Model results and sodium concentration data in granite. Data in FU1-3 are collected from a tunnel at 0.2 m away from the bentonite/granite interface; Data in FU2-2 are data from tunnel 0.6 m away from the bentonite/granite interface.

A reliable prediction of the evolution of potassium concentration is important because potassium is critical for illitization, which is one of the major concerns of the bentonite barrier. The FEBEX in situ

test, the longest field test, provides a great opportunity to learn about the evolution of potassium concentration. The current THMC model reproduces reasonably well the concentration data at 5.3 years and 18.3 years (Figure 3-30). Modeling work shows that, in addition to the transport processes, cation exchange is the most important reaction that regulates the temporal and spatial distribution of potassium, but cannot be confirmed by measured exchange of potassium because the data are unreliable. The final calibrated effective diffusion coefficient for potassium is the $\emptyset^{1/3}S^{10/3}\times3\times10^{-10}[m^2/s]$, ranging from 1.2×10^{-13} m^2/s to 2.1×10^{-12} m^2/s, and at most times and locations the effective diffusion coefficient is around $(0.6 – 2.1)\times10^{-12}$ m^2/s.

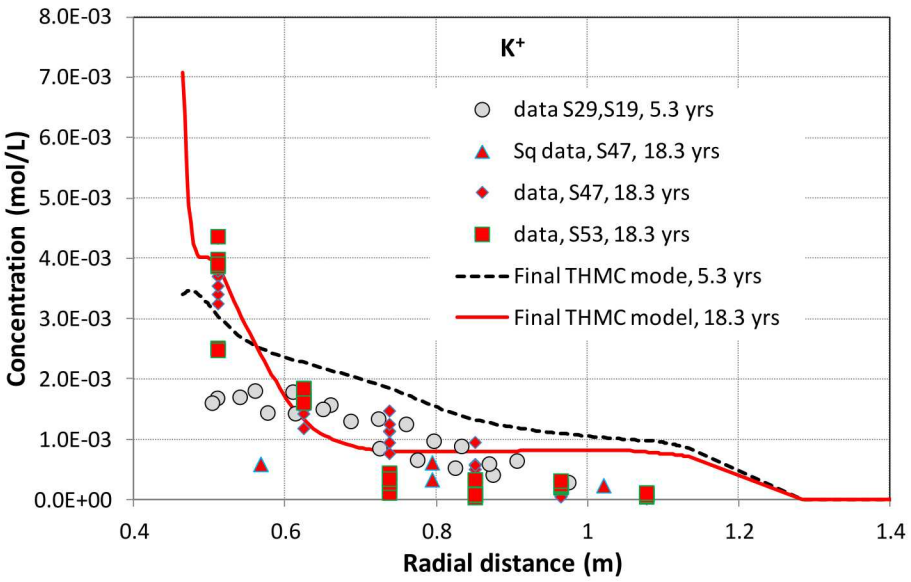

Figure 3-30. Calibrated potassium concentration data at 5.3 years from aqueous extract test for sections 29, 28, and 19 (Zheng et al., 2011), calibrated potassium concentration data at 18.3 years from aqueous extract test for section 47 (data S47, 18.3 yrs) and section 53 (data S53, 18.3 yrs), potassium concentration data from squeezing test for section 47 (Sq data, S47, 18.3 yrs) and model results from the THMC model.

The relevance of calcium evolution in the bentonite to the performance of the bentonite barrier lies in its impact on pH through dissolution/precipitation of carbonate minerals, such as calcite, dolomite, and its complexation with uranium and its impact on redox conditions via gypsum dissolution and sulfate reduction. The current model matches well the calcium data at 5.3 years, but falls short of matching the calcium data at 18.3 years (Figure 3-31). An increase in the initial amount of gypsum in bentonite helps to improve the fits at 18.3 years, but worsens the match at 5.3 years. However, just like inferred aqueous extract data for bicarbonate, calcium data are less reliable, because the involvement of CO_2 gas and calcite dissolution over the course of conducting the aqueous extract experiment, whereas the amount of calcite is unknown before aqueous extract is conducted. In other words, it is not clear if the mismatch between the THMC model data and inferred data is caused by the THMC model or the uncertainty in the inference of aqueous extract data. The final calibrated effective diffusion coefficient for calcium is the $\emptyset^{1/3}S^{10/3}\times3\times10^{-10}[\frac{m^2}{s}]$, ranging from 1.2×10^{-13} m^2/s to 2.1×10^{-12} m^2/s, and at most times and locations the effective diffusion coefficient is around $(0.6 – 2.1)\times10^{-12}$ m^2/s. Model results and calcium concentration data in granite match each other approximately (Figure 3-32), which provides a supplementary support of the parameters for the calcium transport in bentonite. Calcite precipitates more

in bentonite near the granite and less in bentonite near the heater, which is consistent with trend of measured calcium content in the solid phases (see Section 3.2).

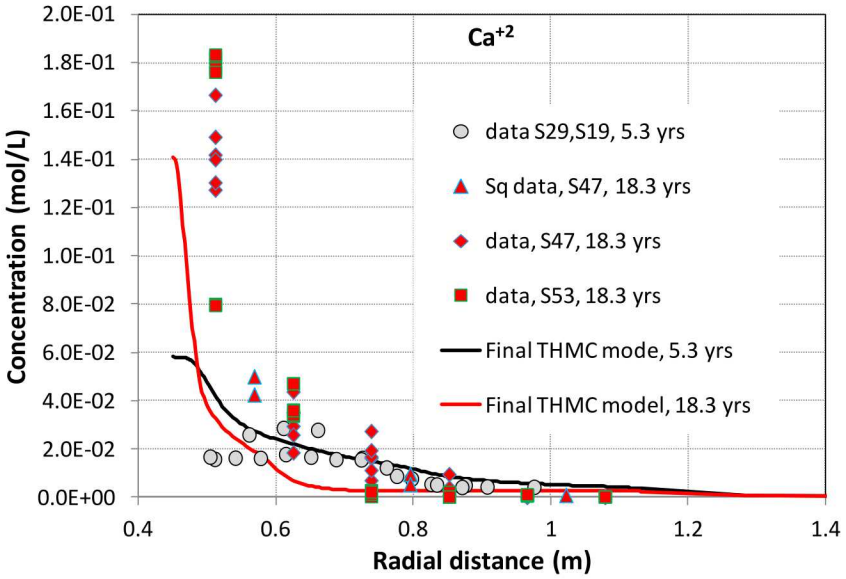

Figure 3-31. Calibrated calcium concentration data at 5.3 years from aqueous extract test for sections 29, 28, and 19 (Zheng et al., 2011), calibrated calcium concentration data at 18.3 years from aqueous extract test for section 47 (data S47, 18.3 yrs), calcium concentration data from squeezing test for section 47 (Sq data, S47, 18.3 yrs) and model results from the THMC model.

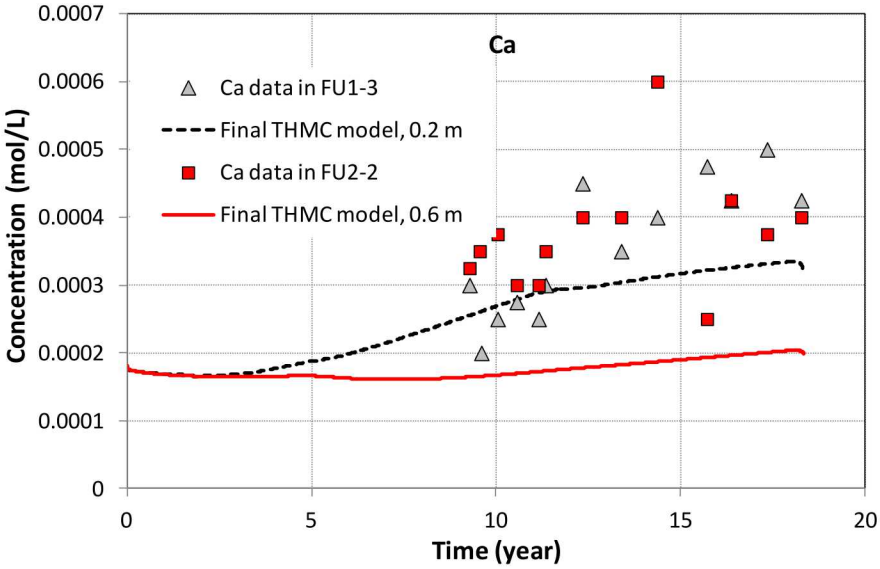

Figure 3-32. Model results and calcium concentration data in granite. Data in FU1-3 are collected from a tunnel at 0.2 m away from the bentonite/granite interface; Data in FU2-2 are data from tunnel 0.6 m away from the bentonite/granite interface.

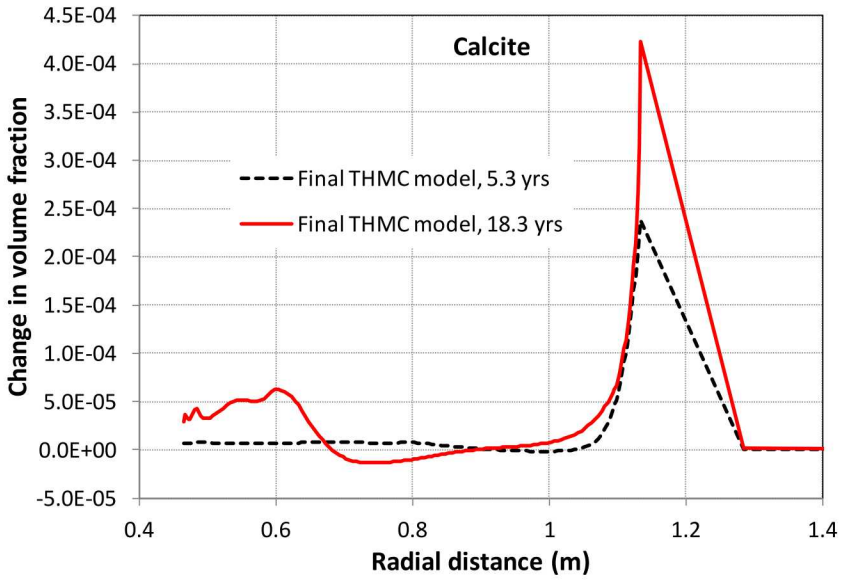

Figure 3-33. Model results of calcite volume fraction change at 5.3 and 18.3 years. Negative value means dissolution and positive value means precipitation.

The current THMC model shows a decent match to the magnesium data at 5.3 years and 18.3 years (Figure 3-34). Data collected after the final dismantling showed that magnesium contents in the solid phases increase towards the heater, which is not explained by the current model. Precipitation of dolomite could be a possible explanation for the increase in magnesium towards heater, but it contradicts the decrease of calcium content in the solid phases towards the heater. Further study on the both the data and model is needed.

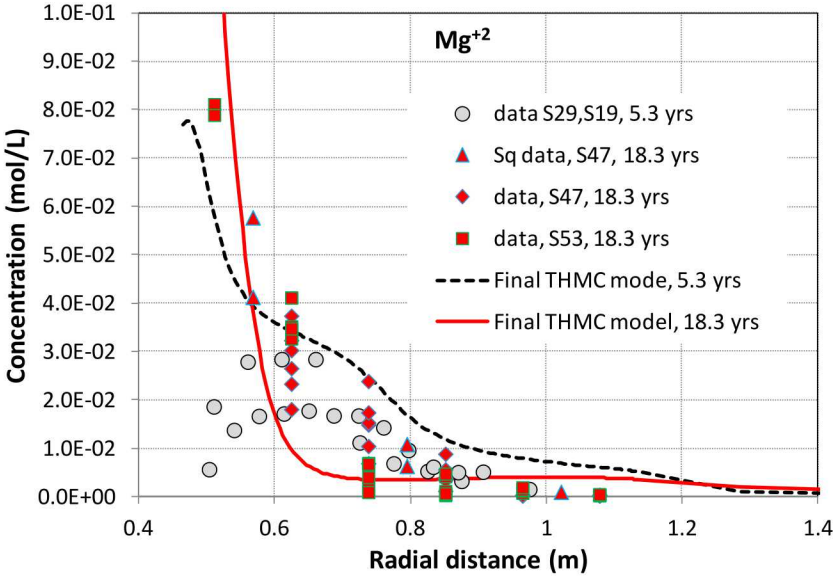

Figure 3-34. Calibrated magnesium concentration data at 5.3 years from aqueous extract test for sections 29, 28, and 19 (Zheng et al., 2011), calibrated magnesium concentration data at 18.3 years from aqueous extract test for section 47 (data S47, 18.3 yrs), magnesium concentration data from squeezing test for section 47 (Sq data, S47, 18.3 yrs) and model results from the THMC model.

The evolution of clay minerals, namely montmorillonite and illite, has great implications to the long-term stability of the bentonite barrier. Many laboratory heating tests are often too short to show significant change in clay minerals. Also, conditions in the laboratory tests are very different from the *in situ* condition and the implications of these test results require interpretation. The mineral characterization of the samples collected after the final dismantling provides insight on the possible change of clay minerals after long-term heating and hydration. Unfortunately, given the large sample-to-sample variation of the illite fraction in the illite/smectite mixed layer clays, it is impossible to delineate if there is any increase or decrease of the illite mass fraction by comparison with the reference bentonite. Models show illitization near the heater, as manifested by illite precipitation and montmorillonite dissolution, but on the order of less than 1%, which cannot be proved or disapproved by the data.

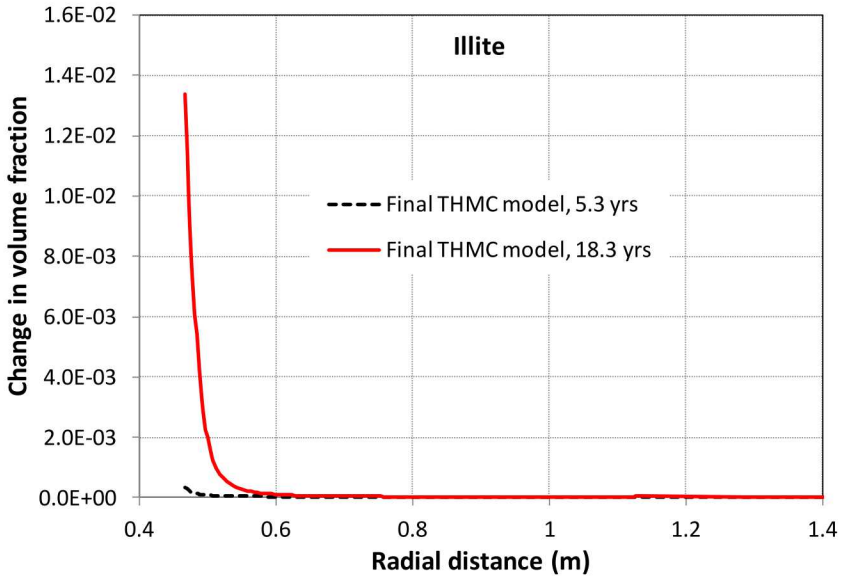

Figure 3-35. Model results of illite volume fraction change at 5.3 and 18.3 years. Negative value means dissolution and positive value means precipitation.

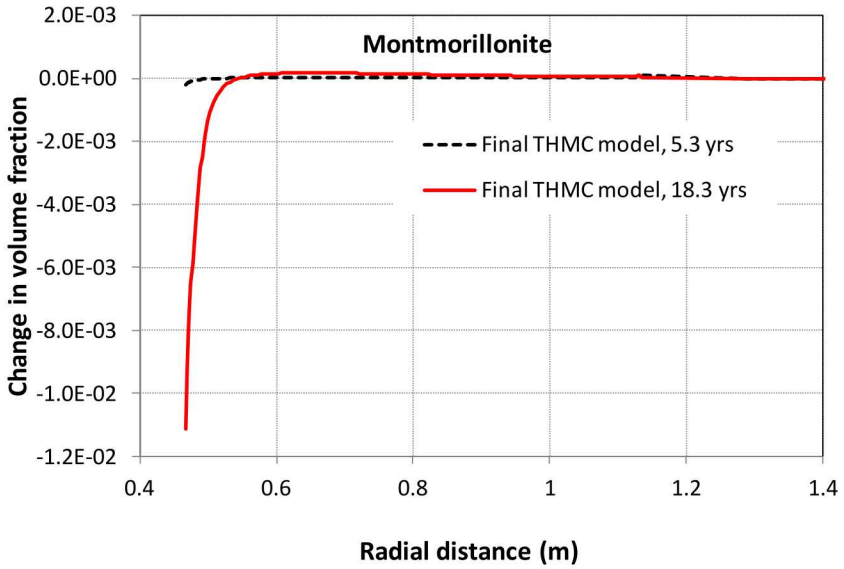

Figure 3-36. Model results of montmorillonite volume fraction change at 5.3 and 18.3 years. Negative value means dissolution and positive value means precipitation.

3.5 Summary and Future Work

The FEBEX *in situ* test, which lasted for more than 18 years, generated extremely valuable data for validating the coupled THMC model and improving our understanding of the factors and processes affecting the temporal and spatial evolution of the bentonite barrier over the course of long-term heating and hydration. In the FEBEX-DP project, Heater #2 was dismantled and extensive THMC characterization was conducted. The ultimate goal is to use THMC data from FEBEX-DP to validate THMC models and to enhance our understanding of coupled THMC processes in bentonite.

Since FY15, the model for the FEBEX *in situ* test evolved from the TH model to the THMC model. Significant efforts were dedicated to understanding the lower-than-expected relative humidity data near the heater. The main scientific problems that have been tested include the Non-Darcian flow model, swelling via Barcelona Expansive Clay model, linear swelling model, state surface model, and various constitutive relationships for saturated permeability in bentonite as functions of either stress or dry density. After extensive calibration, the THMC models developed in FY16 (Zheng et al., 2016) matched reasonably the measured temporal evolution of temperature, relative humidity and stress at several compliance points in the bentonite barrier and the measured spatial distribution of water content and dry density at 5.3 years, when the Heater #1 was dismantled, and at 18.3 years when the Heater #2 was dismantled. However, they failed to explain the spatial profile of chloride concentration at 5.3 years. In FY17, the THMC model was further revised by adding thermal osmosis and using a revised permeability-dry density relationship, and eventually the model matched the THM data and the spatial profile of chloride concentration at 5.3 years. In FY18, after obtaining the geochemical data, including ion concentration in pore water of bentonite and granite, mineral phases and element contents in solid phase of bentonite, and detailed characterization of montmorillonite, the modeling efforts focused on the interpretation of geochemical data. The major findings from the current modeling work are as follows:

– Chemical data isimportant for calibrating the THM model. The model that is tested with more types of data is more reliable.

- The key coupling processes required to match the THM data and concentration of conservative species (e.g., chloride) include vapor diffusion, porosity change due to swelling, permeability change as a function of dry density (and porosity), and thermal osmosis.
- Because geochemical data in solid phases were either too scattered to constrain the model or incomparable with model outputs, the current model predominantly relied on the ion concentration in the aqueous phase to understand the geochemical change in the bentonite.
- The model matched the spatial profiles of most chemical species in the pore water of bentonite and granite, but discrepancies existed because of uncertainties in both the THMC model and the model used to infer aqueous extract data.
- Based on the match between model and data, an increase in sulfur was caused by the formation of anhydrite, and the higher content of calcium in the solid phase resulted from calcite precipitation. However, the model found no explanation of the increase in measured sodium content in the solid phase from the heater toward the granite and the decrease of magnesium content in the solid phase from the heater toward the granite, which warrants the need for further investigation of both the THMC model and data.
- Measured mass fractions of illite in the illite/smectite mixed layer varied a great deal depending on the laboratory samples, and therefore showed no clear spatial trend and were indistinguishable from the reference bentonite. The model results showed a small amount of illite precipitation and montmorillonite dissolution in the vicinity of the heater, which is neither proved nor disapproved by the data.

In FY19, the chemical model will focus on getting a better understanding of the evolution of redox conditions, interaction between steel corrosion products and bentonite, and geochemical changes at the interface between the concrete and the bentonite. Specifically, the model will tackle the following problems:

- Modeling of the evolution of redox conditions in the bentonite barrier. A thorough understanding of the evolution of redox conditions, especially near the canister, is critical for studying canister corrosion and waste form degradation. However, the current modeling effort faces a great challenge of simulating redox-sensitive elements such as Fe^{+2}/Fe^{+3} transformation. Because of the difficulty of obtaining reliable concentration of these species, knowing their concentration in the initial pore water of bentonite before and after FEBEX *in situ* test is very challenging. It is expected that a synthesis of measured gas concentrations, biological data and redox sensitive minerals and aqueous species can help understand the evolution of redox condition in FEBEX bentonite.
- The model of the bentonite-canister interaction, causing the corrosion of the canister and interaction of corrosion products with bentonite will be improved, and the model will be tested against measured mineralogical phase changes in the bentonite and the canister.
- Bentonite-concrete interactions will be modeled to understand mineralogical changes at the interface between concrete and bentonite.

4. COMPARATIVE ANALYSIS OF MODELING APPROACHES TO SUPPORT THE HOTBENT FIELD TEST

4.1 Introduction

Several international disposal programs have recently initiated investigations of whether clay-based barriers, such as bentonite, can withstand temperature higher than the 100 °C. Bentonite is considered as a potentially suitable material for the advanced repository design. For example, the Spent Fuel and Waste Science and Technology (SFWST) campaign has investigated the feasibility of direct geological disposal of large spent nuclear fuel canisters, currently placed in dry storage (Hardin et al., 2014), which would result in much higher emplacement temperatures. The performance of bentonite barriers in the <100 °C temperature range is underpinned by a broad knowledge base built on laboratory and large-scale in-situ experiments. Characterization of bentonite parameters subject to temperature above 100°C, is limited (especially for pelletized materials), although up to about 150 °C no significant changes in safety-relevant properties are determined. At temperatures above 150 °C, it is possible that a potentially detrimental temperature-driven physico-chemical response of materials (i.e., cementation and illitization) may occur, the characteristics of which are highly dependent on, and coupled with, the complex moisture transport processes induced by strong thermal gradients. The impact of such complex processes on the performance of a repository cannot be realistically reproduced and properly (i.e., non-conservatively) assessed at the laboratory scale. Such an assessment needs to be conducted by large-scale *in-situ* experiments in Underground Research Laboratories (URLs), where the most relevant features of future emplacement conditions can be adequately reproduced.

Potential options for a targeted high-temperature experiment (150 °C to 200 °C) in a crystalline rock environment are currently being considered under the leadership of NAGRA with several international partners. The proposed HotBENT experiment, a full-scale high-temperature heater test, will be conducted in the well-characterized FEBEX drift at the Grimsel Test Site. The benefit of such a large-scale test, accompanied by a systematic laboratory program and modeling effort, is that the temperature effects can be evaluated under realistic conditions of strong thermal, hydraulic and density gradients, which cannot be reproduced in the laboratory. This will lead to improved mechanistic models for the prediction of temperature-induced processes, including chemical alteration and mechanical changes, which can then be used for performance assessment (PA) analysis of high-temperature scenarios. The key question is whether higher repository temperature would trigger mechanisms that compromise the various barrier functions of the engineered components and host rock. If the barrier function is (at least partially) compromised, the PA analysis can be used to evaluate whether reduced performance of a sub-barrier (or parts thereof) would still give adequate performance.

To support the Preliminary Design Study (PreDes) (Kober et al., 2017), numerical models have been used to study the evolution of bentonite. It is known that the coupled thermal, hydrological, mechanical and chemical (THMC) processes are highly interactive in bentonite (e.g., Tsang, 2009; Zheng et al., 2015a), which require the use of coupled THMC models. However, a fully coupled THMC model with a 3-D description of HotBENT and all the design components are computationally too demanding to be carried out in a reasonable amount of time. While Finsterle et al. (2017) used a 3-D TH model with complete configuration of the test to study the phenomenological aspects of the HotBENT experiment, in this report the models have a simple geometric 1D or 2-D setup. It considers: (i) coupled THMC processes, (ii) attempts to study the hydrological evolution of bentonite when the impact of mechanical changes (swelling) on porosity and permeability is taken into account and (iii) the chemical evolution in bentonite over the course of the test. The first set of models are 1D axi-symmetric coupled THMC models based on the model for the FEBEX *in situ* test (Zheng et al., 2017) to illustrate the expected THMC response in the hot cross-sections that cut through the middle of the heater. The second set of models consists of 2-D cross-sectional models with THMC processes for one of the scenarios reported in Finsterle et al. (2017).

Conducting coupled THMC simulations is challenging, and one of the difficulties is the parameterization. The advantage of using the THMC model developed for the FEBEX *in situ* test, as a basis to explore the potential changes in HotBENT, is the THMC model for the FEBEX *in situ* test has been systematically calibrated (Zheng et al., 2015b, 2016 and 2017), especially regarding the parameters related to coupling processes (e.g., permeability/porosity change as a result of swelling) and chemical processes, which is expected to make more reliable predictions. Key questions to be addressed in this report are two-fold. One is to study the difference between TH/THC and THMC models in terms of hydrological and chemical behavior in bentonite, or in other words to assess the degree of uncertainty introduced by the TH/THC model given that mechanical processes affect the hydrological behavior due to changes in porosity and permeability. The second is the geochemical evolution in bentonite under high temperature is expected in HotBENT. The answers to these two questions by the modeling work in the PreDes stage will guide the modeling predictions for the final design of the HotBENT.

Potential HotBENT partners include NAGRA, GRS, SURAO, NUMO, RWM, and SKB. Participation in this new collaboration effort would be beneficial for DOE. Substantial cost savings would be achieved in the design of a repository if HotBENT demonstrates that the maximum temperature of bentonite backfill can be raised without drastic changes in the performance implications.

4.2 Status of HotBENT

Currently, partners for HotBENT are working on completing a Preliminary Design Study to encompass various aspects of the test, including the layout and geometry of the test, instrumentation, sampling and optimization, the cost and risk of the experiments, and the expected THMC evolution of bentonite, which are discussed in the current report. The tentatively proposed layout of the test has 4 modules (Figure 4-1), and adding more modules is possible.

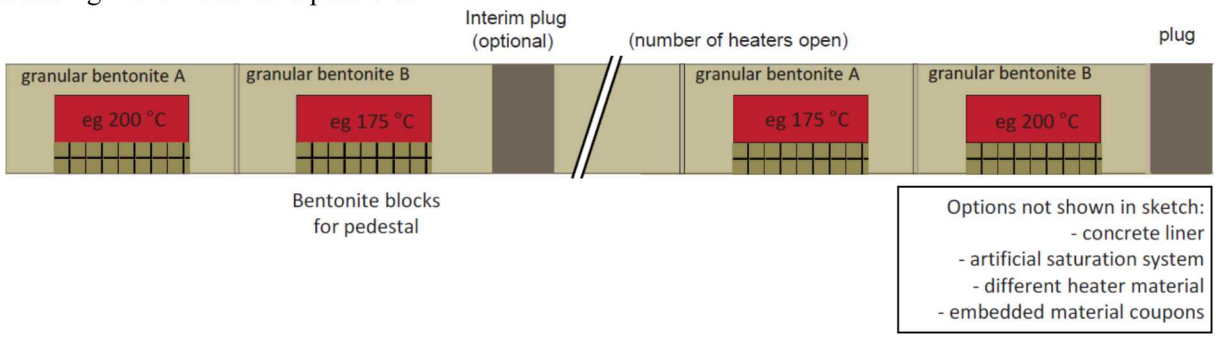

Figure 4-1. Design modules for HotBENT from partners of the project (Kober et al., 2017). Note that the figure illustrates only a bentonite barrier, plug and a heater (red rectangles), and the drift wall is not part of the figure. The plug material hasn't been identified yet.

The provisional time schedule for the HotBENT Experiment (Figure 4-2) was reported in Kober et al. (2017), but adjustment is expected as the number of modules might change.

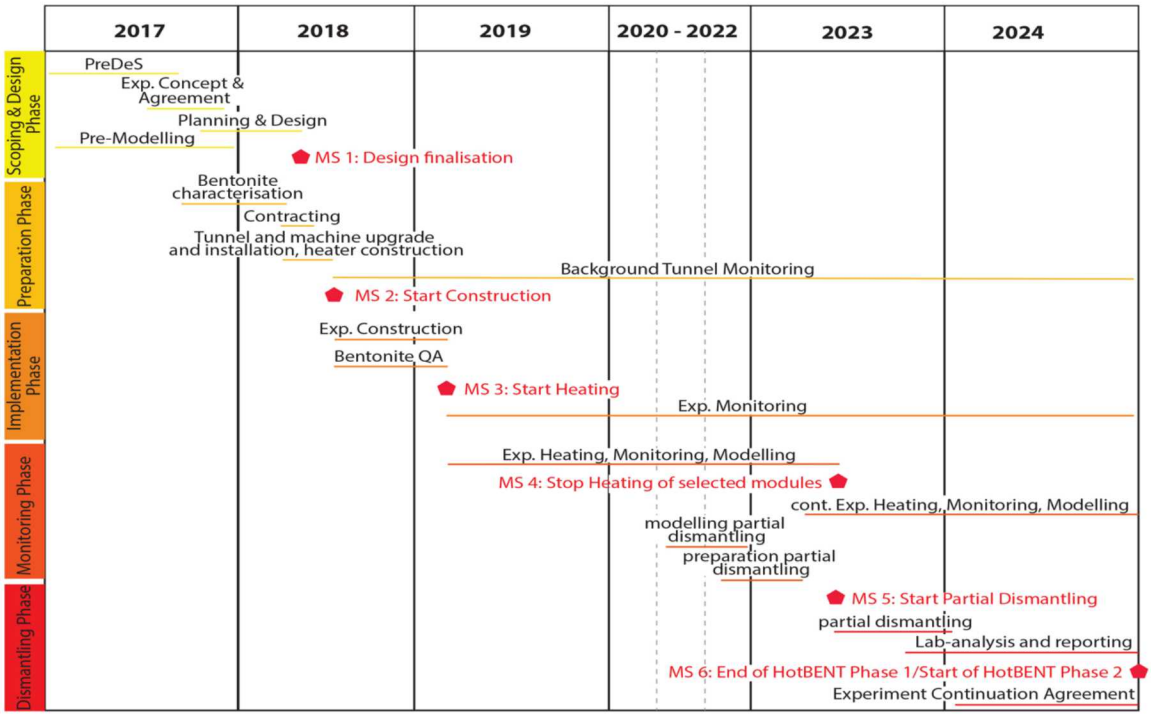

Figure 4-2 Provisional time-schedule for the HotBENT experiment (Kober et al., 2017).

4.3 Simulator

The numerical simulations are conducted with TOUGHREACT-FLAC3D, which sequentially couples the multiphase fluid flow and reactive transport simulator, TOUGHREACT (Xu et al., 2011), with the finite-difference geomechanical code FLAC3D (Itasca, 2009). The coupling of TOUGHREACT and FLAC was initially developed by Zheng et al. (2012) to provide the necessary numerical framework for modeling fully coupled THMC processes.

4.4 1-D Axi-Symmetric Model

The HotBENT experiment will be conducted in the same tunnel in granite where the FEBEX *in situ* test was performed, and the experiment setup along the cross-section is expected to be similar to FEBEX, except that the temperature at the heater surface will be 200 °C (as a potential end member). We therefore used exactly the same 1-D axi-symmetric model as for the FEBEX *in situ* test to conduct scoping calculations for HotBENT, with the only modification being the boundary condition for the heater: instead of fixing it at 100 °C, the heater has a constant temperature of 200 °C.

As the model is largely based on the THMC model for the FEBEX *in situ* test, details of the model can be found in Section 3.3. In Kober et al. (2017) and Finsterle et al. (2017), MX-80, Kunigel VI and Rokle bentonite are assumed to be EBS materials, whereas in current model, FEBEX bentonite is the EBS materials. Although the permeability of FEBEX bentonite is slightly lower than the reference permeability for MX-80, Kunigel VI and Rokle bentonite (Finsterle et al., 2017), permeability of FEBEX bentonite is still within the range of permeability of these bentonites, and thus the calculated hydrological behavior in the report is likely comparable with those in Finsterle et al. (2017). More importantly, because the key processes that control the heat conduction and water movement within the bentonite are the same, findings regarding the difference between the TH/THC and THMC models in this section can be transferable to the models for other type of bentonites as in Finsterle et al. (2017).

Modeling the THMC alteration of the bentonite barrier is an area that has been evolving over the last two decades with new processes added and new modeling methods were tested during that time. The representation of bentonite pore structure and inclusion of coupled processes have been the focus of many modeling studies. Usually a given model involves some simplifications according to the purpose of the model. Similarly, in this report, the complex model of coupled processes was simplified in terms of pore structure. The model assumes one level of pores, which is based on the measured total porosity (for example, 0.41 for the FEBEX bentonite), rather than different levels of pores, such as the dual structural pores for the mechanical model used in BExM (Sánchez et al., 2005) or explicit diffuse layer calculation based on a Donnan Equilibrium assumption (Appelo et al., 2017). Such simplification of the pore structure is first due to the incompatibility of the pore structural concept between THMC processes. For example, if the dual structural BExM is used for mechanical behavior, such pore structures should be applied to chemical processes, as well, which triggers a lot of unknowns that have not been clearly understood. The second reason is that some features, such as explicit diffuse layer calculation based on a Donnan Equilibrium assumption, are still not understood well enough to be included in the large-scale THMC model.

4.4.1 Modeling Results

With a heater maintained at 200 °C in HotBENT, the temperature in bentonite and granite will be much higher when compared with the FEBEX *in situ* test, as shown in Figures 4-3 to 4-5 at several radial distances in bentonite and granite. As in the FEBEX test, which was conducted for 18.3 years, the model for HotBENT reported here was also run for 18.3 years, including a 70-day cooling period during which the heater was switched off. Model results show that the temperature in the bentonite near the granite reached about 90 °C and dropped to 57 °C after the 70-day cooling period, suggesting that a longer cooling period might be needed for HotBENT at the end of experiment before dismantling it.

As expected, the granite will undergo heating, and the heat pulse can penetrate as deep as 10 m into the rock (radial distance of 11 m from the axis of the tunnuel) (Figure 4-6). However, the temperature is expected to be lower than 100 °C, so that boiling in granite should not be a concern.

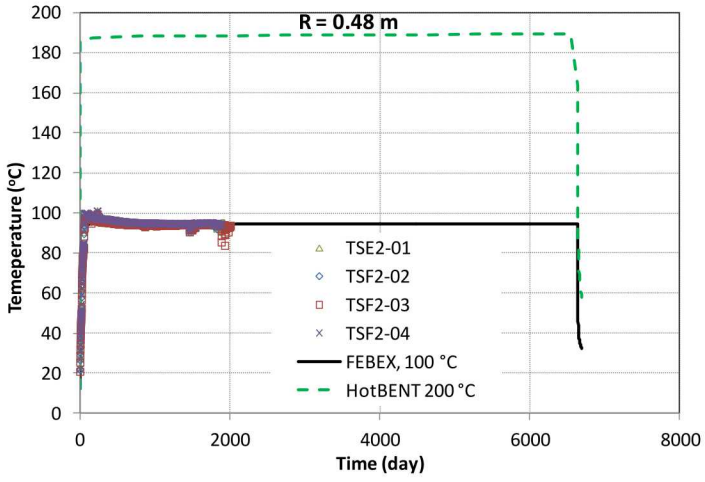

Figure 4-3. Measured and simulated temperature at a radial distance of 0.48 m in the FEBEX *in situ* test and simulated temperature in HotBENT.

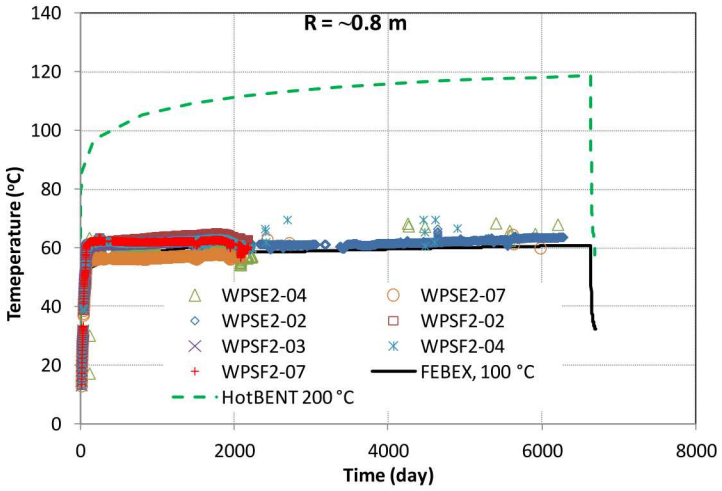

Figure 4-4. Measured and simulated temperature at a radial distance of 0.8 m in the FEBEX *in situ* test and simulated temperature in HotBENT.

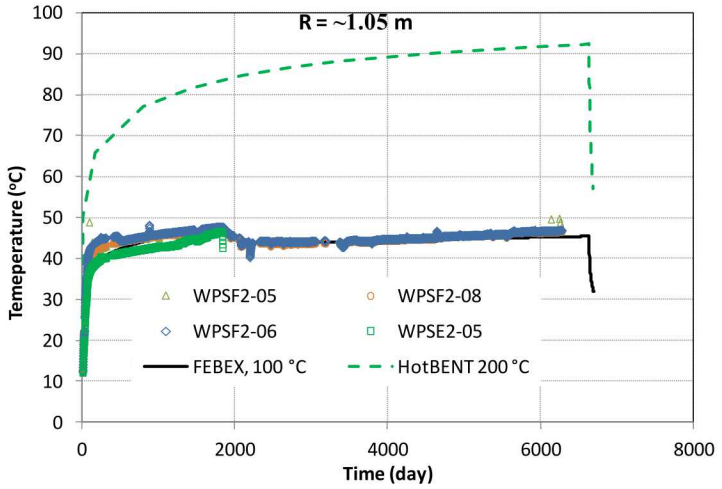

Figure 4-5. Measured and simulated temperature at a radial distance of 1.05 m in the FEBEX *in situ* test and simulated temperature in HotBENT.

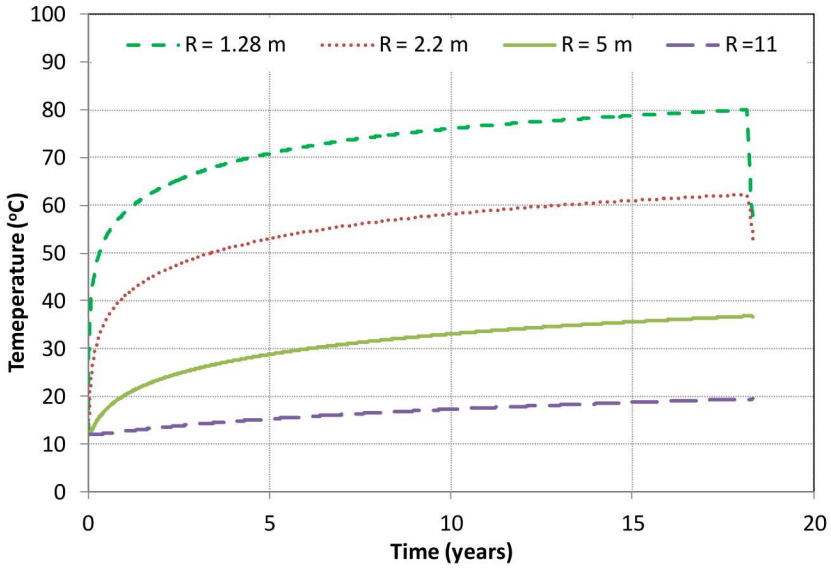

Figure 4-6. Simulated temperature in HotBENT at several radial distances in granite.

Relative humidity, water content and dry density are three types of hydrological data that are available for the FEBEX *in situ* test. In this section, we therefore present model results for relative humidity, water content and dry density for HotBENT to illustrate the expected hydrological behavior in HotBENT. Relative humidity in bentonite near the heater in HotBENT is expected to be much lower than that in the FEBEX test (Figure 4-7): it drops to around 5% after a very short time period and slowly recovers to about 20% before entering into the cooling period, where it eventually rises to 70% after the cooling period. The low relative humidity near the heater raises the concern of the quality of the relative humidity sensor. Sensors with the capacity for detecting much lower relative humidity are needed. Relative humidity at the middle of the bentonite barrier in HotBENT is also expected to be about 10% lower than that observed in the FEBEX test (Figure 4-8), whereas the relative humidity near the granite in HotBENT is quite similar to that in the FEBEX test, quickly reaching 100% (Figure 4-9).

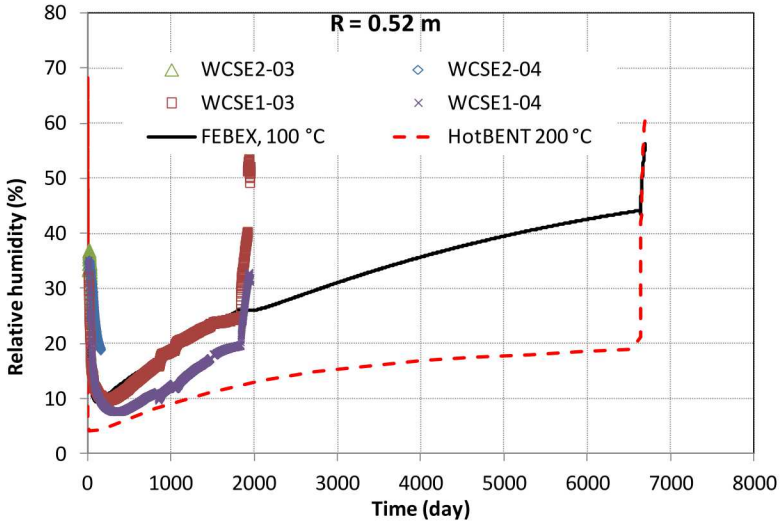

Figure 4-7. Measured and simulated relative humidity at a radial distance of 0.52 m for the FEBEX *in situ* test and simulated results for HotBENT.

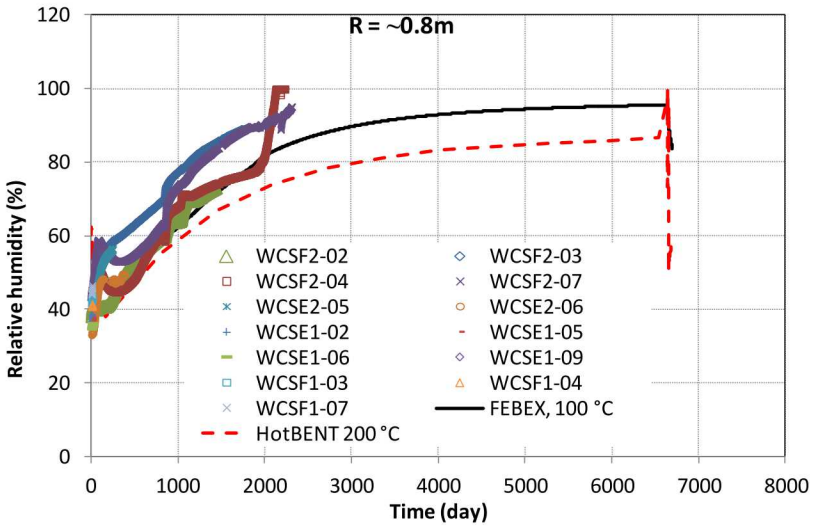

Figure 4-8. Measured and simulated relative humidity at a radial distance of 0.8 m for the FEBEX *in situ* test and simulated results for HotBENT.

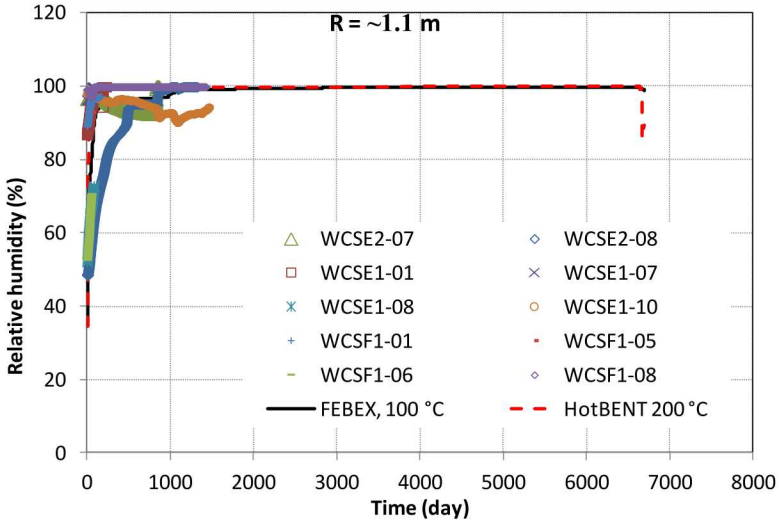

Figure 4-9. Measured and simulated relative humidity at a radial distance of 1.1 m for the FEBEX *in situ* test and simulated results for HotBENT.

One simulation was also stopped at 5.3 years with a cooling period from 5 to 5.3 years and another simulation was stopped at 10.3 years with a cooling period from 10 to 10.3 years, to check the water-content profile, assuming that the HotBENT test will be operated either for 5.3 years or 10.3 years. Modeling results for these two simulations are shown in Figure 4-10, together with the data and modeling results for the FEBEX *in situ* test at 5.3 years. Because of swelling, a water content larger than 25% usually indicates full saturation. For HotBENT, except for the area near the granite (about 0.04 m away from the granite), which is close to full saturation, most areas are still unsaturated even after 10 years.

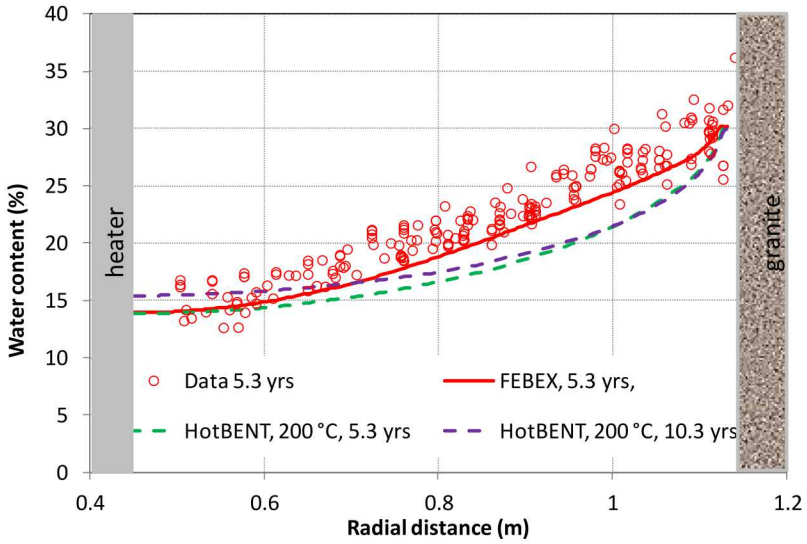

Figure 4-10. Measured and simulated water content at 5.3 years for the FEBEX *in situ* test and simulated results for HotBENT after 5.3 and 10.3 years.

In the FEBEX test, while some properties, such as temperature, relative humidity, pore pressure and stress, were monitored by the sensors installed in the bentonite barrier, other properties, as those related to chemical alteration, have to be measured after dismantling the test. However, before the dismantling, a cooling period is required, so that temperature conditions in the tunnel are suitable for field operations. Such a cooling period leads to a significant redistribution of moisture, which compromises the usefulness of the measured water content data and complicates the model interpretation. In HotBENT, we found that such an effect is even more extreme. First, in both simulations (5.3 years and 10.3 years), after 70 days of cooling the temperature is still about 45-50 °C (Figure 4-11), which is still too high for field operations, indicating that a longer cooling time is needed. Second, the water content during the cooling period undergoes significant changes (Figure 4-12), as water content is predicted to rise as much as 10% near the heater and to drop as much as 10% near the granite.

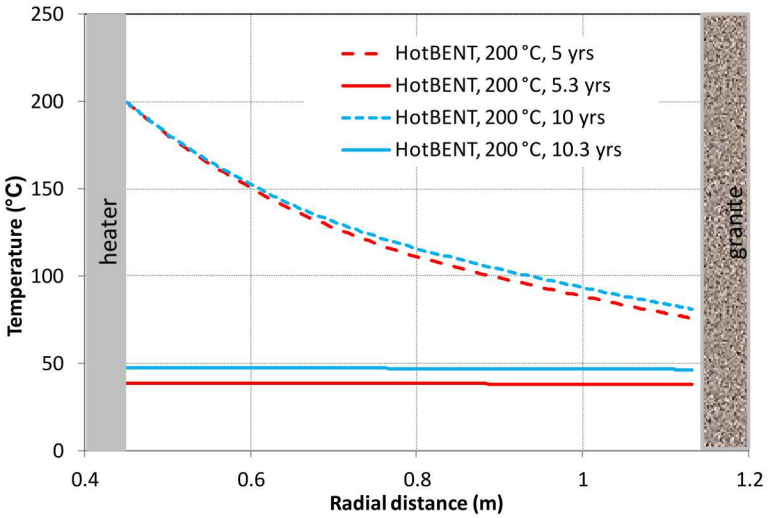

Figure 4-11. Simulated temperature for HotBENT after 5.3 years with 70 days of cooling and 10.3 years with 70 days of cooling.

Sensors for measuring stress were also emplaced in the bentonite block in the FEBEX *in situ* test, and data at two radial distances, 0.5 m (near the heater) and 1.1 m (right at the bentonite/granite interface), were used to validate the model for the FEBEX test. Here we also check the stress data at these two locations predicted by the model for HotBENT. Figures 4-13 and 4-14 show the measured stress and model results for the FEBEX test and predicted by the model for HotBENT. In HotBENT, because of the lower water content throughout most of bentonite barrier and lower pore-water pressure compared with that in FEBEX, the stress is lower than that in the FEBEX test despite of higher temperature for HotBENT.

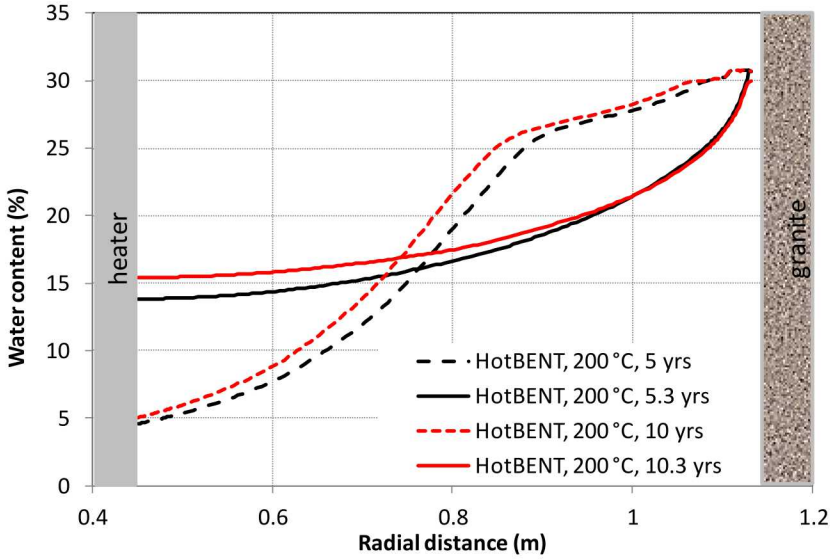

Figure 4-12. Simulated water content for HotBENT after 5.3 years with 70 days of cooling and 10.3 years with 70 days of cooling.

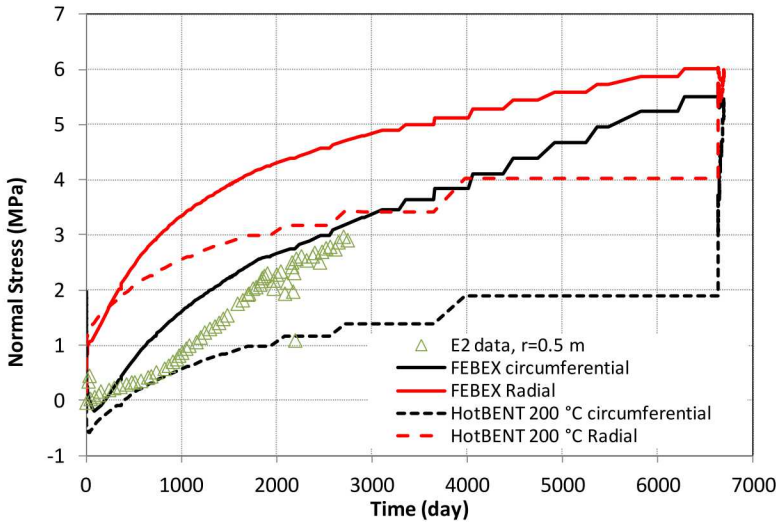

Figure 4-13. Measured and simulated stress at a radial distance of ~0.5 m for the FEBEX *in situ* test and modeling results for HotBENT.

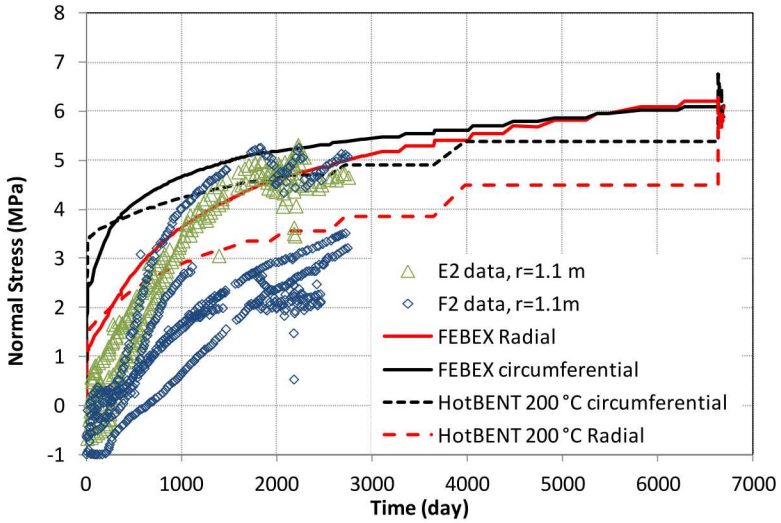

Figure 4-14. Measured and simulated stress at a radial distance of 1.1 m for the FEBEX *in situ* test and modeling results for HotBENT.

After the partial dismantling of the FEBEX test in 2002 (5.3 years after heating started), samples were collected and pore-water concentrations were measured. A model for the FEBEX test matches the chloride concentration profiles reasonably well (Zheng et al., 2017), and the model shows that the concentration of chloride near the heater is quite a bit higher due to evaporation. For HotBENT, it is expected that chloride concentrations will be even higher in the area near the heater (Figure 4-15).

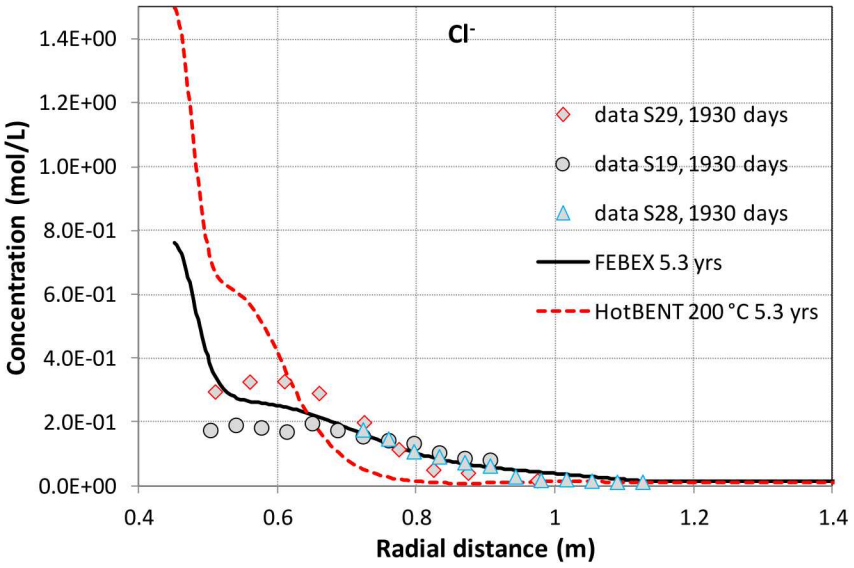

Figure 4-15. Measured concentration profile for chloride at 5.3 years (Zheng et al., 2011) and modeling results for the FEBEX *in situ* test, and simulated for HotBENT at 5.3 years.

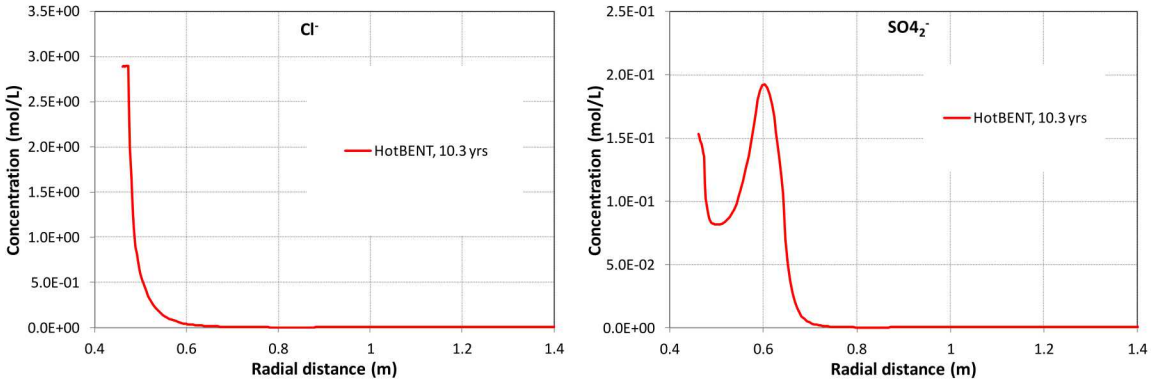

Figure 4-16. Simulated concentration profiles for Cl, SO_4 at 10.3 years for HotBENT.

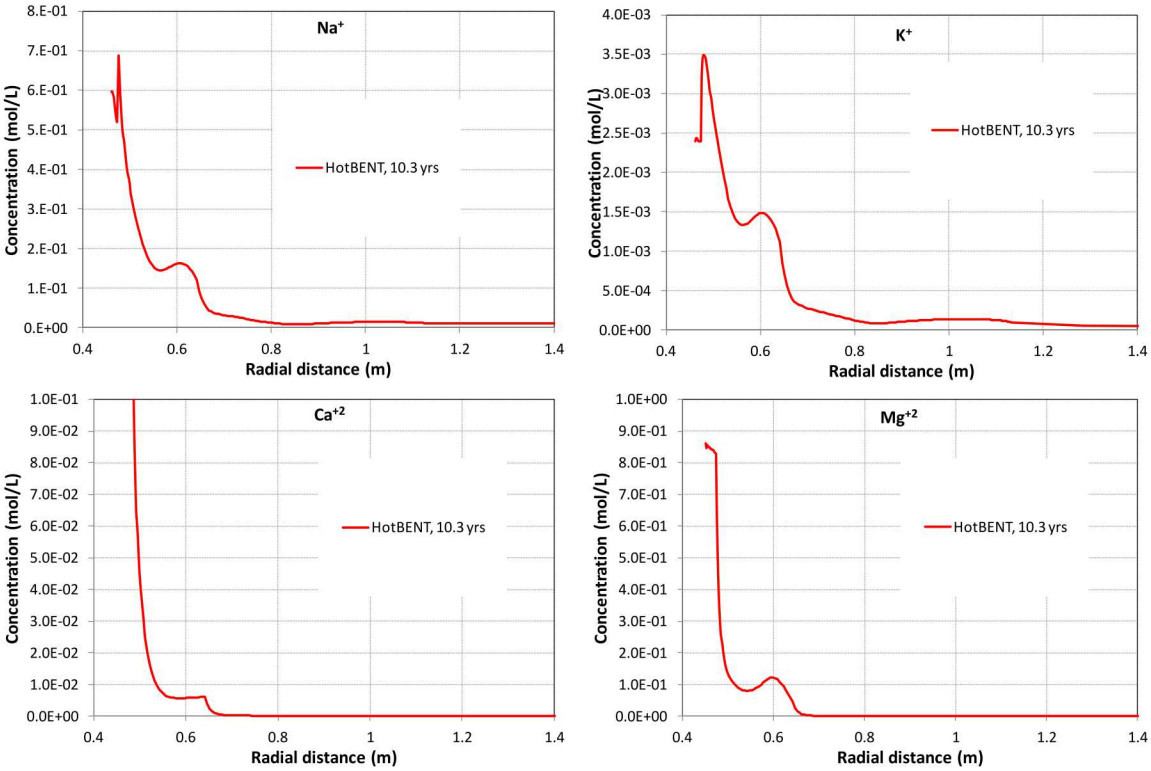

Figure 4-17. Simulated concentration profiles for major cations (calcium, magnesium, sodium and potassium) at 10.3 years for HotBENT.

If the HotBENT experiment runs for 10 years with 0.3 years of cooling and has exactly the same setup as FEBEX, except that the heater temperature is set to 200 °C, the following chemical changes are expected. First, concentrations of major cations and anions will be fairly high near the heater (Figures 4-16 and 4-17). As bentonite stays dry during the test and the temperature in HotBENT is much higher than that in FEBEX, even stronger evaporation would occur causing high concentrations of major cations and anions. Chloride can reach as high as 2.5 molal. Concentration profiles for sodium, potassium, magnesium and sulfate show a local peak at a radial distance of 0.6 m (0.15 m away from the heater), where outflow vapor meets the inflow water from the granite, which could also be related to mineral precipitation/dissolution.

In this section, the THMC model for FEBEX *in situ* test was modified and was run for several durations (5.3, 10.3 and 18.3 years) to explore various aspects of the evolution of bentonite and to illustrate the potential alteration of bentonite in HotBENT. The rationale for running the model at various time intervals is to evaluate the effect of the cooling period (assumed 70 days in current model) on the hydrological and chemical changes in bentonite given that the temporal length of the HotBENT has not been decided or might be changed over the course of experiment. Models with the right simulation time will be conducted when the final decision of how long HotBENT will run is made.

As revealed by previous studies (Zheng et al. 2016; Zheng et al., 2017), most ions have concentration profiles shaped by transport processes (diffusion and advection) and chemical reactions changed the level of concentration, but not the shape of the spatial profile, except for bicarbonate and pH. Here we have a similar case: the concentration profiles of bicarbonate and pH (Figure 4-18) are very different from those of cations (e.g., sodium) or chloride. Dissolution/precipitation of carbonate minerals and dissolution/evolution of CO_2 gas play a major role in shaping their spatial distribution.

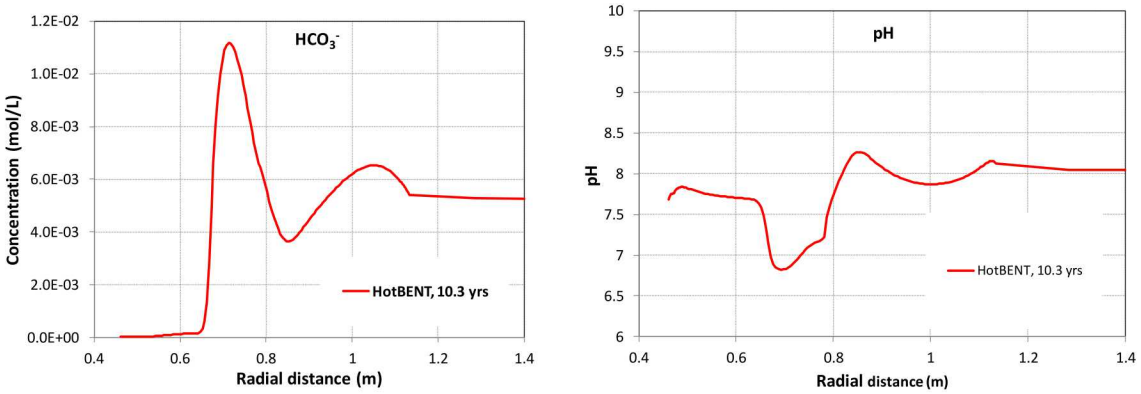

Figure 4-18. Simulated concentration profiles of bicarbonate and pH at 10.3 years for HotBENT.

Alteration of mineral phases is hard to predict, because the results are sensitive to many hydrological and chemical conditions. Regarding the minerals with high solubility, slight perturbation of water saturation in the bentonite, interaction between host rock and bentonite and temperature change over the course of hydration can lead to noticeable precipitation/dissolution. Gypsum and calcite are two of these highly soluble minerals. Precipitation of gypsum has been observed near the heater because evaporation leads to a high sulfate concentration near the heater (Figure 4-19). Calcite dissolves in areas close to the granite due to the dilution of bentonite pore-water by granite water, but precipitates near the heater due to high calcium concentrations caused by evaporation.

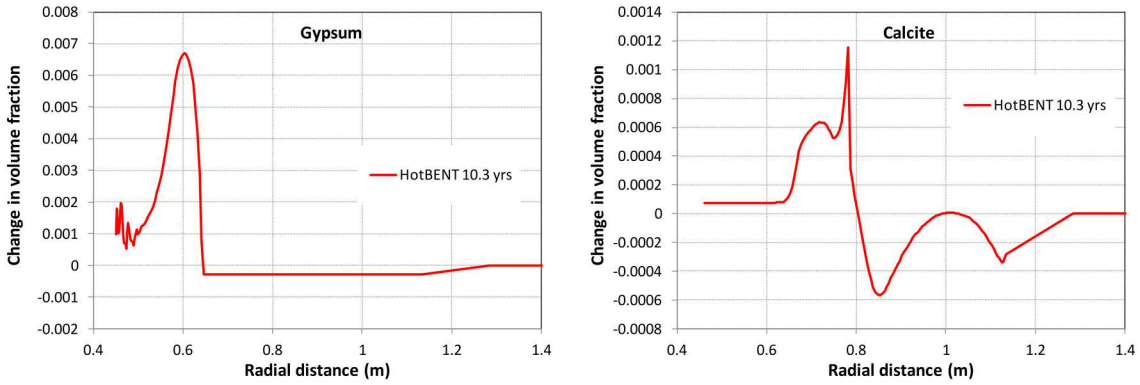

Figure 4-19. Simulated volume fraction change of gypsum (left) and calcite (right) at 10.3 years for HotBENT.

Although illitization (transformation of montmorillonite to illite) is evident in geological systems (Wersin et al., 2007; Cuadros 2006), while illitization depends on many chemical conditions (Zheng et al., 2014). In the current model, illitization is simulated as the dissolution of montmorillonite and precipitation of illite according the following equation:

$$\text{Montmorillonite} + 0.52H^{+} + 0.63AlO_2^{-} + 0.6K = \text{illite} + 0.26H_2O + 0.08Mg^{+2} + 0.33Na^{+} + 0.5SiO_2(aq) \quad 4\text{-}1$$

The key for illitization to proceed is the supply of potassium and aluminum. However, as shown in Figure 4-16, granite water has a very low content of potassium, which dilutes the potassium concentration in the pore-water of the bentonite significantly. As a result, the current model instead shows dissolution of illite and precipitation of montmorillonite (Figure 4-20). Note that the amount of illite dissolution and montmorillonite precipitation is very low, ranging roughly from about 0.01% to 0.05%, which will be hard to detect by some mineralogical characterization methods (e.g., XRD).

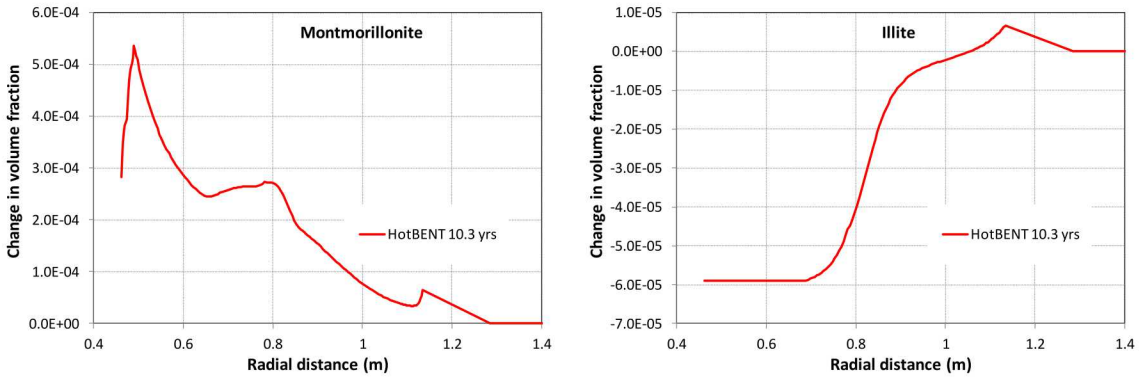

Figure 4-20. Simulated volume fraction change of montmorillonite (left) and illite (right) at 10.3 years for HotBENT.

Increasingly, there seems to be consensus that alteration to montmorillonite and illite is a dissolution/precipitation process mediated by an aqueous solution. In other words, dissolution/precipitation of montmorillonite or illite depends on the thermodynamic equilibrium calculated based on the concentration of relevant ions, including Si, Al, Na, Mg, K and pH. Their concentrations are not only affected by influx of more dilute granite water, but also by the dissolution/precipitation of other minerals. In the current model, the decrease in K concentration in the pore-water of bentonite leads to dissolution of illite and K-feldspar in bentonite, which releases Si and Al, resulting in precipitation of montmorillonite. Some experiments showed a different trend of reactions, such as the dissolution of montmorillonite in Leupin et al (2014), because the chemical conditions are different. Leupin et al. (2014) conducted the test to evaluate the thermal stability of montmorillonite in Na-exchanged MX-80 with the size fraction less than 2 μm mixed with solutions of NaCl, KCl, $CaCl_2$ and $MgCl_2$. Because the test material likely contains only clay minerals and the solution is deficient in Si, Al and any cations other than the one used in the solution, it is determined that montmorillonite dissolved and Si was released.

4.4.2 TH /THC Versus THMC Model

Because of the computation burden and lack of reliable constitutive relationships for coupled processes (e.g., permeability change as a function of porosity or stress), the THMC model was not widely used in calculations of the evolution of the bentonite barrier under heating and hydration conditions. One question that could be raised is if ignoring some of these coupled processes would lead to a large variation in the results in the light of only hydrological behavior. In this section, to shed insight on this issue, we compare two sets of TH/THC and THMC models. Details of these two sets of models are given in Table 4-1 and explained below. Using the THC and THMC model simulations (e.g., Zheng et al., 2015), it was determined that the porosity changes, resulting from the mineral dissolution/precipitation, are minimal, although the porosity in the THC model slightly varied in time and space.

Table 4-1. Major features of the two sets of TH/THC and THMC models that were used to study the difference between these models

Model features	First Set			Second Set		
	THMC model	THC model	TH Model	THMC model	THC model	TH model
Mechanical model	See Section 3.3.4	Not considered	Not considered	See Section 3.3.4	Not considered	Not considered
Chemical model	See Section 3.3.5	See Section 3.3.5	Not considered	Only include Cl and Na	Only include Cl and Na	Not considered
Thermal boundary conditions	T at heater is fixed at 100 °C	T at heater is fixed at 100 °C	T at heater is fixed at 100 °C	T at heater is fixed at 200 °C	T at heater is fixed at 200 °C	T at heater is fixed at 200 °C
Intrinsic permeability	Equation (4-e) with α of 1.78 such that initial permeability is 2.15×10^{-21} m^2	Permeability remains constant at 2.15×10^{-21} m^2	Permeability remains constant at 2.15×10^{-21} m^2	Equation (4-3) with α of 0.375 such that initial permeability is 1×10^{-20} m^2	Permeability remains constant at 1×10^{-20} m^2	Permeability remains constant at 1×10^{-20} m^2
Porosity	Equation (4-2), leading to an initial porosity of 0.41	Porosity remains constant at 0.41	Porosity remains constant at 0.41	Equation (4-2), leading to an initial porosity of 0.41	Porosity remains constant at 0.41	Porosity remains constant at 0.41

In the first set of TH/THC and THMC models, the THMC model was calibrated against the FEBEX *in situ* test. The processes considered in the model and parameters used to describe these processes were detailed in Section 3.3. The key model coupling processes taken into consideration to describe the hydrological-mechanical coupling are:

(a) the relationship between the void ratio and the effective stress and suction given by

$$e = A + B\ln\sigma' + C\ln(\psi + p^a) + D\ln\sigma'\ln(\psi + p^a) \qquad 4\text{-}2$$

where e is the void ratio, which is equal to the volume of voids divided by the volume of the solids; p^a is the atmospheric pressure (Pa), σ' is the mean effective stress (Pa); ψ is the capillary suction (Pa), and

A, B, C and D are empirical constants, which for the FEBEX compacted bentonite are equal to A = 0.91, B = - 0.0552, C = - 0.0606413 and D = 0.00479977 based on the calibration conducted in this report.

The relationship between the intrinsic permeability in dry density given by

$$\log k = (-2.96\rho_d - 8.57)/\alpha \qquad 4\text{-}3$$

where k is intrinsic permeability, ρ_d is dry density, and α is a scaling factor.

Equation (4-2) leads to a porosity equal initially to 0.41, but it changed over time. Equation (4-3) yields an initial permeability of 2.15×10^{-21} m^2, but it changed as the bentonite properties evolved over time (see Figure 4-21 for the spatial distribution of permeability at several times).

The corresponding TH model that is used to compare with the THMC model has the following features. First, the MC processes were not considered in the model. Second, the TH processes and parameters were exactly the same as in the THMC model, except that porosity and intrinsic permeability remained constant (0.41 and 2.15×10^{-21} m^2, respectively). The THC model considered the same TH processes and parameters as the TH model, and the chemical model was the same as in THMC model. Because chemical processes minimally affected TH processes, the TH model results in the THC model were almost identical to the TH model.

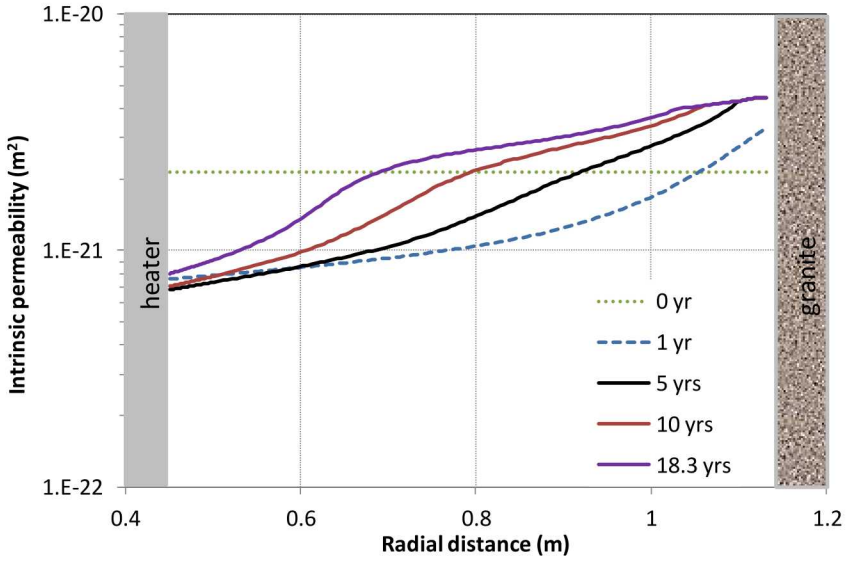

Figure 4-21. Calculated permeability at several times in the THMC model for FEBEX *in situ* test.

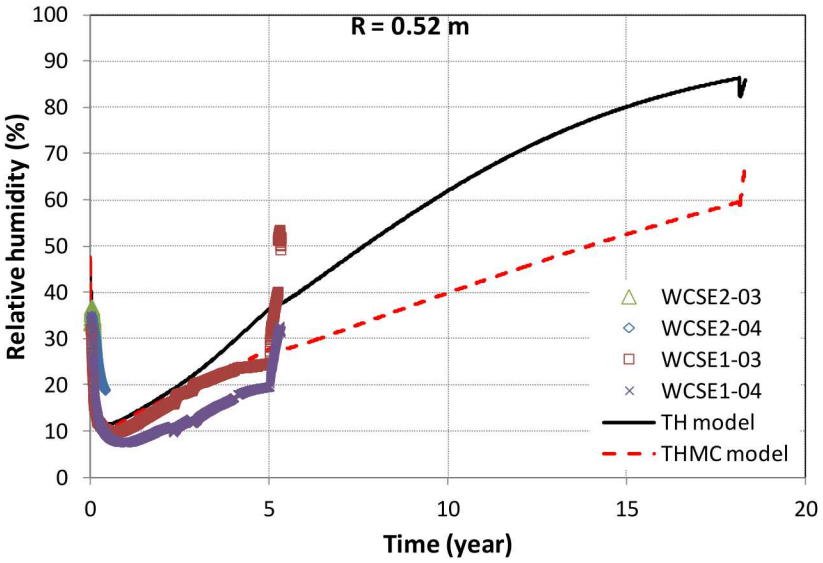

Figure 4-22. Measured and simulated relative humidity at a radial distance of 0.52 m for the FEBEX *in situ* test and simulated results by the TH and THMC models for the *in situ* test.

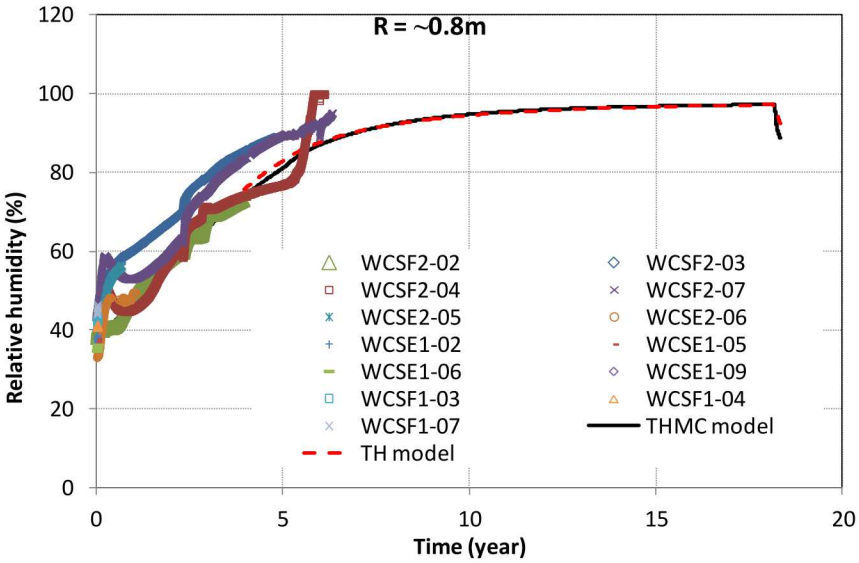

Figure 4-23. Measured and simulated relative humidity at a radial distance of 0.8 m for the FEBEX *in situ* test and simulated results by the TH and THMC models for the *in situ* test.

The relative humidity (RH) at a radial distance of 0.52 m (near the heater) for the TH and THMC models (Figure 4-22) differs by about 20% after 10 years and 25% after 18 years (before the cooling period). In the middle of the bentonite and close to the granite the RH from the TH and THMC models were very similar, as exemplified by the RH evolution at a radial distance of 0.8 m (Figure 4-23).

As revealed by Zheng et al. (2011; 2016), chloride concentration is controlled only by transport processes and matching Cl concentration is a first step to match concentrations of other chemical species because the concentration profiles of cations (calcium, potassium, magnesium and sodium) were largely shaped by

transport processes despite their concentrations are being affected by mineral dissolution/precipitation and cation exchange. The THC model, in which the porosity and permeability changes due to swelling/shrinkage were not taken into account apparently could not match the measured Cl concentration data (Figure 4-24). The THC and THMC models also showed the difference in the K concentration (Figure 4-25). Subsequently, there was also a substantial difference in the calculated montmorillonite volume fraction between the THC and THMC models (Figure 4-26). The change of porosity and permeability brought on by swelling/shrinkage fundamentally alters the transport processes—advection and diffusion of chemical species, and consequently affect mineral precipitation/dissolution. THC models that neglect the change of porosity and permeability are unable to explain the data in FEBEX *in situ* test, and probably won't provide prediction as reliable as the THMC model.

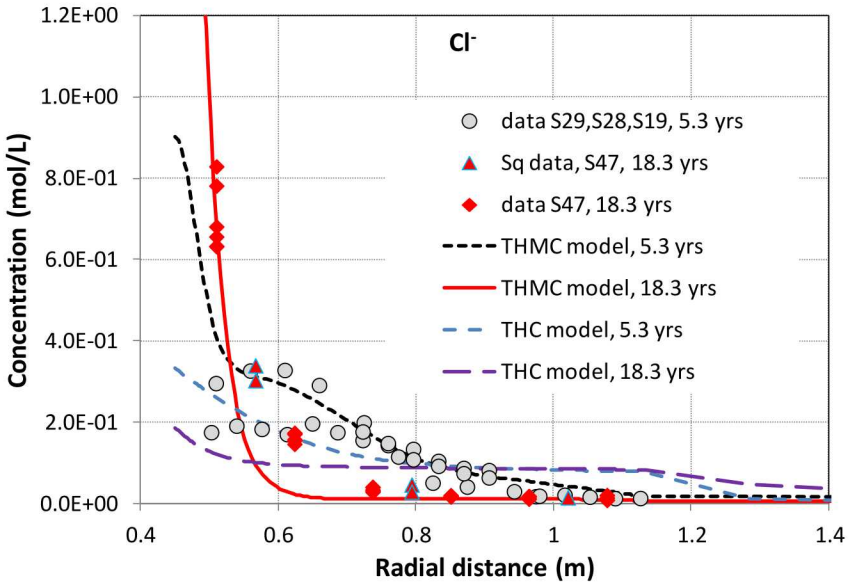

Figure 4-24. Cl concentration at 5.3 and 18.3 years measured in the FEBEX *in situ* test and simulated results by the THC and THMC models for the *in situ* test.

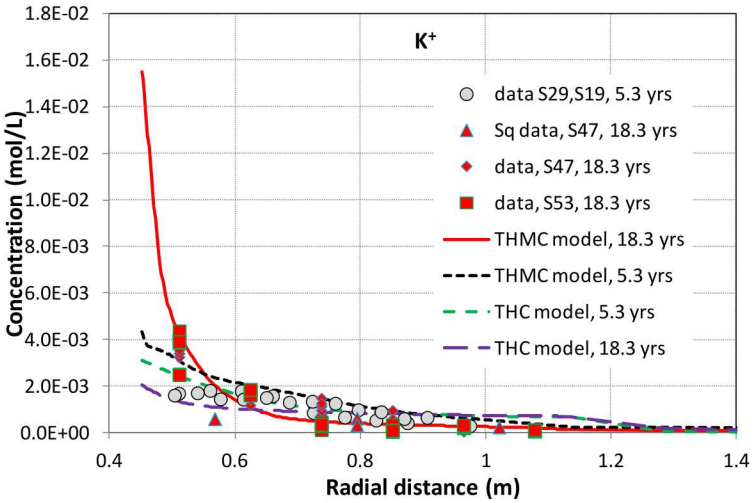

Figure 4-25. K concentration at 5.3 and 18.3 years measured in the FEBEX *in situ* test and simulated results by the THC and THMC models for the *in situ* test.

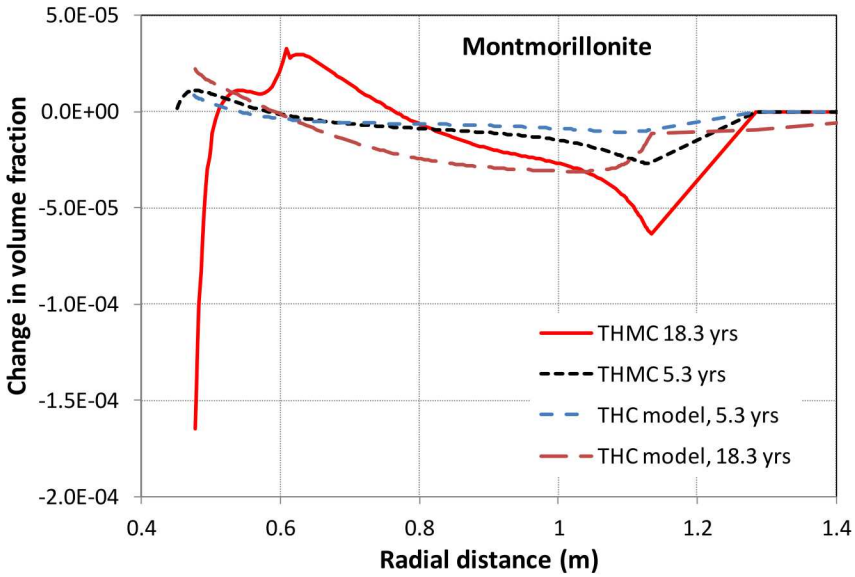

Figure 4-26. Calculated changes in volume fraction of montmorillonite at 5.3 and 18.3 years by the THC and THMC models for the *in situ* test.

The second set of TH/THC and THMC models to study the difference between TH/THC and THMC models was established for HotBENT. Because bentonite in HotBENT is likely to be granular and to have a lower density and higher permeability than the FEBEX bentonite, we set up a case with an initial bentonite intrinsic permeability of 10^{-20} m^2, which is about 5 times larger than that for FEBEX bentonite. Specifically, the THMC model in the second set inherits all features of the THMC model in the first set, with the following variation: the temperature at the heater is fixed at 200 °C, Equation (4-3) with α of 0.375 is adopted such that initial permeability is 1×10^{-20} m^2 but varies with time (see Figure 4-27 for the spatial distribution of intrinsic permeability), and chemical models only include the transport of Cl and Na (see Table 4-1). The TH model apparently excluded the MC function, and intrinsic permeability remains constant at 1×10^{-20} m^2 and porosity remains constant at 0.41. The THC model was used to simulate exactly the same TH processes as the TH model and added the chemical model including only Cl and Na.

Because the rate of hydration of bentonite is largely affected by its permeability, for the second set of TH/THC and THMC models, bentonite becomes saturated more quickly. As water infiltrates into the bentonite, in areas that become fully saturated, bentonite swells, dry density decreases and permeability increases (see Figure 4-27). In contrast, in areas near the heater, where the bentonite becomes drier until the arrival of water, bentonite shrinks, the dry density increases and permeability decreases (Figure 4-27). Figure 4-28 shows that, at an early stage (less than 4 years), the THMC model leads to a lower relative humidity at a radial distance of 0.5 m (near the heater) than the TH model, with a maximum difference of about 15%, but later (after about 4 years) the THMC model has a higher relative humidity than the TH model. This is because the increase in saturation in most areas causes an increase in permeability and a maximum difference of about 17%. Eventually, by the end of 10 years, both the TH and the THMC models have similar relative humidity. For areas far away from the heater, the TH and THMC models have similar results, as shown in Figure 4-29.

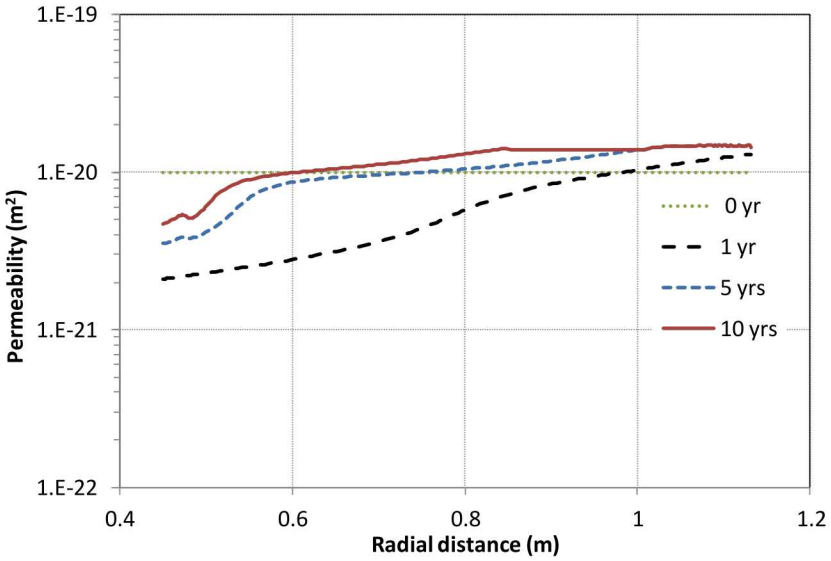

Figure 4-27. Calculated permeability at several times in the THMC model for a HotBENT case.

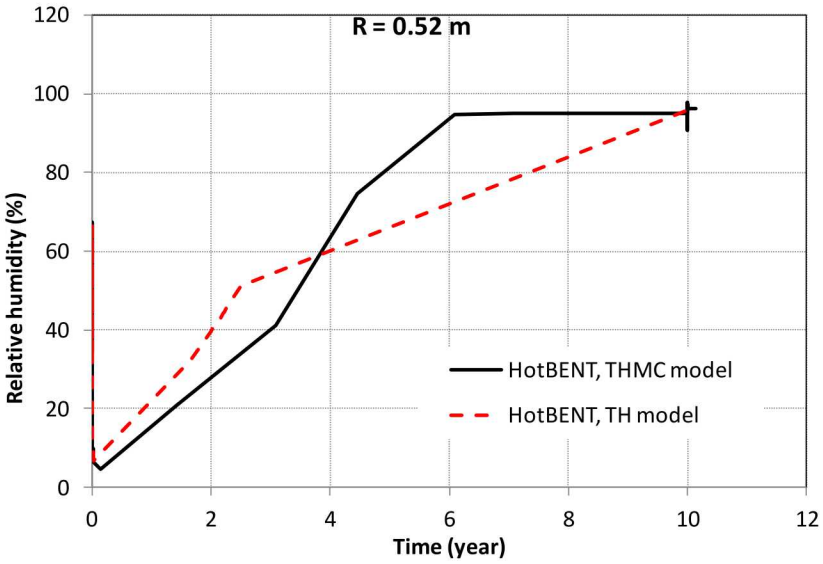

Figure 4-28. Predicted relative humidity at a radial distance of 0.52 m for the TH and THMC models for HotBENT.

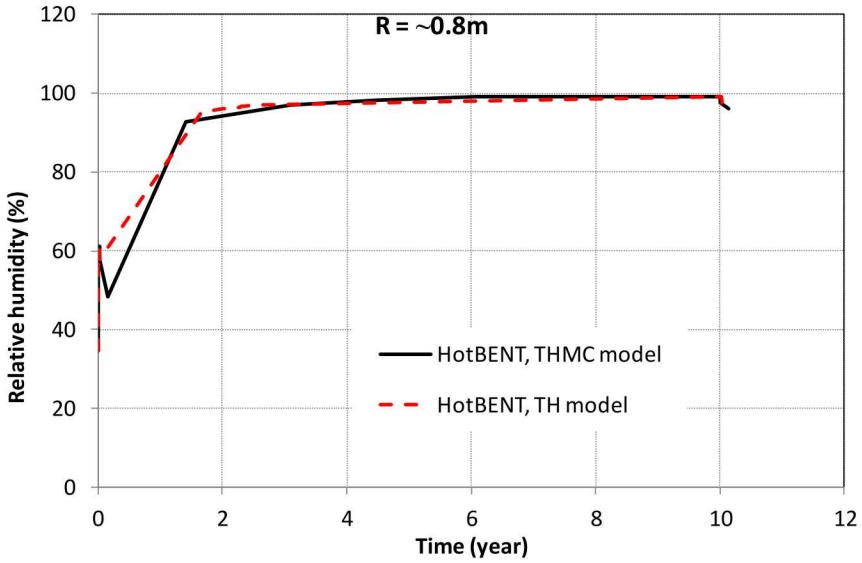

Figure 4-29. Predicted relative humidity at a radial distance of 0.8 m for the TH and THMC models for HotBENT.

In summary, in terms of the difference in hydrological behavior computed by the TH and THMC models, the following observations can be made:

1. Differences in hydrological behavior (using relative humidity as a representative) are more obvious for areas near the heater, and quite minimal from the middle to the outer region of the bentonite barrier.
2. The higher the initial permeability of bentonite is, the less difference between the TH and THMC models in term of hydrological behavior can be observed and the difference is more short-lived. One of the reasons is that when permeability is higher, the relative change in permeability in response to swelling is smaller than for the case of low permeability. Another reason is that swelling of bentonite near the host rock leads to a lower density and higher permeability, and at the same time compression and drying out of bentonite near the heater leads to lower permeability. In terms of the overall permeability of the whole bentonite barrier, the increase in permeability near the host rock and the decrease of permeability near the heater tend to cancel out each other, and such cancelling effect is more pronounced for bentonite with high initial permeability.
3. When the permeability of bentonite is higher, the THMC model does not always lead to a lower relative humidity (or saturation) than the TH model, whereas the THMC model has a lower relative humidity at the early stage, but a higher relative humidity at the later stage than the TH model.

The difference in hydrological behavior in TH and THMC model are mainly caused by the porosity and permeability evolution in the THMC model due to mechanical changes. Swelling upon the hydration, shrinkage due to drying, and thermal expansion make porosity evolve spatially and temporally, and cause subsequently intrinsic permeability changes as well. Chemical change has only a minimal effect on the hydrological behavior, because mineral dissolution/precipitation causes minimally affects porosity. To reliably calculate the hydrological evolution of bentonite, chemical processes can be neglected, but a mechanical process must be included. Because the evolution of porosity and permeability in bentonite is

the result of interactive coupling between thermal, hydrological and mechanical processes, it would be very difficult to extract a simple function for porosity and permeability to be used in the TH model.

When comparing THC and THMC models within the first set of models, it is clear that the difference in Cl concentration profiles is also observed for other chemical components and minerals. Therefore, in the second set of models, we only compared the Cl concentration (Figure 4-30), and substantial differences were observed. The THC model neglects changes in porosity and permeability due to swelling/shrinkage, leading to substantially different results than those produced by the THMC model.

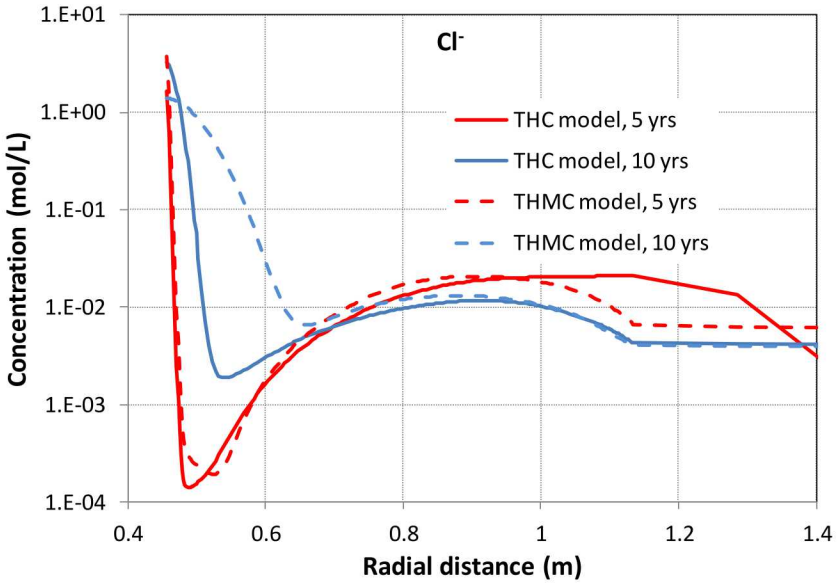

Figure 4-30. Predicted Cl concentration profiles at 5 and 10 years for the THC and THMC models for HotBENT.

4.5 2-D Model

4.5.1 Model Setup

Using the 1D axi-symmetric THMC model for the FEBEX *in situ* test to study the possible changes expected for HotBENT is a good exercise, because the model has been calibrated against data. What is needed to make an adjustment of boundary conditions and certain parameters. A caveat with the 1D axi-symmetric THMC model is that it is difficult to represent a setup with a pedestal- and granular bentonite-filled barrier. We, therefore, developed a 2-D cross-sectional model for HotBENT, as shown in Figure 4-31.

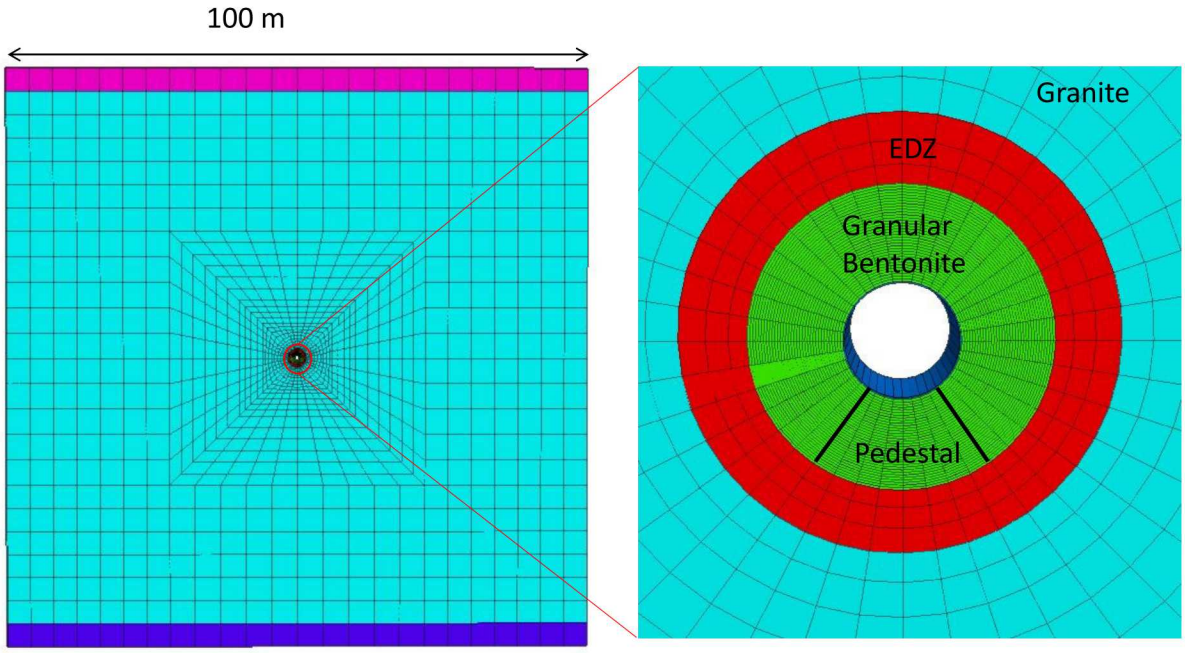

Figure 4-31. 2-D cross-sectional mesh for the THMC model.

Scenario 3.3 in Finsterle et al. (2017) is a generic case with permeability of 10^{-19} m^2 for granular bentonite. In the 2-D THMC model, we used the same hydrological parameters as Scenario 3.3, except that permeability for granular bentonite was initially 10^{-19} m^2 and changed according to Equation (4-3) with $\alpha = 0.025$, and the permeability for the pedestal was initially 3.46×10^{-20} m^2, and changes according to Equation (4-3) with $\alpha = 0.051$. The mechanical and chemical parameters for the granular bentonite and pedestal were assumed to be the same as for the FEBEX bentonite, which are listed in Sections 3.1.2 and 3.1.3.

4.5.2 Modeling Results

Figure 4-32 shows the temperature in the area within about a 20-meter radial distance of the heater. Although the temperature in the bentonite remains fairly stable soon after the heating starts, the area that undergoes a temperature rise keeps expanding.

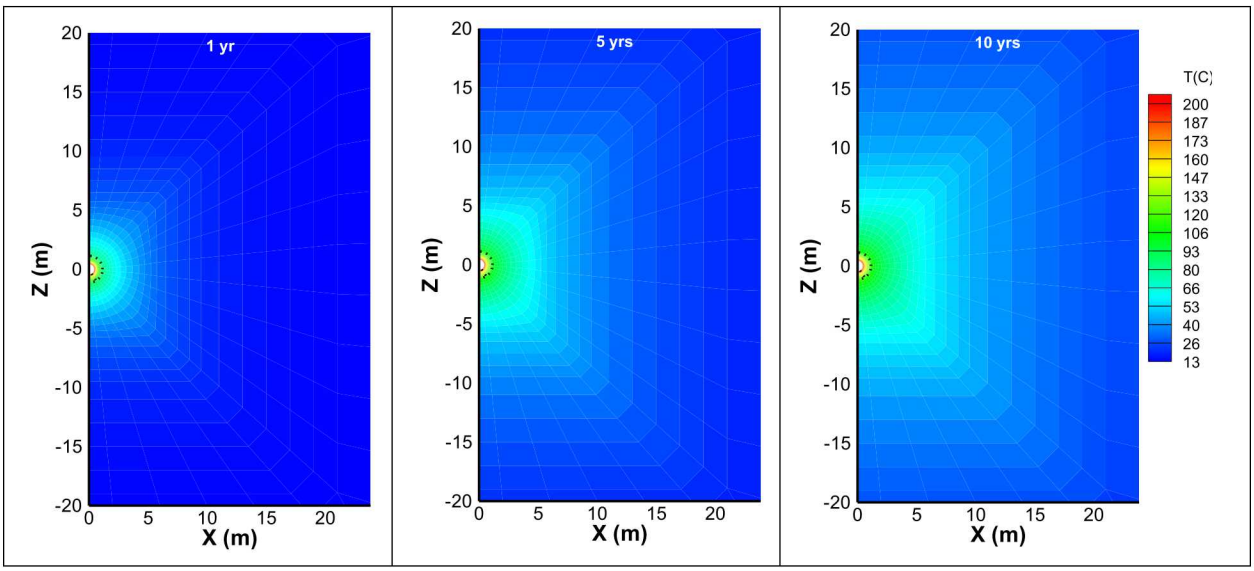

Figure 4-32. Spatial temperature distribution at 1, 5 and 10 years in the 2-D cross-sectional THMC model.

Because most hydrological phenomena have been studied by the 3D TH model (Finsterle et al., 2017), a major objective of running 2-D THMC simulations was to check how much variation would be introduced by the 3D TH model, ignoring the change in porosity and permeability due to swelling. To do this, we first compared the 2-D cross-sectional TH and 3-D TH models for the potential to "reproduce" hydrological results of the 3D TH model with the 2D cross-sectional TH model, and then compared the 2D cross-sectional TH model with the 2D cross-sectional THMC model to evaluate any discrepancy caused by ignoring changes in porosity and permeability due to swelling/shrinkage in the TH model. Figure 4-33 shows the spatial distribution of water saturation at 1, 5 and 10-year intervals in three different models. The 3D TH model and 2-D TH model provide a similar saturation state of the bentonite barrier in terms of the thickness of the area of full saturation at 10 years, but differs slightly at 1 and 5 years, which could be attributed to two plausible reasons. The first one is that a 2-D TH model is based on a mesh that is discretized more finely in the radial direction than the mesh within a 3D model. It is known that vapor diffusion is important for moisture movement in bentonite. Heating generates an outward vapor flux that significantly retards the water infiltration from the host rock into bentonite. For example, Gens et al. (1998), when simulating FEBEX *in situ* test, showed drastically different water saturation profiles with and without considering vapor diffusion in the model. The vapor diffusion coefficient is one of the most sensitive parameters in determining the moisture distribution in bentonite (Zheng and Samper, 2008, Zheng et al., 2015b). In numerical modeling, numerical dispersion is an inherent feature of solving dispersion-advection equations using finite difference and finite element numerical methods (e.g., Lantz, 1971; Van Genuchten and Gray, 1978), which is caused by the temporal and spatial discretization of time and space domains, as well as depends on the numerical scheme of solving the equations. Numerical dispersion is therefore affected by the size of a grid used in the model, particularly, when diffusive or dispersive flux are important. Because (1) vapor diffusion is important in moisture movement in

bentonite, and (2) numerical dispersion is inevitable, the size of grids impacts modeling results. The fact that the 2D TH model in this report and the 3D TH model in Finsterle et al. (2017) have different grids leads to a discrepancy among model results. Another reason is that the retention curve and relative permeability function are implemented in the code iTOUGH (the code for the 3D model) and TOUGHREACT (the code for the 2D TH model), although both are van Genuchten type and have the same parameters. As a result, such different implementations might lead to “slightly” different results that can be observed.

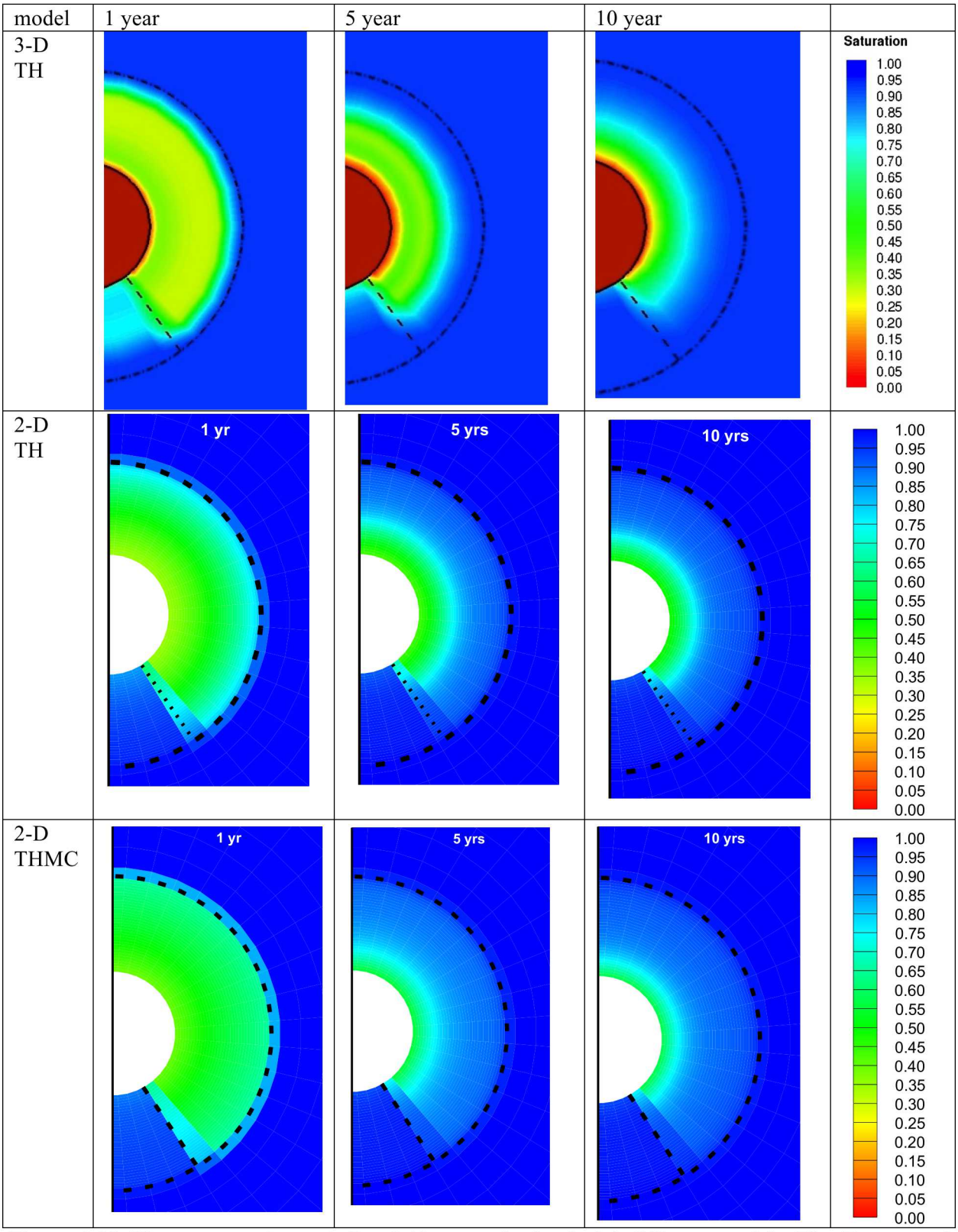

Figure 4-33. Water saturation at 1, 5 and 10 years obtained with different models. The diameter of tunnel is 1.14 m.

A comparison between 2D TH and THMC models suggests that the THMC model leads to a faster hydration of the bentonite, because, in the bentonite near the granite, saturation leads to swelling and a decrease in dry density, and, subsequently, higher permeability. As shown in Figure 4-34, it is fairly clear that the THMC model leads to a faster hydration of the inner part of the bentonite barrier (near the heater), whereas the THMC and TH models are similar in terms of hydration of the outer part of the bentonite barrier (Figures 4-35 and 4-36).

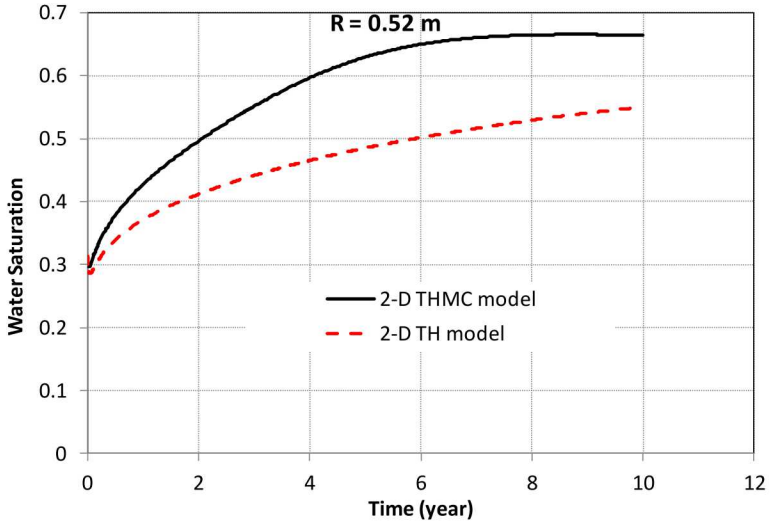

Figure 4-34. Temporal evolution of water saturation at a radial distance of 0.52 m in the 2-D TH and THMC models.

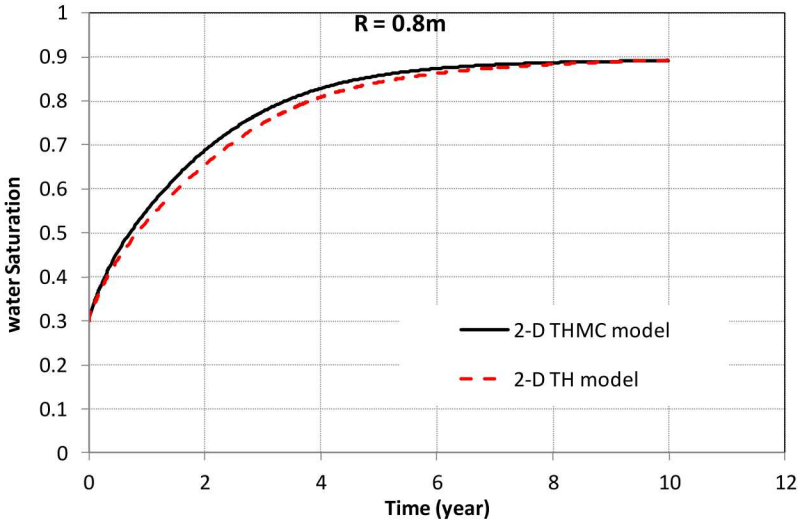

Figure 4-35. Temporal evolution of water saturation at a radial distance of 0.8 m in the 2-D TH and THMC models.

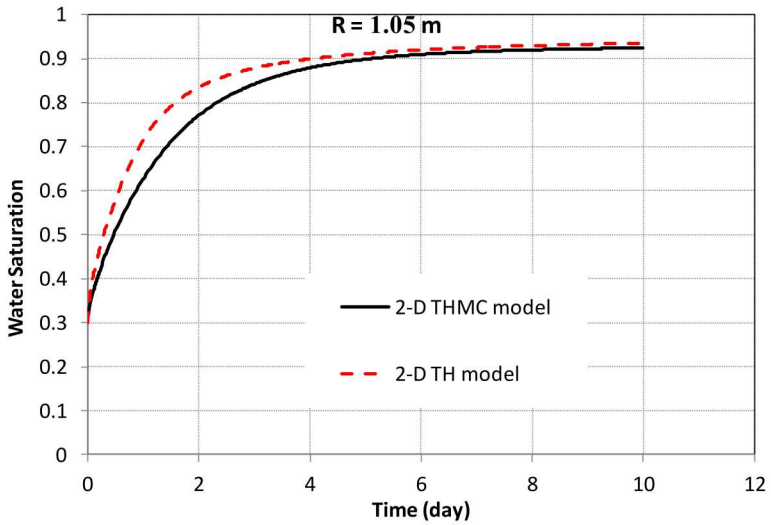

Figure 4-36. Temporal evolution of water saturation at a radial distance of 1.05 m in the 2-D TH and THMC models.

One of the reasons for selecting the current generic case with relatively high permeability is to create a condition with high temperature and water saturation, with the potential to maximize geochemical changes, so that noticeable changes could be observed over the duration of the planned experiment. The geochemical alteration of bentonite is the consequence of the interaction between transport processes, namely advection and diffusion, and chemical reactions, including cation exchange, adsorption/desorption and mineral precipitation/dissolution. Because of the very high solubility of halite, the chance that chloride may precipitate out as halite is very low. It is reasonable to assume that chloride acts as a conservative element that is solely controlled by transport processes. Models and data for the FEBEX *in situ* test (Zheng et al., 2016) show that elevated chloride concentrations appear in the immediate vicinity of the heater, and most areas of bentonite have a very low chloride concentration by the end of the 18-year test. In the current model, we observed the same behavior, except that the accumulation of elevated chloride concentrations appears much earlier, only one year after heating started (Figure 4-37). A plausible reason is that the current model has a bentonite with a much higher permeability than in the FEBEX *in situ* test, where the water infiltration from granite is faster and pushes the bentonite pore-water (with a high chloride concentration) toward the heater, and evaporation near the heater causes the rise of chloride concentration in the area near the heater. Therefore, a high chloride concentration is observed near the heater. At later times, for example, after 5 and 10 years, the concentration of chloride near the heater decreases slightly, but the area with the elevated chloride concentration expands slightly due to the cycling of evaporation and condensation. However, a high chloride concentration near the heater was not observed in the pedestal, because it has a higher initial water saturation than the rest of the granular bentonite, and becomes fully saturated shortly after heating starts. At 1 year, Cl concentration is higher near the heater, but later the dilution dominates and eventually the whole pedestal has a fairly low chloride concentration.

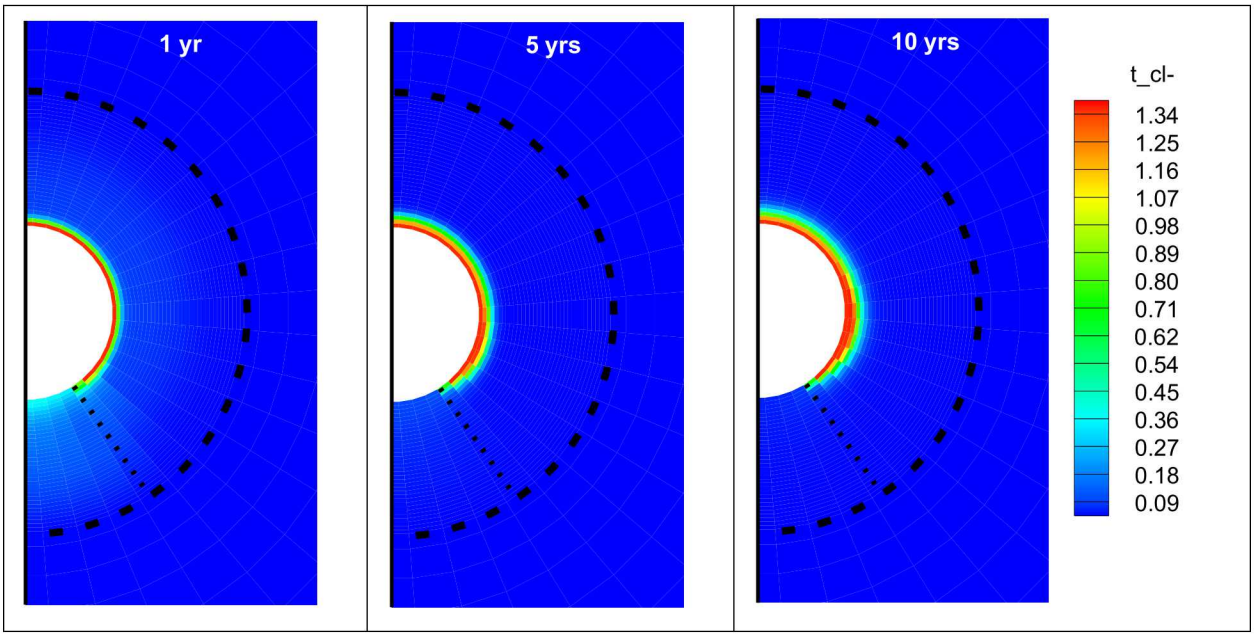

Figure 4-37. Spatial distribution of chloride concentration (M) at 1, 5 and 10 years.

One finding from the THMC model for the FEBEX *in situ* test is that most chemical species (except pH and bicarbonate) have a spatial distribution pattern controlled by the transport processes, whereas the chemical reactions are dependent on concentration levels. The spatial distribution of sulfate (Figure 4-38) clearly confirms this finding—spatially, it is similar to that of chloride (Figure 4-37), although the precipitation of gypsum (Figure 4-39) prevents the sulfate concentration from becoming high in proximity to the heater. Similar in the case of chloride, sulfate concentrations in the pedestal are diluted and remain low during most of the simulation time.

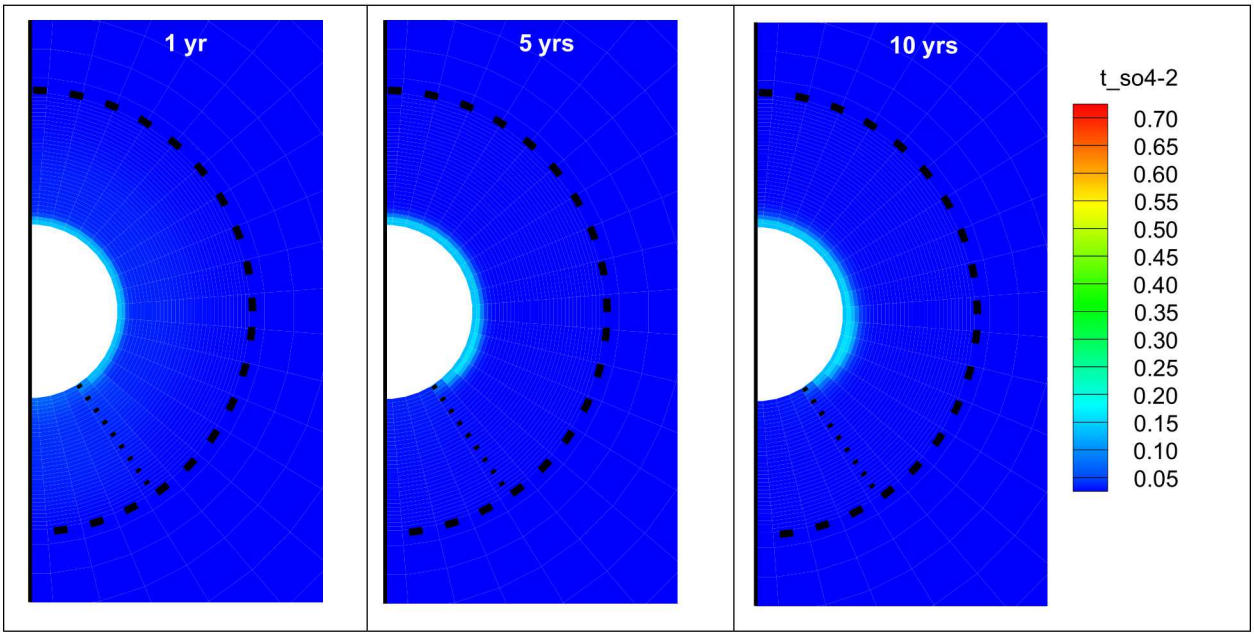

Figure 4-38. Spatial distribution of sulfate concentration (M) at 1, 5 and 10 years.

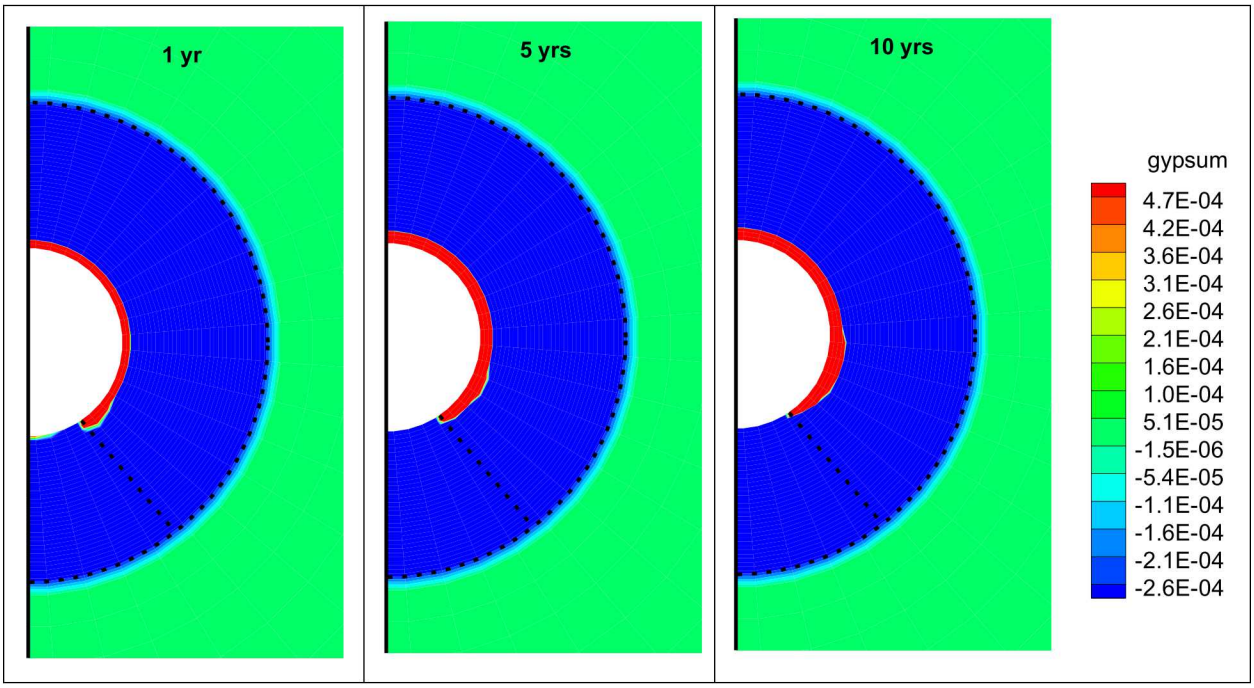

Figure 4-39. Spatial distribution of gypsum volume fraction change at 1, 5 and 10 years.

Bicarbonate (Figure 4-40) and pH (Figure 4-41) are controlled by both the reactions and transport processes, and have fairly complex spatial distributions. The spatial distribution of bicarbonate is different from other species, because (1) although granite water has a lower concentration of most species than bentonite pore-water, it actually has a higher bicarbonate concentration than bentonite pore-water, and (2) bicarbonate concentrations are affected strongly by the dissolution of calcite. In the early stages, a high bicarbonate concentration appears in the bentonite barrier near the granite because of dissolution of calcite (Figure 4-42), while most areas in bentonite remain low in bicarbonate. Later, as water with high bicarbonate concentration moves inwards, the majority of the bentonite has a high bicarbonate concentration, while the peak concentration gradually becomes lower.

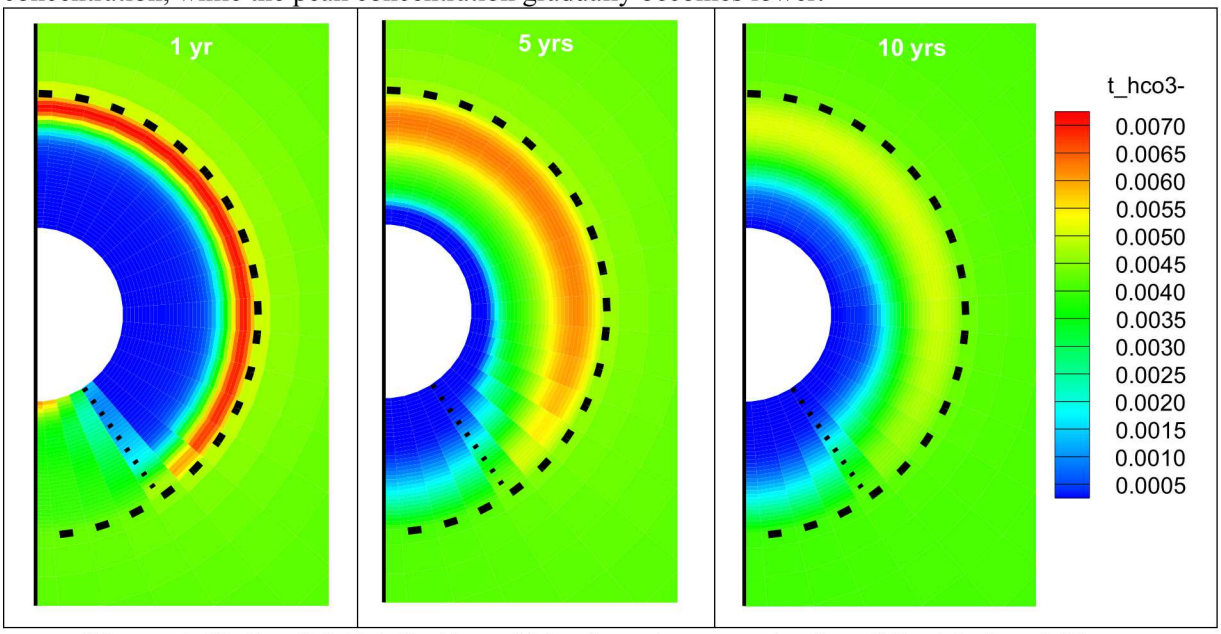

Figure 4-40. Spatial distribution of bicarbonate concentration (M) at 1, 5 and 10 years.

In the granular bentonite, the pH ranges from 7.2 to 7.8 (Figure 4-41). Although infiltration of more alkaline granite water tends to raise the pH, surface protonation in the bentonite buffers the pH. As a result, pH does not vary significantly in bentonite.

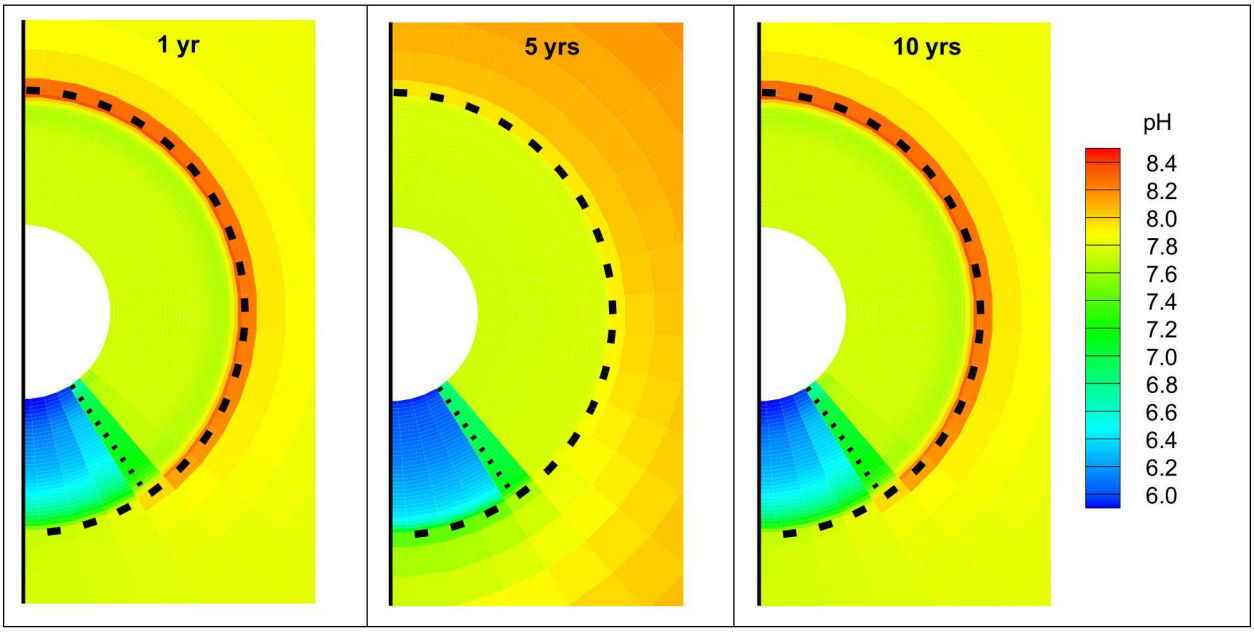

Figure 4-41. Spatial distribution of pH at 1, 5 and 10 years.

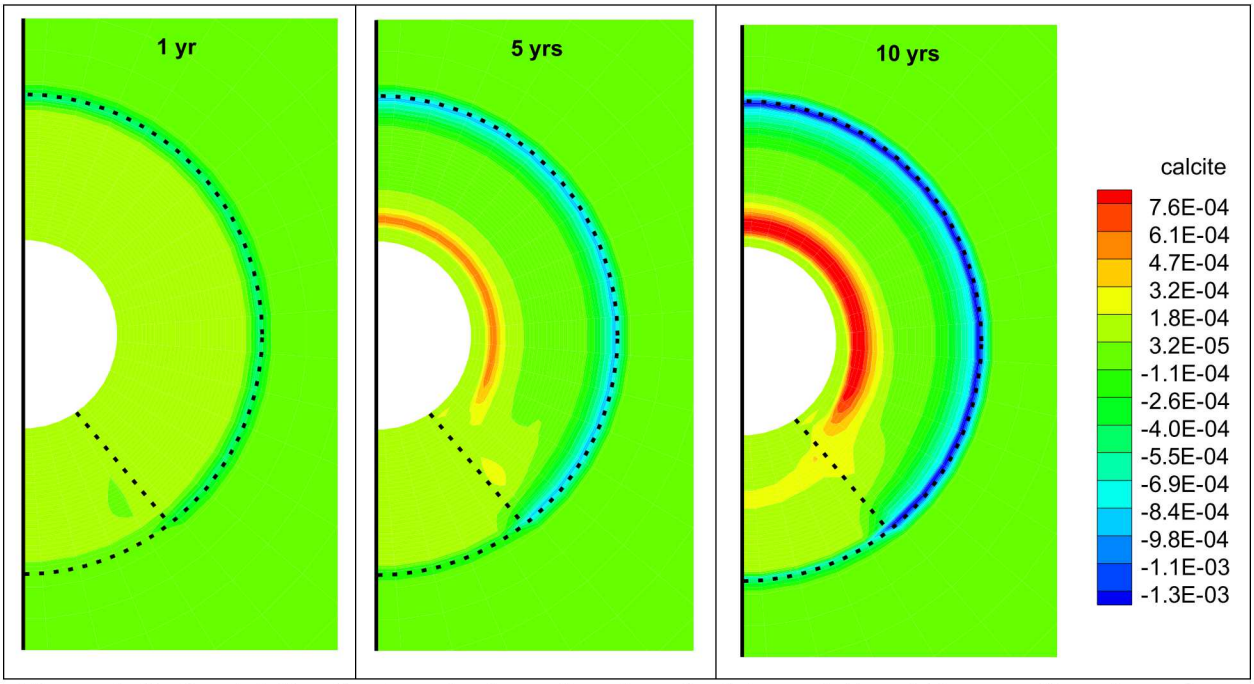

Figure 4-42. Spatial distribution of volume fraction of calcite at 1, 5 and 10 years. Negative values mean dissolution and positive values mean precipitation.

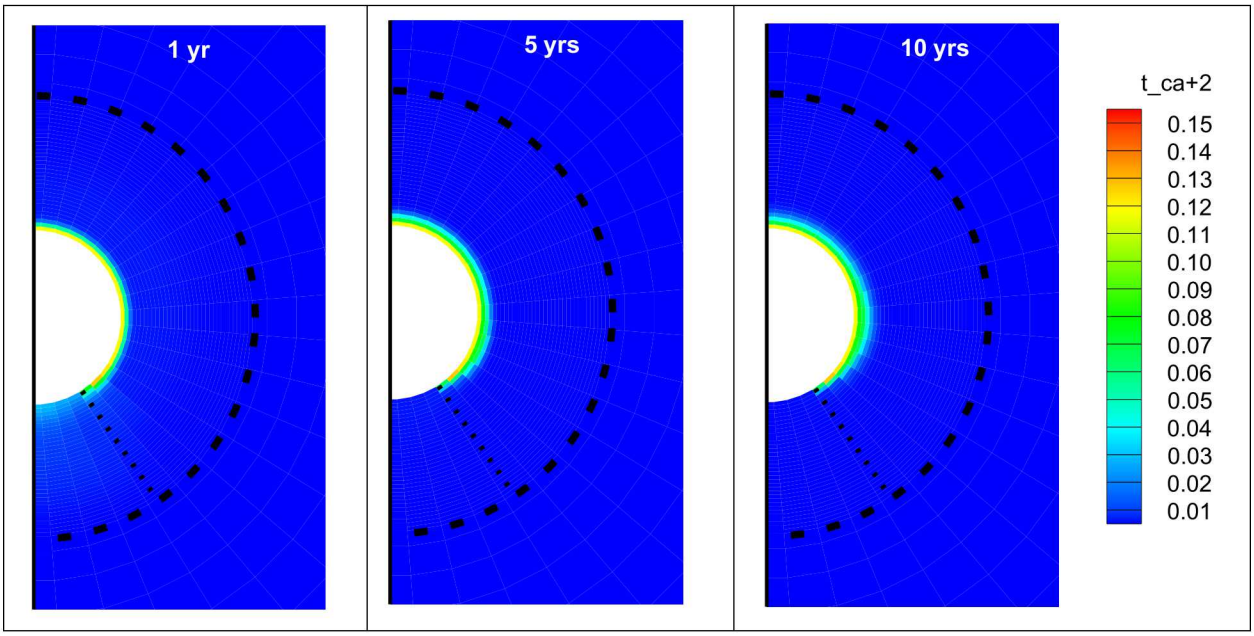

Figure 4-43. Spatial distribution of calcium concentration (mol/L) at 1, 5 and 10 years.

Figures 4-43 – 4-46 show the spatial distribution of the major cations calcium, magnesium, sodium and potassium. Their spatial distribution closely follows that of chloride, but their concentration levels are also affected by chemical reactions. In addition to cation exchange, each of them is also affected by mineral dissolution/precipitation. The calcite precipitation (Figure 4-42) near the heater apparently affects the calcium concentration. Dissolution of illite may alleviate the significant decrease in potassium concentration in the bentonite pore-water due to dilution.

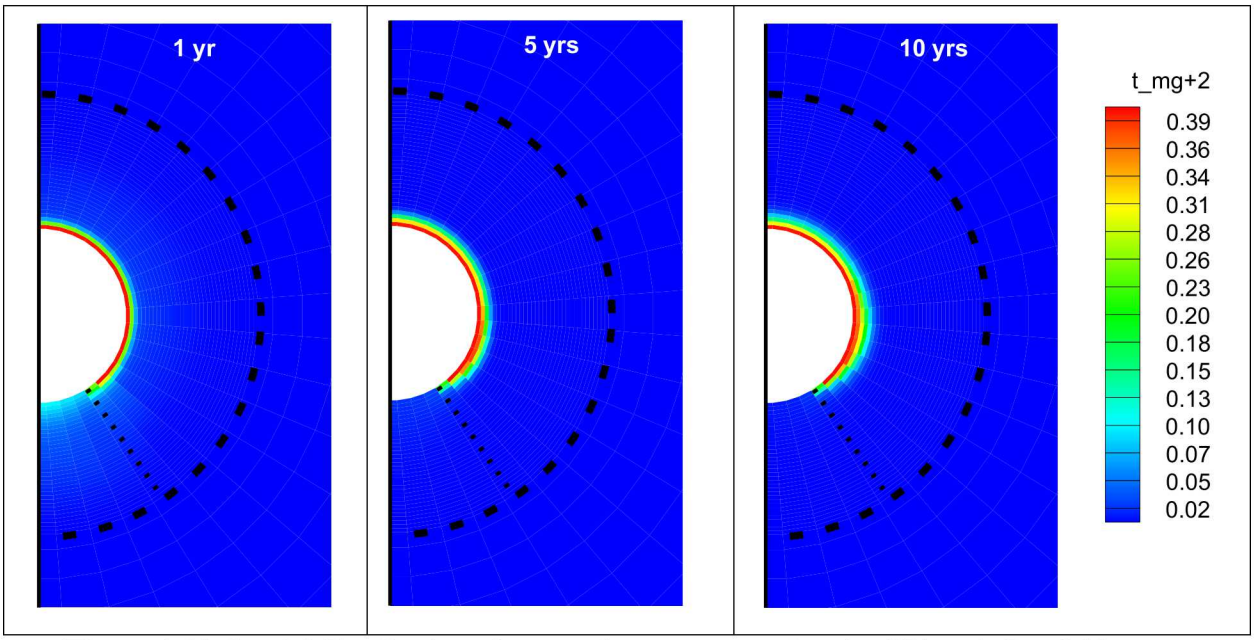

Figure 4-44. Spatial distribution of magnesium concentration (mol/L) at 1, 5 and 10 years.

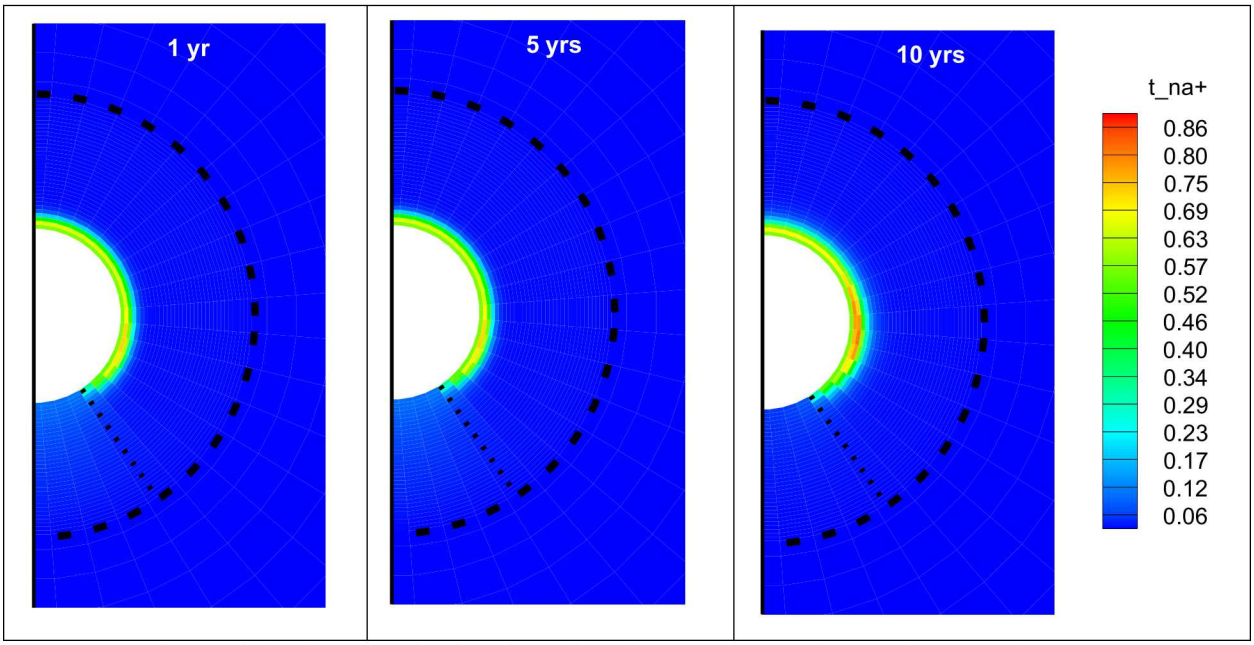

Figure 4-45. Spatial distribution of sodium concentration at 1, 5 and 10 years.

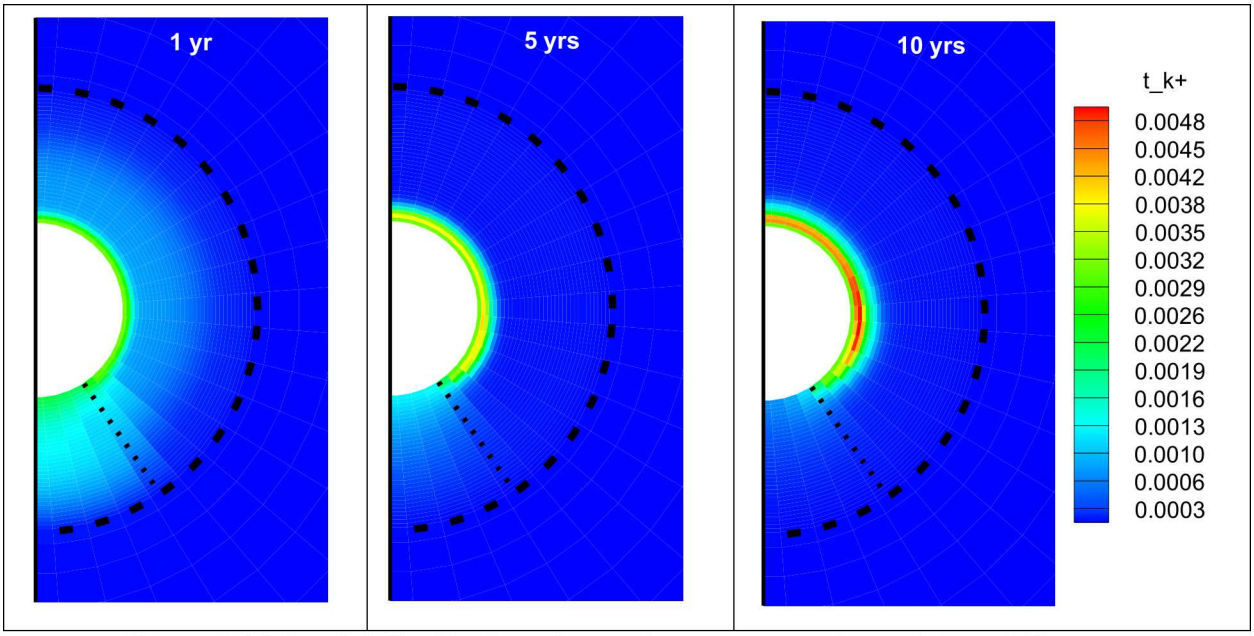

Figure 4-46. Spatial distribution of potassium concentration at 1, 5 and 10 years.

Illitization is a major consideration in determining the thermal limit for a repository with an EBS. However, the reaction rate of illitization is very low, and most laboratory and field tests did not run over a sufficient amount time to detect any changes. Pytte's model (Pytte, 1982) and similar types of models (Elliott and Matisoff 1996; Cuadros and Linares, 1996) have been widely used to calculate the illitization rate in geological formations. In these models, the time derivative of the smectite loss is related to the

concentration of potassium (or the ratio of potassium to sodium concentration) and the smectite mass fraction via a rate constant that is a function of temperature. Because it is hard to know the concentration of potassium over the course of geological time or the inhibition effect from other cations, Cuadros (2006) used an "effective" potassium concentration in the following equation to match the illitization versus depth data for variety of geological formations in the U.S.:

$$-dS/dt = kK^{0.25}S^{n} \qquad 4\text{-}4$$

where S is the fraction (unitless) of smectite, t is time, expressed in days, K is the effective potassium concentration in M, and k is a rate constant in $M^{-0.25}$ $days^{-1}$. Cuadros and Linares (1996) experimentally determined the rate constant, which is about 5E-6 $M^{-0.25}$ $days^{-1}$ at 100 °C and 3.3E-5 $M^{-0.25}$ $days^{-1}$ at 200 °C. Cuadros (2006) used the effective potassium concentration rather than the actual potassium concentration in the pore-water to take into account the competing effects of other cations with potassium for the interlayer space and other possible inhibition effects. The effective potassium concentration, K, ranges from 10^{-10} M to 10^{-24} M, which is calibrated from illitization versus depth data. Taking the maximum K of 10^{-10} M, the smectite mass fraction decreases at a rate of 0.0006%/year at 100 °C and 0.0038%/year at 200 °C, which means an experiment needs to run at 200 °C for around 300 years to realize about 1% change in smectite (which corresponds to the detection limit of X-ray diffraction (XRD)).

Given the very low reaction rate of illitization, in the current model, we deliberately selected a case with low permeability hoping to create conditions with high temperature and water saturation sufficient to elicit a detectable chemical change by the end of the HotBENT experiment. However, the current model does not show any illitization; in fact, it shows the opposite. As shown in Figures 4-47 and 4-48, the model shows slight dissolution of illite, with a maximum of about 0.006%, and slight precipitation of montmorillonite, with a maximum of about 0.2%. Illitization is a complex process and is impacted by many factors, which might retard or even prevent its occurrence. Although the current model is used to simulate high temperature (up to 200°C) and water saturation (close to full saturation after a relatively short time period), which generally favor the occurrence of illitization, other chemical conditions prevent the occurrence of illitization. Most significant is a lack of the supply of potassium. Groundwater in granite contains very little potassium. When bentonite pore-water is diluted by the granite water, the supply of potassium is so low that illitization cannot proceed. In recent years, it has become known that a high Na/K ratio also prevents occurring of illitization. Although granite water is low in both sodium and potassium and will dilute them in the pore-water of bentonite, the high exchangeable sodium in bentonite will make the ratio of Na/K in the pore-water of bentonite slightly higher, which again is unfavorable for the occurrence of illitization. In order to observe the occurrence of illitization, if artificial hydration is employed to accelerate the process, one has to add potassium to infiltrating water.

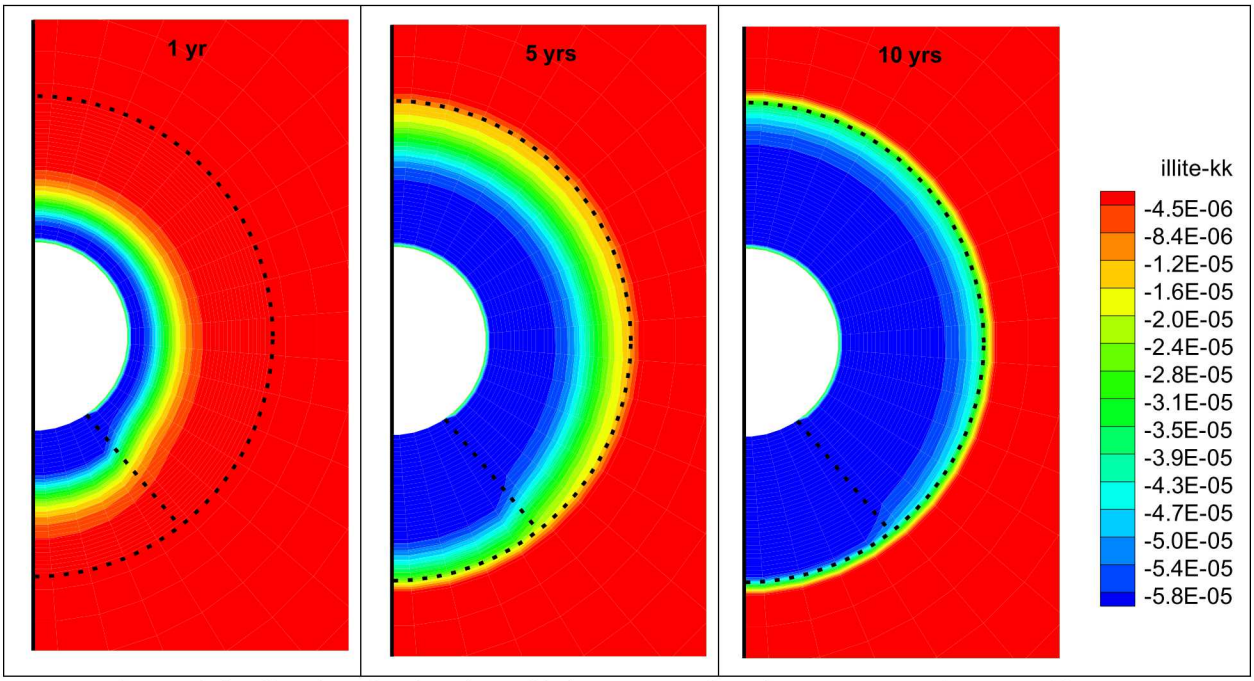

Figure 4-47. Spatial distribution of illite volume fraction change at 1, 5 and 10 years.

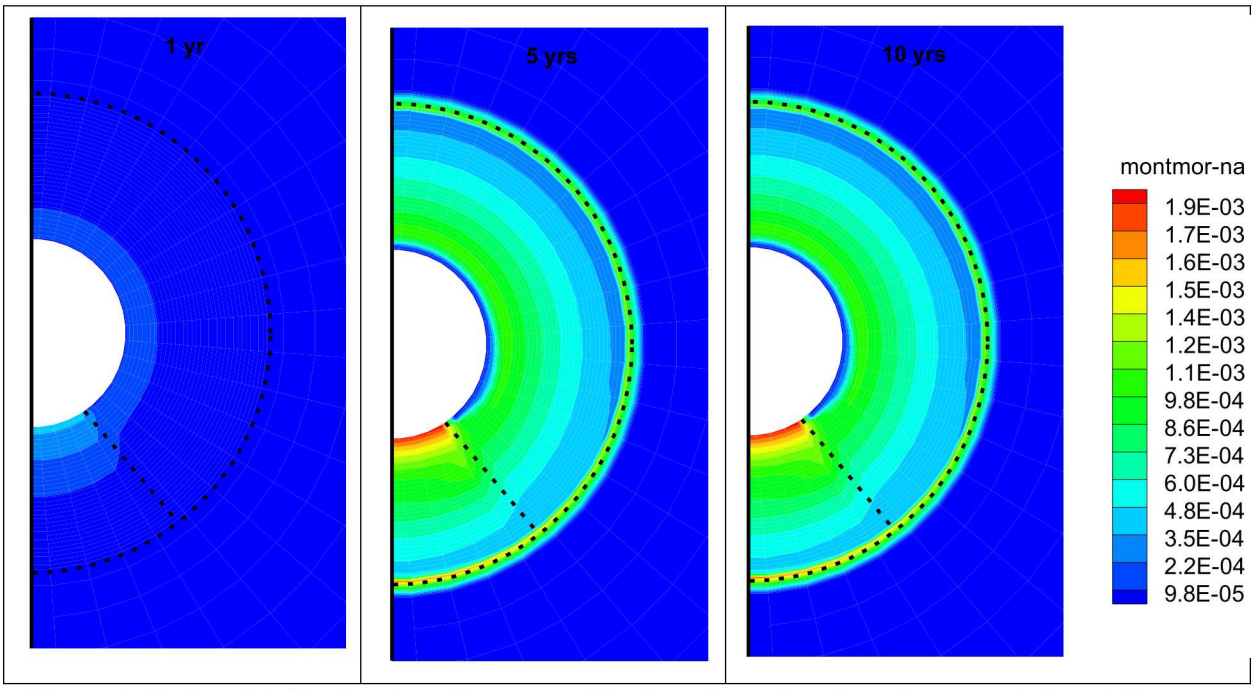

Figure 4-48. Spatial distribution of montmorillonite volume fraction change at 1, 5 and 10 years.

4.6 Summary of Model Results

Raising the maximum permissible temperature for clay-based barriers has a clear benefit for the design of repository layouts, such as decreasing the footprint of the repository. However, higher temperature can lead to complex hydrogeochemical processes that may affect the performance of a repository, and cannot be reproduced realistically and properly (non-conservatively) at the smaller laboratory scale. Such an assessment needs to be conducted by large-scale *in situ* experiments in underground research laboratories (URLs), where the most relevant features of future emplacement conditions can be adequately reproduced. Therefore, HotBENT, a high-temperature experiment (up to 200 °C) in a crystalline rock environment, is currently being considered under the leadership of NAGRA with several international partners, including the US DOE. To support the Preliminary Design Study (PreDes) (Kober et al., 2017), numerical models have been used to study the evolution of bentonite. Because thermal, hydrological, mechanical and chemical (THMC) processes are highly interactive in bentonite, ideally a coupled THMC model with a 3D description of HotBENT should be used. However, such a model is too computationally demanding to be implemented within a feasible time. Moreover, sometimes, it is not necessary to use such a complete model to answer some specific questions. Therefore, in this report, 1D and 2D numerical models with a simple geometric setup were used to simulate coupled THMC processes—hydrological, mechanical and chemical—taking place in bentonite over the course of the test. These modeling exercises supplement the 3D TH model (Finsterle et al., 2017), which provides a complete description of the configuration of the test and studies the phenomenological aspects of the HotBENT experiment.

The first group of models consists of 1D axi-symmetric coupled THMC models based on the model for the FEBEX *in situ* test (Zheng et al., 2017) to illustrate the expected THMC response in the hot cross-sections. The second group of models consists of 2-D cross-sectional models with THMC processes for one of the scenarios reported in Finsterle et al. (2017).

Major observations from the 1D axi-symmetric coupled THMC models for the FEBEX *in situ* test include:

- HotBENT with a heater temperature of 200 °C will lead to a temperature of around 90 °C in granite, thus boiling in granite would probably not be a concern.
- Most of the bentonite barrier for HotBENT with a heater temperature of 200 °C will stay dry for a very long time — an 18-year long simulation shows that the bentonite is far from being fully saturated, suggesting either artificial hydration is needed or permeability of the bentonite has to be higher than that of the FEBEX bentonite (2.15×10^{-21} m^2 for the FEBEX *in situ* test), or both.
- Despite the higher temperature in HotBENT, the stress is actually lower than that in the FEBEX *in situ* test (where the heater temperature was 100 °C).
- HotBENT needs a longer cooling period (time between the shut-down of the heater and dismantling) at the end of test than the FEBEX *in situ* test, and stronger redistribution of moisture in the bentonite during the cooling period is expected.
- The TH model that ignores porosity and permeability changes due to swelling/shrinkage overestimates the relative humidity by 20-25% over the entire simulation period compared with the THMC model, if it is the FEBEX bentonite. However, if the bentonite has a higher permeability than the FEBEX bentonite, the difference between the TH and THMC models is smaller and short-lived. The TH model has a higher relative humidity at the early stage, but a lower relative humidity at later times than the THMC model.
- If HotBENT uses FEBEX bentonite, high concentrations of major ions are expected.
- If HotBENT uses FEBEX bentonite, minerals with high solubility (e.g., calcite and gypsum) tend to dissolve in the area near the granite and precipitate in areas near the heater.

- If HotBENT uses FEBEX bentonite, dissolution of montmorillonite and precipitation of illite are not expected, but rather the opposite is observed in the model, mainly due to the very low potassium concentration in granite water.

The 2D cross-sectional THMC model simulates one of the scenarios in Finsterle et al. (2017), which has a permeability of 10^{-19} m^2 for granular bentonite and the mechanical and chemical parameters for the granular bentonite and the pedestal are assumed to be the same as for the FEBEX bentonite. The relatively high permeability for granular bentonite is expected to create conditions with high temperature and water saturation that foster significant chemical changes. The main observations from modeling results include:

- The 3D TH model (Finsterle et al., 2017) and the 2D cross-sectional TH model provide a similar saturation of the bentonite barrier in terms of the thickness of the full saturation area at 10 years, but differ slightly at 1 and 5 years.
- A comparison between 2D TH and THMC models suggests that the THMC model leads to faster hydration of bentonite because, in the bentonite near the granite, saturation leads to swelling and a decrease in dry density and subsequently to higher permeability.
- Similarly to the prediction based on the THMC model for the FEBEX *in situ* test, high concentrations of major ions (except bicarbonate and pH) in granular bentonite near the heater are expected. Such a high concentration zone near the heater also appears in the pedestal within a short time (< 1 year), but disappears later.
- Bicarbonate and pH show complex spatial patterns because they are affected by dissolution/precipitation of carbonate minerals and surface protonation.
- Despite of the 2D cross-sectional model having a higher permeability for granular bentonite than the 1D THMC model, it leads to similar mineral changes to the 1D THMC model: calcite and gypsum tend to dissolve in the area near the granite and precipitate in the area near the heater; illitization (dissolution of montmorillonite and precipitation of illite) is not expected, but rather the precipitation of montmorillonite and dissolution of illite are observed.
- The pedestal behaves differently from granular bentonite in terms of the change in ion concentration in pore-water despite of the current model hypothesis that they have the same initial geochemical conditions. The high initial water saturation in the pedestal makes it to become fully saturated soon, and, therefore, the pedestal generally has lower ion concentrations than granular bentonite. However, in terms of alteration of clay minerals (montmorillonite and illite), the pedestal behaves qualitatively similarly to granular bentonite.

While more simulations for sensitivity analyses could be conducted, we realize that geochemical changes are rather condition-specific. More reliable predictions can be made when the type of bentonite, initial hydrological and chemical state of the bentonite and the chemical composition of infiltrating water become available, and if artificial hydration is employed. This should be part of a detailed design study.

4.7 Implications of Current Model Results to the Design of HotBENT

Although current modeling work is either based on FEBEX bentonite (1D THMC in Section 3) or on a hypothetical case alone as described in Section 4, considering the similarity between FEBEX bentonite and MX80, major observations from current modeling work are likely qualitatively applicable to MX80. While it cannot be stressed enough that if MX-80 or other type of bentonite is used in HotBENT, THMC models for these bentonites are needed for more reliable calculation, current modeling work has the following implication to the final design of HotBENT in terms of the modeling work for HotBENT design and data collection in HotBENT.

Regarding the modeling work for the final design of HotBENT, the lessons learned from current modeling exercise and to potentially be applied to the final model are:

(1) An increase in stress, swelling in the area near the host rock and shrinkage in the area surrounding the heater are expected in the test. Porosity and permeability due to swelling/shrinkage are key HM coupling processes that need to be included in the model, even though modeling purpose is just TH process in the bentonite.

(2) Chemical processes are significantly affected by THM processes, but not vice versa. Porosity and permeability changes due to swelling/shrinkage affect moisture movement and consequently the transport of chemical components and other reactions such as mineral precipitation/dissolution. It is therefore necessary to have a THMC model to study chemical alteration of bentonite. However, THM model will be adequate if the purpose of modeling is to evaluate THM or TH processes in the bentonite because current models show the porosity change due to mineral precipitation/dissolution to be minimal.

(3) It is challenging to represent HM coupling, i.e. porosity and permeability due to swelling/shrinkage, in a simplified manner (without resorting to include mechanical process for the purpose of simulating TH processes) because of the interactive coupling between HM process—stress and suction changes affect porosity and permeability and changes in porosity and permeability affect the evolution of stress and capillary pressure. Any sort of simplified representation of HM coupling lead to an inevitable loss of such interactive coupling.

(4) Reliable prediction of THMC alteration in HotBENT would benefit greatly from more independently measured parameters. Special attention is called for measuring intrinsic permeability (as a function of dry density), and capillary pressure function. For chemical calculation, concentration of chemical components in bentonite pore-water, detailed mineral composition and CEC are necessary. For mechanical calculation, bulk modulus and swelling capacity are necessary.

Regarding data collection in HotBENT, based on FEBEX *in situ* test and modeling work in this report, the following observations can be made:

(1) Strong moisture re-distribution is expected during the cooling period (time between heater shutdown and dismantling) and it will complicate the interpretation of test result.

(2) THMC data at multiple locations and times are highly recommended. One lesson learned from the THMC modeling of FEBEX *in situ* is that chemical data provide an important additional piece of information for calibrating a THM model. In addition, chemical data collected in two dismantling events provides better constraint of models than chemical data collected just once. Temporal evolution of temperature, pore pressure, relative humidity, stress at various locations, spatial distribution of water content, dry density, water saturation, pore-water concentration, mineral composition at various time (might have to be done through multiple dismantling events) will provide constraints on interpretations of the experiment.

4.8 Future Work

In FY19, we will continue using THMC models to support the design of HotBENT. Specifically, the modeling work will focus on the following tasks:

Development of a 3D model that includes granite, bentonite, concrete (to separate different modules) and heater. Up to now, the models are either 1D axi-symmetrical or 2D cross-sectional. They can be used to simulate the THMC evolution in the “hot” sections, but not the “cold” sections, which do not cross-cut the heaters. The 3D model will allow for examining the THMC evolution of bentonite at both “hot” and “cold” sections, and also for studying an interfacial area such as the concrete-bentonite interface.

Currently, three materials, MX-80, Kunigel VI, Rokle bentonites, have been under consideration as the buffer material. Once the decision is made, THMC model will be developed specifically to simulate the performance of the selected bentonite. As revealed in this report, some phenomena can be generalized for different type of bentonite, but those related to geochemical processes, are largely bentonite-specific. As a result, THMC models for the selected bentonite will provide more support for the final design.

5. CODE COMPARISON OF SEMI-ANALYTICAL THERMAL ANALYSIS SOFTWARE

Semi-analytical codes are frequently used for evaluating the thermal field of heat-generating nuclear waste in a deep geologic repository. These codes offer an ease of use that is ideally applied to the design-phase, where quick scoping calculations can be made to understand waste package surface temperature as a function of waste package spacing and drift spacing. Semi-analytic models are ideal for these calculations, as changes to waste package spacing and drift spacing can easily be made without the complication of re-meshing. The trade-off is, of course, is a less accurate temperature prediction. The main objective of this study was to perform code-to-code benchmarking between semi-analytical codes (one used in the US SFWST Program, the other in the German Program), as we all as comparing both semi-analytical calculations with a more robust solver TH solver (i.e., FLAC3D).

A comparison of semi-analytical thermal analysis software was conducted as part of the KOSINA US-German collaborative work. The benchmark thermal analysis work was done by DBE TECHNOLOGY GmbH in Germany and Sandia National Laboratories. The results of the thermal analysis have been published in Simo et al. (2018). A summary of the collaborative work is presented below.

Thermal design analysis is an essential part of repository safety assessment to investigate thermal conditions in all parts of the repository and determine optimum disposal layout and repository foot print. During the design of the disposal layout temperature limits in the rock are defined based on requirements to reduce damage to the repository and the host rock. These limits vary depending on the type of host rock. For this study, the host rock of interest is bedded salt, which has a thermal limit of about 200°C, to avoid reaching the decrepitation temperature of salt.

Prior to disposal, the configuration of the waste packages in the repository is optimized under the requirement that the maximum temperature in the repository is below the temperature limit of the host rock. Several methods are available to perform this thermal analysis. The methods include simpler semi-analytical codes that provide quick analysis of heat transport, and the more complex numerical methods that provide distributions of heat, often coupled to mechanical phenomena and fluid flow transport. The aim of this present study is to assess the validity of such codes used by researchers in Germany and the United States. To this end, a US-German working group has been set up between DBE TECHNOLOGY GmbH and Sandia National Laboratories.

The comparative benchmark in this study is based on a US disposal layout from Sandia National Laboratories. Conduction-only thermal analysis was carried out at Sandia National Laboratories using the semi-analytical method implemented using Mathcad 14. A numerical simulation was also used at Sandia National Laboratories to test some of the Mathcad-based semi-analytical simulations. Thermal analysis of this example was also done by DBE TECHNOLOGY GmbH with the codes FLAC3D and LinSour. The thermal simulations at both DBE TECHNOLOGY GmbH and Sandia National Laboratories used the same original input parameters. The studies include comparisons of results, which will be used to assess and improve the performance of the codes. As described above, only conductive heat transport was considered,

neglecting convection and thermal radiation. These simplifications are reasonable for low permeability media (such as bedded salt) and enclosed emplacement modes (Hardin et al., 2012).

A short description of each software is given in Sections 5.1-5.3. The benchmark problem, simulations results, and conclusions are described in Section 5.5-5.7.

5.1 Mathcad-Based Thermal Analysis Software

A Mathcad-based semi-analytical transient thermal model developed by DOE (at Lawrence Livermore national Laboratory and Sandia National Laboratories) was also used for the analysis. The model is described further by Hardin et al. (2011, 2012). The model calculates the heat distribution produced by a central waste package including contributions from adjacent waste packages, as well as from waste packages in adjacent drifts. The model also includes convection, radiant heat transfer, ventilation and other processes. Analytical solutions from different sources were utilized in developing the model.

For this study, a backfilled repository in a salt host is assumed. Thus, the analysis will be conduction dominated and other processes (e. g., convection) are excluded on the basis that their contribution to the heat distribution will be negligible in the absence of large, open voids in the repository. The thermal conduction solution is a superposition of three components that represent contributions from the various sources. They include:

- a finite line source representing a central waste package of interest.
- infinite line sources representing laterally spaced adjacent drifts. This is represented by 8 adjacent drifts (four on each side of the central drift).
- Infinite point sources representing adjacent waste packages in the same drift aligned axially with the central waste package. This is represented by 8 adjacent waste packages (four on each side of the central waste package).

The analytical solution representing the central waste package is a finite line source in an infinite medium (Sutton et al., 2011). The finite line source solution is derived from the point source solution as shown in Sutton et al. (2011). The integral form of the finite line source solution in the form of the error function in Cartesian coordinates is given by:

$$T_{cent-line}(t,x,y,z) = \frac{1}{8\pi k}\int_0^t \frac{q_L(t')}{t-t'} e^{\frac{-(x^2+z^2)}{4\alpha(t-t')}} \left[erf\left[\frac{1}{2}\frac{\left(y+\frac{L}{2}\right)}{\sqrt{\alpha(t-t')}}\right] - erf\left[\frac{1}{2}\frac{\left(y-\frac{L}{2}\right)}{\sqrt{\alpha(t-t')}}\right]\right] dt' + T_0 \quad 5\text{-}1$$

where,
T = temperature
T_0 = initial or ambient temperature
L = characteristic length (waste package length)
k = thermal conductivity of medium
τ = dimensionless time (Fourier number) = (α · t)/L^2
$q_L(t)$ = continuous line heat source (heat load of a single waste package divided by its length)

If radial distances are desired, Cartesian coordinates can be converted to radial coordinates using:

$$r^2=(x-x0)^2 + (y-y0)^2 + (z-z0)^2 \quad 5\text{-}2$$

where the source is located at (x0, y0, z0);

The contribution of adjacent drifts is represented by the infinite line source equation. The solution to the equation is given in Carlslaw and Jaeger (1959) and Sutton et al. (2011). Considering two sets of four drifts on both sides of the central waste package, with given drift spacing and waste package spacing, the solution can be represented as:

$$\boldsymbol{T_{adjacent-drifts}(t,x,y,z) = 2\left[\sum_{id=1}^{N_{drifts}} \frac{1}{4\pi k}\int_0^t \frac{q_L(t')\cdot\frac{L}{wps}}{t-t'} e^{\frac{-\left[\left(x^2+z^2\right)+(id\cdot ds)^2\right]}{4\alpha(t-t')}} dt'\right]} \quad 5\text{-}3$$

where;
$T_{adjacent-drifts}$ = temperature contribution of waste packages in adjacent drifts
N_{drifts} = number of adjacent drifts on each side of the central waste package (=4)
wps = waste package center to center spacing
ds = drift center to center spacing

The contribution of adjacent waste packages is represented by the infinite point source equation. The solution to the transient point source equation is provided by Carslaw and Jaeger (1949). Considering two sets of four waste packages on both sides of the central waste package aligned axially, with given waste package spacing, the solution can be represented as:

$$\boldsymbol{T_{adjacent-waste\ packages}(t,x,y,z) = 2\left[\sum_{ip=1}^{N_{wps}} \frac{1}{8\pi k\sqrt{\alpha}\pi^{1.5}}\int_0^t \frac{q(t')}{(t-t')^{1.5}} e^{\frac{-\left[\left(x^2+z^2\right)+\left((ip\cdot wps)^2\right)\right]}{4\alpha(t-t')}} dt'\right]} \quad 5\text{-}4$$

where,
$T_{adjacent-waste\ packages}$ = temperature contribution of adjacent waste packages in the same drift
N_{wps} = number of adjacent waste packages on each side of the central waste package (=4)
q(t) = continuous line heat source.

The Mathcad-based model uses Equations 6-3 through 6-6, the heat source given in Figure 5-1, and properties of the engineered barrier system to evaluate temperature at the waste package surface and the drift wall as a function of time.

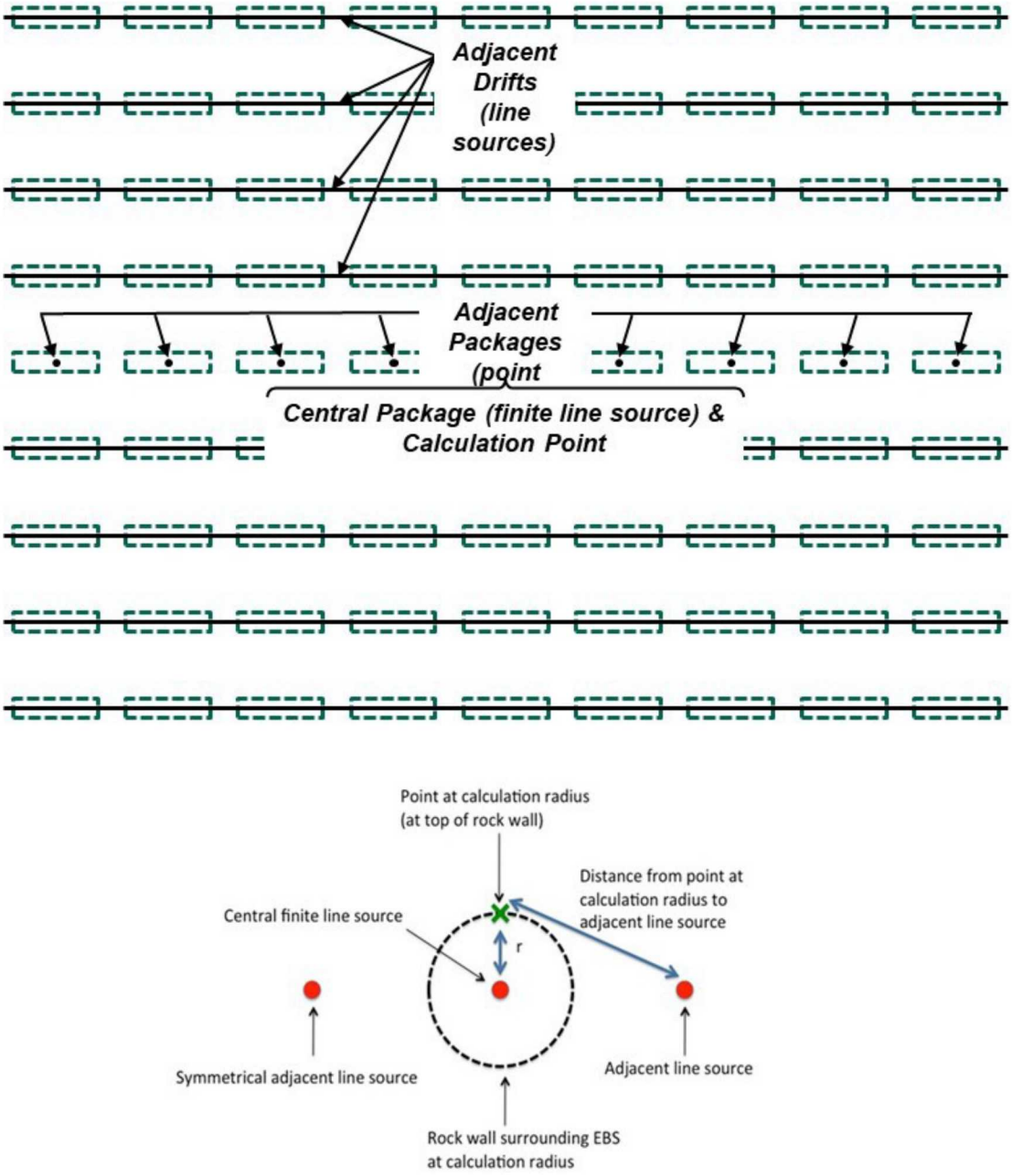

Figure 5-1. Representation of Mathcad based semi-analytical thermal analysis method used by Sandia National Laboratories. Floor layout of disposal area. (from Hardin et al., 2012)

5.2 LinSour Software

LinSour or LINe SOURces is a computer code which has been developed to manage the complexity that arises in numerical codes when the thermal analysis is performed on an entire repository with large dimensions (up to several km^2) and over a time scale of 10^6 years (Figure 5-2). It is the latest development of several research studies on the development of analytical solutions for thermal analysis in repository systems in Germany (Schmidt, 1971, and Ploumen and Strickmann, 1977).

LinSour relies on the analytical solution of the heat transfer differential equation for a finite, linear, stationary heat source emplaced in an infinite, homogeneous and isotropic medium with constant material data. With respect to the linearity of the differential equation LinSour uses superposition to model the temperature field of more than one source. The differential equation solved numerically in LinSour for each line source is displayed below (Ploumen and Strickmann, 1977, and Hahne, 1988):

$$\vartheta(t,R,z) = \frac{1}{8\rho c_p(\pi a)^{3/2}}\left[\int_0^t \frac{\Phi(t')}{(t-t')^{3/2}}\int_{-h}^{h} e^{-\frac{R^2+(z-z')^2}{4a(t-t')}}dz'\right]dt' + \vartheta_0 \qquad 6\text{-}5$$

where,

ϑ	Temperature
ϑ_0	Initial temperature
$\Phi(t)$	Time dependent thermal heat per meter
t	Time
ρc_p	Volumetric specific thermal capacity
a	Thermal diffusivity: $a = \frac{\lambda}{\rho c_p}$
λ	Thermal conductivity
R	Radial distance of the monitored point to the line source
z	Axial distance of the line source
h	Half-length of the line source

The time dependent thermal heat represents, t, the thermal decay of the radioactive waste and is approximated in LinSour by a sum of exponential functions as follows:

$$\Phi(t) = \sum_{i=1}^{m}\{a_i \cdot e^{-b_i t}\} \qquad 6\text{-}6$$

Where;

$\Phi(t)$	Thermal heat at time t
a_i, b_i	Coefficients
m	Number of approximation functions

The analytical solution is a mathematical integral. The integration is achieved using the trapezoidal rule with increasing step size. The trapezoidal rule denotes an A-stable second order method. The temperature distribution in the repository is calculated in LinSour according to the following steps:

1. Input by the user of the coordinates of the line sources and the points where the temperature will be calculated according to a selected coordinate system. In addition, the times at which the temperature is calculated must be specified.
2. LinSour calculates the distance between the line sources and monitored points
3. To increase the numerical efficiency, LinSour calculates the distance between the monitored points and the line sources with a temperature increase of less than 0.1 K/W at selected times. The temperature at such points will be set to a residual value.

4. LinSour calculates the temperature at the monitored points at all selected times through superposition of the temperature produced by all line sources. The temperature at each line source is calculated with Eqns. 1 and 2. Only the monitored points which satisfy Step 3 will be considered in this operation.

The benchmark example problem for the base case described above has been simulated with LinSour. The results of these calculations are presented and compared to the other codes in Section 5.6.

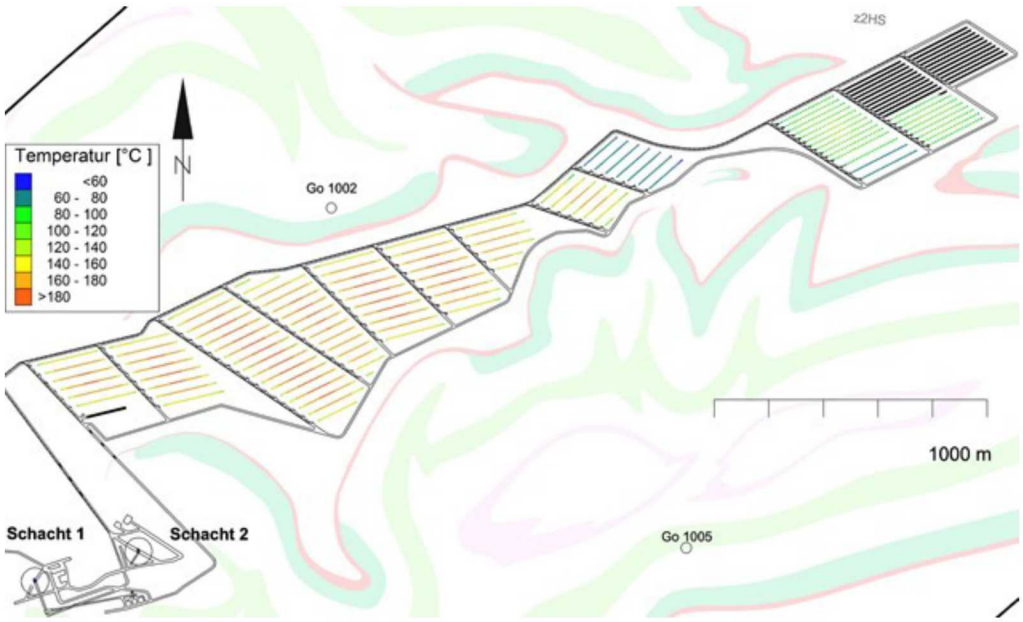

Figure 5-2. Schematic diagram showing capabilities of the LinSour Code from DBE Germany. The code is used in semi-analytical thermal analysis of entire repositories.

5.3 FLAC3D Numerical Code

A repository for radioactive waste is characterized by its complex geometry, heterogeneous materials whose parameters can be nonlinear with respect to time, temperature and pressure. In addition to thermal conduction, other heat transport phenomena such as convection and radiation also take place in a repository. In such conditions, the thermal analysis of heat distribution in a repository system is usually accurately performed with numerical codes. For this reason, the example problem was also solved using the finite difference code FLAC3D. FLAC3D (Fast Lagrangian Analysis of Continua in 3 Dimensions) is a numerical modeling software developed by Itasca Inc. for geotechnical analyses of soil, rock, groundwater, constructs, and ground support. FLAC3D has a thermal option for analyzing both conduction and advection in materials for nuclear waste disposal and cement hydration and a creep option for analyzing time-dependent material behavior, for excavations in salt or potash, for example.

Figure 5-3 shows a FLAC3D representation of the repository setup used for the numerical model that was developed for the model comparison example problem described below. This figure shows an illustration of the host rock with an excavated drift. A waste package (cask) is disposed in the drift and is backfilled with crushed salt buffer. Figure 5-3 also shows two observation points (at the drift wall and at the waste package surface). For the numerical simulations using FLAC3D, the thermal decay curve shown in Figure 5-4 was applied as volume specific heat-generating source in the waste package (cask).

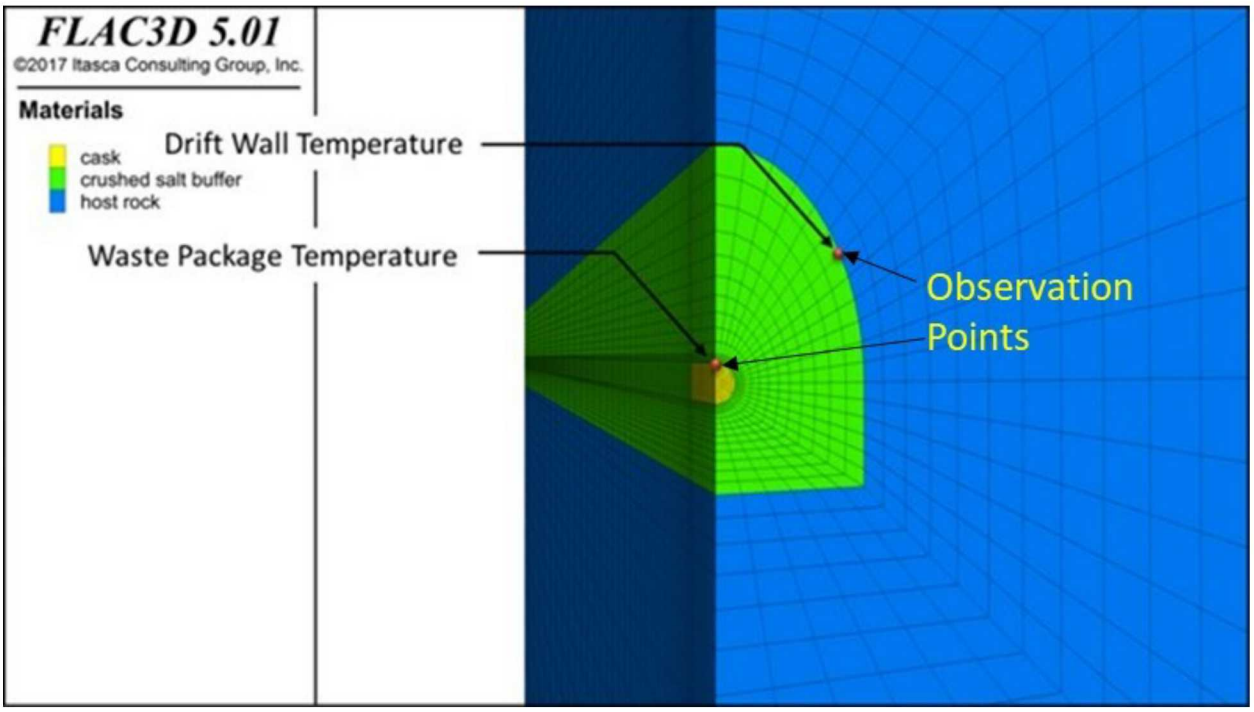

Figure 5-3. Representation of the repository setup for the numerical model used in the example problem.

5.4 PFLOTRAN Numerical Code

The numerical code PFLOTRAN (Hammond et al., 2014) was also used at Sandia National Laboratories to test some of the Mathcad-based semi-analytical thermal simulations. PFLOTRAN is an open source, state-of-the-art massively parallel subsurface flow and reactive transport code in a high-performance computing environment.

5.5 Benchmark Simulations

A bench mark test problem is presented for testing the analytical thermal models used in this study. This case represents thermal analysis of a generic repository in bedded salt at 500 m depth. Heat conduction of a central waste package at a center of a drift with contributions from adjacent waste packages and drifts is considered. The intact salt beyond the drift was assumed to be an infinite medium. The space between the waste package and the drift was assumed to be backfilled with crushed salt. For the base case (Case #1) the same material was assumed for the waste package, the backfilling material in the drift and the host rock to simplify the simulation. Thus, simulations were conducted with the thermal conductivity of crushed salt and the heat capacity of intact salt. This follows the assumption that the heat propagation in the near field is mostly dominated by transport through the crushed salt buffer, whereas transport through the intact salt dominates heat transport in the far field. To quantify the effect of using the same material properties in the base case, a separate simulation was done with a numerical simulator FLAC3D using representative properties for each material (Case #2). Table 5-1 provides material properties used in all simulations.
Ambient average ground surface temperature of 15°C; and a natural geothermal gradient of 25°C/km, were assumed to calculate temperature at the near field. The waste package has a diameter of 0.61 m and is 3.05 m long. The drift diameter is 6.1 m. The decay heat curve for the waste package type is shown in Figure 5-4. Each waste package in the study generates heat according to this heat decay curve. Surface storage of 10 years was assumed.

The heat transport and the resulting maximum temperature in the repository are the result of the heat generation from each waste package and the superposition of the heat from all waste packages. Therefore, the example case will be analyzed in two different surface layout configurations. In the first configuration, a single waste package in the repository is considered. This allows the simulation of the thermal propagation of a single heat source, with no contribution from other sources. In the second configuration, the repository setup with multiple drifts and waste packages, with a drift spacing of 20m and a waste package spacing of 10 m was simulated. The second configuration calculates the superposition of the heat output produced by multiple waste packages.

Table 5-1. Material properties

Material	Thermal Conductivity (W/m/K)	Density (kg/m^3)	Heat Capacity (J/kg/K)	Thermal Diffusivity (m^2/s)
Intact salt	3.20	2200	931	1.562×10^{-6}
Crushed salt	0.57	2200	561.6	4.613×10^{-7}

The waste considered in the analysis is a Savanah River glass canister. The canister size is given in Table 3-7, Carter et al. (2012). The dimensions are 24” (0.61 m) diameter and 10 ft (3.05 m) length. The heat source is from Wilson (2016) for SRS glass canister 300-500 Bin. Figure 5-4 shows thermal output for the selected bin.

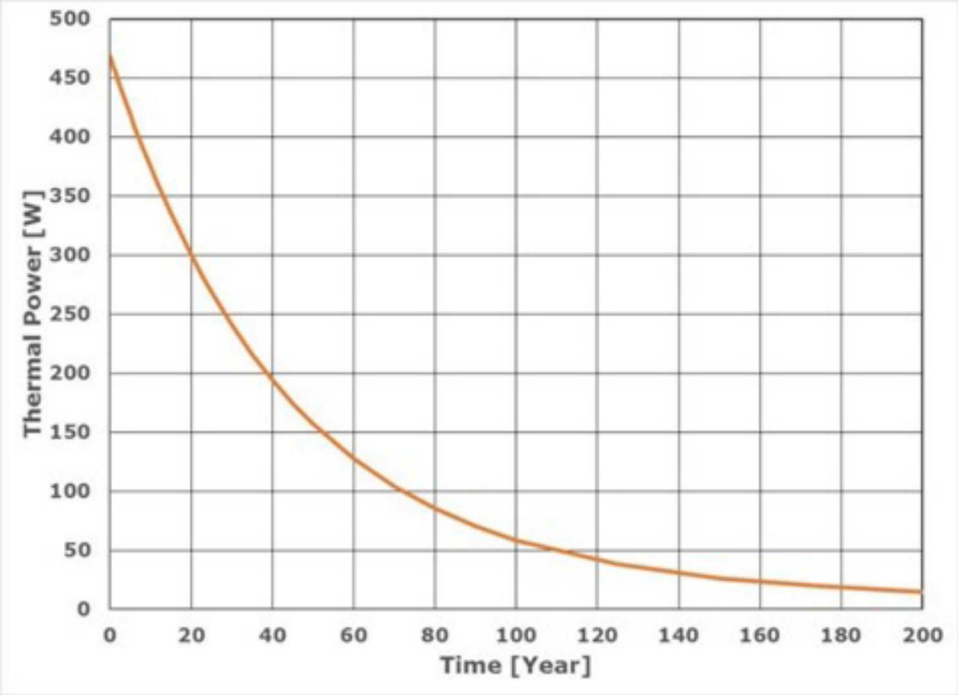

Figure 5-4. Thermal output of Savanah River glass canister (300-500 Bin) (Wilson, 2016)

5.6 Simulation Results

The numerical model is set up so that the initial and boundary conditions are identical to those of the semi-analytical codes. This insures a basis for comparison between all codes under the same conditions. Because of the limitations of the semi-analytical codes thermal conduction only is considered in the simulation. Thus, processes such as the temperature-dependent properties of rock salt and the pressure-dependent properties of crushed salt are not taken into account. Since the semi-analytical code LinSour can be used only for isotropic media, further adjustments were made in the numerical simulations: For Case #1, the same thermal material parameters are assigned to all materials (crushed salt, waste package, rock salt) to establish isotropic conditions in the numerical model. This approach made it possible to determine the accuracy of the analytical codes in comparison to the numerical code under identical input conditions. A second separate numerical simulation with properties of each material according to Table 5-1 was also conducted (Case #2). For this case, the waste package was represented by a thermal conductivity of 1 W/m·K and thermal capacity of 800 J/kg·K. The results of all simulations are presented and discussed below for the two configurations.

A FLAC3D representation of Configuration 1 is shown in Figure 5-5. The corresponding representation for Configuration 2 is shown in Figure 5-6. The results of the analysis using the three codes LinSour, SANDIA Mathcad 14 and FLAC3D are presented in Figures 5-7 and 5-8 for Configuration 1. Configuration 1 represents the case of a single waste package placement. The plots in Figures 5-7 and 5-8 represent the simulated temperature values at the monitoring points at the drift wall (left) and the waste package surface (right) over a simulation period of 100 years using parameters according to Case #1. The results of the numerical simulation with FLAC3D using corresponding properties for each material are also presented in Figure 5-7 and Figure 5-8 (Case #2). Note that in this study it is assumed that the semi-analytical simulations are accurate when their results are comparable to those of the numerical code FLAC3D.

For the case of a single, isolated waste package emplacement (Configuration 1), the temperature results calculated with the two analytical codes and the numerical code FLAC3D, using the same material parameter values, are almost identical (Figures 5-7 and 5-8). The maximum temperature predicted by FLAC3D at the drift wall is equal to 39.1°C (Figure 5-8). This is very close to the maximum temperature of 38.8°C and 38.7 calculated with SANDIA Mathcad 14 and with LinSour, respectively. Similar results were also obtained at the waste package surface where maximum temperatures of 96.3°C, 96.8°C and 96.7°C were calculated with FLAC3D, SANDIA Mathcad 14 and LinSour, respectively, using the same parameter values (Figure 5-7). In addition, the shapes of the temperature curves are also identical over the simulation period. This indicates that the implementation of thermal conduction in the semi-analytical codes produces heat distribution calculations that are comparable to the analytic solution, and thus the physics of thermal conduction is well-captured by the semi-analytic model.

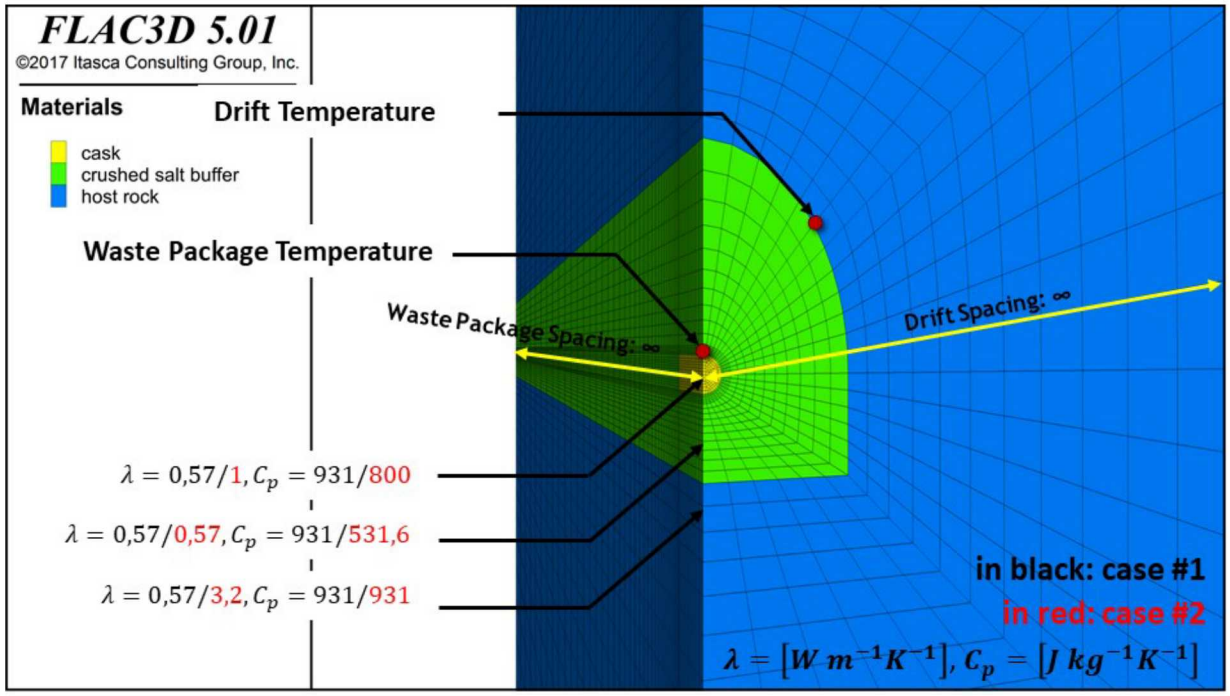

Figure 5-5. Representation of Configuration 1: A single waste package emplaced in an infinite medium

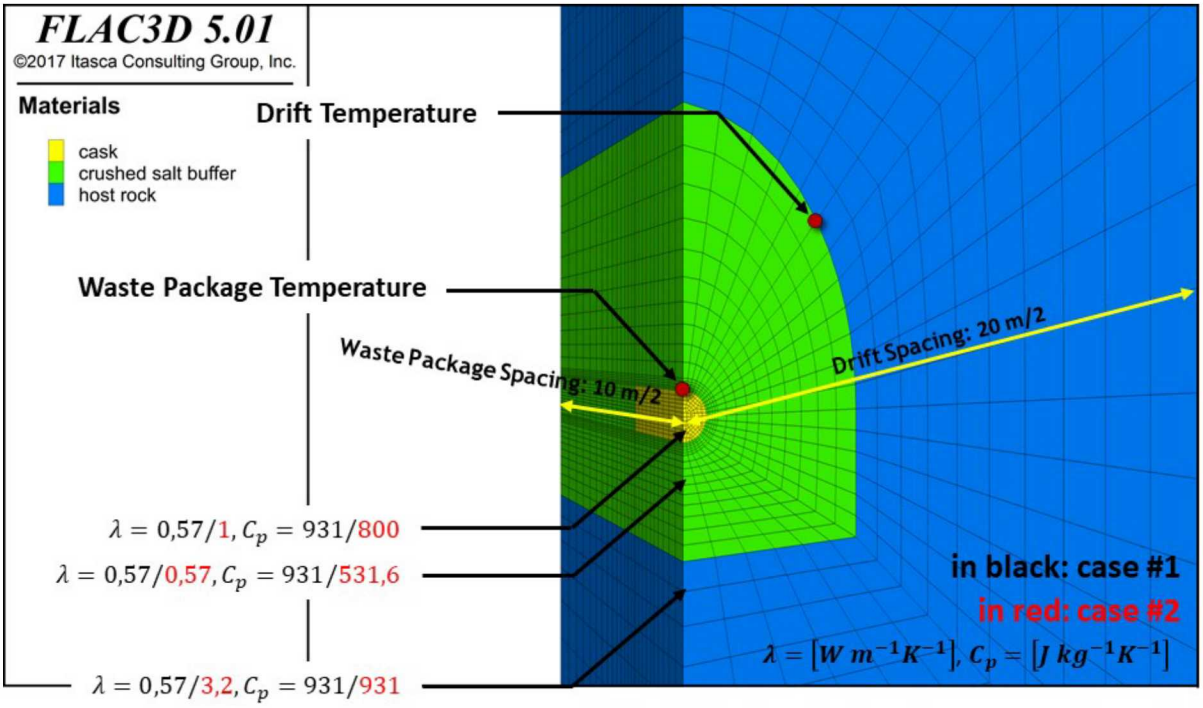

Figure 5-6. Representation of Configuration 2: Representative repository layout with given waste package spacing and drift spacing

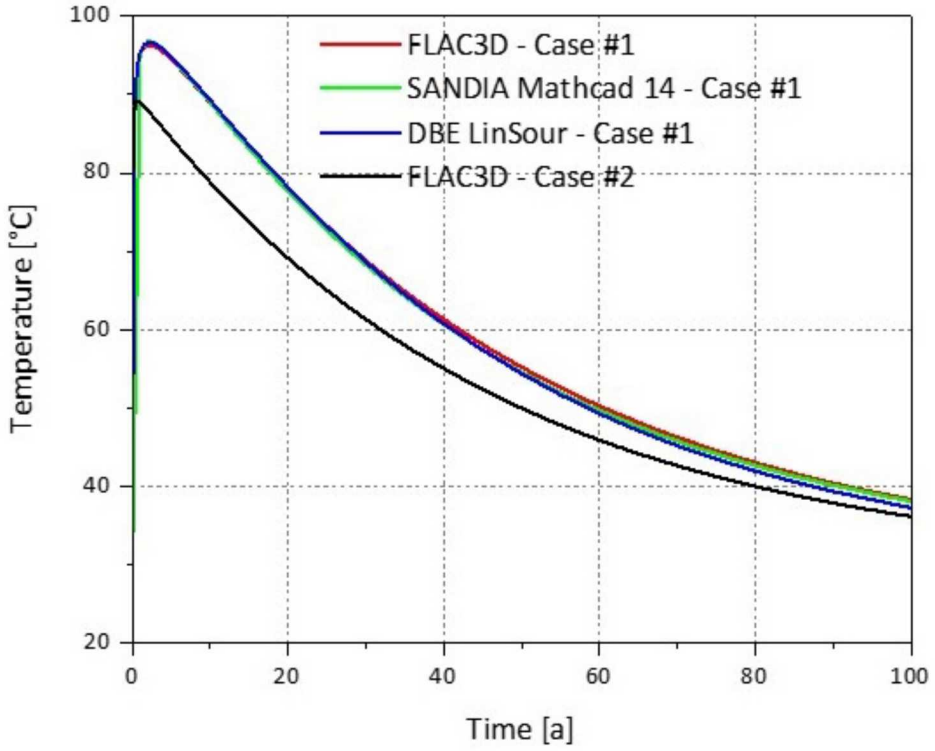

Figure 5-7. Waste package surface temperature-time comparison plots for Configuration 1

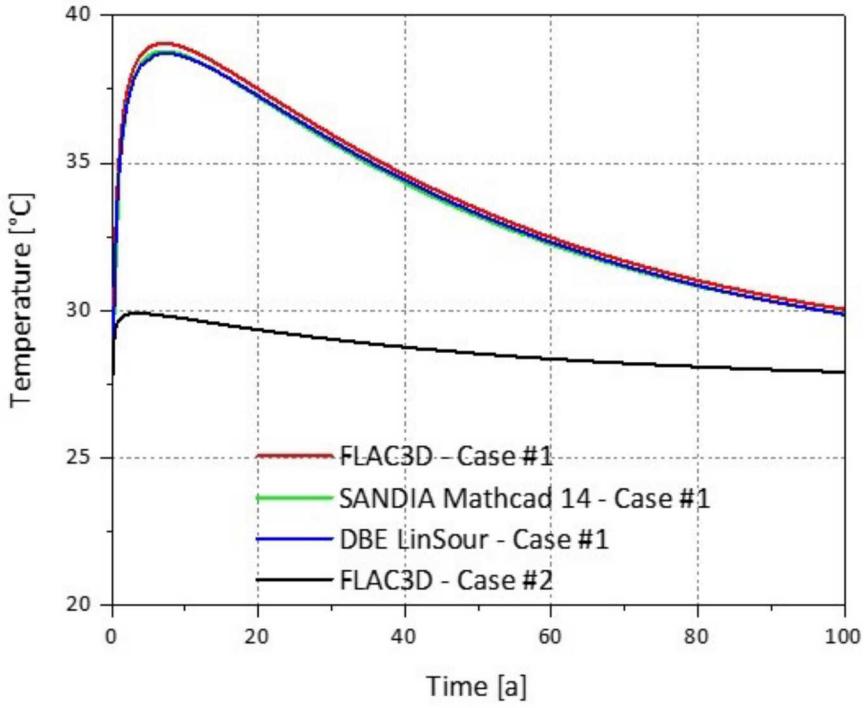

Figure 5-8. Drift wall temperature-time comparison plots for Configuration 1

A separate PFLOTRAN (Hammond et al., 2014) thermal simulation was also carried out at Sandia National Laboratories to provide additional analysis of a numerical method to supplement the Configuration 1 simulations using FLAC3D. For the PFLOTRAN simulations a cylindrical domain with a radius of about 1 km and an axial distance of 1.17 km was used, representing a waste package in an infinite medium. The domain was discretized using refined mesh of 124,800 grid blocks. Radial grid block size progressively increases from a radius of 0.03 m. The medium was represented with a constant thermal conductivity of 0.57 kW/m K (for both dry and wet thermal conductivity). A permeability of 10^{-25} m^2 and porosity of 10^{-4} were assigned to the rock to maintain thermal transport by conduction only. The waste package was represented with a radius of 0.305 m (diameter 0.61 m) and a length of 3.05 m. The heat source was applied to the entire waste package region and an observation point on the surface of the waste package was selected. Ambient temperature of 27.5 C was assigned as an initial condition. The simulation results are shown in Figure 5-9. The plots compare Mathcad based results with those of PFLOTRAN for waste package surface and drift wall temperatures versus time. The plots show that the semi-analytical results (Mathcad) closely match those of the numerical method (PFLOTRAN). Figure 5-10 shows PFLOTRAN results for temperature distribution after 10 years' simulation time.

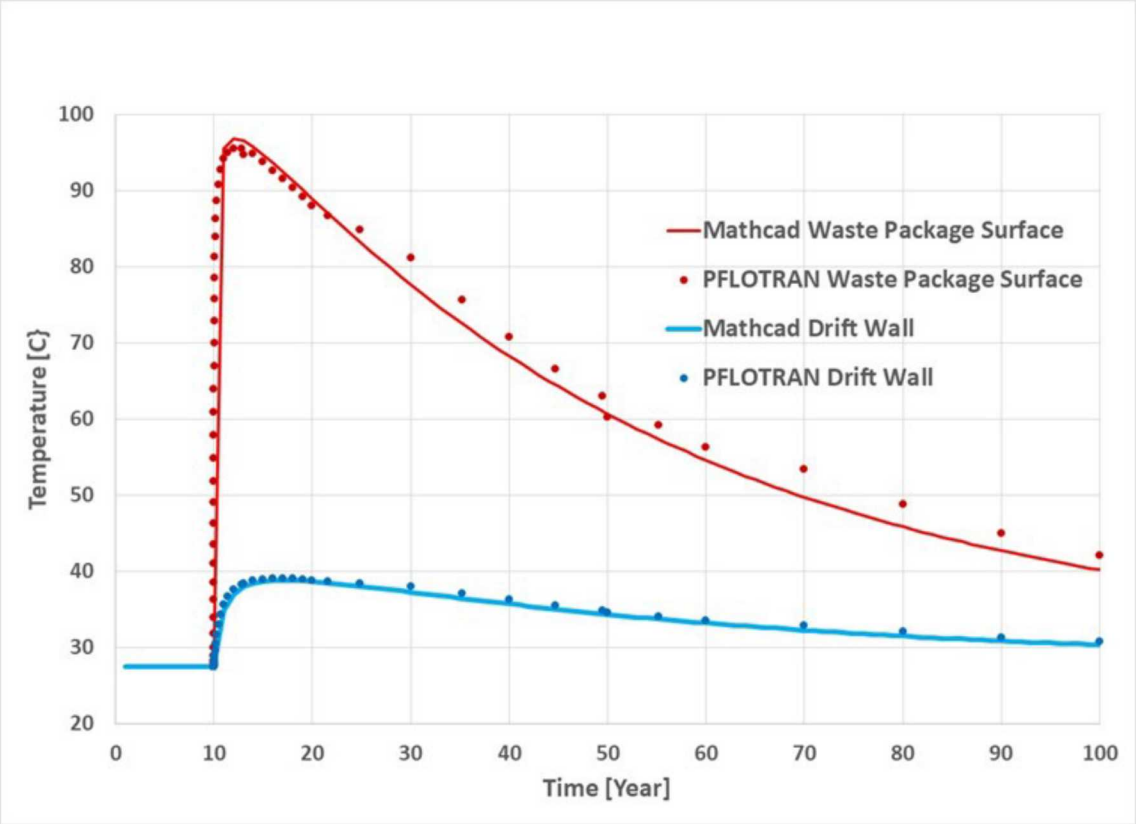

Figure 5-9. Waste package surface and drift wall temperature-time plots using Mathcad and PFLOTRAN for Configuration 1

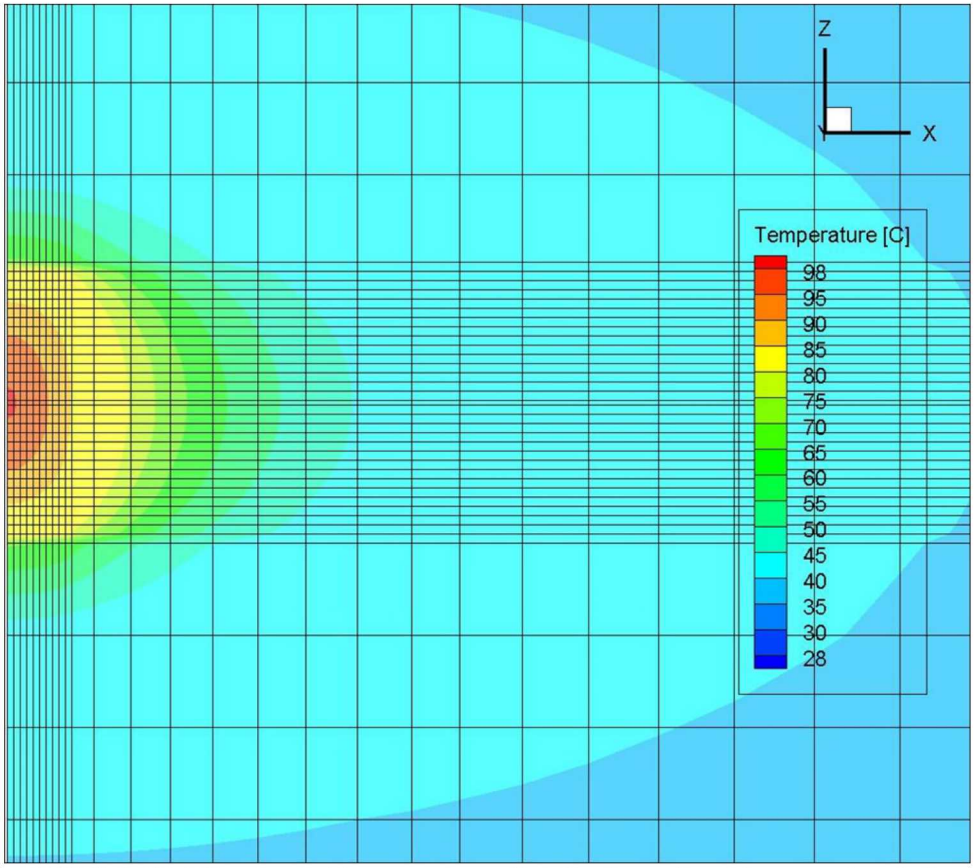

Figure 5-10. PFLOTRAN output: Temperature distribution after 10 years simulation time for Configuration 1

Figures 5-11 and 5-12 show results for Configuration 2. Configuration 2 is a representative repository layout with given drift and waste package spacing. The plots in Figures 5-11 and 5-12 represent the simulated temperature values at the monitoring points at the drift wall (left) and the waste package surface (right) over a simulation period of 100 years using parameters according to Case #1. The results of the numerical simulation with FLAC3D using corresponding properties for each material are also presented in Figures 5-7 and 5-8 for both configurations (Case #2). Note that semi-analytical codes can be considered as accurate when their results are comparable to those of the numerical code FLAC3D (i.e. Temperature vs. Time plots have overlay or nearly overlay at the observation points, see Figure 5-11 and Figure 5-12). Figures 5-11 and 5-12 show the temperature results at the observation points for Configuration 2 (which simulates multiple waste packages). Predictions of temperature with SANDIA Mathcad 14 and LinSour are almost identical to those of FLAC3D at the drift wall (48.6°C for Mathcad 14, 49.1°C for LinSour vs 48.9°C for FLAC3D) as well as at the waste package surface (98.4°C for Mathcad14, 98.4°C for LinSour vs 98.0°C for FLAC3D). Even after 100 years the predicted temperature decay predicted by the semi analytical codes compared to FLAC3D results remain small. One can conclude that both semi-analytical codes are able to calculate the thermal superposition of contributions of adjacent drifts and waste packages with accuracy.

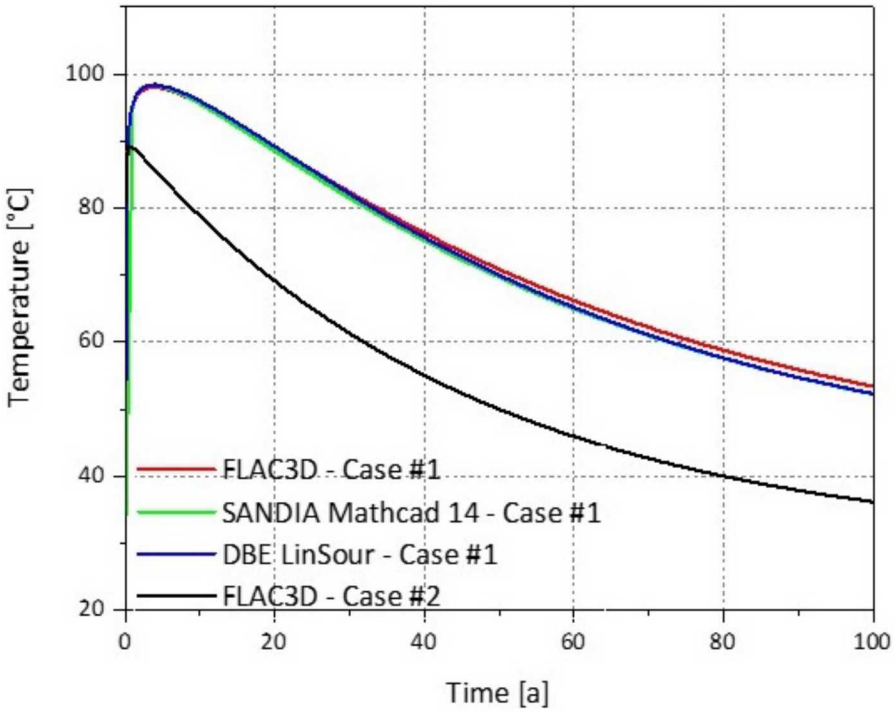

Figure 5-11. Waste package surface temperature-time comparison plots for Configuration 2

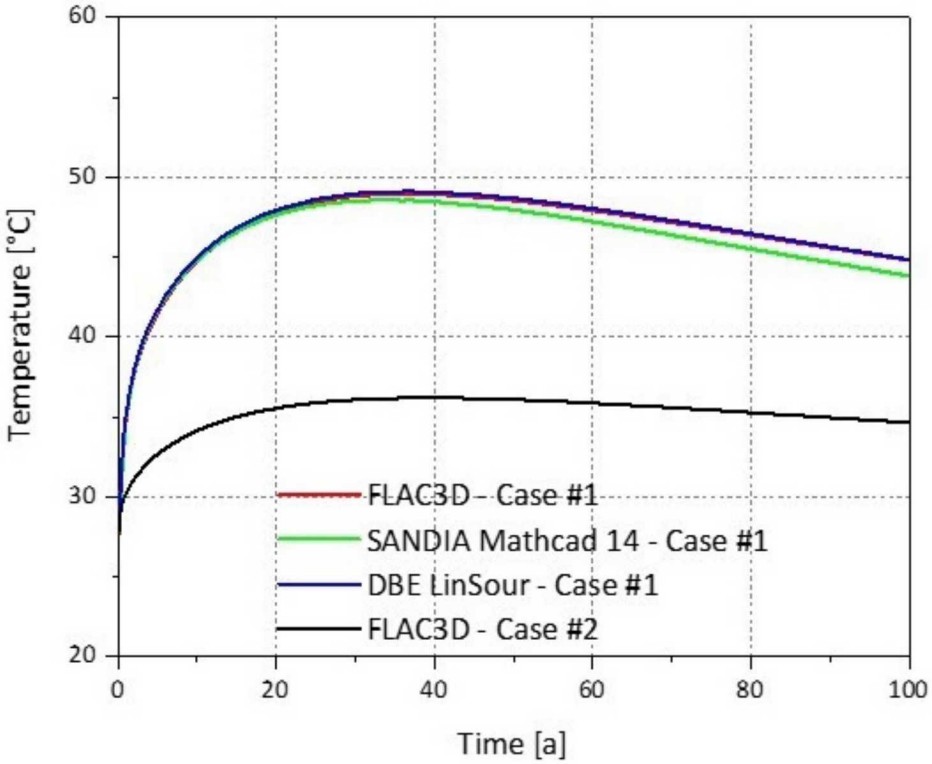

Figure 5-12. Drift wall temperature-time comparison plots for Configuration 2

As discussed above a separate second set of simulations were carried out with FLAC3D. In these simulations, realistic representative parameter values for each material were used (Table 5-1). This analysis was conducted to investigate the effect of the assumption of using the invariant material properties for all materials adopted in the base case. Results of the second separate numerical simulations show that the assumed constant parameter values in the analytical codes for Case #1 lead to an overestimation of the temperature at the drift wall and at the waste package surface for both configurations. According to the second FLAC3D simulations, maximum simulated temperatures at the drift wall and the waste package surface are 29.9°C and 89.9°C respectively, for Configuration 1. This means a discrepancy of around 10°C at the drift wall and 6°C at the waste package surface compared to the semi-analytical results of the base case. For Configuration 2, the discrepancy in drift wall temperature prediction is equal to 12°C when compared to SANDIA Mathcad 14, and almost 13°C compared to LinSour. At the waste package surface, one can measure a difference of 9°C when compared with both semi-analytical codes. These results show that choosing the same material parameter values as used in Case #1 would result in conservative results. Therefore, the thermal design of a repository using a semi-analytical code leads to conservative drift and waste package spacings. However, this approach allows use of simpler and quick simulations using semi-analytical codes to ensure that the temperature limit in rock salt is met.

The accuracy of the semi-analytical codes can be improved for the realistic case (Case #2) by performing a parameter calibration on a representative numerical model where nonlinear material behavior and geometrical heterogeneities are considered. This method is usually used for LinSour. The Mathcad 14 based code has the capability to model multiple materials and can consider non-constant material properties. This capability needs to be tested against a numerical code.

5.7 Conclusions for Semi-Analytical Code Comparison

The thermal analysis presents conduction-based thermal simulations for the emplacement of nuclear waste in a geological repository in bedded salt. Benchmark simulations were conducted to assess the validity of semi-analytical codes to perform thermal simulations. Two waste package configurations were analyzed with the same parameter values applied to all materials. The first configuration involves a single waste package emplaced in an infinite medium. The second configuration represents a repository layout with arrays of waste packages in different drifts. The investigation included use of the semi-analytical code LinSour used at DBE Technology in Germany, a Mathcad 14-based semi-analytical code used at Sandia National Laboratories, and the numerical code FLAC3D. These codes were used to calculate the temperature at the drift wall and waste package surface as a function of time for the two configurations. The results show that predictions of the three codes for Configurations 1 and 2 were comparable under identical initial and boundary conditions. A separate simulation was conducted with PFLOTRAN numerical code to test results of the Mathcad-based semi-analytical calculations for Configuration 1. The results of the separate simulation were also very close. Comparison of simulation results of the different software and simulation methods provided a confidence building measure for further analyses.

6. THERMAL ANALYSIS FOR DISPOSAL OF SPENT NUCLEAR FUEL IN ALLUVIUM HOST ROCK USING THE SEMI-ANALYTICAL METHOD

Thermal-only, semi-analytical analysis was conducted for the disposal of spent nuclear fuel in alluvium host rock. The simulations were conducted in support of the Generic Disposal System Analysis (GDSA). The simulations were designed to provide estimates of temperature at the surface of the waste package and the drift wall to help decide repository layout for performance assessment analysis. The semi-analytical method is based on the approach developed for enclosed emplacement modes by Hardin et al. (2011, 2012). Thermal responses for pressurized water reactor (PWR) waste forms were investigated for a disposal concept in generic alluvium host rock. The output of interest is temperature at the surface of the

waste package and at the drift wall. The analysis looked at effect of drift spacing, waste package spacing, backfill thermal conductivity, burnup, PWR assembly size, surface storage period.

6.1 Simulation input data

The repository was assumed to be at 250 m depth. Ambient average ground surface temperature of 25°C, and a natural geothermal gradient of 30°C/km were used. The disposal concept is based on waste packages emplaced individually horizontally, encapsulated in swelling clay-based buffer material. The selected geometry for the analysis includes a drift diameter of 5.5 m and a waste package diameter of 3.2 m with 5 m length. Thermal conductivity of the alluvium host rock was assumed to be 1.0 W/m-K Hardin et al. (2012). For the semi-analytical simulations, the buffer material is assumed to be initially dry and to remain so during the peak temperature period. For compacted, dry clay-based buffer material a thermal conductivity of 0.5 W/m-K (thermal diffusivity = 6.85 x 10^{-7} m^2/s) was assumed. In this study, a higher thermal conductivity of 1.5 W/m-K was used for sensitivity analysis.

For the semi-analytical simulations, the following variations were used:

- Backfill thermal conductivity used: 0.5, 1.5 W/m K
- Waste type: 21-PWR (40 GWd/MT burnup), 12-PWR (60 GWd/MT burnup)
- Waste package spacing and drift spacing combinations
    - 20 m work package spacing and 50 m drift spacing
    - 20 m work package spacing and 70 m drift spacing
    - 30 m work package spacing and 50 m drift spacing
    - 30 m work package spacing and 70 m drift spacing
    - 50 m work package spacing and 50 m drift spacing
- Surface storage period: 100, 150, 200 years

6.2 Results of semi-analytical thermal analysis

Semi-analytical Mathcad runs were conducted using the host rock and repository layout data, for the variations listed above. Results of the simulations are given below. Maximum waste package and drift wall temperature predictions are given in Table 1 to 4. Temperature history plots for the waste package surface and the drift wall for the various combinations of input are given in Figures 1 to 30.

Table 1 shows peak temperature results for 21 PWR (40 GWd/MT burnup) and backfill thermal conductivity of 0.5 W/m K for the various waste package spacing and drift spacing combinations and surface storage time. Peak temperatures for 100 years storage time average in the range of 230 - 240 C for the waste package surface and 110 – 125 C for the drift wall. Temperatures are lower for longer surface storage times. Table 2 shows results for the same waste type but using a backfill thermal conductivity of 1.5 W/m K. For this case,
maximum temperatures are reduced to an average of 150 – 160 C for the waste package for 100 years storage time.

Table 3 shows peak temperature results for 12 PWR (60 GWd/MT burnup) and backfill thermal conductivity of 0.5 W/m K. Peak temperatures for 100 years storage time average about 200 C for the waste package surface and 100 C for the drift wall. Temperatures are lower for longer surface storage times. Table 4 shows results for the same waste type but using a backfill thermal conductivity of 1.5 W/m K. For this case, maximum temperatures are reduced to an average of 130 – 140 C for the waste package

for 100 years storage time. Peak temperatures for the 12 PWR spent nuclear fuel are lower than those of the 21 PWR. The reduction in peak temperature would be even higher for 12 PWR with lower burnup rate. The peak temperature was not significantly affected by the combinations of waste package spacing and drift spacing selected. Drift wall temperatures were much lower than the waste package surface temperatures. The drift wall temperature is not a function of backfill thermal conductivity. Note that drift wall temperature predictions are conservative.

Table 6-1. Predicted maximum temperature at waste package surface and drift wall for 21 PWR (40 GWd/MT burnup) and backfill thermal conductivity of 0.5 W/m K.

WP Spacing, m	Drift Spacing, m	100 Years Storage		150 Years Storage		200 Years Storage	
		Twp max °C	Tdw max °C	Twp max °C	Tdw max °C	Twp max °C	Tdw max °C
30	50	230.94	115.30	173.28	100.26	149.41	94.09
20	50	236.62	131.31	180.39	119.29	159.60	111.81
50	50	230.16	110.61	171.87	89.35	146.58	81.84
20	70	236.41	123.56	178.72	104.90	154.53	97.95
30	70	230.93	113.64	173.09	93.08	148.38	85.88

Table 6-2. Predicted maximum temperature at waste package surface and drift wall for 21 PWR (40 GWd/MT burnup) and backfill thermal conductivity of 1.5 W/m K.

WP Spacing, m	Drift Spacing, m	100 Years Storage		150 Years Storage		200 Years Storage	
		Twp max °C	Tdw max °C	Twp max °C	Tdw max °C	Twp max °C	Tdw max °C
30	50	151.97	115.30	120.59	100.26	109.72	94.09
20	50	161.53	131.31	135.40	119.29	125.57	111.81
50	50	149.86	110.61	116.00	89.35	101.89	81.84
20	70	159.53	123.56	126.63	104.90	114.55	97.95
30	70	151.70	113.64	118.41	93.08	104.86	85.88

Table 6-3. Predicted maximum temperature at waste package surface and drift wall for 12 PWR (60 GWd/MT burnup) and backfill thermal conductivity of 0.5 W/m K.

WP Spacing, m	Drift Spacing, m	100 Years Storage		150 Years Storage		200 Years Storage	
		Twp max °C	Tdw max °C	Twp max °C	Tdw max °C	Twp max °C	Tdw max °C
30	50	198.14	100.68	144.65	82.53	120.18	75.84
20	50	202.40	111.67	149.25	94.87	126.24	87.90
50	50	197.62	97.46	143.84	77.28	118.73	68.66
20	70	202.30	107.51	148.62	86.79	123.91	78.87
30	70	198.13	99.76	144.59	79.64	119.82	71.21

Table 6-4. Predicted maximum temperature at waste package surface and drift wall for 12 PWR (60 GWd/MT burnup) and backfill thermal conductivity of 1.5 W/m K.

WP Spacing, m	Drift Spacing, m	100 Years Storage		150 Years Storage		200 Years Storage	
		Twp max °C	Tdw max °C	Twp max °C	Tdw max °C	Twp max °C	Tdw max °C
30	50	131.82	100.68	101.35	82.53	88.70	75.84
20	50	138.98	111.67	109.45	94.87	98.40	87.90
50	50	130.34	97.46	98.99	77.28	84.53	68.66
20	70	137.84	107.51	106.14	86.79	92.47	78.87

30	70	131.67	99.76	100.66	79.64	86.42	71.21

Figure A-1 to Figure A-30 (Appendix A) show waste package surface and drift wall temperature history results for disposal in alluvium. Figures 1 to 10 are for storage time of 100 years. Figures A-1 and A-2 show temperature plots for all the various combinations of drift spacing and waste package spacing and the two buffer thermal conductivity values. In Figures A-3 to A-8 the plots are divided along thermal power and buffer thermal conductivity. Figures A-11 to A-20 are results for storage time of 150 years. Figures A-21 to A-30 are results for surface storage time of 200 years. For all cases the plots show that temperatures significantly drop after the peak is reached due to thermal decay. As also shown in Tables 6-1 to 6-4, the peak temperatures are reduced with lower thermal output, higher buffer thermal conductivity and longer surface storage time. Overall, thermal limits and other considerations for disposal in alluvium would help decide the repository layout.

7. THERMAL-HYDROLOGY MODELING FOR DISPOSAL OF SPENT NUCLEAR FUEL IN CRYSTALLINE HOST ROCK

This work is a continuation of the numerical modeling of thermal-hydrology for the disposal of DOE managed DHLW and DSNF waste in crystalline medium, documented in the 2016 milestone report (Matteo, et al., 2016). The current work concentrates on thermal-hydrology modeling for the disposal of spent nuclear fuel, mainly from civilian nuclear power stations. The analysis is designed to estimate thermal distribution in the near field due to the disposal of higher output nuclear waste. This modeling exercise is a preliminary analysis of two-phase flow in the near field with possible evaporation in hotter areas and condensation in cooler areas. In this analysis the fractured crystalline host rock is represented as a homogenous system with a single average permeability. Future work will include fracture characterization of the host rock.

This simulation study closely follows the PA analysis conducted by Mariner et al. (2017) and thus uses similar properties and parameter values to represent the waste and the host rock. As in the PA analysis the spent fuel used in this study is 12 PWR, 60 GWd/MTHM burn-up. The waste is assumed to be 100 years out of reactor (surface storage time). The resulting power output is shown in Figure 7-1.

7.1 Model Setup

As was previously done in the FY16 analysis (Matteo, et al., 2016), the modeling domain includes only a portion of the repository shown in Figure 7-2. Selection of the smaller part of the domain allows detailed thermal analysis with a refined mesh. Symmetry conditions on three faces of the domain allow a reduced computation burden. The geometry of the domain used in the current study is 180 m x 1073 m x 1088.5 m, in the x, y and z directions, extending into the host rock in the y-direction and to the surface in the vertical direction. The mesh detailed in Figure 7-3 to 7-5, includes a grid with extensive refinement near drifts and waste packages. The mesh size is 667,480 grid blocks. The selected domain contains 9 drifts with 9 waste packages in each drift. The drift diameter is 4.5 m with 2 m Disturbed Rock Zone (DRZ) surrounding the drifts. Each waste package is surrounded by buffer material. The domain includes a 10.5 m wide access drift. Representations of these details are shown in Figures 7-6 to 7-8.

The TOUGH suite of codes utilizes several grid generation tools. For the current work, a few of the meshing tools have been explored. An executable of WINGRIDDER 3.0 (Pan, 2007), a Windows based software, was obtained from LBNL and tested. The software gives run time errors when used on Windows 10. The software was developed using Visual Basic and may need to be re-compiled using a current version of Windows. FLAC3D is also used to generate a mesh that is exported for conversion to TOUGH2 mesh using

Matlab scripts. The scripts are available from LBNL. This option was tested by the team for the current study. The FLAC3D software was obtained for a limited time and test cases conducted. The testing has not been completed due to time limitations. Further testing is needed to evaluate the use of this method. This option is widely used by users of the TOUGH suite of codes and thus maybe the option of choice. It may also be possible to convert a CUBIT mesh to the TOUGH3 format. This option is desirable as codes such as TOUGH3 and PFLOTRAN could share the same mesh. This option has not been pursued at this time.

The TOUGH suite of codes includes Meshmaker, an internal grid generation tool. The mesh generator is used for a regular mesh in cartesian coordinates and for radial mesh generation. This option was used for the current study.

The Meshmaker mesh generator was used to generate a 3-D cartesian mesh for use in this study. A script was written to assign materials to each grid block. The script was also used to assign a large volume and a small grid block distance to the top layer that represents the surface. The large volume allows setting a boundary condition at the top. The outputs of Meshmaker and the scripts were then exported to the TOUGH3 (Jung et al., 2018) cards ELEME and CONNE. A script was also used to generate approximate hydrostatic initial conditions.

Base case material properties are as shown in Table 7-1, and the rest of the input parameters are given below. Center-to-center waste package spacing was assumed to be 10.0 m. This gives an end-to-end spacing of 5 m. In addition to the base case values, materials properties were varied to study the impact on thermal distribution. Initial conditions include hydrostatic pressure conditions and a geothermal gradient of 25°C /km for a repository at 500 m depth from the surface. The boundary condition includes ambient conditions at the top of the domain representing the surface (10°C and 1 atm.), and a constant temperature of 35°C and no flux conditions at the bottom of the domain. The boundary conditions also include no fluid or heat fluxes on the sides. For the simulations the TOUGH3 numerical code (Jung et al., 2018) was used.

Drift diameter: 4.5 m
Drift spacing: 20 m
Waste package diameter: 1.46 m
Waste package length: 5.0 m
Waste package spacing: 10. m
Surface storage time:100 years
Buffer dry/wet thermal conductivity – 0.6/0.85 (base case), 2.0/2.0 W/m-K

Table 7-1. Base case material properties

Material	Permeability m^2	Porosity	Thermal conductivity Wet W/mK	Thermal conductivity Dry W/mK	Heat capacity W/mK	Rock grain density kg/m^3
Granite rock	1×10^{-18}	**0.01**	**2.5**	**2.5**	**830**	**2700**
DRZ	1×10^{-16}	**0.01**	**2.5**	**2.5**	**830**	**2700**
Buffer	1×10^{-19}	**0.35**	**0.85**	**0.6**	**830**	**2700**
WP	1×10^{-16}	**0.5**	**46**	**46**	**466**	**2700**

For this study, the van Genuchten characteristic curves were selected representing relative permeability and capillary pressure. The parameters used were:

$\lambda = 0.9$, $S_{lr} = 0.01$, $S_{ls} = 1$, $S_{gr} = 0.01$, $1/P_0 = 1.02 \times 10^{-5}\ Pa^{-1}$, $P_{max} = 5 \times 10^{8}$ Pa

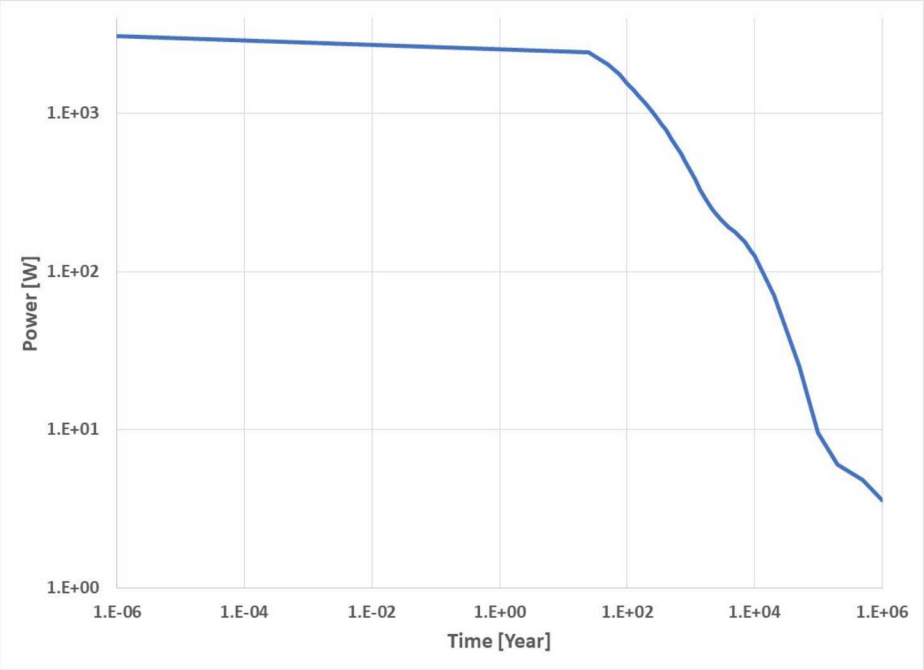

Figure 7-1. Thermal output for 12 PWR waste package with 60 GWd/MTHM burn-up. The decay curve represents 100 years' surface storage time.

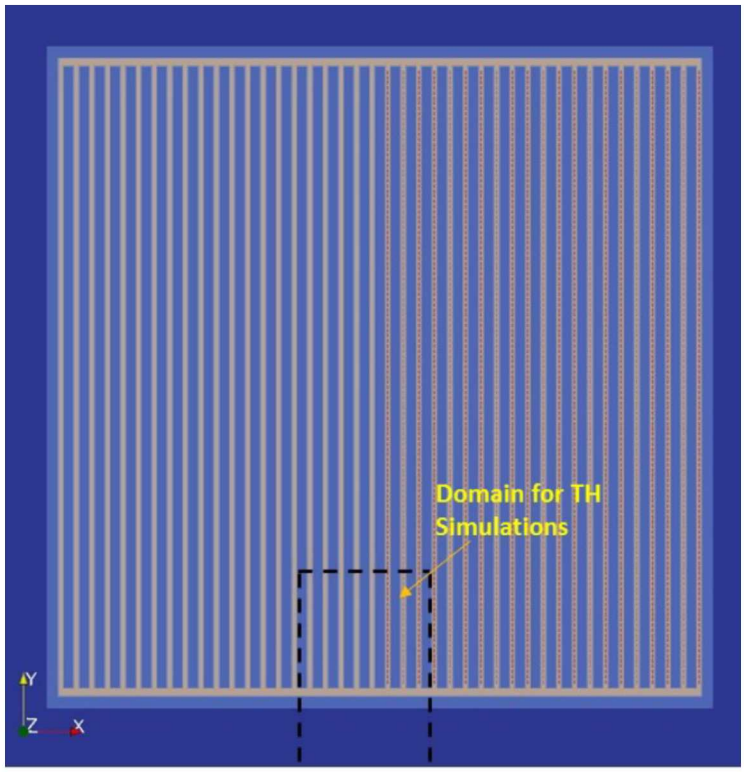

Figure 7-2. Surface layout for disposal in crystalline medium (Stein et al., 2016). The dotted lines represent cross-section of domain used for simulations in this study.

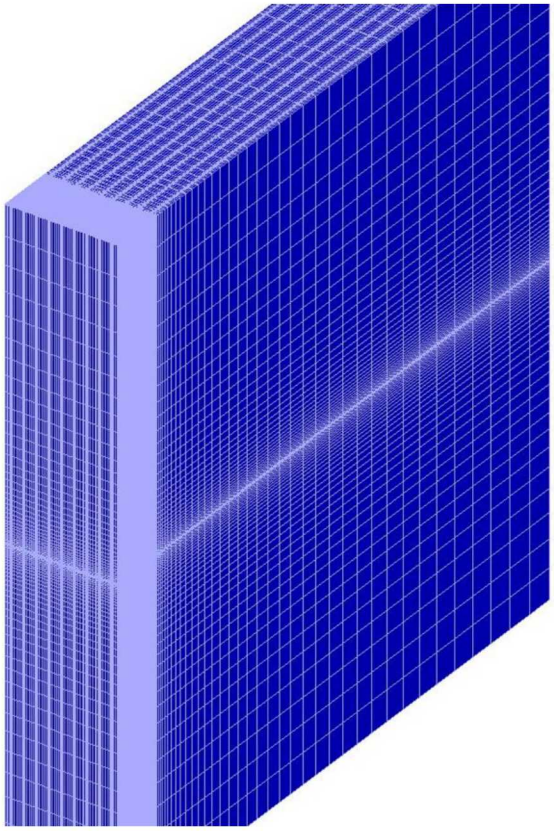

Figure 7-3. Representation of the computational mesh.

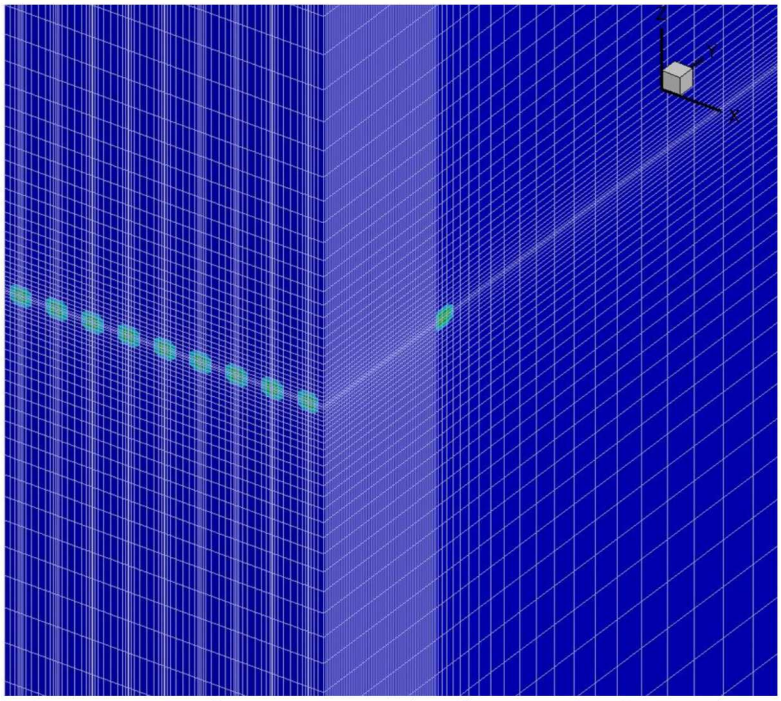

Figure 7-4. A closer look of the mesh showing fine meshing in the disposal region.

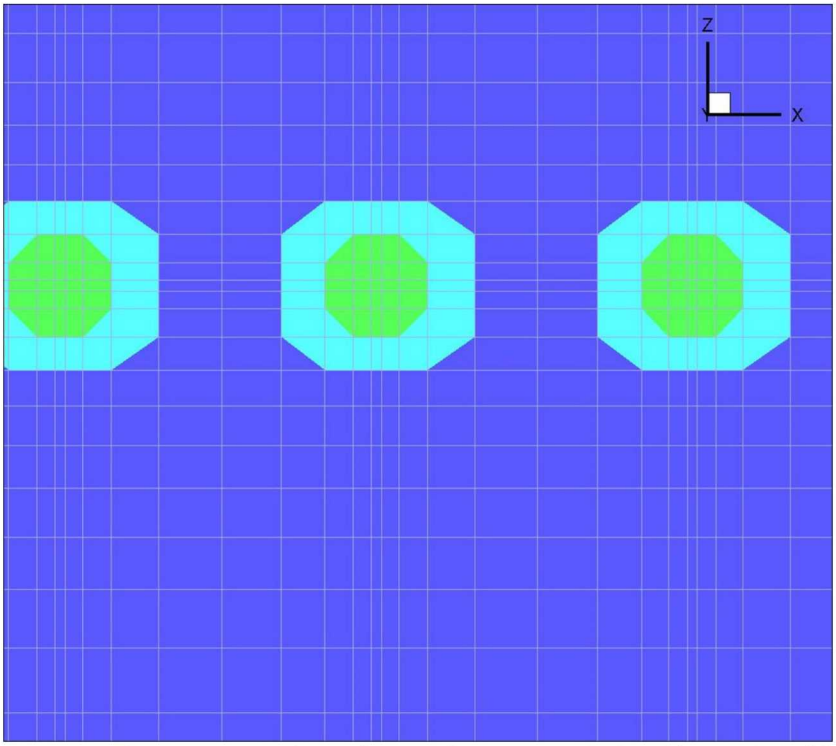

Figure 7-5. Representation of meshing around the disposal drifts.

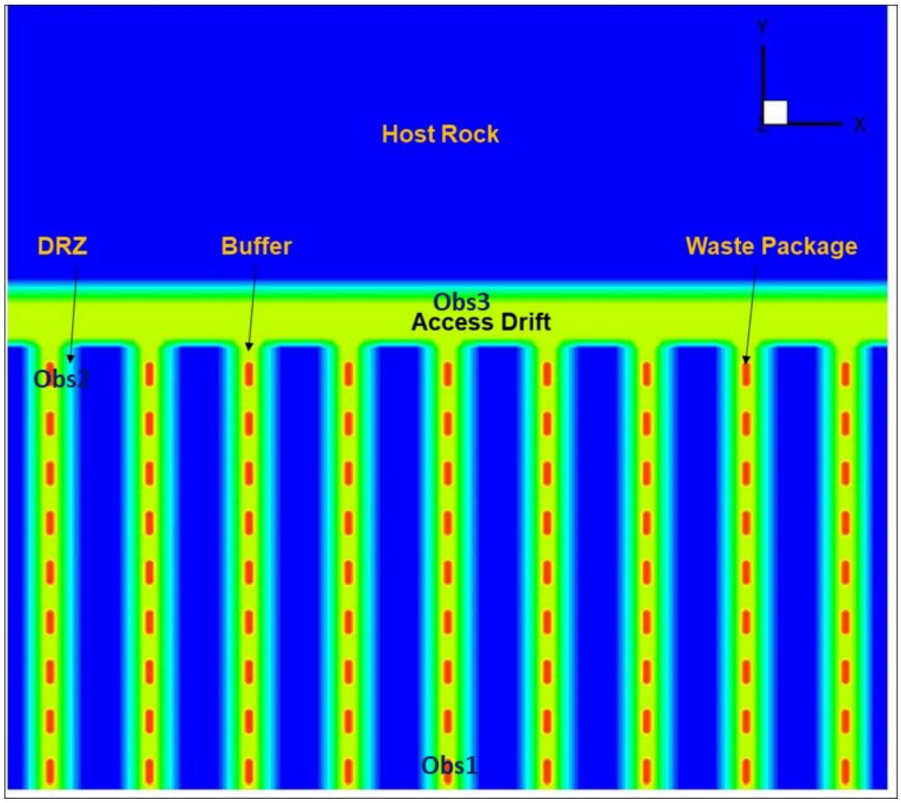

Figure 7-6. Representation of a horizontal slice at the repository level with locations of materials.

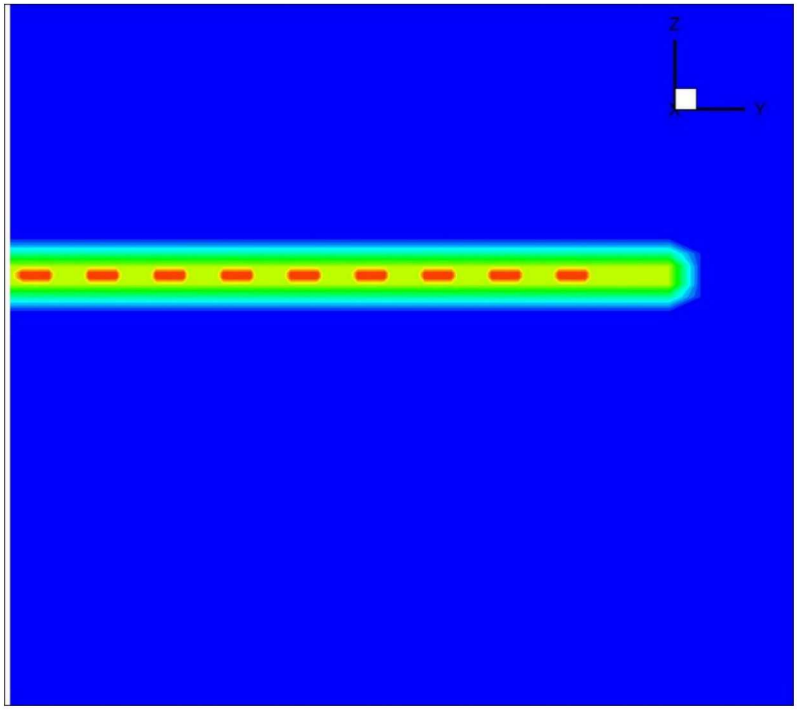

Figure 7-7. Representation of a vertical slice (x-axis) at the repository level with locations of materials.

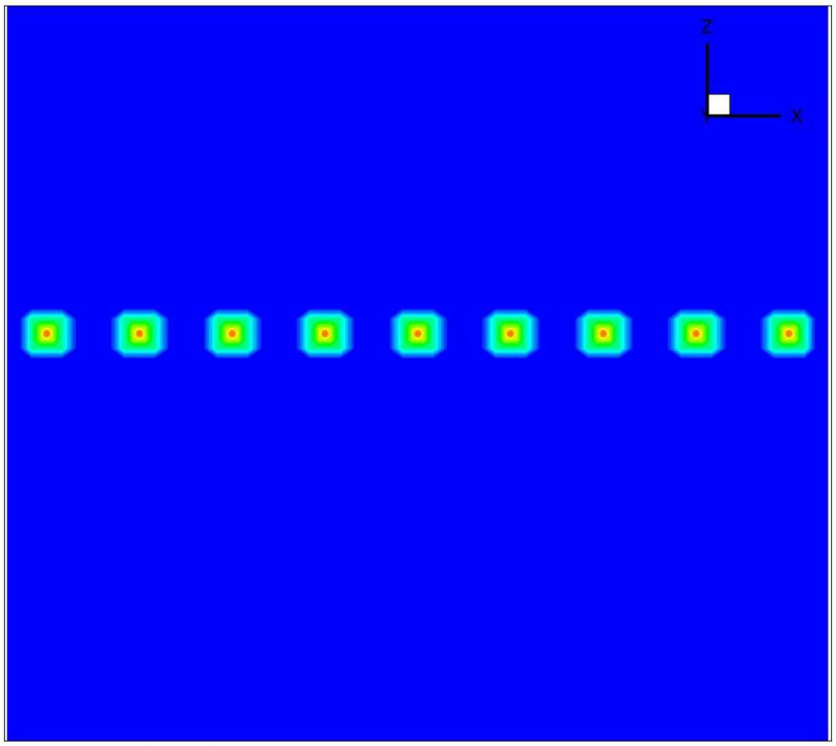

Figure 7-8. Representation of a vertical slice (y-axis) at the repository level with locations of materials.

7.2 Results and Discussion

Thermal-hydrology simulations were conducted using TOUGH3. A base case simulation was conducted using base case material properties shown in Table 7-1. An initial condition run was carried out to generate hydrostatic conditions. For this run the system was assumed to be under saturated conditions with no thermal input. For the thermal simulations, the output of the initial condition run was used as input. In addition, the following changes were made in the TOUGH3 input files:

- Thermal power was applied to each grid block representing the waste package
- The DRZ, buffer and waste package were assigned atmospheric pressure and gas saturation of 0.2
- Three observation points were selected (Figure 6):
    - Obs1: Grid block Ab241 (on central waste package)
    - Obs2: Grid block Cc805 (on waste package near the edge)
    - Obs3: Grid block CdE41 (on access drift)

The results for the base case are given on Figures 7-9 to 7-14. Figures 7-9 to 7-11 show temperature, pressure and gas saturation distribution after 10 years of simulation time, respectively. Because of the high power output of 12 PWR waste packages, even after 100 years of surface storage, and the low buffer thermal conductivity temperatures reach 200 ºC after 10 years of simulation. Gas saturation has increased around the waste packages.

Figures 12 to 14 show temperature time plots for the observation point at the central waste package (Obs1). Comparing the temperature profiles of the two waste packages on Figure 7-12 shows the edge effect. The waste package at the edge has lower temperatures because of its proximity to the access drift and the host rock. Temperatures in the access drift show a slow rise. Figure 7-14 shows the corresponding plots for gas saturation. The gas saturation at the waste packages increases rapidly to full saturation. However, gas saturation decreases in the access drift due to liquid water flow from the host rock driven by the pressure difference (hydrostatic vs 1 atm.).

The current study also includes preliminary sensitivity analysis. For the study the thermal conductivity of the buffer was increased to 2.0 W/m-K. A separate study was also conducted by applying heat in the central waste package only (Grid block Ab241). No heat was assigned to the rest of the waste packages. These two variations were made to quantify the effect of buffer thermal conductivity and thermal effects of neighboring waste packages. The results of the simulation are shown in Figures 7-15 to 7-17. As expected, Figure 7-15 shows considerable decrease in temperature as a result of the higher buffer thermal conductivity. The figure also shows decreased temperatures for the single waste package disposal highlighting the contributions of adjacent waste packages. These changes also affect pressure profiles, as shown in Figure 7-16. Figure 7-17 shows the gas saturation gas saturation profiles. For the single waste package case the gas saturation plot is the same as the base case. This maybe because the changes in temperature are not great enough to affect gas saturation. But the reduced temperature for the higher buffer thermal conductivity case has resulted in lower gas saturation.

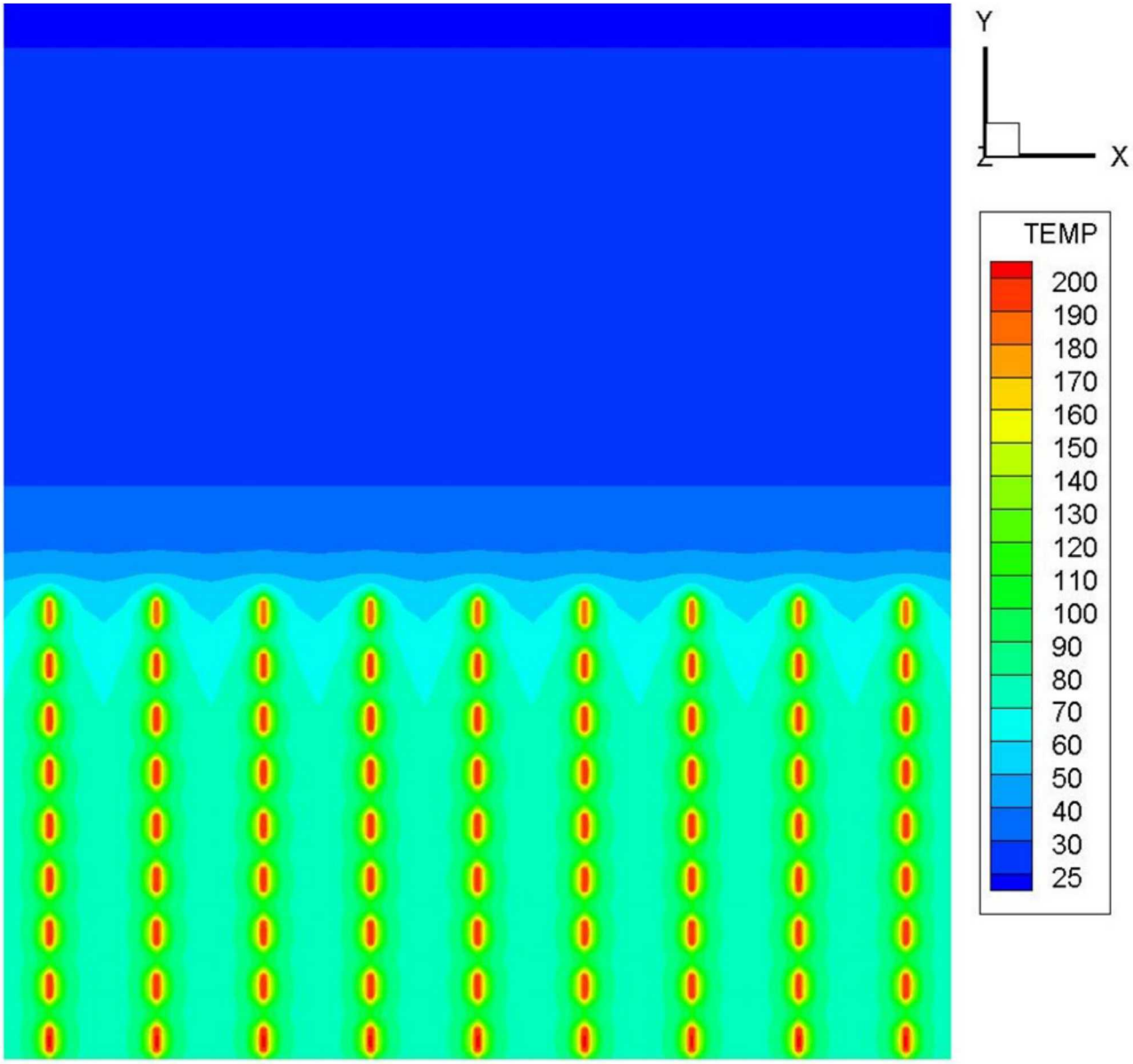

Figure 7-9. Distribution of temperature after 10 years of simulation time for the base case. Figure shows a horizontal slice (z-axis) at the repository.

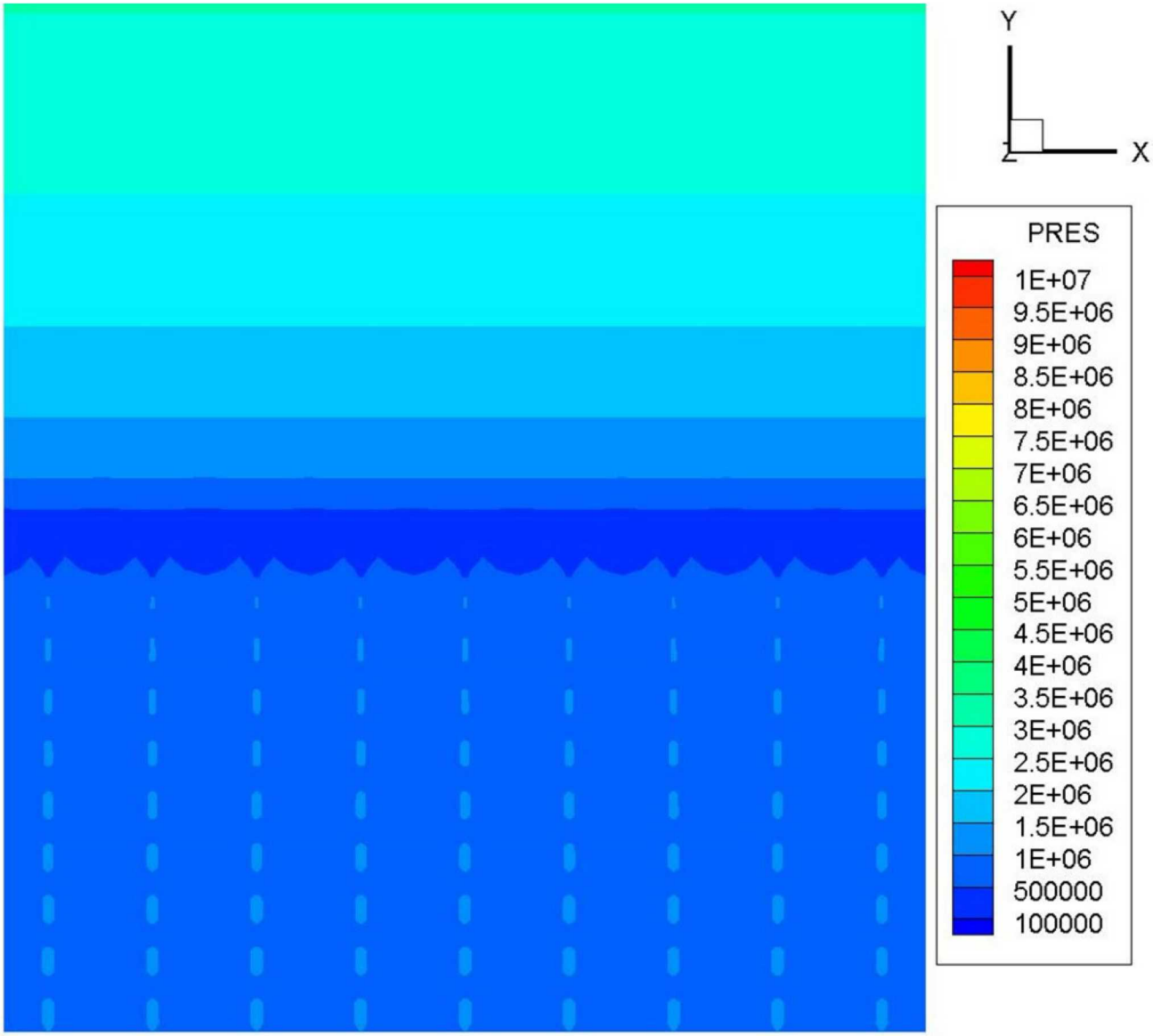

Figure 7-10. Distribution of pressure after 10 years of simulation time for the base case. The figure shows a horizontal slice (z-axis) at the repository.

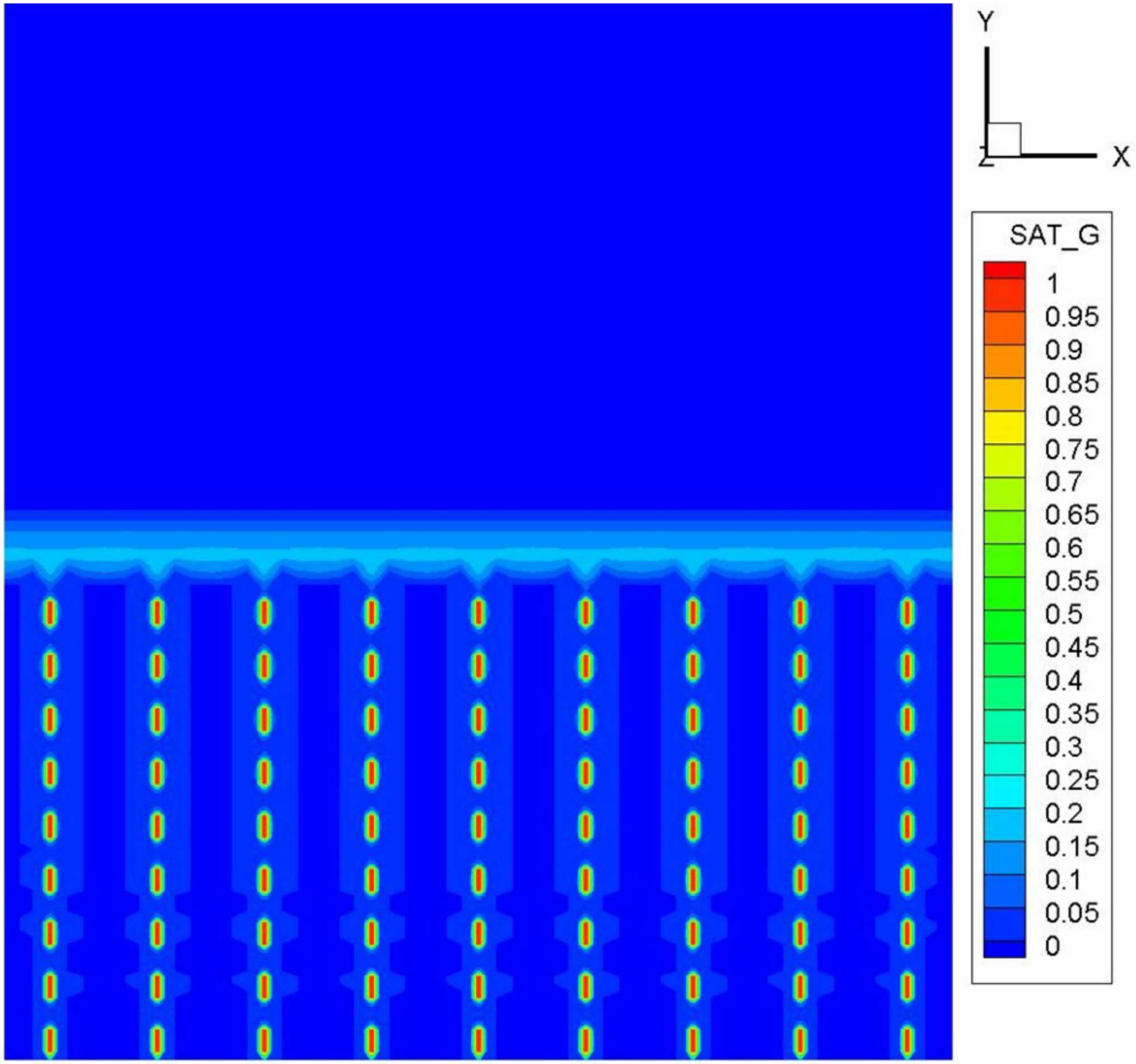

Figure 7-11. Distribution of gas saturation after 10 years of simulation time for the base case. This figure shows a horizontal slice (z-axis) at the repository.

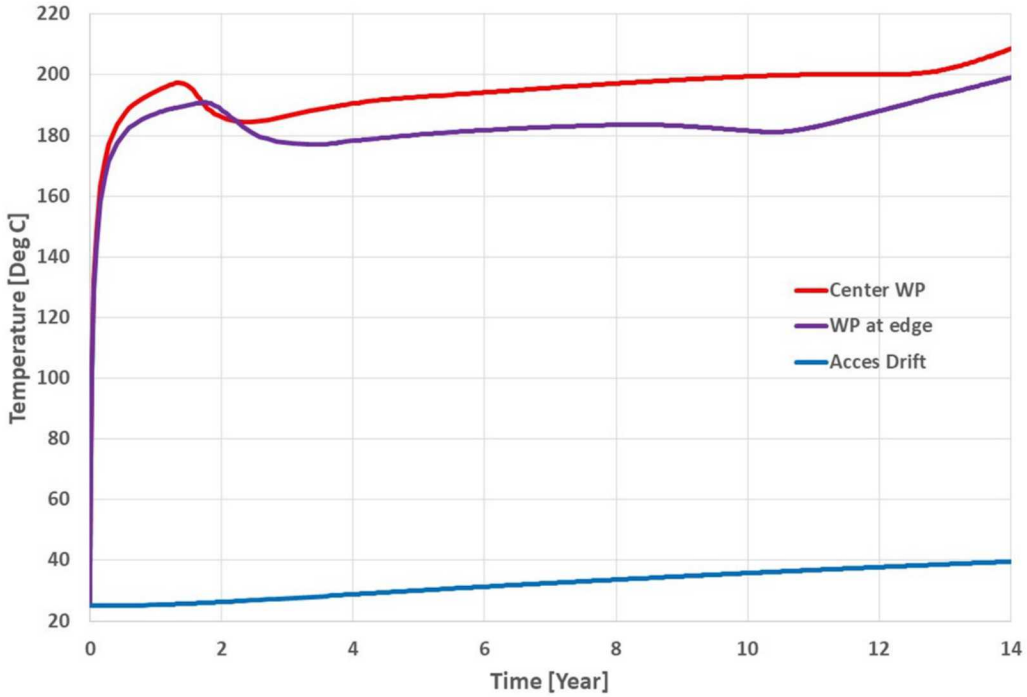

Figure 7-12. Temperature vs time plot for the base case at different observation point locations.

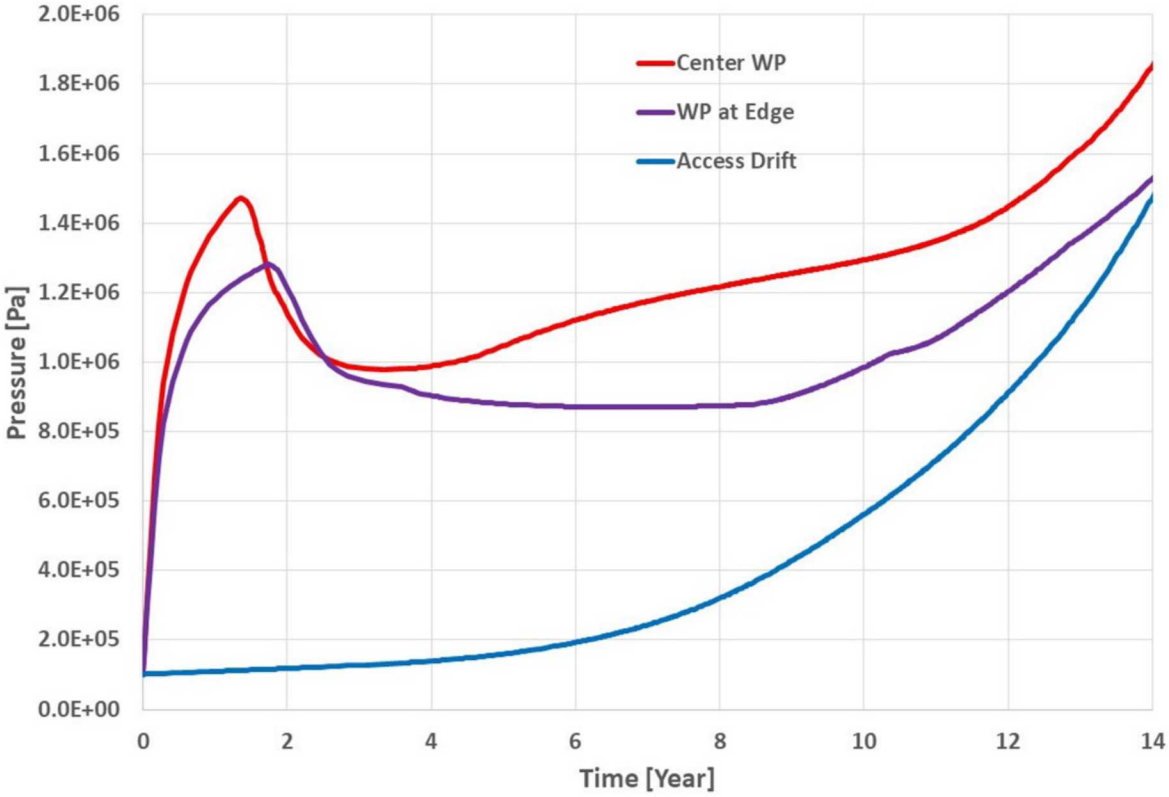

Figure 7-13. Pressure vs time plot for the base case at different observation point locations.

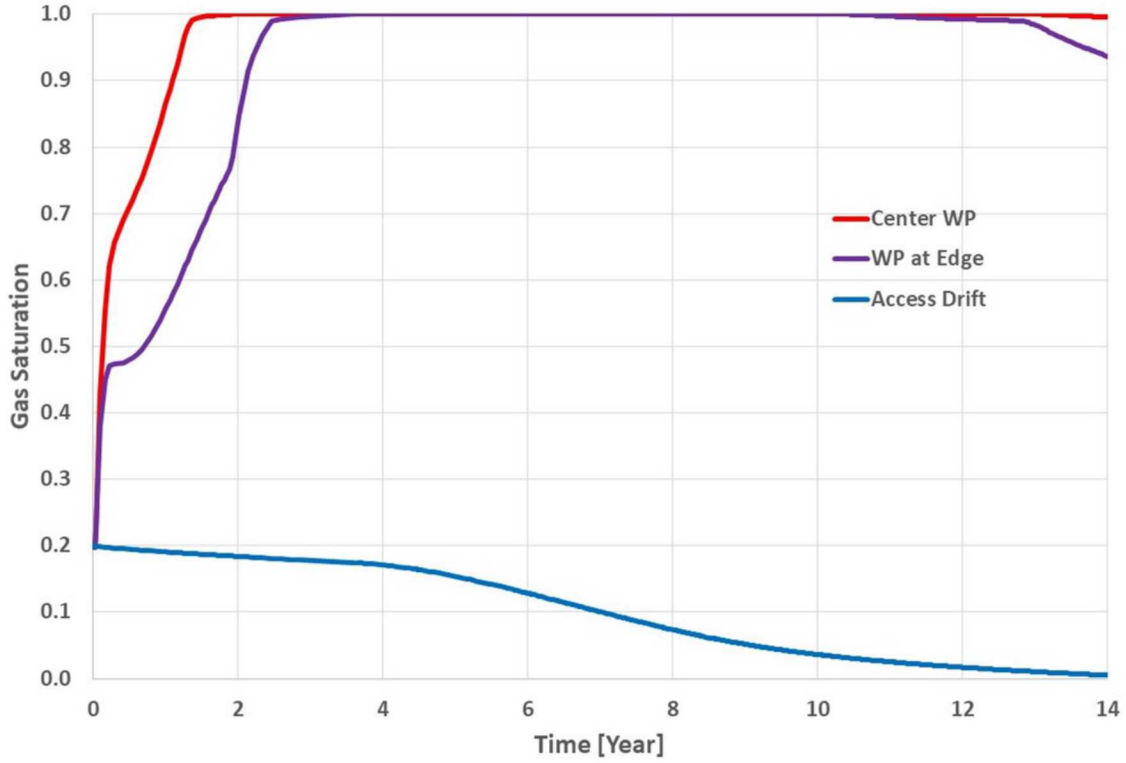

Figure 7-14. Gas saturation vs time plot for the base case at different observation point locations.

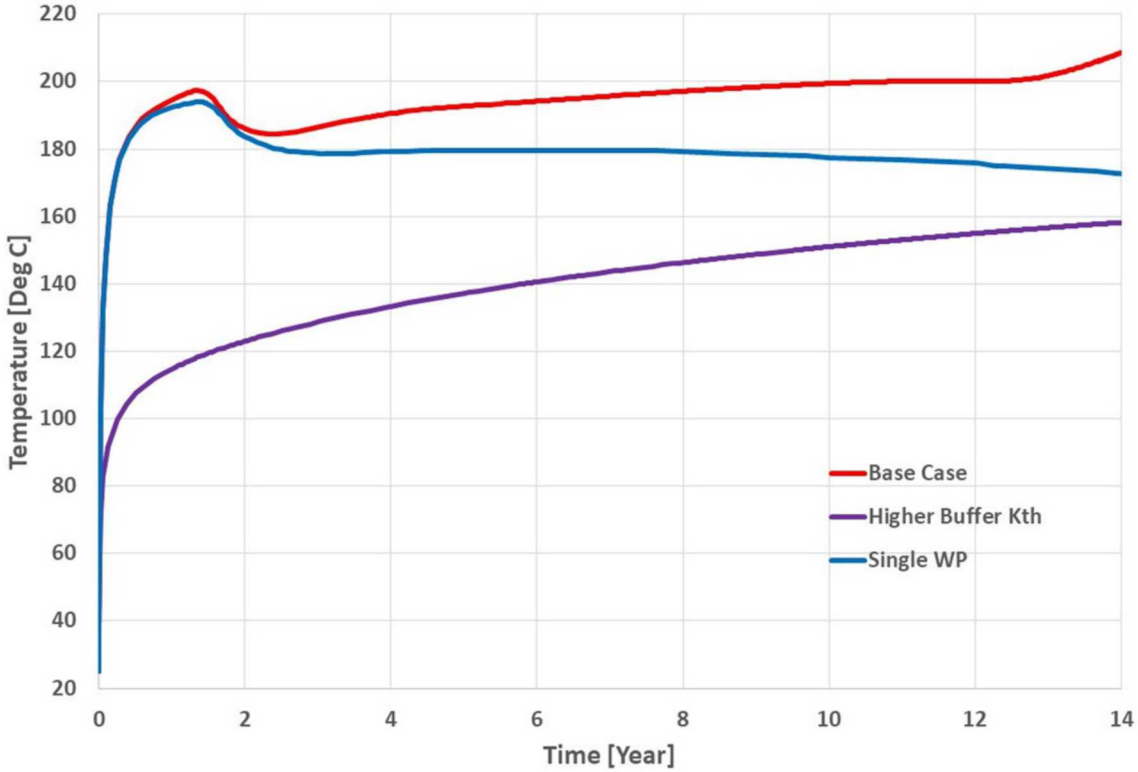

Figure 7-15. Temperature vs time plot for the center waste package for different cases.

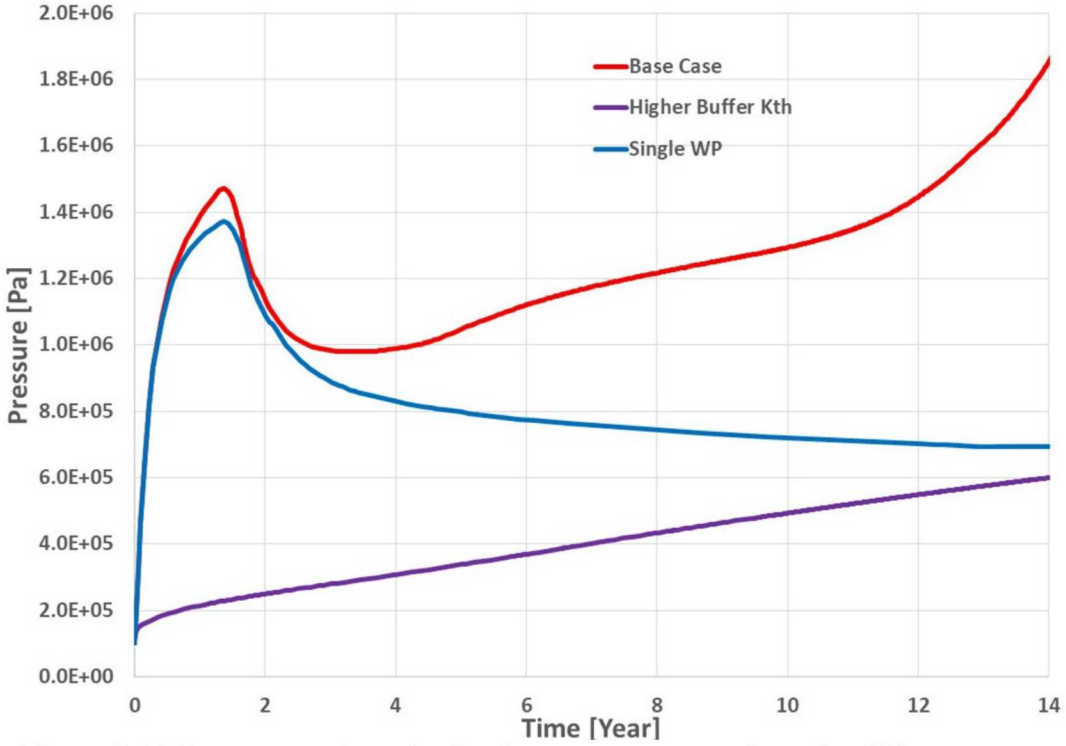

Figure 7-16. Pressure vs time plot for the center waste package for different cases.

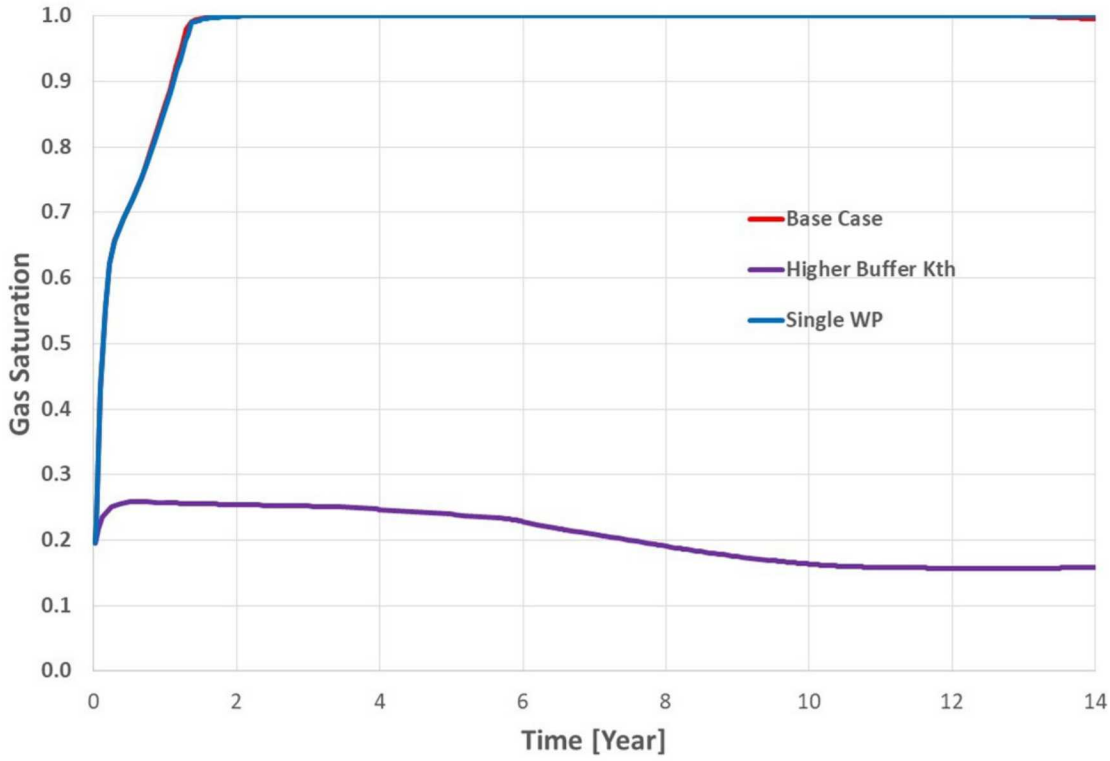

Figure 7-17. Gas saturation vs time plot for the center waste package for different cases.

7.3 Summary

A preliminary numerical thermal analysis was performed for disposal of 12PWR SNF waste packages in a generic repository in crystalline host rock. For the simulations the numerical code TOUGH3 was used. The study was designed to investigate thermal behaviors due to the disposal of SNF waste with higher thermal power and related vapor migration. TOUGH3 simulations were carried out for base case material properties. A limited sensitivity analyses were also conducted that investigated the effects of buffer thermal conductivity and contributions of adjacent waste packages to thermal effects.

The simulations provided a venue for testing TOUGH3, the newest version, and various meshing tools. The results of the base case simulations showed that very high peak temperatures can be expected with the disposal of SNF. As the sensitivity analysis showed, use of buffer materials with higher thermal conductivity could reduce peak temperatures to the design level. Other parameters such as longer surface storage, optimum repository foot print and thermal loading considerations would also lower peak temperatures.

Future work will include running of simulations for longer simulation time, varying homogenous permeability and surface storage time, include fracture characterization of the host rock, and use of different waste types.

8. EXPERIMENTAL INVESTIGATIONS ON BENTONITE AND OTHER CLAY-BASED BUFFER MATERIALS

8.1 Introduction and Research Motivation

Uranium (U) contamination in the subsurface is a part of the legacy of nuclear weapons and energy production, resulting from mining and milling activities, processing of nuclear materials, and nuclear waste disposal. The U.S. Department of Energy (DOE) is tasked with cleaning up U-contaminated aquifers at a number of sites, including the Uranium Mill Tailings Remedial Action (UMTRA) sites and the Savannah River, Oak Ridge, and Hanford sites where a variety of different radionuclides are present.

One of currently considered geological media for nuclear waste repositories is clay formations (*i.e.*, bentonite or shale), which can serve as engineered barriers or as the host rock for geologic storage (Altmann, 2008; Altmann et al., 2012; Delay et al., 2007; Guyonnet et al., 2009; SKB, 2011; Tournassat et al., 2015). Clays are supposed to be good barriers for HLW due to their low hydraulic conductivity, which restricts diffusion-based contaminant transport, and their high adsorption capacity for contaminants, which slows transport even further. Montmorillonite, a smectite mineral, is the dominant clay mineral found in bentonite. It has a 2:1 layer-type phyllosilicate structure, with a large specific surface area (~750 m^2/g) and cation exchange capacity (~1 mol_c/kg).

Uranium can exist in both the tetravalent and hexavalent oxidation state, however, due to the limited solubility of U(IV), U(VI) is the most common oxidation state found in the dissolved phase. U(VI) adsorption varies as a function of pH, bicarbonate, and Ca concentrations due to changes in U(VI) aqueous speciation. At moderate bicarbonate concentrations (> 1 mM) above pH 7, U(VI) speciation is dominated by uranyl-carbonato complexes [$UO_2CO_3(aq)$, $UO_2(CO_3)_2^{2-}$, $UO_2(CO_3)_3^{4-}$] in the absence of Ca, and calcium-uranyl-carbonato ternary complexes [$Ca_2UO_2(CO_3)3(aq)$, $CaUO_2(CO_3)_3^{2-}$] in the presence of typical groundwater Ca concentrations (> 1 mM) (Dong and Brooks, 2006; Fox et al., 2006; Guillaumont et al., 2003). These calcium-uranyl-carbonato complexes adsorb weakly or not at all to mineral surfaces, and thus changes in U(VI) speciation have a large impact on its sorption behavior and transport (Fox et al., 2012; Fox et al., 2006; Stewart et al., 2010). While U(VI) adsorption to purified Na-montmorillonite has been studied extensively over a range of chemical conditions (Marques Fernandes et al., 2012; Pabalan and Turner, 1996; Tournassat et al., 2018; Turner et al., 1996), the presence of mineral impurities and non-sodium forms of montmorillonite complicates U(VI) adsorption behavior and warrants further study.

Storage of HLW can result in high temperatures near the waste canisters resulting from radioactive decay. The effects of elevated temperature on the engineered barrier must be taken into account when designing a nuclear waste repository. Such effects may include changes in the hydrological and mechanical properties of clay, changes in pore water chemical compositions, and changes in the clay and accessory mineral composition (Cuadros and Linares, 1996; Wersin et al., 2007; Zheng et al., 2015). The conversion of montmorillonite to illite, known as illitization, is one of the primary mineralogical changes expected to occur during long-term exposure to high temperatures. Zheng et al. (2015) predicted the extent of illitization over a 1000 year simulation to be 1-8% (volume fraction) at 100 °C, and 1-27% at 200 °C in a modeling study. Concentrations of pore water potassium (K) and the abundance and dissolution rate of K-feldspar were the primary chemical factors controlling the extent of illitization in their study (Zheng et al., 2015). Intrusion of groundwater from the surrounding host rock may also have an effect on the clay properties.

The primary goal of this task of the project was to study the effect of bentonite heating under realistic field conditions on U(VI) adsorption behavior. Furthermore, we aimed to provide mechanistic insight into observed differences in U(VI) adsorption as a result of heat treatment. Bentonite samples from the

FEBEX in situ experiment, which experienced varying temperature and water saturation conditions, were tested for U(VI) adsorption. In FY17, we performed U(VI) adsorption kinetics experiments on FEBEX bentonite samples, which experienced a range of temperature and water saturation conditions at a single chemical condition. As part of the FEBEX *in situ* heater test, highly compacted bentonite blocks, serving as the engineered test barrier, were placed in a radial arrangement around two underground heaters and heated to a maximum of 100 °C in a crystalline host rock. In addition, equilibrium U(VI) adsorption laboratory experiments were conducted over a wider range of chemical conditions on two samples: one which was exposed to high temperature (95°C) and one control sample which was emplaced underground in a cold-zone (20°C). In FY18, we continued these investigations by testing a third sample which was exposed to intermediate heat (50°C) and expanding the chemical conditions to lower pH values for all samples. Results from the new experiments are presented along with results from experiments performed in FY17, in order to allow for direct comparison across samples. In addition, clay characterization and aqueous U(VI) speciation calculations were conducted for all experiments understand the mechanism underpinning the observed differences in U(VI) adsorption. Lastly, we present a brief discussion of planned future work. (The results presented in this Chapter were discussed with Dr. Ruth Tinnacher (CSUEB) and Dr. Christophe Tournassat (BRGM). Dr. Sergio Carrero Romero (LBNL) assisted with the XRD analyses).

8.2 Materials and Methods

8.2.1 Bentonite Samples

Bentonite samples were obtained from the second dismantling of the FEBEX *in situ* heater test in 2015, after 18 years of heating. The FEBEX heater test was conducted by ENRESA under the auspices of the European Union at the Grimsel Test Site. Detailed information on the test can be found elsewhere (ENRESA, 2000). Briefly, bentonite was compacted into blocks ("bentonite rock") at 1650 kg/m^3 dry density, placed in a radial arrangement around two underground heaters and heated to a maximum of 100 °C. The degree of water saturation and temperature varied with radial distance, with water saturation greatest and temperature lowest at the furthest distance from the heater (Table 5-1). Based on results from previous work (Fox and Nico, 2017), we chose to focus on bentonite samples from three locations; two locations in the heater test zone (BD-48) at radial distances of 50 and 75 cm from the center axis and one location from a control non-heated zone (BD-59) at 50 cm. The section layout during dismantling is described by Detzner and Kober (2015). Three replicate blocks, measuring approximately 10 x 12 x 14 cm, were used from each location. The blocks were split open and approximately 200 g of bentonite was removed from the center of each block and dried in an oven at 60°C for 1 week. The water content was determined by loss of water on drying at 60°C. The dried bentonite was then crushed by hand using a porcelain mortar and pestle, and sieved through a 0.063 mm sieve in order to remove sand particles and reduce sample heterogeneity. Equivalent weights of each replicate block were mixed together to form composite samples for the three locations. Average water contents and historical *in situ* temperatures are shown for each composite sample in Table 8-1. The original FEBEX bentonite contained primarily smectite (92%), with minor amounts of quartz (2%), plagioclase (2%), cristobalite (2%), and traces of potassium feldspar, calcite, and trydimite (Fernández et al., 2004). The smectite is made up of a mixed layer illite-montmorillonite with approximately 11% of illite layers (Fernández et al., 2004). Bentonite stock solutions were prepared at concentrations of 10 g/L for each sample and stored at 4 °C for less than 1 week prior to starting experiments.

Table 8-1. Composite FEBEX heater test samples used for U(VI) adsorption experiments.

Test Section	Distance to axis (cm)	Replicate Blocks	Water Content (g water/g dry clay)	Average Temperature[(a)] (°C)
BD-48	50	BD-48-3, BD-48-6, BD-48-9	0.14	95
BD-48	75	BD-48-2, BD-48-5, BD-48-8	0.18	50
BD-59	50	BD-59-10, BD-59-11, BD-59-12	0.22	20

(a) Average temperature from (ENRESA, 2000) and L. Zheng, personal communication

8.2.2 Bentonite Extraction and Purification

Composite FEBEX bentonite samples were extracted and purified in order to compare extractable metal concentrations between the samples and produce a purified clay sample for U(VI) adsorption experiments. The extraction and purification procedure was adapted from Tinnacher et al. (2016), allowing for the characterization of extracted metals. The procedure included the following major steps: (1) leaching of clay samples with water, (2) leaching with, and dialysis against, sodium acetate at pH 5 for carbonate mineral removal, (3) dialysis against NaCl to remove acetate and complete Na-saturation, (4) dialysis against water to remove excess salts, and (5) centrifugation to remove particles greater than 2 μm. Triplicate samples were extracted and purified for each composite sample, and extraction data are presented as the average and standard deviation of the replicates. Composite clay (2.5 g) was weighed into 40-mL polycarbonate centrifuge tubes and 25-mL of MilliQ water was added. Samples were placed on an end-over-end sample rotator and allowed to react for 5 hours, then centrifuged at 39,000 x *g* for 20 minutes. The supernatant was filtered through a 0.2 μm syringe filter polyvinylidene fluoride (PVDF) and retained for analysis of water soluble metals, dissolved inorganic carbon (DIC), dissolved organic carbon (DOC), and pH. Centrifuge tubes containing clay were weighed to determine the volume of entrained solution, then 25-mL of 1 M sodium acetate solution buffered at pH 5 with acetic acid was added. Samples were placed on the sample rotator and allowed to react for six days, then centrifuged, filtered, and retained for analysis of metals as described above. Clay samples were re-suspended in 15 mL of acetate buffer, transferred to pre-rinsed dialysis tubing (SpectraPor7, 8 kDa), and dialyzed against 900 mL of acetate buffer in a 1 L glass beaker for three days, changing dialysis solution daily. The acetate buffer dialysis solution was then exchanged with 1 M NaCl (dialyzed for one week), then with MilliQ water (dialyzed for two weeks), again changing dialysis solution daily. The purified clay suspensions were then transferred into plastic bottles and diluted and dispersed in MilliQ water to reach a clay concentration of approximately 15 g/L, and centrifuged at 1000 x *g* for 7 minutes. This centrifugation speed and time was deemed sufficient to remove all particles > 2 μm as calculated from Stoke's Law. The replicate < 2 μm clay fractions were then combined into a single bottle and diluted to reach a final clay stock concentration of 10 g/L. The exact clay stock concentration was determined by drying a subsample in a porcelain crucible at 85 °C. Clay stock solutions were stored at 4 °C for less than 2 weeks prior to starting experiments. Clay samples were then dried at 30 °C and gently ground in an agate mortar and pestle for longer-term storage.

8.2.3 Batch Adsorption Experiments

Equilibrium batch U(VI) adsorption experiments were conducted on purified and un-purified ("bulk") FEBEX bentonite composite samples at two Ca concentrations over the pH range 7 to 8 at an ionic

strength of 0.1 M, using NaCl as the background electrolyte. Clay concentrations were 0.5 g/L and total initial U(VI) concentrations were approximately $1x10^{-6}$ M. For purified clay samples, two separate experiments were conducted with Ca added to yield concentrations of 0.1 and 2.0 mM in solution, respectively. The 0.1 mM Ca concentration was chosen based on the concentrations of Ca released from unpurified bentonite samples. In unpurified bentonite samples, some Ca was present in the clay, so two samples were prepared, one without added Ca, and another spiked with 2.0 mM Ca, achieving final dissolved Ca concentrations of approximately 0.1 and 2.1 mM, respectively. Additional adsorption experiments were conducted between pH 4 and 5 for purified bentonite at 0.1 and 2.0 mM Ca and 0.1 M NaCl.

Adsorption experiments were conducted in 40-mL polycarbonate centrifuge tubes. Clay samples were suspended in water and aliquots of 1 M NaCl, 0.1 M $CaCl_2$, and 0.1 M $NaHCO_3$ stock solutions were added to reach the desired final concentrations of Ca and HCO_3^- (to facilitate equilibration with atmospheric CO_2 for samples above pH 7), and an ionic strength of 0.1 M. The pH was then adjusted to the desired pH using 0.1 M HCl or NaOH and samples were allowed to equilibrate for 24 hours on an end-over-end sample rotator. After equilibration, samples were spiked with U(VI), the pH was re-adjusted, and samples were placed on an end-over-end rotator for 48 hours to allow for U(VI) adsorption. Samples were then centrifuged at 39,000 x *g* for 20 minutes and the supernatant was removed for analysis by ICP-MS (U, Ca, and other metals), DIC, and pH. The remaining clay was rinsed out of the centrifuge tubes using a 3-5 mL of MilliQ water, then 10 mL of 0.15 M nitric acid (ultra-high purity grade) was added to the empty tube and placed on an end-over-end sample rotator for 24-hours. The nitric acid was then sampled and analyzed for U by ICP-MS. This final nitric acid rinse mobilizes any U(VI) which had adsorbed to the walls of the container during the experiment. Total U(VI) concentrations were corrected for wall adsorption, which ranged from 0.15 to 10%. Adsorbed U(VI) was calculated by subtracting the final dissolved U(VI) concentration from the total (wall-sorption corrected) U(VI) concentration. U(VI)-free control samples were prepared in the same manner as samples at pH 8, but without the addition of U(VI) to verify that samples were not contaminated with U(VI). No contamination was observed.

8.2.4 Analytical Techniques

DIC and DOC were measured on a Shimadzu TOC-V analyzer. DOC was measured by non-purgeable organic carbon by acidifying with HCl and purging with N_2 in order to remove inorganic carbon prior to analysis. Total carbon was measured by catalytically aided combustion oxidation at 900°C and a Nondispersive Infrared Detector (NDIR) on a Shimadzu TOC-V analyzer equipped with a solids module (SSM). Samples were analyzed for metal concentrations by ICP-MS (Perkin-Elmer Elan DRC II) after acidification and dilution with ultrapure (ultrex grade) 0.15 M nitric acid and internal standard addition.

The mineralogical composition of the purified FEBEX clay samples were analyzed using X-ray diffraction (XRD) in oriented aggregate. 10 ml of clay mineral suspensions were placed in an ultrasonic bath for 30 min. Once clay particles were disaggregated, sediment was centrifuged, supernatant removed, and a 1 mM sodium pyrophosphate dispersive solution added to avoid clay flocculation and decant all other minerals. Finally, the sample was centrifuged at 750 rpm for 3.3 min leaving single clay particles with a 2 µm diameter in suspension. The final suspension was dropped onto a glass slide and dried at room temperature until a thin homogeneous clay film covered the glass. Each sample was measured under 4 different conditions: 1) dry at room temperature, 2) saturated with ethylene-glycol for 1 hour at 60°C, 3) heated at 400°C for 1 hour, and 4) heated at 550°C for 1 hour.

The diffraction pattern was collected on a diffractometer in Bragg-Brentano geometry, equipped with a theta-theta goniometer with a rotating sample holder. The patterns were collected using Cu kα 1 ($\lambda k\alpha 1$ = 1.5406 Å) and kα 2 ($\lambda k\alpha 2$ = 1.5444 Å) radiation in the range 2Θ = 3-25° and 2Θ= 3-75°, with a step size of 0.02Θ and a counting time of 10 s and 2 s per step, respectively. The diffraction patters were analyzed using the software Macth extended with the PDF mineral database. Illite/smectite proportion (w_s) were calculated using the method described by Drits et al. (1994), where the ethylene-glycol saturated observed

basal position, $d_{ob,}$ is in linear correlation between the closest interlayer distance of the reference mineral in c axis:

$$Ws = 0.5\ \frac{1/d_H - 1/d_{ob}}{1/d_H - 1/d_L}$$

where d_H and d_L are the higher and lower *d* space *c* axis distances in the reference clay mineral, respectively, being d_{ob} in between. In this case, the reference clay minerals were illite and rectorate, where rectorite is a species composed by a 50% of illite and 50% smectite with a periodic mixed illite-layer smectite-layer distribution (R = 1).

8.2.5 U(VI) Aqueous Speciation Calculations

Thermodynamic calculations were performed in order to determine aqueous U(VI) speciation during batch adsorption experiments using Visual Minteq version 3.1. The standard Visual Minteq database was used, which uses data for U from the NEA database (Guillaumont et al., 2003), the THERMOCHIMIE database (Giffaut et al., 2014), and Dong and Brooks (2006). Data for other species are from the NIST database (Smith et al., 2003). The final measured values for pH, DIC, Ca, Mg, K, and total U(VI) were used along with an assumed NaCl concentration of 0.1 M for the calculations. The partial pressure of CO_2 was calculated, and varied between 300 and 620 ppm, values that are reasonable given that the experiments were performed under atmospheric conditions (approximate CO_2 of 380 ppm) in closed vessels.

8.3 Results and Discussion

8.3.1 Bentonite Characterization Results

Water extractions of unpurified FEBEX bentonite released greater concentrations of metals (Na, K, Ca, and Mg) for the 95 °C heated sample compared to the intermediate heated (50°C) and cold-zone samples (20°C) as shown in Table 8-2. The 95 °C heated sample water leachates yielded lower inorganic carbon (IC) and pH values. Some variation was observed in the water extractable OC, with the 50°C sample having the highest concentration. It is possible that the soluble ion concentrations in the *in situ* samples have been altered compared to the original material due to intrusion of groundwater and/or heat-caused alterations. For example, the lower concentrations of soluble metals and OC in the cold-zone sample may represent a loss due to groundwater leaching in this sample or an increase in the heated sample through, for example, transport of salts from the surrounding bentonite or granite and deposition after evaporation in the heated zone. While we did not perform extractions on the original bentonite sample, (Fernández et al., 2004) reported concentrations of soluble salts during leaching experiments with the original FEBEX bentonite, although at a slightly higher solid to liquid ratio (0.15 kg/L compared to 0.1 kg/L in our study). In general, salt concentrations observed in the leachates of the original bentonite were in between the values observed in our study for the two samples (Na = 10.3 mM, K = 0.10, Mg = 0.12 mM, Ca = 0.10 mM), while pH (8.76) was closer to the pH in our cold-zone sample (Fernández et al., 2004). Because of the slightly higher solid to liquid ratio used in their study, it is very likely that the differences observed between the heated and cold-zone sample primarily represent a change in the heated sample. The change in pH and IC in particular is noteworthy; suggesting that carbonate minerals may have been depleted from or altered in the heated sample. For example, a fraction of the calcite may have been converted to a lower-solubility carbonate mineral as a result of heating. The pH 5 acetate extractions released slightly higher Mg and Ca concentrations in the 95°C heated sample. The acetate extractions are designed to dissolve carbonate minerals, but can also release adsorbed cations.

Table 8-2. Chemical characterization of FEBEX bentonite samples by water and acetate extractions. Concentrations of extracted constituents are expressed as the average and standard deviation of replicate extracts.

	Water Extractions			Acetate Extractions		
	BD-48, 50 cm (95°C)	BD-48, 75 cm (50°C)	BD-59, 50 cm (20°C)	BD-48, 50 cm (95°C)	BD-48, 75 cm (50°C)	BD-59, 50 cm (20°C)
pH	7.96 ± 0.02	8.33 ± 0.03	8.63 ± 0.12	--	--	--
IC (mM)	1.02 ± 0.04	1.55 ± 0.04	2.07 ± 0.04	--	--	--
OC (mM)	0.786 ± 0.072	3.20 ± 0.03	0.164 ± 0.007	--	--	--
Na (mM)	11.3 ± 0.1	7.52 ± 0.09	7.69 ± 0.20	--	--	--
K (mM)	0.192 ± 0.008	0.077 ± 0.001	0.077 ± 0.000	1.37 ± 0.03	1.25 ± 0.03	1.34 ± 0.05
Ca (mM)	0.370 ± 0.004	0.068 ± 0.005	0.069 ± 0.001	25.0 ± 0.6	23.7 ± 0.4	24.2 ± 0.2
Mg (mM)	0.356 ± 0.002	0.050 ± 0.001	0.088 ± 0.002	16.8 ± 0.1	14.3 ± 0.4	15.3 ± 0.1

Results from the XRD analysis of purified FEBEX bentonite showed a mixed layer illite-smectite in all samples, with a low fraction of interstratified illite (Figure 8-1). Samples dried at room temperature display a 001 distance at 11.98 Å, 11.72 Å, 11.85 Å, which are expanded to 16.77 Å, 16.27 Å and 16.67 Å in saturated ethylene-glycol atmosphere and collapsed to 9.43 Å, 9.51 Å and 9.51 Å after heating to 450°C for clay samples from the 95°C heated zone, 50°C intermediate heated zone, and 20°C cold-zone, respectively (Figure 8-2). The presence of a single basal 001 position in both natural and glycolated samples indicate that FEBEX bentonite samples are composed of a single mineral phase. However, the position of the 001 peaks are slightly shifted to lower interlayer space with respect to ideal smectite, indicating that expansive clay minerals form a mixed-layer structure with illite. FEBEX bentonite samples from the 95°C heated zone and 20°C cold-zone showed ~5% illite layers and the intermediate heated (50°C) sample showed ~10% illite layers. The 5% illite fraction observed for the 95°C and 20°C samples is slightly lower than the 11% reported for the original bentonite (Fernández et al., 2004), but is likely within the range of normal variation in bentonite deposit. Therefore, we do not believe that significant illitization has occurred as a result of the 18-years of heating these samples experienced.

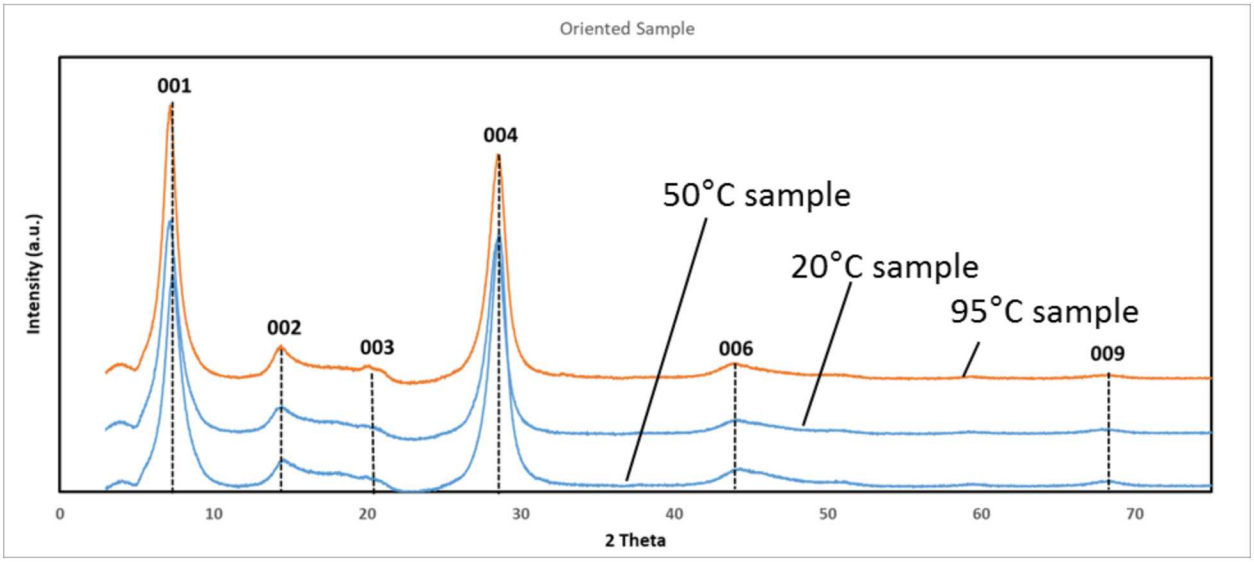

Figure 8-1. Comparison of XRD patterns on purified clay minerals collected on air-dried sample at room temperature.

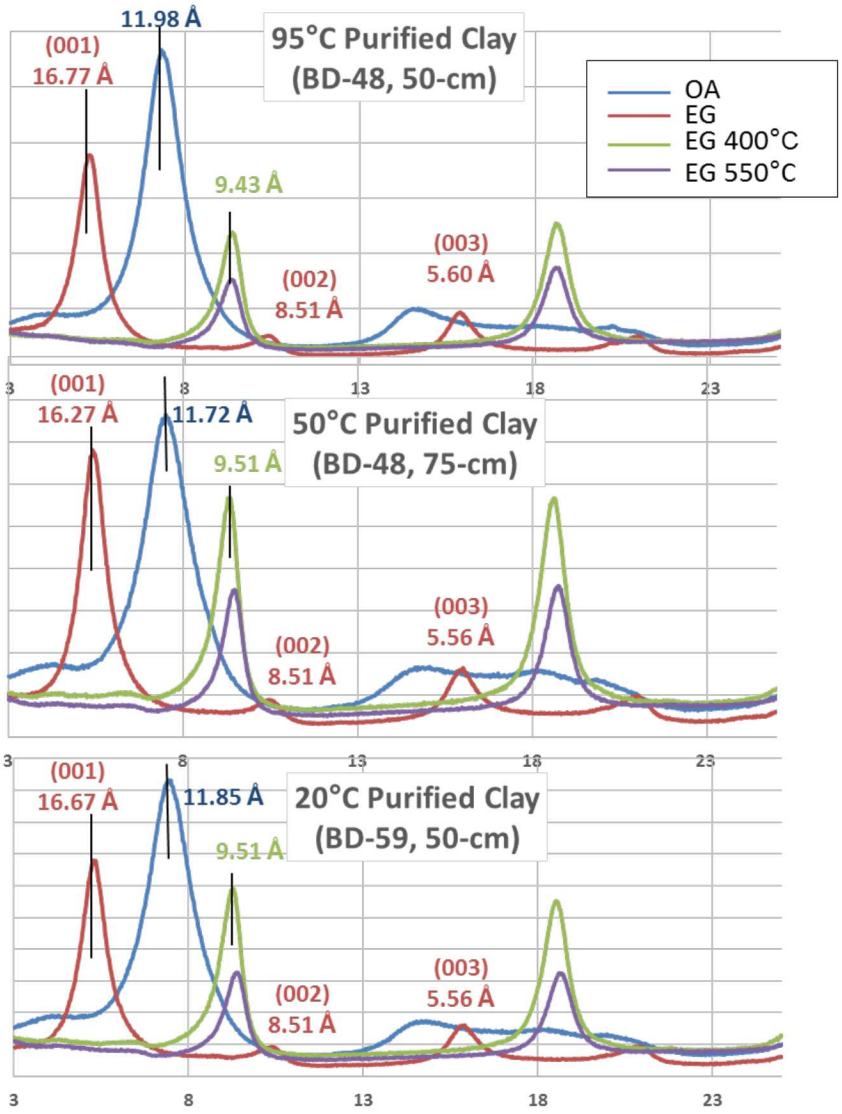

Figure 8-2. XRD patterns for purified FEBEX clay samples on dried oriented aggregate at room temperature (OA), samples solvated in ethylene glycol at 60°C (EG), then heated to 400 and 550°C. Note the shift in the 001 peak position with EG solvation and heating. The y-axis is intensity in arbitrary units.

8.3.2 Comparison of Uranium(VI) Adsorption on Heated and Cold-Zone Bentonite

U(VI) adsorption to purified and unpurified FEBEX bentonite was studied over a range of chemical conditions which are considered relevant for waste disposal scenarios, including the pH range 7 to 8 and Ca concentrations of approximately 0.1 and 2.0 mM. We did not test pH values greater than 8 due to supersaturation with respect to calcite (at 2 mM Ca) and low U(VI) adsorption at alkaline pH. Results from these experiments are shown in Figure 8-3, plotted as both % U(VI) adsorbed and log Kd, where Kd is the final U(VI) concentration on the solid (in mol/kg) divided by the final dissolved concentration (in mol/L). As expected, U(VI) adsorption decreased with increasing pH. U(VI) adsorption was also lower in the presence of high Ca (~2 mM) compared to low Ca (~0.1 mM), especially above pH 7.2.

U(VI) adsorption onto unpurified (bulk) bentonite was higher on the 20°C sample (BD-59, 50 cm) compared to the 95°C heated sample (BD-49, 50 cm) over the entire pH range at both low and high Ca. However, U(VI) sorption on the intermediate heated sample was inconsistent for the bulk bentonite, appearing closer to the 95°C sample in the presence of 0.1 mM Ca and closer to the 20°C sample in the presence of 2 mM Ca.

U(VI) adsorption onto purified bentonite was consistently lower on the 95°C heated sample compared to the cold-zone (20°C) and intermediate-heated (50°C) sample. This suggests that the difference in U(VI) adsorption between 95°C heated and cold zone samples is due to structural alteration of the smectite (montmorillonite) clay mineral, and not due simply to differences in pore water chemistry or the types and relative masses of accessory minerals. No significant differences were observed in the XRD data from the cold-zone and 95°C heated clay samples, allowing us to rule out illitization as the cause of changes in U(VI) adsorption. Under the pH conditions tested here (pH 7-8), U(VI) is known to adsorb to the edge sites of montmorillonite forming inner-sphere bidentate complexes (Hennig et al., 2002; Marques Fernandes et al., 2012; Schlegel and Descostes, 2009; Tournassat et al., 2018; Zhang et al., 2018). Recently, Tournassat et al. (2018) developed a new surface complexation model for montmorillonite edge surfaces which takes the spillover effect of the electrostatic potential at the basal surface on the electrostatic potential at the edge surfaces. Therefore, changes in the montmorillonite edge structure, relative abundance of edge sites, and electrostatic characteristics of both the basal surface and edge sites may affect U(VI) adsorption to montmorillonite and may represent the types of structural changes which occur during heating. These changes would not be detected by XRD analysis. Furthermore, the similarity between the U(VI) adsorption onto 50°C heated purified bentonite and cold-zone (20°C) purified bentonite suggests that this temperature is not sufficient to cause structural changes to the montmorillonite over the 18-year time frame of the FEBEX experiment, although some changes may have occurred in the accessory mineral fraction of the bentonite.

In all cases, U(VI) adsorption was higher on purified bentonite compared to unpurified bentonite. This is expected and likely due to a ‘dilution’ effect from accessory minerals that have a much lower adsorption capacity compared to montmorillonite in the unpurified bentonite. These minerals may include silica and feldspar minerals as well as carbonate minerals (*e.g.*, calcite).

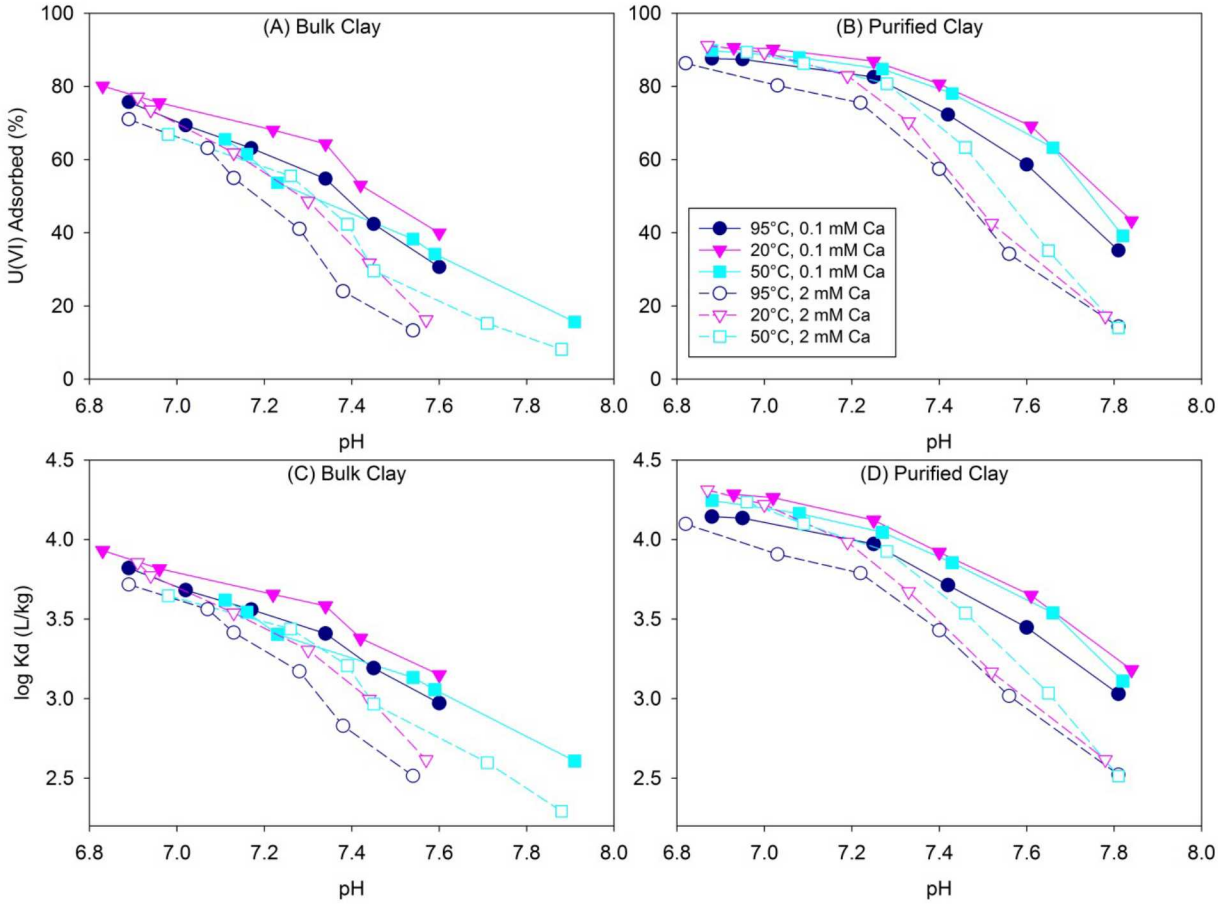

Figure 8-3. U(VI) adsorption as a function of pH onto bulk (A, C) and purified (B, D) FEBEX bentonite samples from the heated zone and cold zone. Experiments were conducted at two different Ca concentrations. (A) and (B) show U(VI) sorption as % adsorbed, while (C) and (D) show U(VI) adsorption expressed as the log K_d.

U(VI) adsorption experiments were also conducted at low pH (4-5) onto purified bentonite, and the results are shown in Figure 8-4. At these lower pH conditions, U(VI) aqueous speciation calculations indicate that U(VI) speciation is dominated by cationic species, with 92% of U as UO_2^{+2} at pH 4, and >90% of U as UO_2^{+2} and UO_2OH^+ at pH 5. Cation exchange reactions may influence U(VI) adsorption over this pH range (Tournassat et al., 2018). We did not observe any difference in U(VI) adsorption across the three purified FEBEX clay samples tested under these conditions. Slightly lower adsorption was observed in the presence of 2 mM Ca (compared to 0.1 mM Ca) for the lowest pH values only (4.0-4.4) as shown in Figure 8-5. At this pH value, the lower adsorption in the presence of 2 mM Ca is most likely due to a competition effect between Ca and UO_2^{+2}.

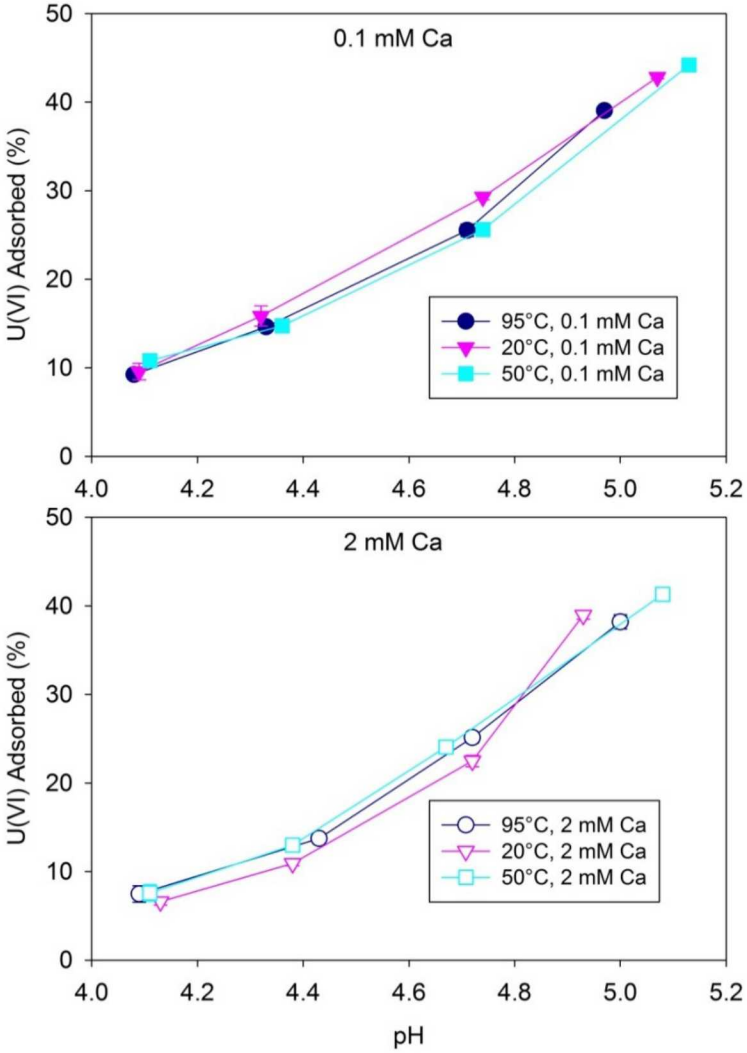

Figure 8-4. U(VI) adsorption onto purified FEBEX bentonite from heated and cold zones at low pH in the presence of 0.1 mM (top) and 2 mM (bottom) Ca.

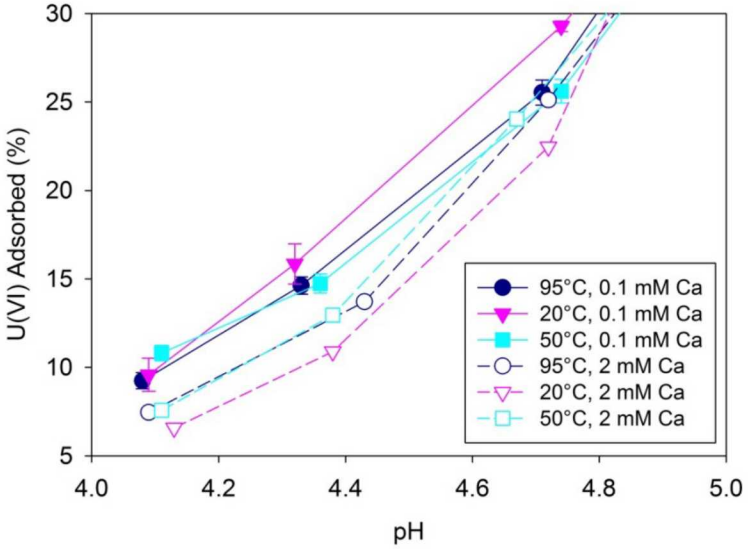

Figure 8-5. Comparison of U(VI) adsorption onto purified FEBEX bentonite in the presence of 0.1 and 2 mM Ca at low pH. Note the y-axis scale is expanded to better show the difference in adsorption at the low pH values.

8.3.3 U(VI) Aqueous Speciation

Aqueous U(VI) speciation was calculated for each experiment conducted. U(VI) speciation is very complicated, and the concentrations of over 20 U(VI) species were determined. Example U(VI) speciation diagrams are shown in Figure 8-6, where only species which had concentrations of >0.1% of the total U(VI) concentration (*i.e.*, 10^{-9} M) are plotted. Calcium-uranyl-carbonato ternary complexes [$Ca_2UO_2(CO_3)_3(aq)$, $CaUO_2(CO_3)_3^{2-}$] dominate the U(VI) speciation in the presence of 2 mM Ca at pH >7.4. At lower Ca concentrations (0.1 mM) the $CaUO_2(CO_3)_3^{2-}$ species is still very important at pH >7.4, but the $Ca_2UO_2(CO_3)_3(aq)$ species is much lower in concentration. Uranyl-carbonato complexes are important at both lower Ca and lower pH conditions. Aqueous U(VI) speciation is similar, but not identical, for purified and bulk bentonite samples, with the primary difference being the formation of the magnesium-uranyl-carbonato complex [$MgUO_2(CO_3)_3^{-2}$] in the bulk samples. This results from the small amount of Mg found in porewater of the unpurified bentonite (Table 8-2) which is re-dissolved upon wetting of dried samples. A comparison of the calcium-uranyl-carbonato and magnesium-uranyl-carbonato species concentrations between the 95°C heated and 20°C cold-zone sample is shown in Figure 8-7. Differences between the concentrations of species for these two samples are negligible, with the exception of the magnesium-uranyl-carbonato species for purified bentonite in the presence of 0.1 mM Ca. However, the concentration of this species is so low (<6 x 10^{-10} M) under those conditions that it is not expected to cause a difference in U(VI) adsorption between the two samples.

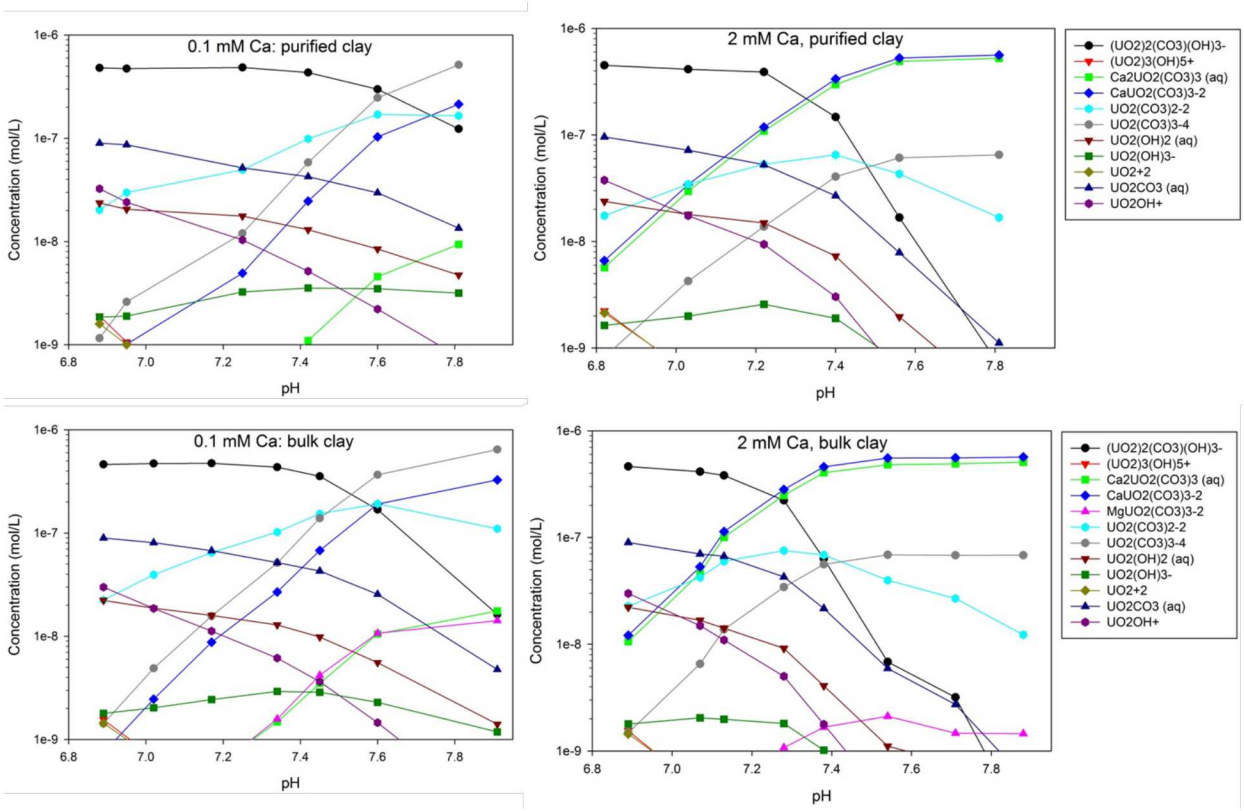

Figure 8-6. Example of aqueous U(VI) speciation over the pH range 6.9-7.9 for purified (top) and bulk (bottom) FEBEX bentonite in the presence of 0.1 (left) and 2 mM Ca (right).

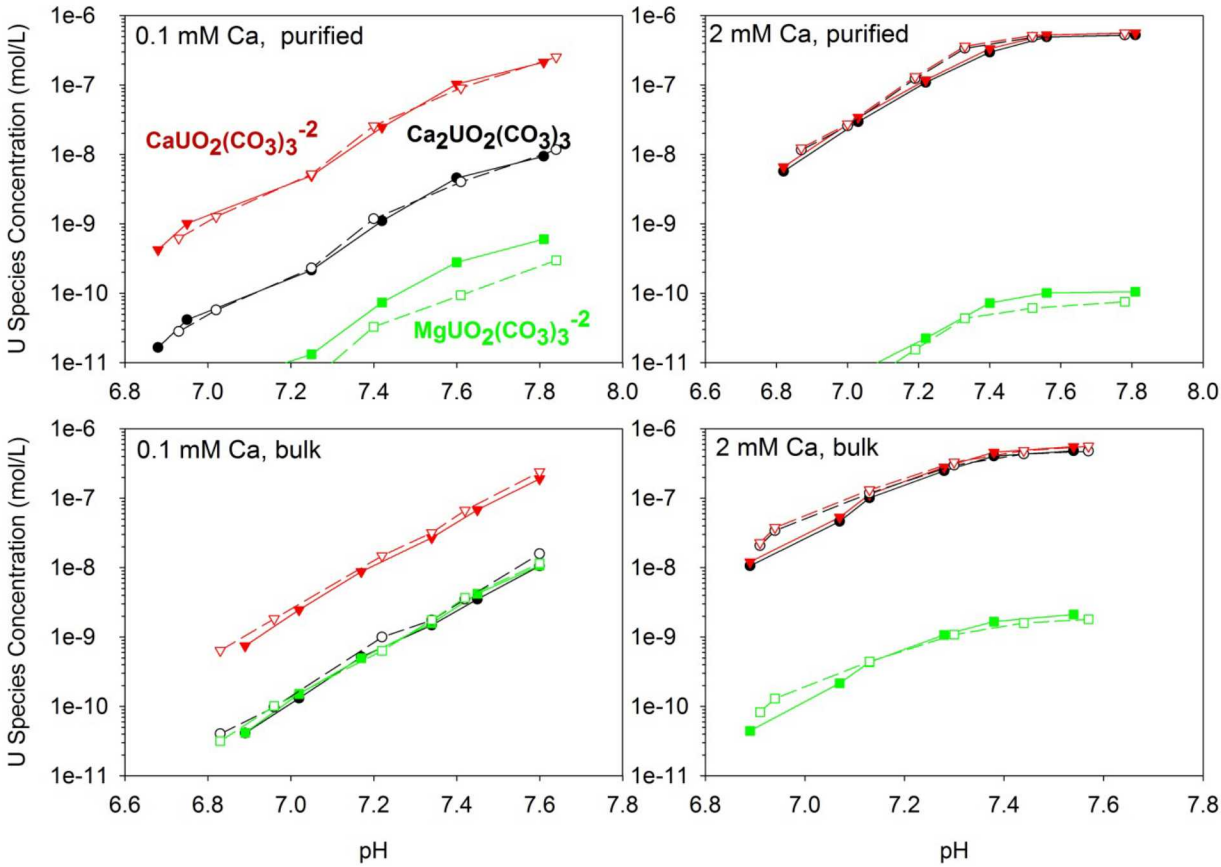

Figure 8-7. Calculated concentrations of calcium-uranyl-carbonato and magnesium-uranyl-carbonato complexes during U(VI) adsorption experiments on purified (top) and bulk (bottom) FEBEX bentonite in the presence of 0.1 (left) and 2 mM Ca (right). For clarity, data is only shown for 95°C heated (solid lines and filled symbols) and 20°C cold zone (dashed lines and open symbols) samples.

According to Tournassat et al., (2018), uranyl-carbonato surface complexes are not necessary to explain U(VI) sorption to montmorillonite over a range of aqueous chemical conditions. They developed a surface complexation model which accurately described U(VI) adsorption to montmorillonite over a range of pH, DIC, and Ca concentrations. The model employed a single U(VI) adsorption site and three surface complexes: $>SiteH_3UO_2^{+2}$, $>SiteHUO_2$, and $>SiteUO_2(OH)_2^{-3}$, with log K values of 4.8, -4.8, and -25.3, respectively (Tournassat et al., 2018). Thus, only the uranyl cation (UO_2^{+2}) and uranyl hydroxyl species [$UO_2(OH)^+$, $UO_2(OH)_2$, and $UO_2(OH)_3^-$] are responsible for adsorption over a wide range of chemical conditions. We have calculated the sum of the uranyl and uranyl hydroxyl species for each experiment and the results are shown in Figure 8-8. Several observations can be made based on these calculations. First, uranyl-hydroxyl species concentrations are nearly identical across all samples and Ca concentrations at pH 6.8-7.2, while at pH >7.3 uranyl-hydroxyl concentrations are higher in the presence of 0.1 mM Ca compared to 2 mM Ca. These observations are consistent with the U(VI) sorption data (Figure 8-3) which show a divergence in the U(VI) adsorption as a function of Ca concentration around pH 7.3, providing further evidence that changes in aqueous U(VI) speciation are the cause of differences in U(VI) adsorption for the two Ca concentrations. Second, uranyl-hydroxyl concentrations are slightly lower for bulk samples compared to purified at pH >7.3. While this difference in uranyl-hydroxyl concentrations is small, it may be due to the formation of the magnesium-uranyl-carbonato complex in bulk samples as shown in Figure 8-7.

Lastly, there is no systematic difference in uranyl-hydroxyl concentrations for the 95°C heated, 50°C heated, and 20°C heated samples. This important observation verifies that the observed differences in U(VI) adsorption to the 95°C heated and 20°C cold-zone samples (Figure 8-3) must be due to structural differences in the clay minerals, and not to differences in aqueous U(VI) speciation.

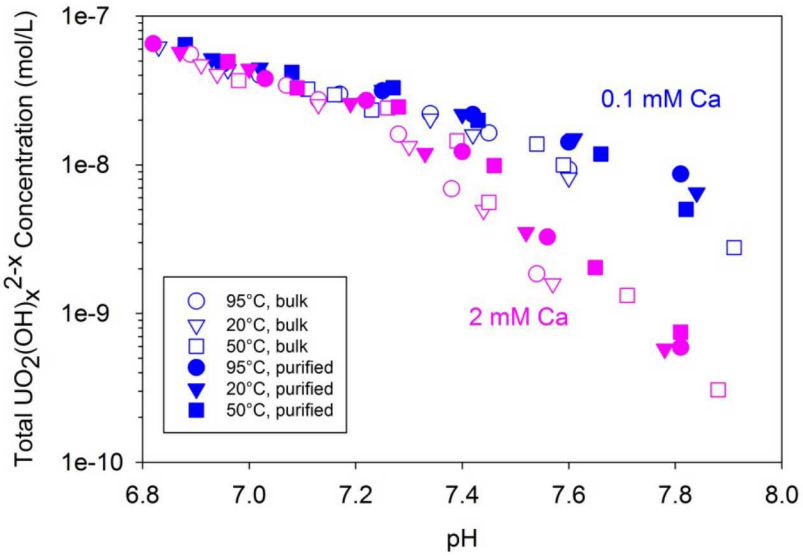

Figure 8-8. Sum of uranyl hydroxyl aqueous species ($UO_2(OH)_x^{2-x}$, where x varies between 0 and 3) during experiments on purified (open symbols) and bulk (filled symbols) FEBEX bentonite over a range of chemical conditions. Low Ca (0.1 mM) experiments are shown in blue and high Ca (2 mM) experiments are shown in pink.

8.4 Summary and Conclusions

In this report, we have detailed the results from a series of experiments designed to test the effect of bentonite heating on U(VI) adsorption. U(VI) adsorption onto bentonite samples from the FEBEX *in situ* experiment, which were subjected to 18 years of heating at temperatures of 50-100 °C, was compared to adsorption onto cold-zone FEBEX bentonite from the *in situ* experiment. We found that U(VI) adsorption is 5-10% lower on the 95°C heated sample compared to 20°C cold-zone sample for both bulk bentonite (<0.063 mm) and purified bentonite clay (<0.002 mm). Aqueous speciation calculations demonstrated that there is no systematic difference in the U(VI) speciation between these two samples during the experiments. This observation, combined with the persistence of a difference in U(VI) adsorption after the bentonite had been purified to remove non-clay minerals (e.g., calcite, quartz, and feldspars), allows us to conclude that the observed difference in U(VI) adsorption between the 95°C heated and 20°C cold-zone samples is due to structural differences in the clay minerals rather than differences in U(VI) speciation. By contrast, U(VI) adsorption to the intermediate (50°C) heated purified clay sample is nearly identical to cold-zone sample, despite the observation of slightly higher fraction of illite layers (10%) in this sample compared to other samples (5% illite). This suggests that effects of heat on U(VI) adsorption may only be observed at the highest temperatures expected in an engineered barrier system, and will be limited to the area immediately surrounding waste canisters (i.e., within 25 cm). Furthermore, small differences in illitization (i.e., 5% vs 10%) will likely have a small to negligible effect on U(VI) adsorption. The structural differences in the clay minerals from the 95°C heated and 20°C cold-zone are currently unknown, but are not due to differences

in the degree of illitization. Instead, they may be due to small differences in the edge structure or number of edge adsorption sites of the montmorillonite or to differences in the electrostatic characteristics of the montmorillonite. Such changes are difficult to impossible to accurately and quantitatively characterize, but may have a significant impact on the adsorption capacity of the mineral. The results from this study provide key information necessary for performance assessment of HLW disposal scenarios. The decreased adsorption observed in this study as a result of bentonite heating may impact the diffusion of U(VI) through engineered clay barriers. Because the decreased U(VI) adsorption was due to changes in the clay mineral structure and *not* to aqueous U(VI) speciation, other radionuclides may be similarly affected.

8.5 Future Work

During the remaining time in this fiscal year (FY18) we plan to complete clay characterization work, including measurement of cation exchange capacity. Beginning in FY19, we will then combine the existing data set collected for U(VI) adsorption onto FEBEX bentonite with U(VI) adsorption data previously collected on laboratory-heated bentonite into a single journal publication. Future laboratory work will focus on the two samples which showed the largest difference in U(VI) adsorption: the 95°C heated and 20°C cold-zone FEBEX bentonite samples. We will conduct diffusion experiments with these two samples under realistic waste disposal conditions (compaction and chemical conditions) in order to investigate how differences in U(VI) adsorption affect the diffusive transport of U(VI). This work will be closely coordinated with work being performed under the NEUP project led by Dr. Ruth Tinnacher at CSUEB where U(VI) diffusion experiments will be conducted on synthetic mixtures of montmorillonite and calcite before and after laboratory heat treatment, and data from the two studies should be complementary.

9. HIGH TEMPERATURE EXPERIMENTS OF EBS COMPONENT INTERACTIONS

9.1 Introduction

The U.S. Department of Energy's Spent Fuel and Waste Science and Technology R&D (SFWST) Campaign is investigating the design and safety function of generic nuclear geologic repositories in a variety of geologic settings. The evaluation of the International Engineered Barrier System (IEBS) concepts and interaction with the wall rock (i.e., natural barriers), waste canisters, or other IEBS interfaces are important to the long-term performance and safety of geologic repositories (Nutt et al., 2011; Jove-Colon et al., 2011). The European community, especially the French, have investigated bentonite stability in contact with steel under a variety of experimental conditions in an attempt to replicate repository conditions (Pusch, 1979; Madsen, 1998; Meunier et al., 1998; Guillaume et al., 2003; Wersin et al., 2007; Mosser-Ruck et al., 2010; Ferrage et al., 2011, Mosser-Ruck et al., 2016). The majority of their research was focused on lower temperature environments and atmospheric pressures. Our experimental program for FY18 aims to 1) characterize how IEBS components (steel, Grimsel Granodiorite wall rock) react and change in the presence of Wyoming bentonite and 2) capture steel corrosion rates and interface mineralogy at reasonable high temperature (up to 250 °C, 150 bar) in-situ repository conditions.

9.2 Background and Objective

This IEBS collaboration has a focus on natural barrier systems and engineered barrier system aspects related to the EBS work package of the Spent Fuel and Waste Science and Technology R&D (SFWST). There are multiple international analytical programs with planned experimental setup to enable studying a number of issues relevant for repository design. The objective of this IEBS study was to determine the Grimsel Granodiorite host rock/groundwater interactions with bentonite and the steel canister at elevated

pressure/temperature (250 °C, 150 bar) conditions (see Table 9-1). The groundwater composition at the Grimsel site is well characterized (Table 9-2). There is an ancillary work (Argillite R&D) that characterized Full Scale High-Level Waste Engineered Barrier System Experiment-Dismantling Project (FEBEX-DP) materials which served as a lower P,T analog to the experiments presented here. A description of the FEBEX experiment is described in the next section.

The Grimsel Test Site (GTS) is located in the Swiss Alps near the Grimsel Pass (Bern Canton, Switzerland). The site was established in 1984 as a center for underground Research and Development (R&D) supporting the geological disposal of radioactive waste (Grimsel, 2017). The FEBEX is a 1:1 scale demonstration project for the emplacement of Spent Nuclear Fuel (SNF). The FEBEX tunnel proper is located in Grimsel granodiorite at a depth of 450 meters below the surface. This is an in situ migration experiment conducted between boreholes situated in sparsely fractured crystalline, Grimsel granodiorite, host rock focusing on bentonite solubility, colloidal mineral migration/formation, and colloid-associated radionuclide transport. Two heaters replicating SNF canisters (4.5 meters long, 12 ton each) were emplaced and surrounded by blocks of compacted bentonite clay. In February 1997, heaters were switched on and data acquisition began. The experiment ran from February 1997 to 2002 at a constant temperature of 180 °C at the surface of the canister (FEBEX, 2014). After the heating of the first canister was stopped and that portion (including the canister) of the experiment was excavated. After removal, a dummy canister (no heating capability) was emplaced, EBS blocks were reinserted, and a concrete plug was constructed. The second portion of the experiment ran until 2015, when full excavation of FEBEX was initiated.

Table 9-1. Initial components and reaction conditions for the IEBS experiments.

Experiment	Clay (g)	Brine (g)	IEBS Components	Run Temp (°C)	Run Time
IEBS-1	10.91	144.0	Bentonite, and G.G. only	250	6 weeks
IEBS-2	11.02	182.0	Bentonite, G.G, 316 SS	250	6 weeks

G.G. = Grimsel Granodiorite

Table 9-2. Initial groundwater chemical composition from the experimental shear zone at the GTS used as the bases of the synthetic groundwater used in these experiments (Missana et al., 2006).

		[M]*	[M]**	[M]***
Cations	Na^+	$6.9x10^{-4}$	$7.0\text{-}7.2x10^{-4}$	$7.0x10^{-4}$
	K^+	$5.0x10^{-6}$	$1.8\text{-}4.6x10^{-6}$	$1.0\text{-}3.6x10^{-6}$
	Mg^{2+}	$6.2x10^{-7}$	$<1.0x10^{-5}$	$2.0\text{-}4.1x10^{-5}$
	Ca^{2+}	$1.4x10^{-4}$	$1.4\text{-}1.6x10^{-4}$	$1.4x10^{-4}$
	Sr^{2+}	$2.0x10^{-6}$	$2.4\text{-}2.6x10^{-6}$	$1.9\text{-}2.3x10^{-6}$
	Rb^+	$2.5x10^{-8}$	not determined	$1.6x10^{-8}$
	Cs^+	$5.0x10^{-9}$	$4.3x10^{-9}$	$3.8\text{-}7.5x10^{-9}$
	Li^+	not determined	$1.1x10^{-5}$	$1.2x10^{-5}$
Anions:	SO_4^{2-}	$6.1x10^{-5}$	$2.8\text{-}6.3x10^{-5}$	$1.8x10^{-4}$
	F^-	$6.1x10^{-5}$	$3.4x10^{-4}$	$3.2x10^{-4}$
	Cl^-	$1.6x10^{-4}$	$1.6\text{-}2.2x10^{-4}$	$1.4x10^{-4}$
	Br^-	$3.8x10^{-7}$	not determined	$3.6x10^{-7}$
	I^-	$1.0x10^{-9}$	$\leq 1.58x10^{-7}$	$7.9x10^{-10}$
	PO_4^{3-}	not determined	$<1.0x10^{-6}$	not determined
Other Species:	Si	$2.5x10^{-4}$	$3.4x10^{-4}$	$2.0x10^{-4}$
	CO_2	$<7.0x10^{-7}$	not determined	not determined
	O_2	$<3.0x10^{-8}$	not determined	not determined
	N_2	$7\text{-}8x10^{-4}$	not determined	not determined
	U	not determined	$<4.2x10^{-9}$	$1.3\text{-}6.3x10^{-10}$
	Th	not determined	$<2.1x10^{-9}$	$<2.2x10^{-10}$
	Ti	not determined	$1.5x10^{-8}$	$6.3x10^{-8}$
	Fe	not determined	$<5.4x10^{-7}$	$6.3x10^{-7}$
	Al	not determined	$3.0\text{-}4.0x10^{-6}$	$0.5\text{-}1.7x10^{-6}$
Calculated(3)	HCO_3^-	$2.9x10^{-4}$	$4.7x10^{-4}$	$1.4x10^{-4}$
	CO_3^- (CO_3^{2-})	$4.2x10^{-5}$	$<1.0x10^{-4}$	-
	OH^-	$1.3x10^{-5}$	not determined	not determined
	$H_3SiO_4^-$	$4.2x10^{-5}$	not determined	not determined
	H_4SiO_4	$2.1x10^{-4}$	not determined	not determined
pH		9.6±0.2	9.5±0.2	9.6
Ionic strength [M]		0.0012	not determined	
Temperature [°C]		12±1	not determined	
Electrical Conductivity [µS cm^{-1}]		103±5	93-103	12
Eh [mV]		<300	-200±50	106

* Data are compiled from Bajo et al. (1989), Aksoyoglu et al. (1990) and Eikenberg et al. (1991) and represent the top of the range of data reported in Tab. 3.3 of Frick et al. (1992).
** After Missana et. al. (2001)
*** Grimsel Colloid Exercise (NTB 90-01) PSI data from Degueldre et al. 1996a
M= molar

9.3 Methods

Analytical methods (Experimental Setup, Mineral Characterization, and Aqueous Geochemical Analyses) remain unchanged from Caporuscio et al. (2014). They are listed in Appendix A for convenience.

Post-reaction steel coupons were mounted in epoxy then polished exposing the cross-sectioned surfaces. These mounts were then imaged using two different methods: SEM and reflected light microscopy. For each IEBS run 15 to 40 images will be taken for each method. These image locations will be mapped and chosen to give a random distribution of the corrosion in the coupons. All images will be analyzed in Photoshop where the thickness of the silicate interface reaction minerals (chlorite and Fe-saponite) and the depth of the corrosion will be measured and then labeled for future analysis. Corrosion rates will be determined by dividing the average corrosion depth by the number of days in the run.

9.3.1 Experimental Setup

The bentonite used in this experimental work was mined from a reducing horizon in Colony, Wyoming. The bentonite was pulverized and sieved to < 3 mm and used with a free moisture content of ~15.5 wt. %. The groundwater solution was prepared using reagent grade materials dissolved in double deionized water. NaOH and HCl were added to adjust the initial solution pH. This solution was then filtered through a 0.45 μm filter and sparged with He before each experiment. The salt solution was added at 9:1 water:bentonite ratio. Initial components for wall rock experiments have been summarized in Table 1.

A second series of experiments were performed to examine the bentonite system with host rock inclusion. Host-rock experiments focused on Grimsel Granodiorite from the Swiss Underground Research Laboratory located near Grimsel Pass. A portion of the Grimsel Granodiorite was crushed and sieved with 10 mesh (~2 mm). Grimsel Granodiorite to be used in experiments was reconstituted at 80 wt. % -10 mesh and 20 wt. % +10 mesh. Synthetic groundwater was chosen to replicate the groundwater composition that represents Grimsel Granodiorite pore water (Table 2, Missana & Geckeis, 2006). The brine solution was added at 9:1 water: rock ratio.

The redox conditions for each system were buffered using a 1:1 mixture (by mass) of Fe_3O_4 and Fe° added at 0.07 wt. % of the bentonite mass. Approximately 7 wt. % (of total solids mass) 304 stainless steel (NIST SRM 101 g), and 316 stainless steel (NIST SRM 160b), (provided by Sandia National Laboratory) were added to the experiments to mimic the presence of a waste canister.

Reactants were loaded into a flexible gold and fixed into a 500 mL Gasket Confined Closure reactor (Seyfried et al., 1987). Experiments were pressurized to 150 to 160 bar and were heated isothermally at 250 °C for 4 to 6 weeks. Reaction liquids were extracted during the experiments and analyzed to investigate the aqueous geochemical evolution in relationship to mineralogical alterations. The sampled reaction liquids were split three-ways producing aliquots for unfiltered anion, unfiltered cation, and filtered (0.45 μm syringe filter) cation determination. All aliquots were stored in a refrigerator at 1 °C until analysis. The steel corrosion experiment was conducted in a cold seal reaction vessel. The reactants (Opalinus Clay, 316 LC SS, Opalinus Clay brine, and solid buffers) were loaded into a gold capsule. The water/rock ratio was 2:1. The run was pressurized to 150 bar and heated isothermally at 150 ^{o}C for 8 weeks.

9.3.2 Mineral Characterization

9.3.2.1 Chesapeake Energy Laboratory QXRD

X-ray diffraction (XRD) analyses of experimental materials determined mineral compositions. Each sample was ground with 20 wt. % corundum (Al_2O_3) for quantitative XRD analysis of the bulk rock

(Chung, 1974). XRD measurements were conducted with a Siemens D500 diffractometer using Cu-Kα radiation. Data were collected from 2 to 70 °2θ with a 0.02 º2θ step-size and count times of 8 to 12 seconds per step. To better analyze the non-clay and clay fractions, the < 2 μm particles were separated via sedimentation in DI H_2O. An aliquot of the < 2 μm suspension was dropped on a zero-background quartz plate and dried. This oriented mount was X-rayed from 2 to 40 °2θ at 8 to 12 s per step. The oriented mount was then saturated with ethylene glycol in a 60°C oven for 24 hours and XRD analysis was repeated. A portion of the > 2 μm particles was ground with a mortar/pestle, deposited on a zero-background quartz plate, and X-rayed under the same parameters as the bulk powder material. The remaining > 2 μm portion was used for electron microscopy. Mineral identification and unit-cell parameters analysis was performed using Jade© 9.5 X-ray data evaluation program with ICDD PDF-4 database. Quantitative phase analysis (QXRD) was performed using FULLPAT (Chipera and Bish, 2002). Illite-smectite composition of higher-ordered (R1-3) illite-smectites were modeled via ClayStrat+ (developed by Hongji Yuan and David Bish). Expandable component abundances for the disordered illite-smectites were calculated via the Δ°2Θ method (Środoń, 1980; Eberl et al., 1993; Moore and Reynolds, 1997). A regression from calculated data were used to calculate the % expandable (%Exp) component in each untreated and reacted bentonite. The equation is:

$$\%Exp = 973.76 - 323.45\Delta + 38.43\Delta^2 - 1.62\Delta^3$$

(Eberl et al., 1993, Eq. 3, R^2=0.99)

with Δ corresponding to Δ°2Θ between the 002 and 003 peak positions for the oriented, ethylene glycol saturated samples.

9.3.2.2 University Texas-Austin Geoscience Laboratory QXRD

Samples were milled to a fine powder in a tungsten carbide ring mill. Approximately 0.2 g of 0.3 μm corundum (Buehler) was added to a 1 g aliquot of each sample. The corundum and sample mixtures were homogenized by dry milling in an alumina mortar and pestle. A thin layer of petroleum jelly was applied to a one-inch round glass slide. Homogenized mixtures of corundum and sample were loaded onto glass slides such to form a thin layer of sample across the entirety of the glass slide. Samples were then loaded into the X-ray diffractometer (XRD) for analysis.

9.3.2.3 XRD Instrument Type and Scan Conditions

All XRD measurements were made at the University of Texas at Austin using a Bruker D8 Advance. The instrument is equipped with a Cu source and a LynxEye detector. The following optically configuration was used for all scans: 1.0 mm divergence slit at the source and a 3.0 mm slit, an anti-scatter tube, a Ni filter for Kb Cu radiation, and a 2.5° axial soller slit at the detector. The source was run at 45 kV and 40 mA for all scans. All samples were scanned between 4° and 70° 2Θ with a stepsize of 0.01° and a counting time of 1 s per step. Samples were rotated during acquisition to maximize random orientation of phases. Total run time for each sample was two hours.

9.3.2.4 Scan Processing: QXRD

Post-acquisition processing and quantitative XRD (QXRD) were performed using Bruker's DIFFRACplusBasic Evaluation Package (EVA v.15). EVA was used for background subtraction, Kα2 stripping, scan smoothing, and 2Θ displacement. The reference intensity ratio (RIR) method was used for QXRD. The RIR method uses the most intense peak of corundum as a reference intensity to calculate weight fractions of other phases in a sample. Preferred orientation of phases results in poor-quality QXRD results. Rotation of samples during measurement and the method for loading samples in XRD holders minimized preferred orientation. QXRD results for most samples yielded approximately 18 wt.% corundum, which closely matches the amount of corundum added to the sample.

9.3.2.5 SEM analyses

Analytical electron microscopy was performed using a FEITM Inspect F scanning electron microscope (SEM). All samples were Au/Pd-coated prior to SEM analysis. Imaging with the SEM was performed using a 5.0 kV accelerating voltage and 1.5 spot size. Energy dispersive X-ray spectroscopy (EDS) was performed at 30 kV and a 3.0 spot size.

Analytical electron microscopy was performed using a FEITM Inspect F scanning electron microscope (SEM). All samples were Au/Pd-coated prior to SEM analysis. Imaging with the SEM was performed using a 5.0 kV accelerating voltage and 1.5 spot size. Energy dispersive X-ray spectroscopy (EDX) was performed at 30 kV and a 3.0 spot size.

9.3.3 Aqueous Geochemical Analyses

Major cations and trace metals were analyzed via inductively coupled plasma-optical emission spectrometry (Perkin Elmer Optima 2100 DV) and inductively coupled plasma-mass spectrometry (Elan 6100) utilizing EPA methods 200.7 and 200.8. Ultra-high purity nitric acid was used in sample and calibration preparation prior to sample analysis. Internal standards (Sc, Ge, Bi, and In) were added to samples and standards to correct for matrix effects. Standard Reference Material (SRM) 1643e Trace Elements in Water was used to check the accuracy of the multi-element calibrations. Inorganic anion samples were analyzed by ion chromatography (IC) following EPA method 300 on a Dionex DX-600 system. Aqueous geochemical results are presented in Appendix B.

9.4 Results

9.4.1 Starting Material Characteristics

Wyoming Bentonite: The bentonite used in this experimental work is mined from a reducing horizon in Colony, Wyoming. Unprocessed Wyoming bentonite contains primarily smectite with minor amounts of clinoptilolite and lesser plagioclase, biotite, calcite, and sulfide minerals. The QXRD results from unheated bentonite are presented in Table 9-3.

Table 9-3. Quantitative X-Ray Diffraction (QXRD) analyses of the buffer clay (Wyoming Bentonite) the wall rock (Opalinus Clay). Values are in weight percent. b.d.l. = below detection limit, * represents data set was normalized to 100.0, (+) represents material detectable but below 0.5 wt. %.

	Wyoming Bentonite	Grimsel Granodiorite
Analcime / Wairakite	b.d.l.	
Clinoptilolite	12.0	
Smectite	66.4	
Kaolinite	b.d.l.	
Albite		25.14
Plagioclase	8.3	
Orthoclase		30.84
Anorthite		
K-Feldspar	b.d.l.	
Biotite	2.8	
Muscovite		
Chlorite	b.d.l.	
Calcite	5.5	
Dolomite	+	
Quartz	0.9	44.02
Cristobalite/ Opal-C	1.8	
Pyrite	0.4	
Siderite	1.8	
Total:	100.0*	100.00

Grimsel Granodiorite: Major mineral phases are K-feldspar, plagioclase, and quartz. Minor phases are muscovite and biotite. Trace phases are allanite, zircon, titanite, and apatite. The QXRD results from unheated granodiorite are presented in Table 9-3 and Figure 9-1.

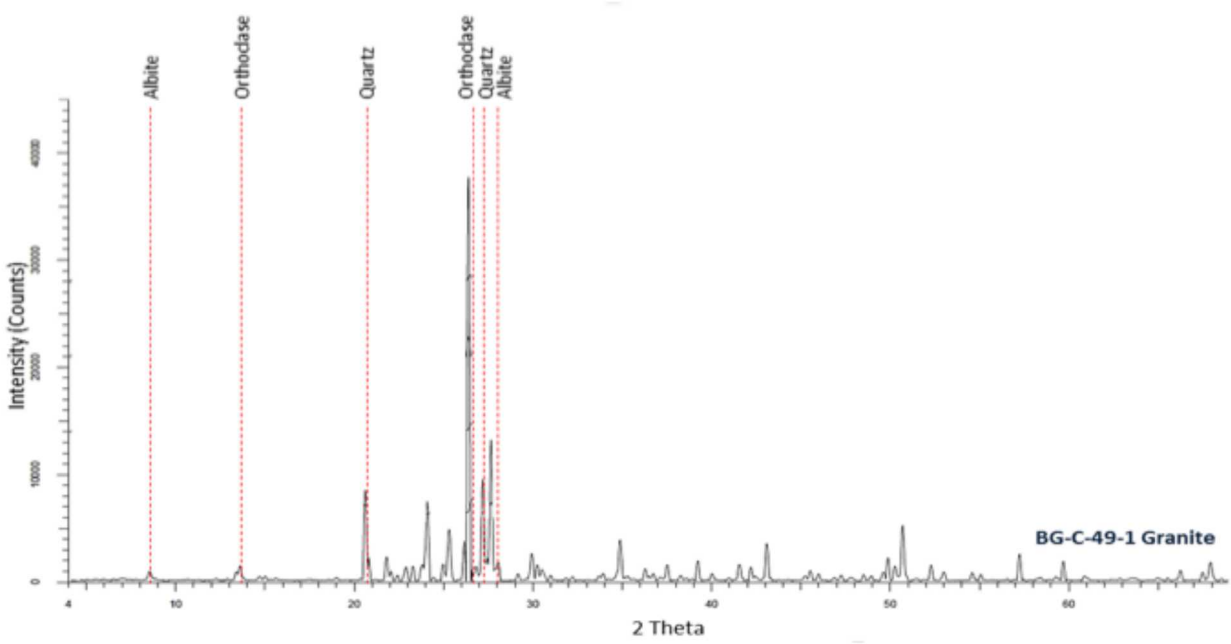

Figure 9-1. XRD pattern for the Grimsel granodiorite. The peaks are labeled to their corresponding minerals and unmarked peaks belong to the corundum standard.

Synthetic Grimsel groundwater: Synthetic groundwater (Table 9-4) was created to mimic the pore water found in the Grimsel Granodiorite (Missana & Geckeis, 2006). This solution has a pH of around 7.5 and the initial chemistry is reported in Table 9-4.

Table 9-4. Synthetic groundwater chemistry used in the IEBS experiments.

Components	Concentration (M)
Na_2SO4	$9.08x10^{-4}$
KCl	$6.44x10^{-5}$
$MgCO_3$	$5.06x10^{-4}$
$NaHCO_3$	$3.25x10^{-3}$
$CaCl_2$	$1.72x10^{-4}$
H_4SiO_4	$5.73x10^{-4}$

9.4.2 Results from IEBS-1 to IEBS-2 Experiments

9.4.2.1 Aqueous Geochemistry

Water samples were collected periodically during the course of each experiment. The aqueous geochemistry results are reported and plotted in Appendix B, and described below.

pH

The starting solution for the IEBS experiments, Grimsel Granodiorite groundwater, has a pH of ~7.5. The pH of the fluid periodically extracted from the reaction vessels dropped over the course of both experiments. The pH of IEBS-1 initially dropped to ~7, and then remained ~6.5 for the experiment

duration. Experiment IEBS-2 had a slightly more acidic solution during the middle of the experiment: the pH dropped to ~5 by week 3 and then increased to ~6.2 by the end of the experiment (Figure 5).

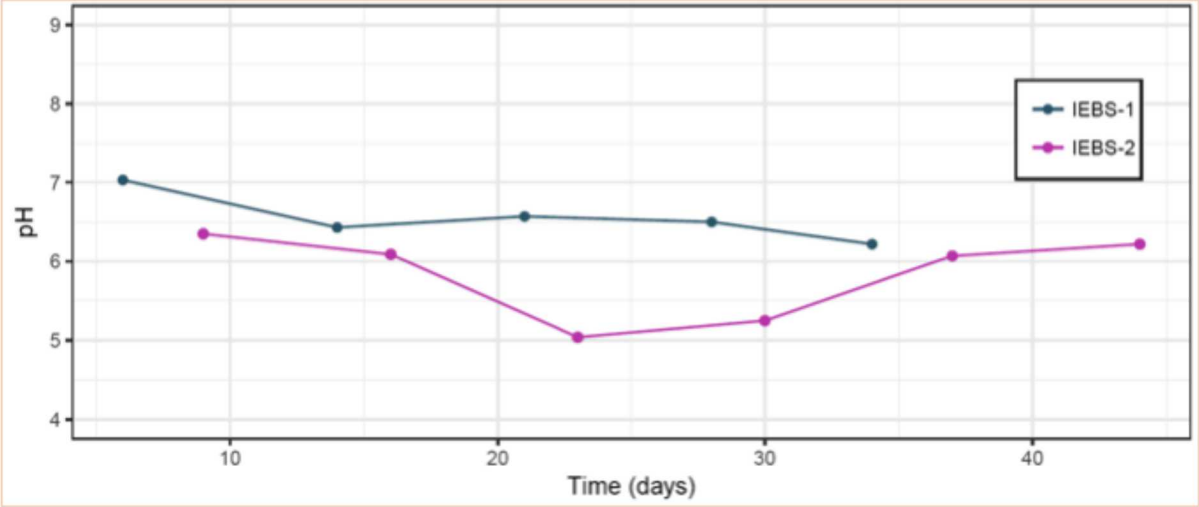

Figure 9-2. Solution pH from fluid collected throughout the duration of each IEBS experiment

Cations

K+, Na+: In IEBS-1, the concentration of K^+ and Na^+ in solution decreases steadily during the experiment. The K^+ concentration for both filtered and unfiltered aliquots is initially ~2 mg/L and decreases to ~1.5 mg/L by week 6. The [Na^+] is ~150 mg/L at week 1 and reaches 120 mg/L by week 6. In IEBS-2, the unfiltered K^+ concentration initially increases from ~1.7 mg/L in week 1 to ~2.2 mg/L in week 2 before dropping to between ~1.4–1.7 for the remainder of the experiment. The [Na^+] decreases from ~140 mg/L to ~100 mg/L over the 6 week experiment. The filtered results show a large spike in [Na^+] and [K^+] around week two to 2000 mg/L and 100 mg/L, respectively. As this spike is not observed in the unfiltered results, it is likely not representative of chemical changes in the sample.

Ca2+: In IEBS-1, the Ca^{2+} concentration in the filtered and unfiltered sample decreases steadily from ~2.0 to 1.0 mg/L over 6 weeks. The [Ca^{2+}] in the unfiltered sample in IEBS-2 is ~2.0 mg/L at the experiment start, drops to ~1.0 mg/L by week 3, and increases steadily to ~1.5 mg/L by the end of the run. The filtered sample shows a spike to ~90 mg/L around week 2.
SiO_2: The SiO_{2aq} concentration in IEBS-1 is higher in the filtered vs. unfiltered sample. Both stay between ~400 and 700 mg/L. The unfiltered results show an initial drop in concentration (weeks 1–3 followed by and increase to similar values as observed in the filtered sample by weeks 4 and 5 (~650–700 mg/L).
The filtered and unfiltered results from IEBS-2 show the same patterns for aqueous SiO_2. Concentrations remain around ~600 mg/L with the exception of a dip to ~500 and ~100 mg/L for unfiltered and filtered sample, respectively.

Fe^{2+}: The [Fe^{2+}] in both IEBS-1 and IEBS-2 remains relatively constant between ~0.25 and 0.75 mg/L for the majority of both experiments.

Anions

Cl⁻: The chloride concentration in IEBS-1 is ~32 mg/L at week 1, decreases to ~18 mg/L by week three, and stays around the same value for the run duration. The [Cl^-] in IEBS-2 follows a similar patterns: chloride decreases from ~22 mg/L to ~16 mg/L from week 1 to week 3, and next remains constant for the rest of the experiment.

***SO_4^{2-}*:** The sulfate in both IEBS-1 and IEBS-2 follows the same trend as the chloride concentration. In both experiments, the [SO_4^{2-}] decreases from week 1 to week 3, and then remains relatively constant for the remaining 3 weeks. The sulfate concentrations in IEBS-1 and IEBS-2 range from ~200 to 170 mg/L and 350 to 200 mg/L, respectively. The solutions from IEBS-1 and IEBS-2 were characterized by a strong sulfur smell.

9.4.2.2 XRD Patterns

The reaction products from both experiments (IEBS-1, IEBS-2) have similar XRD peak patterns (Figure 9-3). The main peaks correspond to quartz, feldspar (albite, anorthite), and muscovite. There are no obvious differences in peak height or location in the XRD results from the two experiments.

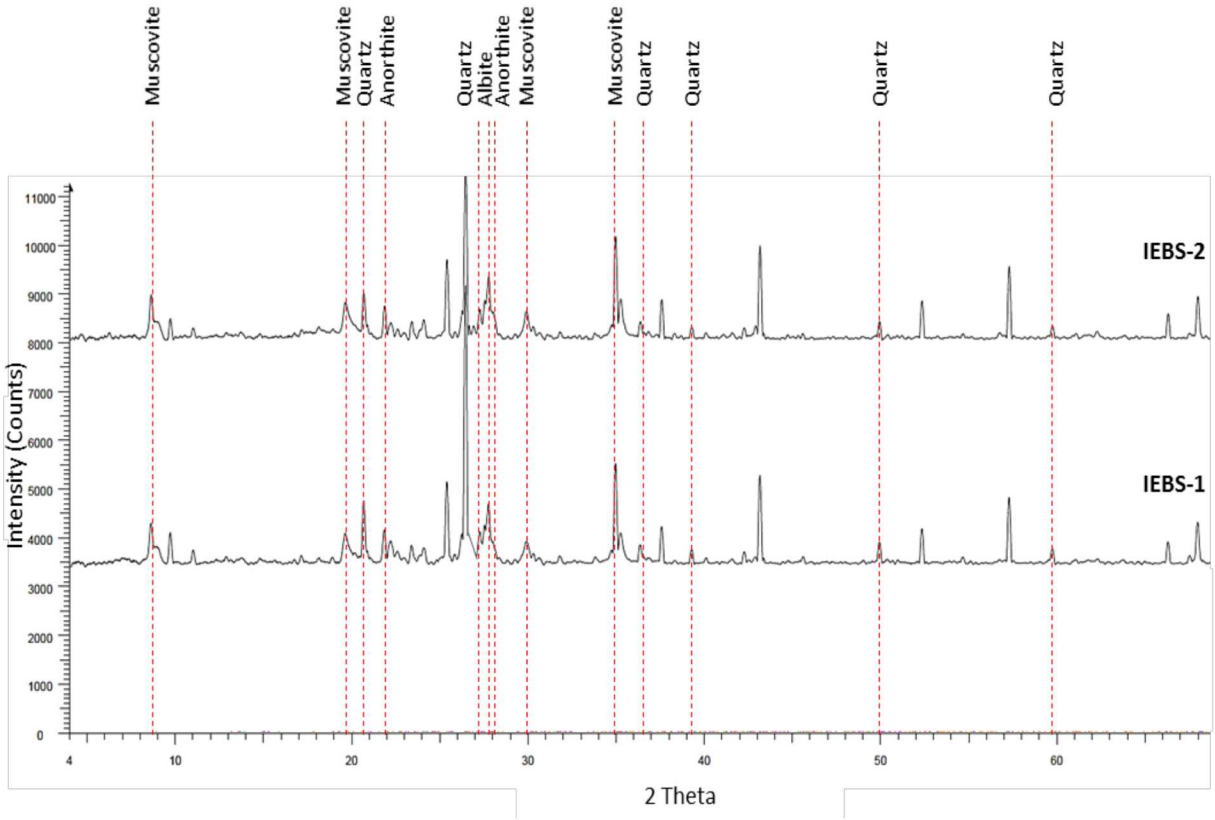

Figure 9-3. XRD pattern for IEBS-1 and the IEBS-2. The peaks are labeled to their corresponding minerals and unmarked peaks belong to the corundum standard.

9.4.2.3 QXRD Results

The QXRD results for IEBS-1 and IEBS-2, compared to the starting Wyoming bentonite and Grimsel Granodiorite, are reported in Table 9-5. The QXRD results show some major differences from the XRD peak patterns and are discussed below.

IEBS-1. The QXRD results from experiment IEBS-1 report smectite, feldspar (orthoclase, albite), muscovite, and quartz. Anorthite, which was observed in the XRD results, is not present in the QXRD data. In addition, both smectite and muscovite as observed in the QXRD results, whereas only muscovite was recognized in the XRD peak patterns.

IEBS-2. The QXRD results from the IEBS-2 reaction products include feldspar (orthoclase, albite, anorthite), muscovite, and quartz. Orthoclase was not observed in the XRD peak results.

Table 9-5. Quantitative X-Ray Diffraction (QXRD) analyses of the buffer clay (Wyoming Bentonite) the wall rock (Grimsel Granodiorite) and product results of experiments IEBS-1 to IEBS-2.

	Wyoming Bentonite	BG-C-49-1 Granite	IEBS-1 Bentonite only	IEBS-2 316 SS
			6 weeks 250°C	6 weeks 250°C
Analcime / Wairakite	b.d.l.			
Clinoptilolite	12.0			
Smectite	66.4		11.73	
Kaolinite	b.d.l.			
Albite		25.14	14.81	4.87
Plagioclase	8.3			
Orthoclase		30.84	19.51	9.47
Anorthite				43.55
K-Feldspar	b.d.l.			
Biotite	2.8			
Muscovite			28.02	23.68
Chlorite	b.d.l.			
Calcite	5.5			
Dolomite	+			
Quartz	0.9	44.02	26.17	18.68
Cristobalite/ Opal-C	1.8			
Pyrite	0.4			
Siderite	1.8			
Total:	100.0*	100.00	100.24	100.25

Values are in weight percent, *b.d.l. = below detection limit,* * represents data set was normalized to 100.0, (+) represents material detectable but below 0.5 wt. %.

9.4.2.4 SEM/EDS Results

Reaction products, including loose powder, epoxy mounts, and thin sections, from the two IEBS experiments were characterized using the scanning electron microscope and qualitative elemental abundances were evaluated using EDS. The SEM images are presented in Appendix D and described below.

The SEM images of IEBS-1 and IEBS-2 reaction products show similar features. In both, montmorillonite clay is observed to transition to smectite (Figure D-1A, B; D-4A, B). Spherical crystals are embedded in the fine-grained clay matrix (Figure D-1C, D, E; D-2C, D; D-3A, C; D-4B, C, D, E; D-6B, C). The EDS analyses of these crystals reveal large Ca peaks, with smaller Si, Al, C, and F peaks. The composition of these unknown phases is discussed further in the next section (3.2.5 Electron Microprobe Results). The unknown Ca-phase is more abundant in IEBS-2 than IEBS-1 (Figure 9-4). Feldspar surfaces are observed to be variably corroded (Figure D-1F). Glass shards (clinoptilolite) that have a "fishbone" morphology and are preserved in both reaction products (Figure 9-4).

Images of the 316 SS coupons from IEBS-2 (IEBS-2-steel) show two layers of mineral growth that formed perpendicular to the steel surface (Figure 4). Fe-saponite forms directly adjacent to the pitted steel surface (~30 μm) (Figure D-6A) and chlorite is observed to form a thin layer outside of the Fe-saponite (~7 μm) (Figure 4). Sulfide minerals, such as pyrrhotite are also observed (Figure D-6A).

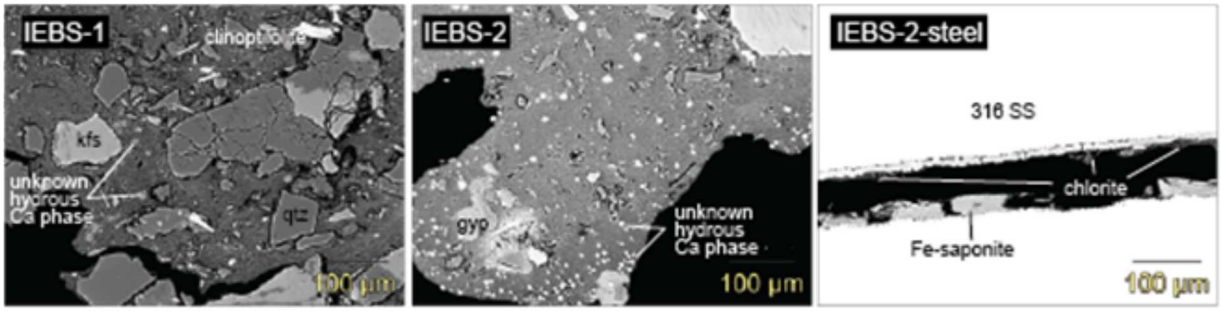

Figure 9-4. Backscattered electron images of thin sections of IEBS-1 and IEBS-2 reaction products and post-reaction polished 316 SS coupons. Abbreviations: gyp, gypsum; kfs, K-Feldspar; qtz, quartz.

9.4.3 Electron Microprobe Results

Reactions products from IEBS-1, IEBS-2, and IEBS-2-steel were analyzed via electron microprobe (EMP) to determine the major element composition of mineral phases. The EMP analyses primarily targeted the clay matrix, steel alteration products, altered glass shards, and other authigenic minerals. The EMP results are reported in Appendix C and described below.

Clay matrix. The fine-grained groundmass of the reaction products of IEBS-1 and IEBS-2 have similar major element compositions. Both contain ~60 wt. % SiO_2, 20 wt. % Al_2O_3, 5-6 wt% FeO and 1-2% MgO, and ~1% of Na_2O, ~0.3 K_2O, 0.2-0.5 wt. % CaO, and 0.2 wt. % F.

Clinoptilolite. Glass shards present in the precursor bentonite clay were altered to the zeolite clinoptilolite. The Si/Al ratios for the clinoptilolite are dominantly between 4 and 6, with the exception of one analysis with Si/Al = 7.5. The Na/(Na+Ca) values range from 0.55 to 0.75 (Figure 9-5).

Calcium (aluminum) silicate hydrates (tobermorite, zeophyllite?). In both IEBS-1 and IEBS-2, <10 µm round mineral grains were observed with the fine-grained matrix. The grains in IEBS-1 were too small to analyze, but some grains in IEBS-2 were large enough to target. However, the small size and beam sensitivity of this mineral made obtaining EMP analyses difficult. The collected data indicate low SiO_2 wt. % (~12 wt. %) and Al_2O_3 (~1wt. %) and very high CaO (~48%). The low SiO_2 content may be

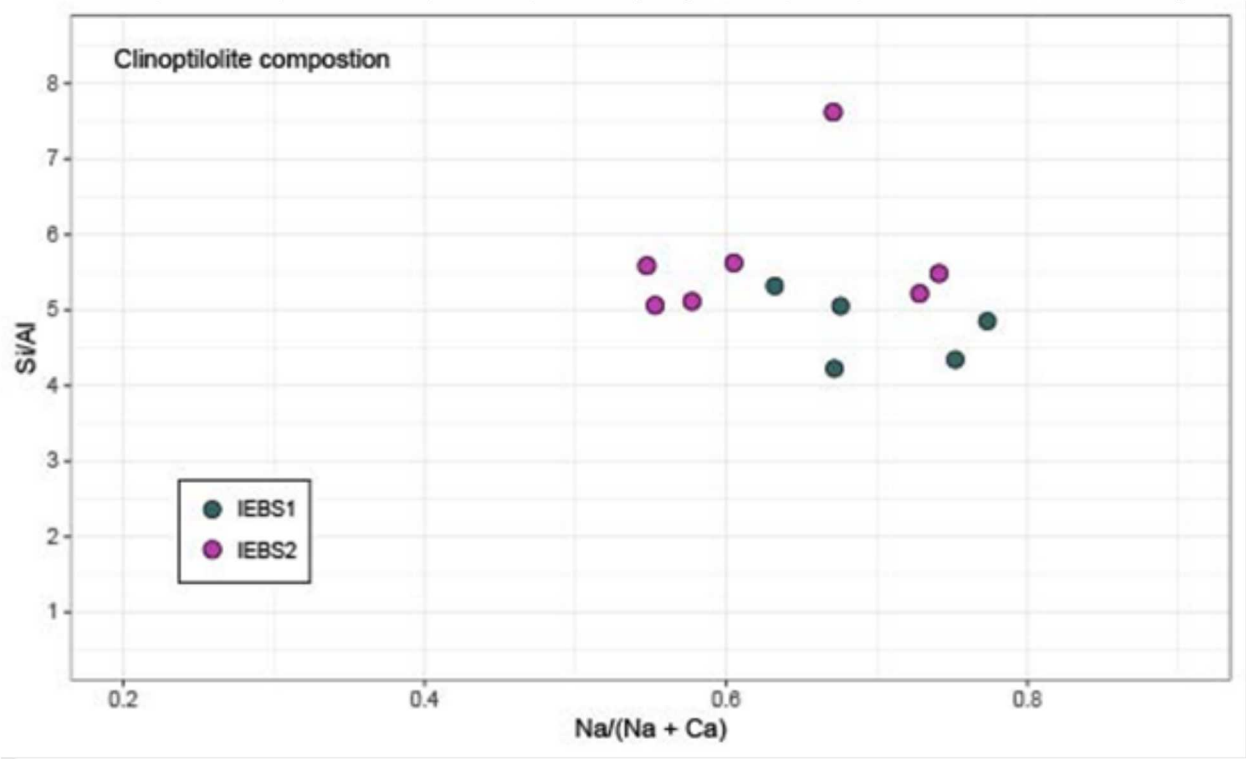

Figure 9-5. Clinoptilolite compositions in experiments IEBS-1 and IEBS-2 analyzed by EMP.

due to sample decrepidation in the beam line prior to SiO_2 analysis. These minerals could be seen actively being destroyed during analysis. Fluorine is present in trace amounts (~0.2–1.2%) Low oxide totals (<60%) indicate the likely presence of H_2O. In addition, EDS analyses demonstrate presence of CO_3. Based on the composition and rounded crystal form, this mineral is likely a calcium (aluminum) silicate hydrate (C(A)SH) and may be identified as mineral zeophyllite ($Ca_4Si_3O_8(OH,F)_4•2(H_2O)$) or tobermorite ($Ca_5Si_6O_{16}(OH)_2•4(H_2O)$), with a small carbonate component.

Steel/Fe alteration. Mineral growth is observed at the surface of the 316 SS coupons in IEBS-2 and around the FeO buffer material in both IEBS-1 and IEBS-2. Fe-saponite is observed to form on the steel interface, and a thin chlorite rim forms outside of the saponite. Stilpnomelane rims the FeO buffer material. The composition of the authigenic Fe-rich minerals is plotted in Figure 9-6 shows the variation in FeO + MgO wt% versus SiO_2 wt% for these alteration minerals.

9.5 Discussion

9.5.1 Grimsel Granodiorite interactions with Wyoming Bentonite

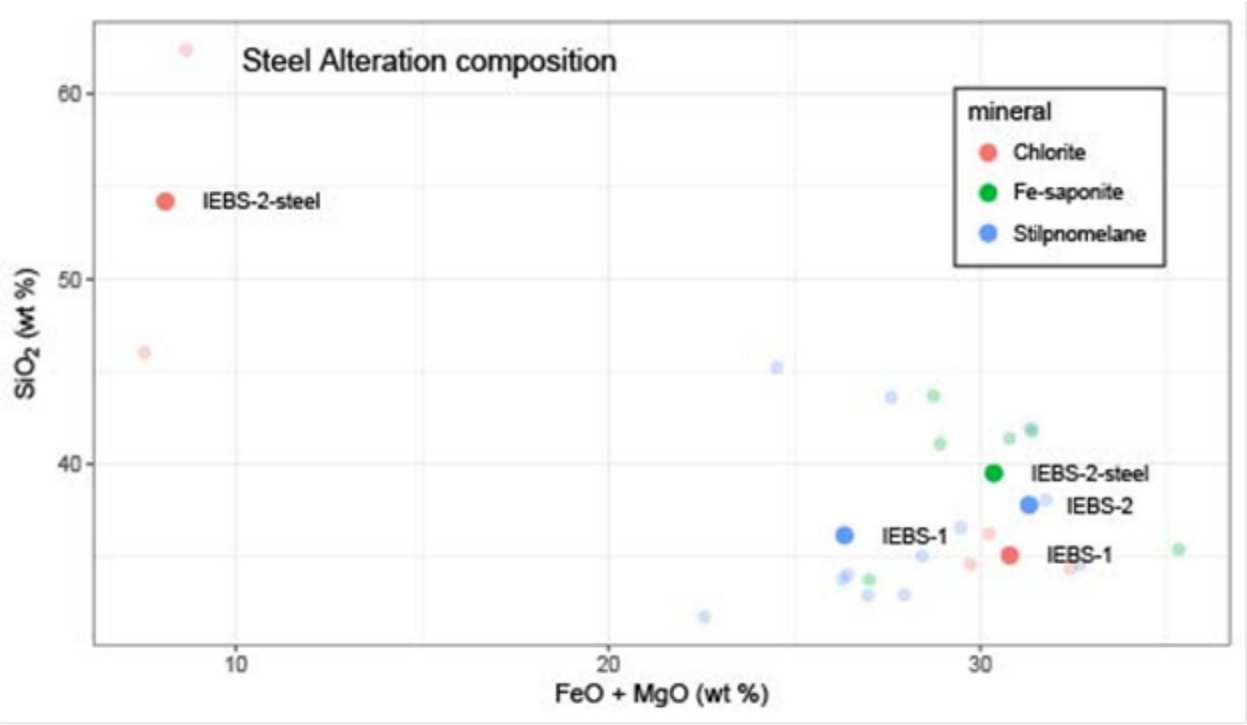

Figure 9-6. Variation in wt. % FeO and MgO vs. SiO_2. Each point corresponds to a single analysis, and the bold points correspond to averages for all data from each experiment.

The reaction products formed in the two IEBS experiments include a fine-grained, recrystallized clay matrix with variably altered phenocrysts derived from the starting Grimsel Granodiorite and Wyoming Bentonite, such as feldspars, micas, and quartz. Other authigenic minerals include calcite, quartz, gypsum, and a C(A)SH phase. The following describes our preliminary observations on hydrothermal mineralization and alteration in the IEBS experiments.

Phyllosilicate minerals. SEM imaging of loose powder mounts of the IEBS reaction products show fine-grained clay transitioning to foily phyllosilicate minerals (sericite?) (e.g., Figure D-1A). In addition, the QXRD and XRD analyses of the reaction products show the presence of mixed muscovite and smectite. However, the clay matrix is too fine grained for individual mineral identification. The EMP analyses from the clay matrix of both IEBS-1 and IEBS-2 have very similar compositions (Appendix C). The high silica content of the matrix (~60%) may suggest that fine-grained quartz is interlayered with the phyllosilicate minerals. In terms of alkali elements, the matrix is most enriched in Na (0.15–0.17 atoms per formula unit) in comparison to K (0.02–0.03 apfu) and Ca (0.02–0.03 apfu). The bulk chemistry of the starting

materials (i.e., Na-montmorillonite in the Wyoming Bentonite) may prevent illitization due to low K+ in the system. This is a similar result to our previous experimental work with Wyoming Bentonite ± Opalinus Clay, in which illitization was prohibited by the bulk chemistry of the system (Cheshire, et al, 2014)

Feldspars

Low temperature authigenic feldspars have been identified in both experimental runs; however, further characterization is needed in future experiments to understand their significance.

Calcium (aluminum) silicate hydrates

In both experiments with Grimsel Granodiorite and Wyoming Bentonite, spherical, C(A)SH phases formed within the fine-grained clay matrix. Small amounts of this mineral are observed in IEBS-1, and it is abundant in IEBS-2 (Figure 9-4). Based on the composition of this mineral (Appendix C), it is likely a hydrated calcium silicate, such as zeophyllite ($Ca4Si_3O_8(OH,F)_4•2(H_2O)$) or tobermorite ($Ca_5Si_6O_{16}(OH)_2•4(H_2O)$).

The formation of C(A)SH minerals contrasts with the products of previous experiments with Wyoming Bentonite ± Opalinus Clay host rock. In these experiments, zeolites (analcime–wairakite solid solution) formed, that have similar morphologies and textural contexts. However, the EMP analyses of the spherical minerals formed in the IEBS experiments had significantly lower SiO_2 and Al_2O_3 content and very high CaO. Very Ca-rich minerals, such as tobermorite, have been observed in experiments involving bentonite and cement with highly alkaline bulk chemistries and pH > ~10 (Savage et al., 2007). In comparison, the solution pH over the course of the IEBS experiments did not exceed ~7 (Figure 9-2) and the experiments did not involve cement. Future investigations will focus on why C(A)SH minerals formed instead of zeolites in the IEBS experiments with Grimsel Granodiorite and Wyoming Bentonite.

H_2S Generation

The IEBS experiments were accompanied by strong $H_2S_{(aq,g)}$ smells during the course of the 250 °C experiments. The $H_2S_{(aq,g)}$ is most likely related to pyrite solubility from the starting Wyoming Bentonite in a chloride-bearing solution (Crerar et al. 1978; Ohmoto et al. 1994) and the sulfate concentration in the synthetic Grimsel groundwater solution. The reducing nature of the experimental system easily preserved the H2S(aq,g) species. Pyrite contents obtained by QXRD analyses for the Colony Wyoming bentonite (0.4 wt %) are listed in Table 5. Grimsel Granodiorite lacks pyrite, but the synthetic Grimsel groundwater contains appreciable SO_4^{2-} (Table 4). Sulfide-induced corrosion of the waste canisters is the primary concern for the Swedish repository systems (Börjesson et al. 2010), therefore the Swedish Nuclear Fuel and Waste Management Company (SKB) have emplaced fairly strict sulfur specifications (sulfide content < 0.5 wt. %; total sulfur < 1 wt. %) for the bentonite buffer used in their repositories (Börjesson et al. 2010).

pH effects

In both IEBS experiments, the solution starts with a pH of 7.5 and ends ~6. In IEBS-2, the pH drops to ~5 in the middle of the 6 week experiment (Figure 9-2). Many of the mineral-forming reactions described above are strongly influenced by the pH of the system. Most mineral reaction rates that are of concern to a repository are increased under high pH systems. Chermak (1992) showed that under pH conditions of 11–13, Na-rectorite was formed at 150–200 °C within 17 days. Fully formed Na-mica (paragonite) developed after 32 days. Work from Eberl and Hower (1977) and Eberl (1978) do not show illitization until 260–400 °C at quenched pH's ranging from 4–5. These observations are consistent with the current IEBS research; illitization was not observed and Na-rich phyllosilicates formed.

The formation of C(A)SH minerals may also affect the pH of the system. Savage et al. (2002) describe the formation of tobermorite with the generalized reaction:

$$\mathbf{Ca^{2+} + SiO_{2(aq)} + H_2O \rightarrow tobermorite + H^+}$$

in which H^+ is produced. Thus, the formation of C(A)SH minerals, such as tobermorite, may buffer the solution to lower pH values. Savage (1997) reported that zeolite formation within bentonite in contact with cement occurs at lower pH values and C(A)SH mineral formation is favored at high pH (> 11.5). In the IEBS experiments C(A)SH minerals formed, but solution pH values remained below ~7 for the duration of the run. The formation of C(A)SH minerals at low pH (<7) in the IEBS experiments is at odds with previous experiments, and will be the subject of our future investigations.

9.5.2 Steel interface mineralization

The following mineral phases have been previously identified (Caporuscio et al., 2014) as growing at the interface between bentonite backfill and various steels: Fe-saponite ($(Ca/2,Na)_3(Fe^{++})_3(Si,Al)_4O_{10}(OH)_2$, pentlandite ($(Fe,Ni)_9S_8$) (Figure 5), chromite ($Fe^{++}Cr_2O_4$), pyrrhotite (FeS), millerite (NiS). We have just recently identified another interface material: stilpnomelane (Figure 9-7). This Fe-bearing phase occurs in IEBS mantling iron metal (one of our solid buffer materials).

Although stilpnomelane is a common metamorphic mineral and occurs over a wide P, T spectra (Winkler, 1976) there is a dearth of occurrences reported in experimental literature. Similar experimental work by Ferrage (2011), Mosser-Ruck et al. (2010), Guillaume et al. (2003) and Meunier et al. (1998) do not report this mineral phase in their reaction products. The chemical formula of stilpnomelane [$K\ (Fe^{++},Mg,Fe^{+++})_8(Si,Al)_{12}(O,OH)_{27}$] indicates that iron occurs in both oxidation states. Given that the iron metal in our experiments (Figure 9-7) is mantled first by an iron oxide (magnetite?), followed by an Fe sulfide (pyrrhotite) and finally by stilpnomelane, there is a potential that micro-domains of differing oxygen fugacity may be at play. This phenomena and mineral genesis deserves further investigation concerning iron corrosion.

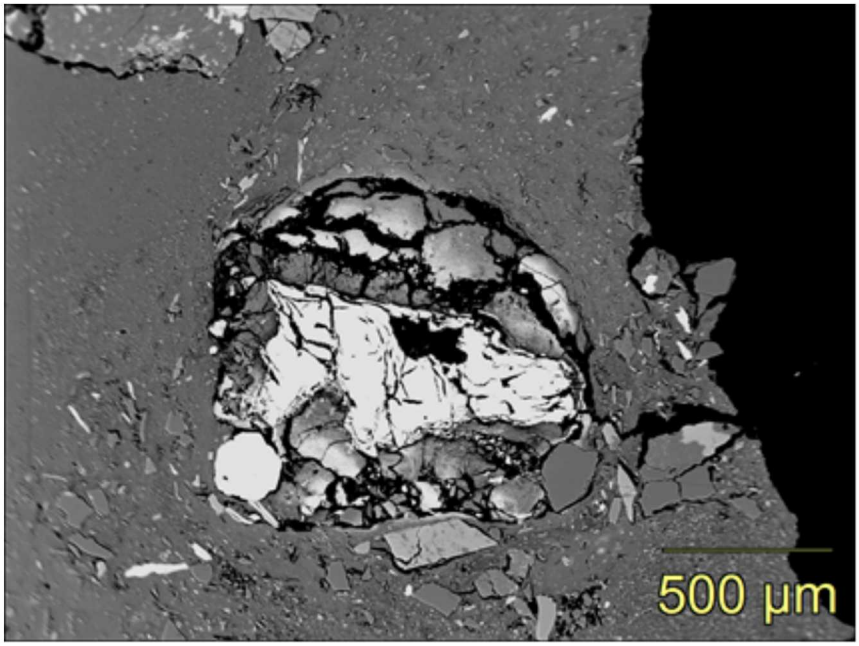

Figure 9-7. BSE image of iron metal with concentric alteration zones from IEBS-1. Bright white core is remnant iron metal, dark grey is iron oxide, remaining mottled intermediate grey is stilpnomelane.

9.5.3 Steel/bentonite interface reactions

Results from these experiments have shown the more dynamic environment associated with this system is at the bentonite-metal interface. Fe-rich phyllosilicates (i.e., trioctahedral, Fe-rich saponite and chlorite) are crystallized on steel surfaces forming a reactive substrate with a high surface area compared to the original steel surfaces. It is evident that the formation of these surface bound minerals is from the direct crystallization from solution in the localized environments surrounding the metal plates. The reaction is stylized in Figure 9-8. However, it is uncertain to what extent these authigenic minerals will have an effect on the repository system.

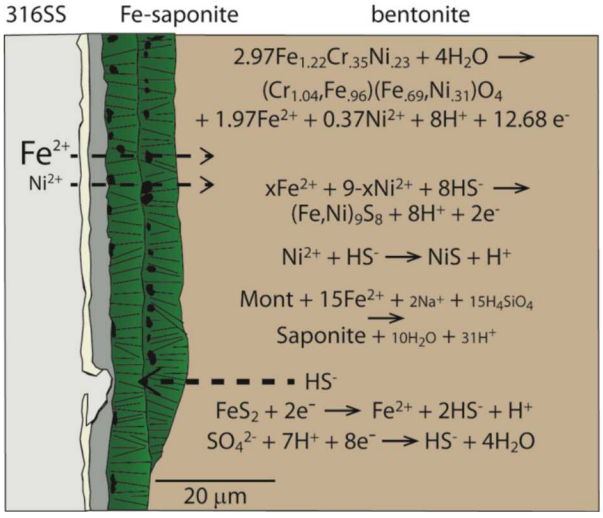

Figure 9-8. A stylized representation of phyllosilicate mineral growth at the steel interface. Of particular interest is the reaction Montmorillonite → Fe-saponite.

Synthetic Fe-saponites have been crystallized in dilute solutions and gels of silica, Fe-, Al-chlorides at temperatures up to 850 °C and pH of 8.5–9.5 (Kloprogge et al. 1999). This is consistent with a partial dissolution of the steel plates contributing ferrous iron into a fluid phase with silica and aluminum, thereby facilitating Fe-saponite (smectite) crystallization with the steel surfaces acting as a growth substrate. Further, Fe-saponite alteration into chlorite has been suggested (Mosser-Ruck et al., 2010) in the presence of ferrous iron at temperatures approaching 300 °C and near-neutral pH. This was confirmed by Mosser-Ruck et al (2016) through long duration experiments (up to 9 years).The authors were able to demonstrate that smectite is consumed by dissolution to produce chlorite (chamosite) by precipitation. Mosser-Ruck et al. (2016) depicts this reaction by:

3 smectite + 3 Fe +4H_2O → 1 chlorite + 3 quartz + 2 albite +3H_2 + zeolite

Furthermore, we were able to gather microprobe analyses (Appendix C) and images indicating chlorite grows in contact with the steel (where Si is relatively deficient) and then Fe-saponite with a higher Si content (Figure 8).

The stainless steel interaction with bentonite via congruent dissolution/oxidation can be detailed by the following reactions.

Stainless steel dissolution

$Fe_{1.22}Cr_{0.37}Ni_{0.22}$ → $1.22Fe^{2+} + 0.37Cr^{3+} + 0.22Ni^{2+} + 3.99e^-$

Smectite evolution

$Fe^{2+} + Ni^{2+} + Cr^{3+} + H_2S_{(aq)} + (Na,K,Ca)_{0.33}(Al_{1.67},Fe^{3+}_{0.20},Mg_{0.13})Si_4O_{10}(OH)_2$ → $(Fe,Ni,Cr)_9S_8$ +

Smectite pentlandite

$(Na, K, Ca)_{0.33}Fe_3(Si_{3.67},Al_{0.33})O_{10}(OH)_2$

Fe Saponite

The mechanisms and rates of stainless steel dissolution will be an area of future study. In addition, future IEBS experiments will involve other types of stainless steel (304 SS, LCS).

9.6 Conclusions

There have been a large number of investigations on bentonite stability under various repository conditions (Madsen, 1998; Meunier et al., 1998; Guillaume et al., 2003; Guillaume et al., 2004; Mosser-Ruck et al., 2010; Ferrage et al., 2011). Yet, there remain questions regarding bentonite's overall stability and more importantly whether montmorillonite will remain relatively unaltered through the repository life-time.

After initial used-fuel emplacement there will be a pulse of heat flowing into the bentonite buffer producing an environment in which montmorillonite is typically not stable. It would be expected during the early stages of canister emplacement that silica saturation and exchange reactions will take place. However, the relatively dry environment would significantly restrict the mineral reactions due to the limited ion mobility and early saturation. As temperatures increase to peak temperature (currently unknown and will be determined during repository design), various possible zeolite reactions (mordenite, laumontite, analcime, wairakite formation) have the potential to occur if repository conditions shift to the zeolite metamorphic facies (typically starts at 50–150 °C; 100–500 bars). These zeolite reactions, along with silica saturation reactions, will control the pore water solution chemistry and determine any further mineral alteration. Illite formation can still progress, if a K-source is available, but, K-source stability with respect to the repository conditions will determine the illitization rates. It is expected that the initial heat pulse should start to decay after about 100 to 1,000 years (Wersin et al., 2007). After the high temperature pulse passes and temperatures begin to decrease, retrograde reaction have the potential to further change the high temperature mineralogy. As observed in current work, no significant retrograde reactions took place, but as with any experimental work slow kinetics of such reactions make them difficult to show experimentally. It would be expected silica saturation is maintained at continuing lower temperatures by releasing silica from solution, cementing the bentonite. Retrograde zeolite reactions are expected, but currently the extent of such reaction and types are unknown.

There have been a number of similar investigations on bentonite stability under various repository conditions and in contact with various metals replicating possible canister compositions (Guillaume et al., 2003; Guillaume et al., 2004; Wilson et al., 2006; Mosser-Ruck et al., 2010; Ferrage et al., 2011, Mosser-Ruck et al., 2016). Partial dissolution of the steel plates contributing ferrous iron into a fluid phase with silica and aluminum facilitates Fe-saponite (smectite) crystallization. Bentonite not in contact with the steel waste container does not show the formation of these Fe-rich phyllosilicates. The occurrence of Fe-rich phyllosilicates most likely will not form in the bentonite away from the waste container because there is a low abundance of iron in the system. There are two possible scenarios for Fe-saponite formation: 1) direct crystallization in a Fe- and Si-rich solution as a result from bulk mineralogy influences or 2) Fe^{++} montmorillonite interactions breaking down montmorillonite and producing Fe-saponite. The latter mechanism would be a deleterious reaction to the overall repository as montmorillonite is primary mineral in the barrier.

In this work, we consider the impact host rock (i.e., Grimsel Granodiorite from Switzerland) will have on the bentonite barrier. Several mineral alterations were observed in the heating of Grimsel Granodiorite. The primary mineral reaction is the retention of clinoptilolite in volcanic glass shards and formation of a calcium (aluminum) silicate hydrate (C(A)SH) mineral (tobermorite, zeophyllite?) in the Wyoming Bentonite. Interpreting clay mineral evolution within Grimsel materials is complicated due to the variety of clay minerals present in the Grimsel experimental systems. It does appear that muscovite genesis does occur within the bentonite fraction in the mixed reactions at the current experimental conditions. With any of these experiments representing repository system, kinetics is always an issue that has to be taken into account when interpreting data.

This document summarizes the EBS Grimsel Granodiorite wall rock experiments IEBS-1 and IEBS-2 and attempts to compile pertinent 1) SEM images, 2) XRD (QXRD and clay determination) analyses, 3) electron microprobe data for major mineral phases, and 4) aqueous geochemistry data from both starting materials and the two experiments conducted so far.

Concepts developed so far include:

- Illitization of smectites may be restricted due to the bulk chemistry of the overall system,
- The interface between bentonite and steel develops a well characterized new mineral phase, Fe-saponite (especially at 300 °C), that grows perpendicular to the steel surface,
- Another Fe layered phyllosilicate, stilpnomelane, grows in the presence of native iron (one of our solid buffer materials), which alludes to the idea that oxygen fugacity may be quite variable, depending on scale,
- Zeolites transform as temperature increases. Mine-run bentonite contains clinoptilolite, which was preserved in relict glass shards
- C(A)SH minerals formed within the Wyoming Bentonite mixed with Grimsel Granodiorite
- No abundant zeolites have been observed
- Further work to understand formation of C(A)SH minerals at relatively low pH (< 7)

Research needs to be emphasized in the following areas for FY19:

- Continue to build an experimental data base of Grimsel Granodiorite / EBS materials
- Perform transmission electron microscope (TEM) investigation looking at very local chemical changes within a pit corrosion metal surface.
- Corrosion of steels/ interface silicate mantling effect must remain a focus of the upcoming year.
- Incorporate results into Generic modeling codes.

This database, along with summary conclusions will be of use to other experimental teams on the DOE complex, system modeler, and the international repository science community.

10. CONCLUSIONS

10.1 Chapter 2 – Investigating the Thermal Limit for Bentonite Buffer

Investigations of the thermal limit of a clay repository are very important for the design of a nuclear waste repository. A reliable evaluation of the impact of a long-term geochemical on mechanical behavior, using a coupled THMC model, is critical for studying whether a clay repository can sustain high (>100 °C) temperature. To increase the model reliability, we first implemented a more mechanistic constitutive relationship for C-M coupling, the BExM, then calibrated the key parameters based on the results of the laboratory test, which were used for a large scale generic model. In FY 18, we simulated a series of swelling pressure tests, in which partially saturated FEBEX bentonite was saturated with various salinity solutions. By using simulations to reproduce the measured swelling pressure, we were able to calibrate the parameters related to the C-M coupling, which affect the smectite volume fraction, and exchangeable cations and the effect of the ionic strength on the stress were taken into account. Eventually, the THMC model, with calibrated C-M coupling parameters, was used to perform simulations for the generic case of nuclear waste disposal. The following conclusions have been drawn from the modeling results:

- Dissolution of smectite leads to the decrease in the volume fraction of smectite, which, in turn, decreases the stress. The new model predicts the reduction of exchangeable sodium in the interlayer, which is different from what was found in FY17. The change in exchangeable cations also causes the decrease in stress. Infiltration of higher salinity water from the surrounding clay formation to the EBS bentonite leads to the increase in osmotic suction and subsequently lowers the stress. The combination of these three effects as a whole reduces both the total stress and the effective/net stress in the bentonite buffer in the “high T” cases. The difference between the computed stress in bentonite with C-M coupling (THMC”) and without C-M coupling (THM) ranges within 1 MPa.
- The THMC model, using BExM, showed less influence of the chemical effect on the stress compared to the previous THMC model with the extended linear swelling model (Zheng *et al.*, 2015). The primary reason is that a previous extended linear swelling model computed the swelling pressure as a linear state function of material’s saturation, which predicted a higher stress accumulation than the elasto-plastical model, such as BExM. The BExM model generates more plastical strain to resist the increased swelling stress, and the stress is redistributed in the material. The other reasons are: the mechanical-chemical coupling via BExM and the dissolution of smectite were factored in directly into the model via the volume fraction of smectite by means of modifying the bulk modulus for micro-structure, and the bulk modulus is a function of stress and changed significantly in the model. Moreover, the bulk modulus changes by smectite dissolution were overshadowed by the stress change.

The developed coupled THMC model has greatly improved our understanding of the coupled processes contributing to chemical and mechanical alteration in the EBS bentonite and NS argillite formations, which helped answer questions regarding the thermal limit of EBS bentonite in the clay repository. Nevertheless, the simulator for conducting modeling of coupled THMC processes causing the alteration of bentonite and clay formations needs to be further improved. In the remaining time of FY18 and in FY19 we are planning:

- To investigate chemical controls on montmorillonite structure and swelling pressure. After implementing C-M in TOUGHREACT-FLAC via BExM, we are going to evaluate how the chemical change controls the montmorillonite structure and swelling pressure. We are planning to investigate how exchangeable cations affect swelling of montmorillonite, to improve an empirical relationship describing this process, and to implement it in our simulator. Research will be conducted to calibrate model parameters. We also propose to conduct complementary experimental

and simulation studies to evaluate the swelling clay structure as a function of the solution composition, and to derive an improved constitutional model to describe variations of the swelling pressure in compacted clay barriers.

- To derive a reduced order model that can be integrated into the performance assessment model GDSA. The importance of bentonite alteration and its impact on mechanical behavior needs to be integrated to PA model to assess its relevance to the safety of a repository. Specifically, we will first implement the bentonite swelling models, such as linear swelling, state surface, BBM, and BExM into a parallel THMC simulator TREACTMECH, and will then derive a reduced order model based on the large number of THMC simulations.

We will also conduct other exploratory modeling studies, including the following activities:

- Numerical verification of the applicability of BExM with C-M coupling based on laboratory and field tests with bentonite other than FEBEX bentonite, and simulations of *in-situ* experiments. Model for Kunigel-V1 bentonite, which was used in the previous modeling study (e.g., Zheng et al., 2015) will be improved and the robustness of x C-M coupling via BExM will be tested.
- Comparing BExM simulations with computations by other available constitutive models to investigate the material behavior under the same environmental conditions and to better understand a possibility of using BExM for other materials.

10.2 Chapter 3 – THMC Modelling of the FEBEX Heater Test

The FEBEX *in situ* test, which lasted for more than 18 years, generated extremely valuable data for validating the coupled THMC model and improving our understanding of the factors and processes affecting the temporal and spatial evolution of the bentonite barrier over the course of long-term heating and hydration. In the FEBEX-DP project, Heater #2 was dismantled and extensive THMC characterization was conducted. The ultimate goal is to use THMC data from FEBEX-DP to validate THMC models and to enhance our understanding of coupled THMC processes in bentonite.

In FY18, after obtaining the geochemical data, including ion concentration in pore water of bentonite and granite, mineral phases and element contents in solid phase of bentonite, and detailed characterization of montmorillonite, the modeling efforts focused on the interpretation of geochemical data. The major findings from the current modeling work are as follows:

- Chemical data isimportant for calibrating the THM model. The model that is tested with more types of data is more reliable.
- The key coupling processes required to match the THM data and concentration of conservative species (e.g., chloride) include vapor diffusion, porosity change due to swelling, permeability change as a function of dry density (and porosity), and thermal osmosis.
- Because geochemical data in solid phases were either too scattered to constrain the model or incomparable with model outputs, the current model predominantly relied on the ion concentration in the aqueous phase to understand the geochemical change in the bentonite.
- The model matched the spatial profiles of most chemical species in the pore water of bentonite and granite, but discrepancies existed because of uncertainties in both the THMC model and the model used to infer aqueous extract data.
- Based on the match between model and data, an increase in sulfur was caused by the formation of anhydrite, and the higher content of calcium in the solid phase resulted from calcite precipitation. However, the model found no explanation of the increase in measured sodium content in the solid phase from the heater toward the granite and the decrease of magnesium content in the solid phase

from the heater toward the granite, which warrants the need for further investigation of both the THMC model and data.

- Measured mass fractions of illite in the illite/smectite mixed layer varied a great deal depending on the laboratory samples, and therefore showed no clear spatial trend and were indistinguishable from the reference bentonite. The model results showed a small amount of illite precipitation and montmorillonite dissolution in the vicinity of the heater, which is neither proved nor disapproved by the data.

In FY19, the chemical model will focus on getting a better understanding of the evolution of redox conditions, interaction between steel corrosion products and bentonite, and geochemical changes at the interface between the concrete and the bentonite. Specifically, the model will tackle the following problems:

- Modeling of the evolution of redox conditions in the bentonite barrier. A thorough understanding of the evolution of redox conditions, especially near the canister, is critical for studying canister corrosion and waste form degradation. However, the current modeling effort faces a great challenge of simulating redox-sensitive elements such as Fe^{+2}/Fe^{+3} transformation. Because of the difficulty of obtaining reliable concentration of these species, knowing their concentration in the initial pore water of bentonite before and after FEBEX *in situ* test is very challenging. It is expected that a synthesis of measured gas concentrations, biological data and redox sensitive minerals and aqueous species can help understand the evolution of redox condition in FEBEX bentonite.
- The model of the bentonite-canister interaction, causing the corrosion of the canister and interaction of corrosion products with bentonite will be improved, and the model will be tested against measured mineralogical phase changes in the bentonite and the canister.
- Bentonite-concrete interactions will be modeled to understand mineralogical changes at the interface between concrete and bentonite.

10.3 Chapter 4 – Developing Models for the HotBENT Field Test

Although current modeling work is either based on FEBEX bentonite (1D THMC in Section 3) or on a hypothetical case alone as described in Section 4, considering the similarity between FEBEX bentonite and MX80, major observations from current modeling work are likely qualitatively applicable to MX80. While it cannot be stressed enough that if MX-80 or other type of bentonite is used in HotBENT, THMC models for these bentonites are needed for more reliable calculation, current modeling work has the following implication to the final design of HotBENT in terms of the modeling work for HotBENT design and data collection in HotBENT.

Regarding the modeling work for the final design of HotBENT, the lessons learned from current modeling exercise and to potentially be applied to the final model are:

- *Porosity and permeability due to swelling/shrinkage are key HM coupling processes that need to be included in the model, even though modeling purpose is just TH process in the bentonite.* An increase in stress, swelling in the area near the host rock, and shrinkage in the area surrounding the heater are expected in the test.
- *Chemical processes are significantly affected by THM processes, but not vice versa.* Porosity and permeability changes due to swelling/shrinkage affect moisture movement and consequently the transport of chemical components and other reactions such as mineral precipitation/dissolution. It is therefore necessary to have a THMC model to study chemical alteration of bentonite. However, THM model will be adequate if the purpose of modeling is to evaluate THM or TH processes in the bentonite because current models show the porosity change due to mineral precipitation/dissolution to be minimal.

- *Porosity and permeability alteration due to swelling/shrinkage make it challenging to de-cpiple HM coupling from TH coupling.* It is challenging to represent HM coupling, i.e. porosity and permeability due to swelling/shrinkage, in a simplified manner (without resorting to include mechanical process for the purpose of simulating TH processes) because of the interactive coupling between HM process—stress and suction changes affect porosity and permeability and changes in porosity and permeability affect the evolution of stress and capillary pressure. Any sort of simplified representation of HM coupling lead to an inevitable loss of such interactive coupling.
- *Reliable prediction of THMC alteration in HotBENT would benefit greatly from more independently measured parameters.* Special attention is called for measuring intrinsic permeability (as a function of dry density), and capillary pressure function. For chemical calculation, concentration of chemical components in bentonite pore-water, detailed mineral composition and CEC are necessary. For mechanical calculation, bulk modulus and swelling capacity are necessary.

Regarding data collection in HotBENT, based on FEBEX *in situ* test and modeling work in this report, the following observations can be made:

- *Strong moisture re-distribution is expected during the cooling period* (time between heater shutdown and dismantling) and it will complicate the interpretation of test result.
- *THMC data at multiple locations and times are highly recommended*. One lesson learned from the THMC modeling of FEBEX *in situ* is that chemical data provide an important additional piece of information for calibrating a THM model. In addition, chemical data collected in two dismantling events provides better constraint of models than chemical data collected just once. Temporal evolution of temperature, pore pressure, relative humidity, stress at various locations, spatial distribution of water content, dry density, water saturation, pore-water concentration, mineral composition at various time (might have to be done through multiple dismantling events) will provide constraints on interpretations of the experiment.

In FY19, we will continue using THMC models to support the design of HotBENT. Specifically, the modeling work will focus on the following tasks:

- *Development of a 3D model that includes granite, bentonite, concrete (to separate different modules) and heater*. Up to now, the models are either 1D axi-symmetrical or 2D cross-sectional. They can be used to simulate the THMC evolution in the "hot" sections, but not the "cold" sections, which do not cross-cut the heaters. The 3D model will allow for examining the THMC evolution of bentonite at both "hot" and "cold" sections, and also for studying an interfacial area such as the concrete-bentonite interface.

- *Selection of a buffer material*. Currently, three materials, MX-80, Kunigel VI, Rokle bentonites, have been under consideration as the buffer material. Once the decision is made, THMC model will be developed specifically to simulate the performance of the selected bentonite. As revealed in this report, some phenomena can be generalized for different type of bentonite, but those related to geochemical processes, are largely bentonite-specific. As a result, THMC models for the selected bentonite will provide more support for the final design.

10.4 Chapter 5 – Benchamarking of Semianalytic Thermal Analysis Codes

The thermal analysis presents conduction-based thermal simulations for the emplacement of nuclear waste in a geological repository in bedded salt. Benchmark simulations were conducted to assess the validity of semi-analytical codes to perform thermal simulations. Two waste package configurations were analyzed with the same parameter values applied to all materials. The first configuration involves a single waste package emplaced in an infinite medium. The second configuration represents a repository layout with arrays of waste packages in different drifts. The investigation included use of the semi-analytical code LinSour used at DBE Technology in Germany, a Mathcad 14-based semi-analytical code used at Sandia National Laboratories, and the numerical code FLAC3D. These codes were used to calculate the temperature at the drift wall and waste package surface as a function of time for the two configurations.

- The results show that predictions of the three codes for Configurations 1 and 2 were comparable under identical initial and boundary conditions.

- A separate simulation was conducted with PFLOTRAN numerical code to test results of the Mathcad-based semi-analytical calculations for Configuration 1. The results of the separate simulation were also very close.

- Comparison of simulation results of the different software and simulation methods provided a confidence building measure for further analyses.

Future work in this area of benchmarking could include comparions of TH or THM models at the drift-scale or partial-repository scale.

10.5 Chapter 6 – Thermal Analysis for Repository Layout

Thermal-only, semi-analytical analysis was conducted for the disposal of spent nuclear fuel in alluvium host rock. The simulations were conducted in support of the Generic Disposal System Analysis (GDSA). The simulations were designed to provide estimates of temperature at the surface of the waste package and the drift wall to help decide repository layout for performance assessment analysis. The semi-analytical method is based on the approach developed for enclosed emplacement modes by Hardin et al. (2011, 2012).

- Thermal responses for pressurized water reactor (PWR) waste forms were investigated for a disposal concept in generic alluvium host rock. The output of interest is temperature at the surface of the waste package and at the drift wall.

- The analysis looked at effect of drift spacing, waste package spacing, backfill thermal conductivity, burnup, PWR assembly size, surface storage period.

- For all cases the plots show that temperatures significantly drop after the peak is reached due to thermal decay. The results show that the peak temperatures are reduced with lower thermal output, higher buffer thermal conductivity and longer surface storage time. Overall, thermal limits and other considerations for disposal in alluvium would help decide the repository layout.

10.6 Chapter 7 – TH Modelling to study Buffer Re-saturation

A preliminary numerical thermal analysis was performed for disposal of 12PWR SNF waste packages in a generic repository in crystalline host rock. For the simulations the numerical code TOUGH3 was used. The study was designed to investigate thermal behaviors due to the disposal of SNF waste with higher thermal power and related vapor migration.

- TOUGH3 simulations were carried out for base case material properties. A limited sensitivity analyses were also conducted that investigated the effects of buffer thermal conductivity and contributions of adjacent waste packages to thermal effects. The simulations provided a venue for testing TOUGH3, the newest version, and various meshing tools.

- The results of the base case simulations showed that very high peak temperatures can be expected with the disposal of SNF. As the sensitivity analysis showed, use of buffer materials with higher thermal conductivity could reduce peak temperatures to the design level. Other parameters such as longer surface storage, optimum repository foot print and thermal loading considerations would also lower peak temperatures.

Future work will include running of simulations for longer simulation time, varying homogenous permeability and surface storage time, include fracture characterization of the host rock, and use of different waste types.

10.7 Chapter 8 – U(VI) Sorption Studies on Heated Bentonite

Thi chapter summarizes the results from a series of experiments designed to test the effect of bentonite heating on U(VI) adsorption. U(VI) adsorption onto bentonite samples from the FEBEX *in situ* experiment, which were subjected to 18 years of heating at temperatures of 50-100 °C, was compared to adsorption onto cold-zone FEBEX bentonite from the *in situ* experiment. We found that:

- U(VI) adsorption is 5-10% lower on the 95°C heated sample compared to 20°C cold-zone sample for both bulk bentonite (<0.063 mm) and purified bentonite clay (<0.002 mm). Aqueous speciation calculations demonstrated that there is no systematic difference in the U(VI) speciation between these two samples during the experiments. This observation, combined with the persistence of a difference in U(VI) adsorption after the bentonite had been purified to remove non-clay minerals (e.g., calcite, quartz, and feldspars), allows us to conclude that the observed difference in U(VI) adsorption between the 95°C heated and 20°C cold-zone samples is due to structural differences in the clay minerals rather than differences in U(VI) speciation.
- By contrast, U(VI) adsorption to the intermediate (50°C) heated purified clay sample is nearly identical to cold-zone sample, despite the observation of slightly higher fraction of illite layers (10%) in this sample compared to other samples (5% illite). This suggests that effects of heat on U(VI) adsorption may only be observed at the highest temperatures expected in an engineered barrier system, and will be limited to the area immediately surrounding waste canisters (i.e., within 25 cm).
- Furthermore, small differences in illitization (i.e., 5% vs 10%) will likely have a small to negligible effect on U(VI) adsorption. The structural differences in the clay minerals from the 95°C heated and 20°C cold-zone are currently unknown, but are not due to differences in the degree of illitization. Instead, they may be due to small differences in the edge structure or number of edge adsorption sites of the montmorillonite or to differences in the electrostatic characteristics of the

montmorillonite. Such changes are difficult to impossible to accurately and quantitatively characterize, but may have a significant impact on the adsorption capacity of the mineral.

The results from this study provide key information necessary for performance assessment of HLW disposal scenarios. The decreased adsorption observed in this study as a result of bentonite heating may impact the diffusion of U(VI) through engineered clay barriers. Because the decreased U(VI) adsorption was due to changes in the clay mineral structure and *not* to aqueous U(VI) speciation, other radionuclides may be similarly affected.

During the remaining time in this fiscal year (FY18) we plan to complete clay characterization work, including measurement of cation exchange capacity. Beginning in FY19, we will:

- Combine the existing data set collected for U(VI) adsorption onto FEBEX bentonite with U(VI) adsorption data previously collected on laboratory-heated bentonite into a single journal publication.
- Focus on the two samples which showed the largest difference in U(VI) adsorption: the 95°C heated and 20°C cold-zone FEBEX bentonite samples.
- Conduct diffusion experiments with these two samples under realistic waste disposal conditions (compaction and chemical conditions) in order to investigate how differences in U(VI) adsorption affect the diffusive transport of U(VI). This work will be closely coordinated with work being performed under the NEUP project led by Dr. Ruth Tinnacher at CSUEB where U(VI) diffusion experiments will be conducted on synthetic mixtures of montmorillonite and calcite before and after laboratory heat treatment, and data from the two studies should be complementary.

10.8 Chapter 9 – High Temperature EBS Component Interactions

There have been a large number of investigations on bentonite stability under various repository conditions (Madsen, 1998; Meunier et al., 1998; Guillaume et al., 2003; Guillaume et al., 2004; Mosser-Ruck et al., 2010; Ferrage et al., 2011). Yet, there remain questions regarding bentonite's overall stability and more importantly whether montmorillonite will remain relatively unaltered through the repository life-time. It is expected that the initial heat pulse should start to decay after about 100 to 1,000 years (Wersin et al., 2007). After the high temperature pulse passes and temperatures begin to decrease, retrograde reaction have the potential to further change the high temperature mineralogy.

High-temperature, high-pressure expreiments (T= 250 ºC for 6 weeks), were carried out to examine interactions amongst EBS materials:

- Buffer material(Bentonite sourced from Colony, WY, USA) and canister materials (stainless steel coupons), plus Grimsel Granodiorite as a representative host material.

In this work, we consider the impact host rock (i.e., Grimsel Granodiorite from Switzerland) will have on the bentonite barrier. Several mineral alterations were observed in the heating of Grimsel Granodiorite. The primary mineral reaction is the retention of clinoptilolite in volcanic glass shards and formation of a calcium (aluminum) silicate hydrate (C(A)SH) mineral (tobermorite, zeophyllite?) in the Wyoming Bentonite. Interpreting clay mineral evolution within Grimsel materials is complicated due to the variety of clay minerals present in the Grimsel experimental systems. It does appear that muscovite genesis does occur within the bentonite fraction in the mixed reactions at the current experimental conditions. With any of these experiments representing repository system, kinetics is always an issue that has to be taken into account when interpreting data.

This chapter focused on the EBS Grimsel Granodiorite wall rock experiments IEBS-1 and IEBS-2. The following data on these samples have been acquired: 1) SEM images, 2) XRD (QXRD and clay determination) analyses, 3) electron microprobe data for major mineral phases, and 4) aqueous geochemistry data from both starting materials and the two experiments conductedto date.

Concepts developed so far include:

- Illitization of smectites may be restricted due to the bulk chemistry of the overall system,
- The interface between bentonite and steel develops a well characterized new mineral phase, Fe-saponite (especially at 300 °C), that grows perpendicular to the steel surface,
- Another Fe layered phyllosilicate, stilpnomelane, grows in the presence of native iron (one of our solid buffer materials), which alludes to the idea that oxygen fugacity may be quite variable, depending on scale,
- Zeolites transform as temperature increases. Mine-run bentonite contains clinoptilolite, which was preserved in relict glass shards
- C(A)SH minerals formed within the Wyoming Bentonite mixed with Grimsel Granodiorite
- No abundant zeolites have been observed
- Further work to understand formation of C(A)SH minerals at relatively low pH (< 7)

Research needs to be emphasized in the following areas for FY19:

- Continue to build an experimental data base of Grimsel Granodiorite / EBS materials
- Perform transmission electron microscope (TEM) investigation looking at very local chemical changes within a pit corrosion metal surface.
- Corrosion of steels/ interface silicate mantling effect must remain a focus of the upcoming year.
- Incorporate results into Generic modeling codes.

This database, along with summary conclusions will be of use to other experimental teams on the DOE complex, system modeler, and the international repository science community.

REFERENCES

Aksoyoglu S., Bajo C. & Mantovani M. (1990). Grimsel Test Site: Batch sorption experiments with iodine, bromine, strontium, sodium and cesium on Grimsel mylonite. Nagra Technical Report NTB 91-06; Nagra, Wettingen, Switzerland (February 1991).

Altmann, S. (2008). 'Geo'chemical research: A key building block for nuclear waste disposal safety cases. Journal of Contaminant Hydrology 102, 174-179.

Altmann, S., Tournassat, C., Goutelard, F., Parneix, J.-C., Gimmi, T., Maes, N. (2012) Diffusion-driven transport in clayrock formations. Applied Geochemistry 27, 463-478.

Appelo, C.A.J. (2017) Solute transport solved with the Nernst-Planck equation for concrete pores with 'free' water and a double layer. Cement and Concrete Research 101: 102-113.

Bajo C., Hoehn E., Keil R. & Baeyens B. (1989). Chemical characterization of the groundwater from fault zone AU 96m. In Grimsel test site-laboratory investigations in support of the migration experiments. Nagra Technical Report NTB 88-23; Nagra, Wettingen, Switzerland.

Börjesson, L., Gunnarsson, D., Johannesson, L-E., and Jonsson, E. (2010). Design, production and initial state of the buffer. Svensk Kärnbränslehantering Technical Report, TR-10-15, 89.

Bossart P. (2011) Characteristics of the Opalinus Clay at Mont Terri, http://www.mont-terri.ch/internet/mont-terri/en/home/geology/key_characteristics.html

Bradbury, M.H. and Baeyens, B. (2003). Pore-water chemistry in compacted resaturated MX-80 bentonite. Journal Contaminant Hydrology 61, 329–338.

Caporuscio, F.A., Cheshire, M.C., Rearick, M.S., and Jove-Colon, C. (2014). LANL argillite EBS experimental program 2014. (FCRD-USED-2014-000491). Los Alamos National Lab. (LANL), Los Alamos, NM (United States).

Carslaw, H. S., and J. C. Jaeger, "Conduction of Heat in Solids", 2nd Edition, Clarendon Press, Oxford (1959).

Carter, J. T., Rodwell, P. O, Robinson, B., Kehrman, B., "Costing Study for a Generic Salt Repository: Systems Engineering and Analysis in Support of a Policy Review of Comingling Decision and Related System Design Considerations", FCRD-UFD-2012-000113, Rev. 1., (2012).

Castellanos E., Gens A., Lloret A., and Romero E. (2006) Influence of water chemistry on the swelling capacity of a high-density bentonite. In: Miller, G.A., Zapata, C.E., Houston, S.L., Fredlund, D.G. (Eds.), Unsaturated Soils 2006. Geotechnical Special Publication 147 (1). ASCE, pp. 962–971.

Castellanos, E., Villar, M.V., Romero, E., Lloret, A., Gens, A. (2008). Chemical impact on the hydro-mechanical behaviour of high-density FEBEX bentonite. Physics and Chemistry of the Earth, Parts A/B/C 33, Supplement 1(0): S516-S526.

Chen, Y., Zhou, C. and Jing, L. (2009) Modeling coupled THM processes of geological porous media with multiphase flow: Theory and validation against laboratory and field scale experiments. Computers and Geotechnics 36(8): 1308-1329.

Chermak, J.A. (1992). Low temperature experimental investigation of the effect of high pH NaOH solutions on the opalinus shale, Switzerland. Clays and Clay Minerals, 40, 650-658.

Cheshire, M.C., Caporuscio, F.A., Jove-Colon, C., and McCarney, M.K. (2014) Bentonite Clay Evolution at Elevated Pressures and Temperatures: An experimental study for generic nuclear repositories. American Mineralogist, V99, pp. 1662-1675.

Chipera, S.J. and Bish, D.L. (2002). FULLPAT: a full-pattern quantitative analysis program for X-ray powder diffraction using measured and calculated patterns. Journal of Applied Crystallography, 35, 744–749.

Chung, F.H. (1974). Quantitative interpretations of X-ray diffraction patterns of mixtures. I. Matrix flushing method for quantitative multicomponent analysis. Journal of Applied Crystallography, 7, 519-525.

Crerar, D.A., Susak, N.J., Borcsik, M., and Schwartz, S. (1978). Solubility of the buffer assemblage pyrite + pyrrhotite + magnetite in NaCl solution from 200 to 350 °C. Geochimica et Cosmochimica Acta, 42, 1427-1437.

Cuadros, J. and Linares, J. (1996). Experimental kinetic study of the smectite-to-illite transformation. Geochimica et Cosmochimica Acta 60(3): 439-453.

Cuadros, J. (2006). Modeling of smectite illitization in burial diagenesis environments. Geochimica et Cosmochimica Acta 70(16): 4181-4195.

Degueldre C., Pfeiffer H.-R., Alexander W. R., Wernli B. & Bruetsch R. (1996a). Colloid properties in granitic groundwater systems. I: sampling and characterization. Applied Geochemistry, 11, 677-695.

Delay, J., Vinsot, A., Krieguer, J.-M., Rebours, H., Armand, G. (2007) Making of the underground scientific experimental programme at the Meuse/Haute-Marne underground research laboratory, North Eastern France. Physics and Chemistry of the Earth, Parts A/B/C 32, 2-18.

Detzner, K., Kober, F. (2015) FEBEX-DP drilling and sampling report sections 32-34, Internal Report. NAGRA.

Dirksen, D. (1969). Thermo-osmosis through compacted saturated clay membranes. Soil Sci. Soc. Am. Proc., 33(6): 821-826.

Dong, W., Brooks, S.C. (2006). Determination of the Formation Constants of Ternary Complexes of Uranyl and Carbonate with Alkaline Earth Metals (Mg2+, Ca2+, Sr2+, and Ba2+) Using Anion Exchange Method. Environmental Science & Technology 40, 4689-4695.

Drits, V.A., Varaxina, T.V., Sakharov, B.A., Plancon, A. (1994) A simple technique for identification of one-dimensional powder X-ray diffraction patterns for mixed-layer illite-smectites and other interstratified minerals. Clays and Clay Minerals 42, 382-390.

Eberl, D. and Hower, J. (1977). The hydrothermal transformation of sodium and potassium smectite into mixed-layer clay. Clays and Clay Minerals, 25, 215-227.

Eberl, D. (1978). Reaction series for dioctahedral smectites. Clays and Clay Minerals, 26, 327-340.

Eberl, D.D., Velde, B., and McCormick, T. (1993) Synthesis of illite-smectite from smectite at Earth surface temperatures and high pH. Clay Minerals, 28, 49-60.

Elliott, W.C. and Matisoff, G. (1996). Evaluation of kinetic models for the smectite to illite transformation. Clays and Clay Minerals 44(1): 77-87.

ENRESA (2000) FEBEX Project: Full-scale engineered barriers experiment for a deep geological repository for high level radioactive waste in crystalline host rock. Final Report. ENRESA.

ENRESA (2000). Full-scale engineered barriers experiment for a deep geological repository in crystalline host rock, FEBEX Project, European Commission: 403.

ENRESA (2006). FEBEX: Updated final report. ENRESA Tech. Publ. PT 05-0/2006, 589 pp.

Fernández, A., Cuevas, J., Rivas, P. (2001). Pore water chemistry of the FEBEX bentonite. Mat. Res. Soc. Symp. Proc. 663, 573–588.

Fernández, A., Rivas, P. (2003). Task 141: post-mortem bentonite analysis. geochemical behaviour. CIEMAT/DIAE/54520/05/03, Internal Note 70-IMA-L-0-107 v0.

Eikenberg J., Baeyens B. & Bradbury M. H. (1991). The Grimsel Migration Experiment: A hydrogeochemical equilibration test. Nagra Technical Report NTB 90-39; Nagra, Wettingen, Switzerland.

FEBEX (2014). FEBEX-DP Kick-off Meeting. Co-conveners: Gaus, I., Kober, F., Lanyon, G.W. NAGRA, Thun, Switzerland, June 10, 2014, 66 pp.

Fernández, A. M., B. Baeyens, M. Bradbury and P. Rivas (2004). Analysis of the porewater chemical composition of a Spanish compacted bentonite used in an engineered barrier. Physics and Chemistry of the Earth, Parts A/B/C 29(1): 105-118.

Fernández, A. M., Turrero, M. J., Sánchez, D. M., Yllera, A., Melón, A. M., Sánchez, M., Peña, J., Garralón, A., Rivas, P., Bossart, P. and Hernán, P. (2007) On site measurements of the redox and carbonate system parameters in the low-permeability Opalinus Clay formation at the Mont Terri Rock Laboratory. Physics and Chemistry of the Earth, Parts A/B/C 32(1-7): 181-195 .

Ferrage, E., Vidal, O., Mosser-Ruck, R., Cathelineau, M., and Cuadros, J. (2011). A reinvestigation of smectite illitization in experimental hydrothermal conditions: Results from X-ray diffraction and transmission electron microscopy. American Mineralogist, 96, 207-223.

Finsterle S., Kowalsky M., Kober F. and Vomvoris, S. (2017). HotBENT – Preliminary Design Study of Phenomenological Aspects, NAB 17-30.

Fox, P.M., Davis, J.A., Zachara, J.M. (2006) The effect of calcium on aqueous uranium(VI) speciation and adsorption to ferrihydrite and quartz. Geochimica et Cosmochimica Acta 70, 1379-1387.

Fox, P.M., Davis, J.A., Hay, M.B., Conrad, M.E., Campbell, K.M., Williams, K.H., Long, P.E. (2012) Rate-limited U(VI) desorption during a small-scale tracer test in a heterogeneous uranium-contaminated aquifer. Water Resour. Res. 48, W05512.

Fox, P.M., Nico, P.S. (2017) Laboratory Experiments on Bentonite Samples: FY17 Progress. US Department of Energy, Spent Fuel and Waste Science and Technology.

Frick U., Alexander W. R., Baeyens B., Bossart P., Bradbury M. H., Bühler Ch., Eikenberg J., Fierz Th., Heer W., Hoehn E., McKinley I. G. & Smith P. A. (1992). Grimsel test site - The radionuclide migration experiment-Overview of investigations 1985 -1990. Nagra Technical Report NTB 91-04, Nagra, Wettingen, Switzerland.

Gens, A., Garcia-Molina, A. J, Olivella, S. Alonso, E. E. and Huertas, F. (1998) Analysis of a full scale in situ test simulating repository conditions. International Journal for Numerical and Analytical Methods in Geomechanics 22(7): 515-548.

Gens, A. (2010) Soil environment interactions in geotechnical engineering. Géotechnique 60, 3-74.

Ghabezloo S, Sulem J, Guédon S, Martineau F. (2009) Effective stress law for the permeability of a limestone. Int. J. Rock Mech. Min. Sci. 2009;46:297-306.

Ghassemi, A. and Diek, A. (2002). Porothermoelasticity for swelling shales. Journal of Petroleum Science and Engineering, 34: 123-125.

Giffaut, E., Grivé, M., Blanc, P., Vieillard, P., Colàs, E., Gailhanou, H., Gaboreau, S., Marty, N., Madé, B., Duro, L. (2014) Andra thermodynamic database for performance assessment: ThermoChimie. Applied Geochemistry 49, 225-236.

Grimsel (2017). FEBEX-DP Full-scale Engineered Barrier Experiment – Dismantling Project http://www.grimsel.com/gts-phase-vi/febex-dp/febex-dp-introduction.

Guillaume, D., Neaman, A., Cathelineau, M., Mosser-Ruck, R., Peiffert, C., Abdelmoula, M., Dubessy, J., Villieras, F., Baronnet, A., and Michau, N. (2003). Experimental synthesis of chlorite from smectite at 300 °C in the presence of metallic Fe. Clay Minerals, 38, 281-302.

Guillaume, D., Neaman, A., Cathelineau, M., Mosser-Ruck, R., Peiffert, C., Abdelmoula, M., Dubessy, J., Villieras, F., and Michau, N. (2004). Experimental study of the transformation of smectite at 80 to 300 °C in the presence of Fe oxides. Clay Minerals, 39, 17-34.

Guillaumont, R., Fanghanel, T., Neck, V., Fuger, J., Palmer, D.A., Grenthe, I., Rand, M.H. (2003) Update on the chemical thermodynamics of uranium, neptunium, plutonium, americium, and technetium. Elsevier, Amsterdam.

Guimarães LDN, Gens A, Sánchez M, Olivella S (2013) A chemo-mechanical constitutive model accounting for cation exchange in expansive clays. Géotechnique 63, 221–234.

Guyonnet, D., Touze-Foltz, N., Norotte, V., Pothier, C., Didier, G., Gailhanou, H., Blanc, P., Warmont, F. (2009) Performance-based indicators for controlling geosynthetic clay liners in landfill applications. Geotextiles and Geomembranes 27, 321-331.

Hahne, K., Vergleich von Methoden zur Berechnung der zeitabhängigen Temperaturverteilung in einem Endlager für radioaktive Abfälle, Dissertation (1988).

Hammond, G. E., Lichtner, P. C., and Mills, R. T., "Evaluating the performance of parallel subsurface simulators: An illustrative example with PFLOTRAN". J. Water Resources Research. 2014; 50, doi:10.1002/2012WR013483.

Hardin, E., Bryan, C., Ilgen, A., Kalinina, E., Teich-Goldrick, S., Banerjee, K., Clarity, J., Howard, R., Jubin, R., Scaglione, J., Perry, F., Zheng, L., Rutqvist, J., Birkholzer, J.T., Greenberg, H., Carter, J., and Severynse, T. (2014). Investigation of Dual-Purpose Canister Direct Disposal Feasibility, prepared for U.S. Department of Energy Used Fuel Disposition Campaign, FCRD-UFD-2014-000069 REV 1, Sandia Laboratories.

Hardin, E., T. Hadgu, D. Clayton, R. Howard, H. Greenberg, J. Blink, M. Sharma, M. Sutton, J. Carter, M. Dupont, and P. Rodwell, "Disposal Concepts/Thermal Load Management (FY11/12 Summary Report)", FCRD-UFD-2012-00219, Milestone: M3FT-12SN0804032, Work Package: FT-12SN080403, (2012).

Hardin, E., J. Blink, H. Greenberg, M. Sutton, M. Fratoni, J. Carter, M. Dupont, and R. Howard, "Generic repository design Concepts and Thermal Analysis", FCRD-USED-2011-000143, Rev. 0 (2011).

Hennig, C., Reich, T., Dähn, R., Scheidegger, A.M.(2002). Structure of uranium sorption complexes at montmorillonite edge sites, Radiochimica Acta, p. 653.

Itasca, (2009). FLAC3D, Fast Lagrangian Analysis of Continua in 3 Dimensions, Version 4.0, Minneapolis, Minnesota, Itasca Consulting Group.

Jové-Colón, C. F., Caporuscio, F. A., Levy, S. S., Sutton, M., Blink, J., Greenberg, H. R., Fratoni, M., Halsey, W. G., Wolery, T. J., Rutqvist, J., et al. (2011). Disposal systems evaluations and tool development - Engineered Barrier System (EBS) Evaluation (Fuel Cycle Research and Development). Sandia National Laboratory, (FCRD-USED-2011-000132), 1-192.

Jung, Y., Pau, G. S. H., Finsterle, S., and Doughty, C., "TOUGH3 User's Guide", Version 1.0, LBNL-2001093, Energy Geosciences Division, Lawrence Berkeley National Laboratory, University of California, Berkeley, California (2018).

Kober, F., Vomvoris, S., Finsterle, S., and snf Sineriz, J.L. (2017). HotBENT – High Temperature Buffer Experiment: Preliminary Design Study (PreDeS), NAB 17-XXX.

Kloprogge, J.T., Komarneni, S. and Amonette, J.E. (1999). Synthesis of smectite clay minerals: a critical review. Clays and Clay Minerals, 47, 529-554

Kuhlman U. and Gaus, I. (2014). THM Model validation modelling of selected WP2 experiments: Inverse Modelling of the FEBEX in situ test using iTOUGH2. DELIVERABLE-N°: D3.3-1, NAGRA.

Kwon O, Kronenberg AK, Gangi AF, Johnson B. (2001) Permeability of Wilcox shale and its effective pressure law. J. Geophys. Res.-Sol. Ea. 2001;106:19339-53.

Lantz, R.B. (1971). Quantitative evaluation of numerical diffusion truncation error. Society Petroleum Engineering Journal 11, 315e320.

Lauber, M., B. Baeyens and Bradbury, M. H. (2000) Physico-Chemical Characterisation and Sorption Measurements of Cs, Sr, Ni, Eu, Th, Sn and Se on Opalinus Clay from Mont Terri. PSI Bericht Nr. 00-10 December 2000 ISSN 1019-0643.

Leupin Olivier, X. (ed.), Birgersson Martin, Karnland O., Korkeakoski P., Sellin P., Mäder U., Wersin P. (2014): Montmorillonite stability under near-field conditions. Nagra Technical Report NTB 14-12.

Liu, H.H., J. Houseworth, J. Rutqvist, L. Zheng, D. Asahina, L. Li, V. Vilarrasa, F. Chen, S. Nakagawa, S. Finsterle, C. Doughty, T. Kneafsey and J. Birkholzer. (2013) Report on THMC modeling of the near field evolution of a generic clay repository: Model validation and demonstration, Lawrence Berkeley National Laboratory, August, 2013, FCRD-UFD-2013-0000244.

Lloret, A. and Alonso, E.E. (1995). State surfaces for partially saturated soils, In proceedings of the International Conference on Soils Mechanics and Foundation Engineering, Balkema, pp. 557-562.

Lloret A, Villar MV, Sánchez M, Gens A, Pintado X, Alonso EE. (2003) Mechanical behaviour of heavily compacted bentonite under high suction changes. Géotechnique 2003; 53(1):27–40.

Madsen, F.T. (1998). Clay mineralogical investigations related to nuclear waste disposal. Clay Minerals, 33, 109-129.

Mariner, P. E., Stein, E. R., Frederick, J. M., Sevougian, S. D., Hammond, G. E., and Fascitelli, D. G., "Advances in geologic Disposal System Modeling and Application to Crystalline Rock", FCRD-UFD-2016-000440, SAND2016-9610 R.

Marques Fernandes, M., Baeyens, B., Dähn, R., Scheinost, A.C., Bradbury, M.H. (2012) U(VI) sorption on montmorillonite in the absence and presence of carbonate: A macroscopic and microscopic study. Geochimica et Cosmochimica Acta 93, 262-277.

Matteo, E. N., Hardin, E. L., Hadgu, T., Park, H., Rigali, M., Jove-Colon, C. "Status of Progress Made Toward Preliminary Design Concepts for the Inventory in Select Media for DOE Managed HLW/SNF", FCRD-UFD-2016-000081, SAND2016-9823 R.

Meunier, A., Velde, B., and Griffault, L. (1998). The reactivity of bentonites: A Review. An application to clay barrier stability for nuclear waste storage. Clay Minerals, 33, 187-196.

Missana T., Fernández V., Gutiérrez M. G., Alonso U. & Mingarro M. (2001). CRR project: Sorption studies final report; Unpubl. CIEMAT internal report CIEMAT/DIAE/ 54431/2/2001, CIEMAT, Madrid, Spain.

Missana, T., & Geckeis, H. (2006). Grimsel Test Site–Investigation Phase V. The CRR Final Project Report Series II: Supporting Laboratory Experiments with Radionuclides and Bentonite Colloids NAGRA Technical Report Series NTB, 03-02.

Moore, D. M. and Reynolds, R.C. (1997). X-ray Diffraction and the identification and analysis of clay minerals. Oxford University Press, New York, New York, 377.

Mosser-Ruck, R., Cathelineau, M., Guillaume, D., Charpentier, D., Rousset, D., Barres, O., and Michau, N. (2010). Effects of temperature, pH, and iron/clay and liquid/clay ratios on experimental conversion of dioctahedral smectite to berthierine, chlorite, vermiculite, or saponite. Clays and Clay Minerals, 58, 280-291.

Mosser‐Ruck, R., Pignatelli, I., Bourdelle, F., Abdelmoula, M., Odile Barres, O., Guillaume, D., Charpentier, D., Rousset, D., · Cathelineau, M., and Michau, N. (2016). Contribution of long‐term hydrothermal experiments for understanding the smectite‐to‐chlorite conversion in geological environments. Contributions to Mineralogy and Petrology, 171, 97-118.

Nutt, M. Voegele, M., Jové-Colón, C.F., Wang, Y., Howard, R., Blink, J., Liu, H.H., Hardin, E., and Jenni, K. (2011). Used fuel disposition campaign disposal research and development road map (Fuel cycle research and development). Sandia National Laboratory, (FCRD-USED-2011-000065), 1-121.

Ohmoto, H., Hayashi, K-I, and Kajisa, Y. (1994). Experimental study of the solubilities of pyrite in NaCl-bearing aqueous solutions at 250-350°C. Geochimica et Cosmochimica Acta, 58, 2169-2185.

Pan, L., "User Information Document for WINGRIDDER Version 3.0", Document ID: 10024-UID-3.0-00, STN: 10024-3.0-00, U.S Department of Energy Office of Repository Development (2007).

Ploumen, P., G. Strickmann, Berechnungen der zeitlichen und räumlichen Temperaturverteilung bei der säkularen Lagerung hochradioaktiver Abfälle in Salzstöcken, Technical Report (1977)

Pouchou, J.L. and Pichoir, F. (1985) "PAP" (φ-ρ-*Z*) correction procedure for improved quantitative microanalysis. Microbeam Analysis, Ed. Armstrong, J.T., San Francisco Press, pp. 104-106.

Pusch, R. (1979). Highly compacted sodium bentonite for isolating rock-deposited radioactive waste products. Nuclear Technology, 45, 153-157.

Pabalan, R.T., Turner, D.R. (1996) Uranium(6+) sorption on montmorillonite: Experimental and surface complexation modeling study. Aquatic Geochemistry 2, 203-226.

Pruess, K., C. Oldenburg and G. Moridis (1999) TOUGH2 User's Guide, Version 2.0, Lawrence Berkeley National Laboratory, Berkeley, CA.

Pytte, A. (1982). The kinetics of the smectite to illite reaction in contact metamorphic shales [M.A. Thesis]. Dartmouth College: Hanover, N.H. 78p.

Ramírez, S., Cuevas, J., Vigil, R., and Leguey, S. (2002). Hydrothermal alteration of "La Serrata" bentonite (Almeria, Spain) by alkaline solutions. Applied Clay Science 21(5–6): 257-269.

Rutqvist, J., Y. Ijiri and H. Yamamoto (2011) Implementation of the Barcelona Basic Model into TOUGH–FLAC for simulations of the geomechanical behavior of unsaturated soils. Computers & Geosciences 37(6): 751-762.

Rutqvist, J., Zheng, L., Chen, F., Liu, H.-H. and Birkholzer, J. (2013). Modeling of Coupled Thermo-Hydro-Mechanical Processes with Links to Geochemistry Associated with Bentonite-Backfilled Repository Tunnels in Clay Formations. Rock Mechanics and Rock Engineering: 1-20.

Rutqvist, J., Zheng, L., Chen, F., Liu, H.-H. and Birkholzer, J. (2014) Modeling of Coupled Thermo-Hydro-Mechanical Processes with Links to Geochemistry Associated with Bentonite-Backfilled Repository Tunnels in Clay Formations. Rock Mechanics and Rock Engineering: 47(1): 167-186.

Sacchi, E., Michelot, J.L., Pitsch, H., Lalieux, P., Aranyossy, J.F., (2001). Extraction of water and solution from argillaceous rock for geochemical characterisation: methods, processes, and current understanding. Hydrogeology Journal 9, 17–33.

Samper, J., Zheng, L., Montenegro, L., Fernández, A.M., and Rivas, P. (2008). Coupled thermo-hydro-chemical models of compacted bentonite after FEBEX in situ test. Applied Geochemistry 23(5): 1186-1201.

Sánchez, M., A. Gens, L. J. D. N. Guimarães and S. Olivella (2005) A double structure generalized plasticity model for expansive materials. International Journal for numerical and analytical methods in geomechanics 29: 751-787.

Sánchez, M., Gens, A., and Olivella, S. (2012). THM analysis of a large-scale heating test incorporating material fabric changes. International Journal for Numerical and Analytical Methods in Geomechanics 36(4): 391-421.

Savage, D. (1997). Review of the potential effects of alkaline plume migration from a cementitious repository for radioactive waste. Research & Development Technical Report P60, UK Environment Agency, Bristol, UK.

Savage, D., Noy, D.J., Mihara, M., 2002. Modelling the interaction of bentonite with hyperalkaline fluids. Applied Geochemistry 17, 207–223.

Savage, D., Walker, C., Arthur, R., Rochelle, C., Oda, C., and Takase, H. (2007). Alteration of bentonite by hyperalkaline fluids: A review of the role of secondary minerals. Physics and Chemistry of the Earth, 32, 287-297.

Schlegel, M.L., Descostes, M. (2009) Uranium Uptake by Hectorite and Montmorillonite: A Solution Chemistry and Polarized EXAFS Study. Environmental Science & Technology 43, 8593-8598.

Schmidt, H., Numerische Langzeitberechnungen instationärer Temperaturfelder mit diskreter Quellenverteilung unter Berücksichtigung temperatur- und ortabhängiger Stoffwerte,Dissertation, RWTH Aachen (1971).

Seyfried, J.R., Janecky, D.R., and Berndt, M.E. (1987). Rocking autoclaves for hydrothermal experiments II. The flexible reaction-cell system. Hydrothermal Experimental Techniques, Eds. Ulmer, G.C. and Barnes, H.L. John Wiley & Sons, pp. 216 – 239.

Siitari-Kauppi, M., Leskinen, A., Kelokaski, M., Togneri, L. Alonso, U., Missana, T., and García - Gutiérrez, M. (2007). Physical Matrix Characterisation: Studies of Crystalline Rocks and Consolidated Clays by PMMA Method and Electron Microscopy as Support of Diffusion Analyses. CIEMAT Technical Report, 1127, December 2007.

Simo, E. K., Hadgu, T., and Matteo, E., "Qualification of Numerical and Semi-Analytical Modeling Codes for Thermal Design of HLW Repository", Proceedings of the Waste Management Symposia, Phoenix, AZ, March 18-22, 2018. SAND2018-1174 C.

SKB (2011) Long-term safety for the final repository for spent nuclear fuel at Forsmark. Main report of the SR-Site project. Swedish Nuclear Fuel and Waste Management Co.

Smith, R.M., Martell, A.E., Motekaitis, R.J. (2003) NIST critically selected stability constants of metal complexes database, NIST standard reference database 46, version 7.0. NIST, Gaithersburg, MD, USA.

Stein, E. R., S. D. Sevougian, G. E. Hammond, J. M. Frederick, and P. E. Mariner, "D-Repo Performance Assessment: Crystalline Reference Case". SAND2016-5405 PE. Sandia National Laboratories, Albuquerque, NM (2016).

Stewart, B.D., Mayes, M.A., Fendorf, S. (2010) Impact of Uranyl−Calcium−Carbonato Complexes on Uranium(VI) Adsorption to Synthetic and Natural Sediments. Environ. Sci. Technol. 44, 928-934.

Środoń, J. (1980). Precise identification of illite/smectite interstratifications by X-ray powder diffraction. Clays and Clay Minerals, 28, 401-411.

Sutton, M., J. A. Blink, M. Fratoni, H. R. Greenberg, W. G. Halsey, and T. J. Wolery, "Disposal System Evaluation Framework (DSEF) Version 1.0 – Progress report", LLNL-TR-484011, Lawrence Livermore National laboratories, (2011).

Tinnacher, R.M., Holmboe, M., Tournassat, C., Bourg, I.C., Davis, J.A. (2016) Ion adsorption and diffusion in smectite: Molecular, pore, and continuum scale views. Geochimica et Cosmochimica Acta 177, 130-149.

Tournassat, C., Steefel, C.I., Bourg, I.C., Bergaya, F. (2015) Natural and engineered clay barriers. Elsevier.

Tournassat, C., Tinnacher, R.M., Grangeon, S., Davis, J.A. (2018) Modeling uranium(VI) adsorption onto montmorillonite under varying carbonate concentrations: A surface complexation model accounting for the spillover effect on surface potential. Geochimica et Cosmochimica Acta 220, 291-308.

Tsang, C.-F. (2009) Introductory editorial to the special issue on the DECOVALEX-THMC project. Environmental Geology 57(6): 1217-1219.

Turner, G.D., Zachara, J.M., McKinley, J.P., Smith, S.C. (1996) Surface-charge properties and UO22+ adsorption of a subsurface smectite. Geochimica et Cosmochimica Acta 60, 3399-3414.

Van Genuchten, M.Th., and Gray, W.G. (1978) Analysis of some dispersion corrected numerical schemes for solution of the transport equation. International Journal of Numerical Methods in Engineering 12, 387e404.

Wersin, P., Johnson, L.H., McKinley, I.G. (2007) Performance of the bentonite barrier at temperatures beyond 100°C: A critical review. Physics and Chemistry of the Earth, Parts A/B/C 32, 780-788.

Wilson, J., Cressey, G., Cressey, B., Cuadros, J., Ragnarsdottir, K. V., Savage, D., and M. Shibata. The effect of iron on montmorillonite stability.(II) Experimental investigation. Geochimica et Cosmochimica Acta, 70(2), 323-336, (2006).

Wilson, J., "Decay Heat of Selected DOE Defense Waste Materials", FCRD-UFD-2016-000636, SRNL-RP-2016-00249, (2016).

Winkler, H.G.F. (1976) Petrogenesis of Metamorphic Rocks. Springer-Verlag, New York, 329.

Wolery, T.J. (1993) EQ3/6, A software package for geochemical modelling of aqueous systems, Version 7.2. Lawrence Livermore National Laboratory, USA.

Xu T., Spycher N., Sonnenthal E., Zhang G., Zheng L., and Pruess K. (2011) TOUGHREACT Version 2.0: A simulator for subsurface reactive transport under non-isothermal multiphase flow conditions. Computers & Geosciences 37(6): 763–774.

Zheng, L. and Samper, J. (2008) A coupled THMC model of FEBEX mock-up test. Physics and Chemistry of the Earth, Parts A/B/C 33, Supplement 1: S486-S498.

Zheng, L., Samper, J., and Montenegro, L. (2008) Inverse hydrochemical models of aqueous extracts tests. Physics and Chemistry of the Earth, Parts A/B/C 33(14–16): 1009-1018.

Zheng, L., Samper, J., and Montenegro, L. (2011) A coupled THC model of the FEBEX in situ test with bentonite swelling and chemical and thermal osmosis. Journal of Contaminant Hydrology 126(1–2): 45-60.

Zheng, L., Li, L., Rutqvist, J., Liu, H. and Birkholzer, J.T., (2012) Modeling Radionuclide Transport in Clays. Lawrence Berkeley National Laboratory. FCRD-URD-2012-000128.

Zheng, L., Rutqvist, J., Steefel, C., Kim, K., Chen, F., Vilarrasa, V., Nakagawa, S., Houseworth, J., and Birkholzer, J. (2014) Investigation of Coupled Processes and Impact of High Temperature Limits in Argillite Rock. Prepared for U.S. Department of Energy, Used Fuel Disposition, FCRD-UFD-2014-000493, Lawrence Berkeley National Laboratory, LBNL-6719E.

Zheng, L., Rutqvist, J., Birkholzer, J.T., and Liu, H.-H. (2015a) On the impact of temperatures up to 200 °C in clay repositories with bentonite engineer barrier systems: A study with coupled thermal, hydrological, chemical, and mechanical modeling. Engineering Geology 197: 278-295.

Zheng, L., Rutqvist, J. Kim, K., and Houseworth, J. (2015b) Investigation of Coupled Processes and Impact of High Temperature Limits in Argillite Rock. FCRD-UFD-2015-000362, LBNL-187644.

Zheng L., Rutqvist J., Kim, K., and Houseworth J. (2015) Investigation of Coupled Processes and Impact of High Temperature Limits in Argillite Rock. FCRD-UFD-2015-000362, LBNL-187644.

Zheng, L., Kim, K., Xu, H., and Rutqvist, J. (2016) DR Argillite Disposal R&D at LBNL. FCRD-UFD-2016-000437, LBNL-1006013, Lawrence Berkeley National Laboratory.

Zheng, L., Rutqvist J., Xu H., Kim K., Voltolini M., and Cao X. (2017) Investigation of Coupled Processes and Impact of High Temperature Limits in Argillite Rock. SFWD-SFWST-2017-000040, LBNL-2001014. Lawrence Berkeley National Laboratory.

Zhang, C., Liu, X., Tinnacher, R.M., Tournassat, C. (2018) Mechanistic Understanding of Uranyl Ion Complexation on Montmorillonite Edges: A Combined First-Principles Molecular Dynamics–Surface Complexation Modeling Approach. Environmental Science & Technology.

Zhou, Y., Rajapakse, R.K.N.D., and Graham, J. (1999) Coupled Field in a deformable unsaturated medium. International Journal of Solid and Structures, 36: 4841-4868.

Appendix A Semi-Analytic Thermal Calculations

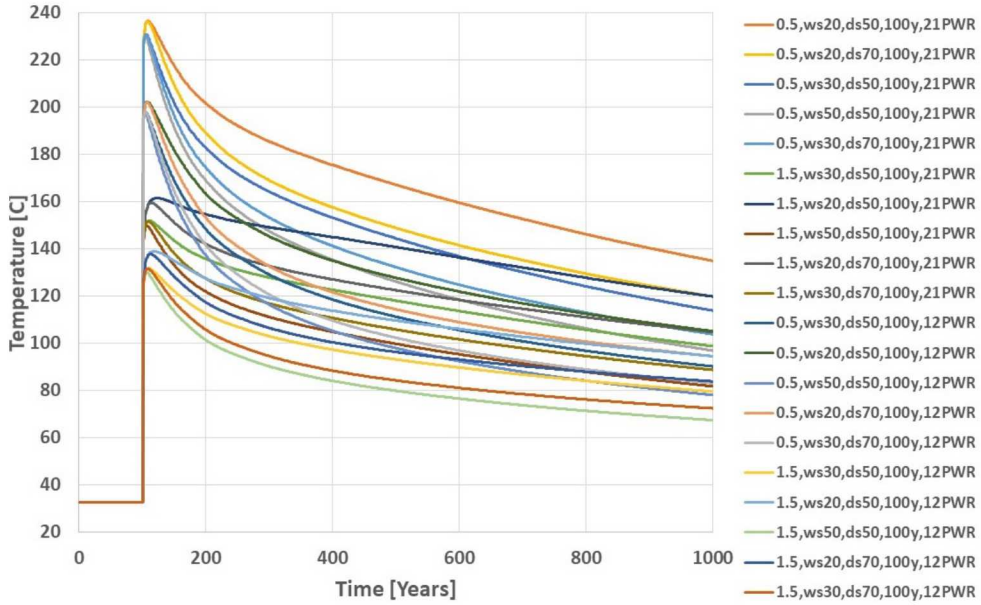

Figure A-1. Predicted waste package surface temperature for storage time of 100 years. Results show temperature plots for various parameters.

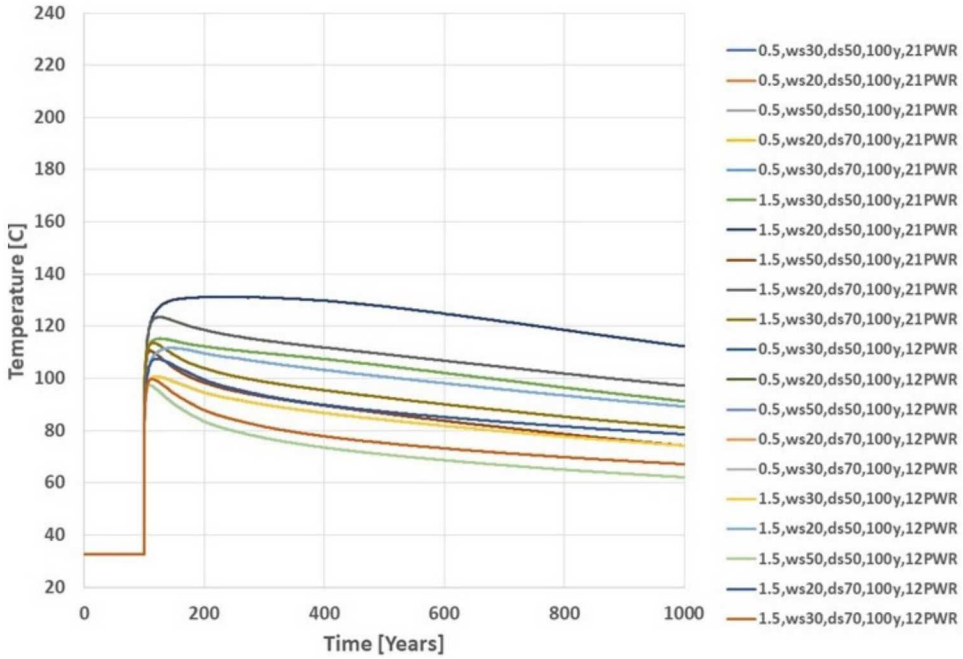

Figure A-2. Predicted drift wall temperature for storage time of 100 years. Results show temperature plots for various parameters.

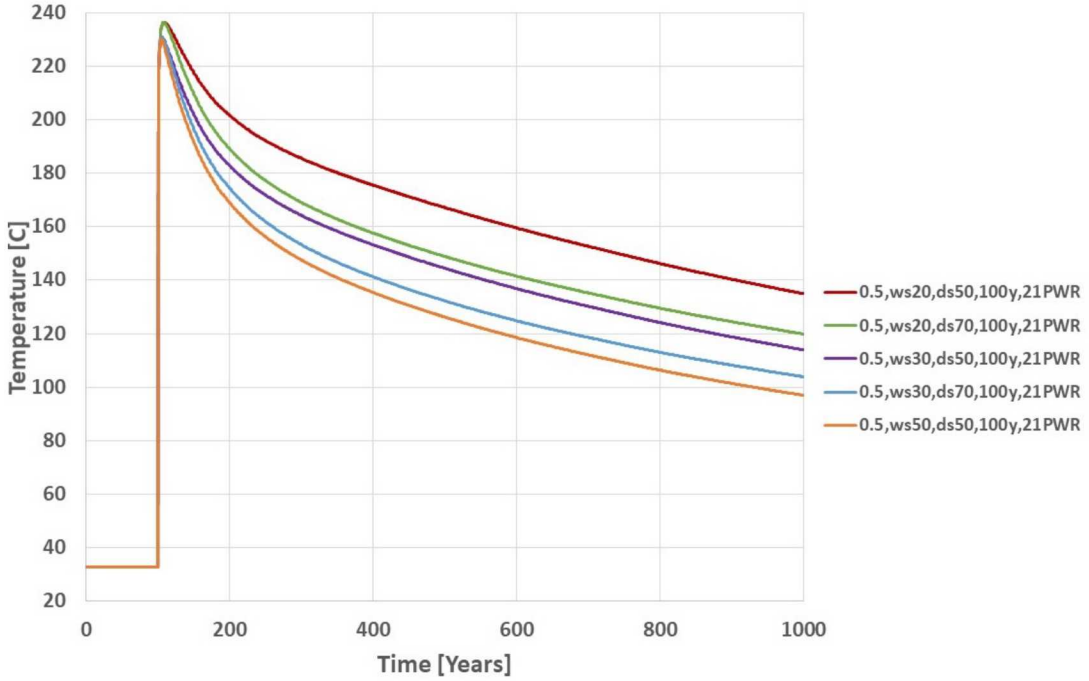

Figure A-3. Predicted waste package surface temperature for storage time of 100 year: 21 PWR with buffer thermal conductivity of 0.5 W/m K.

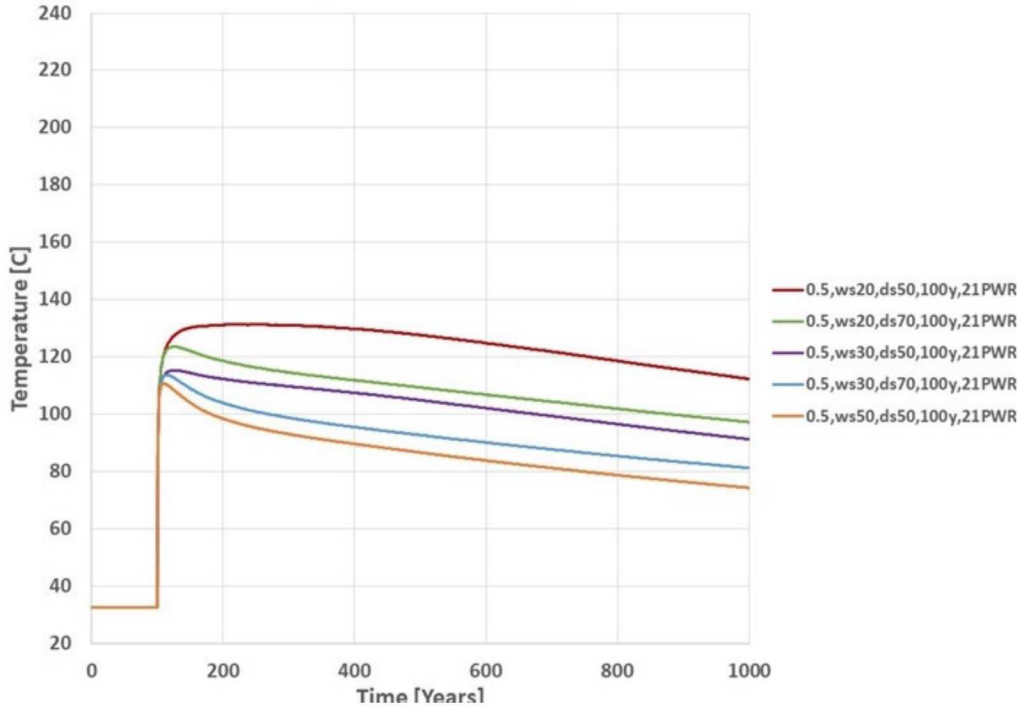

Figure A-4. Predicted drift wall temperature for storage time of 100 year: 21 PWR with buffer thermal conductivity of 0.5 W/m K.

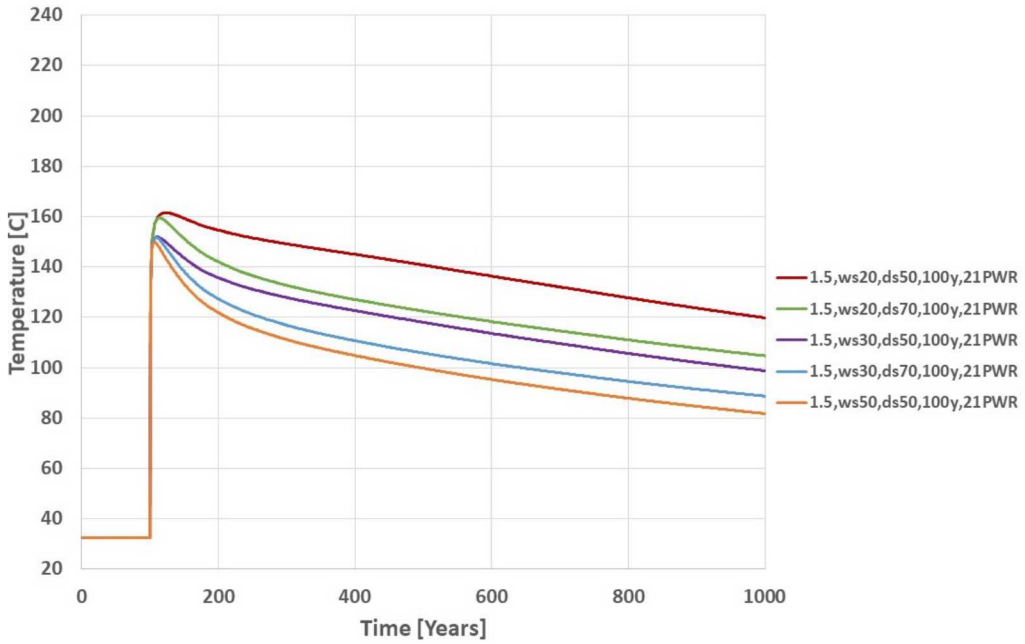

Figure A-5. Predicted waste package surface temperature for storage time of 100 years: 21 PWR with buffer thermal conductivity of 1.5 W/m K.

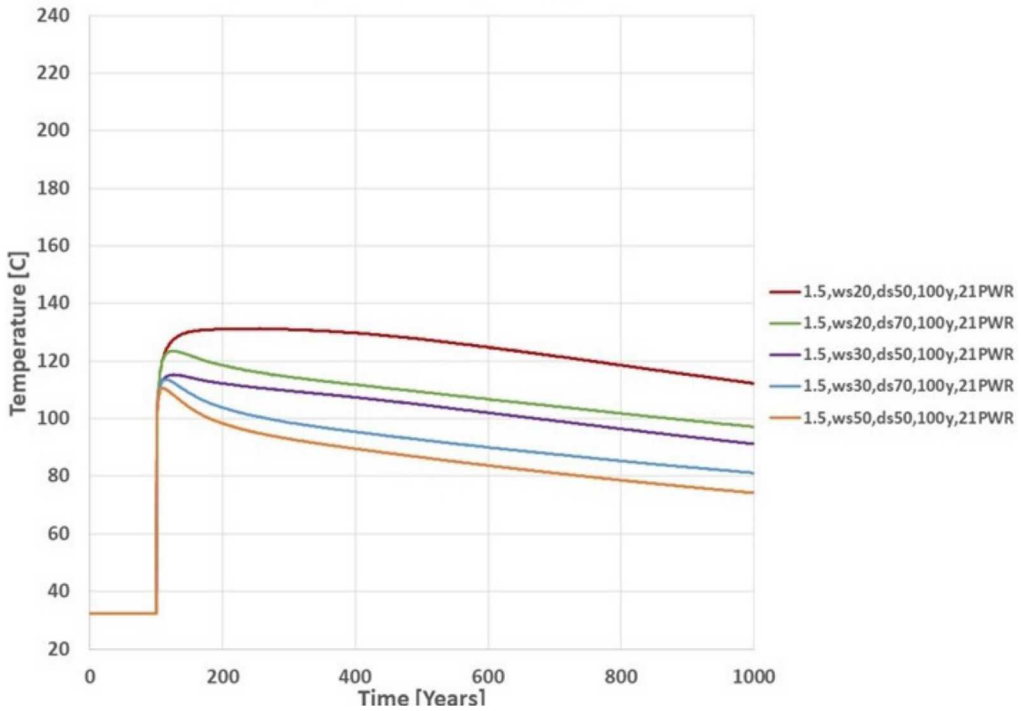

Figure A-6. Predicted drift wall temperature for storage time of 100 years: 21 PWR with buffer thermal conductivity of 1.5 W/m K.

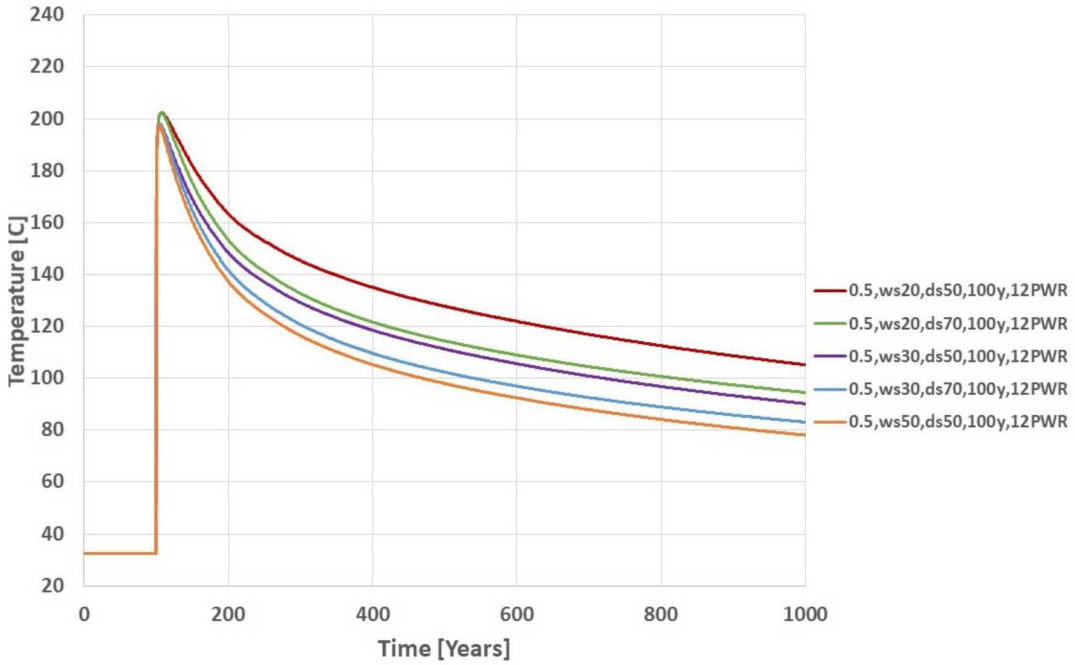

Figure A-7. Predicted waste package surface temperature for storage time of 100 years: 12 PWR with buffer thermal conductivity of 0.5 W/m K.

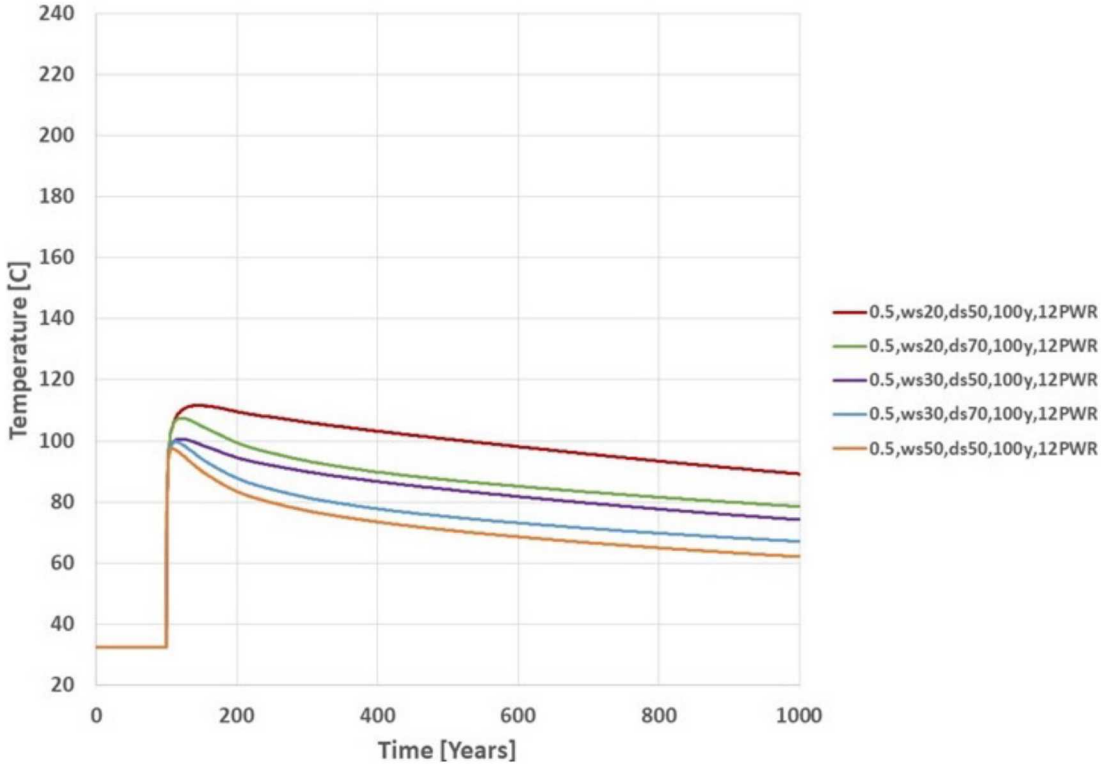

Figure A-8. Predicted drift wall temperature for storage time of 100 years: 12 PWR with buffer thermal conductivity of 0.5 W/m K.

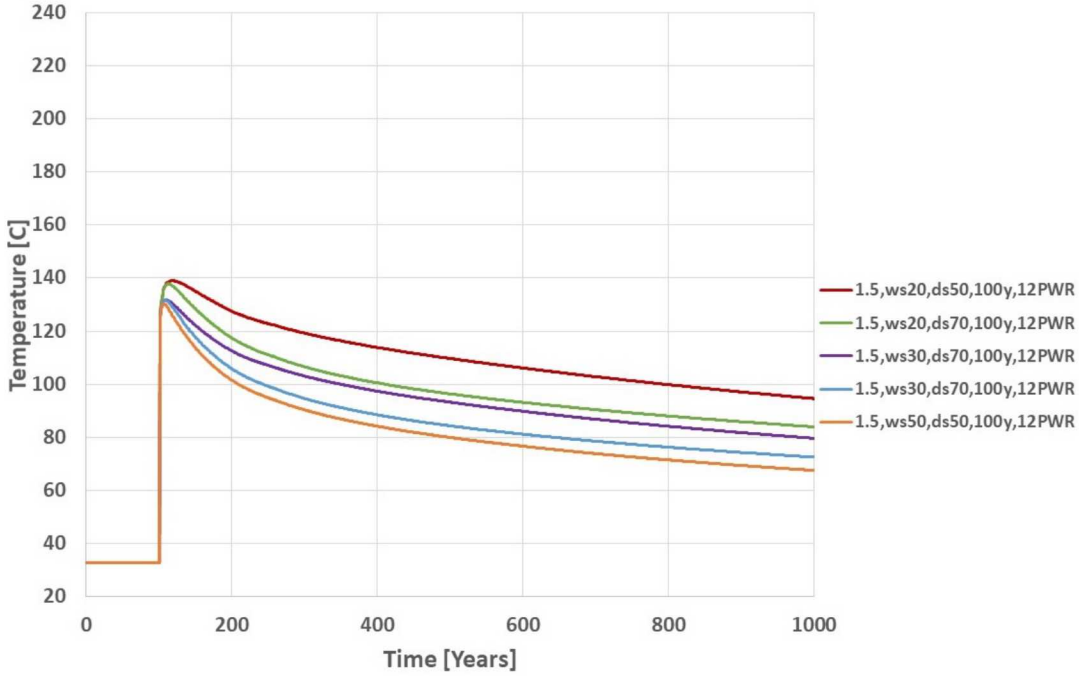

Figure A-9. Predicted waste package surface temperature for storage time of 100 years: 12 PWR with buffer thermal conductivity of 1.5 W/m K.

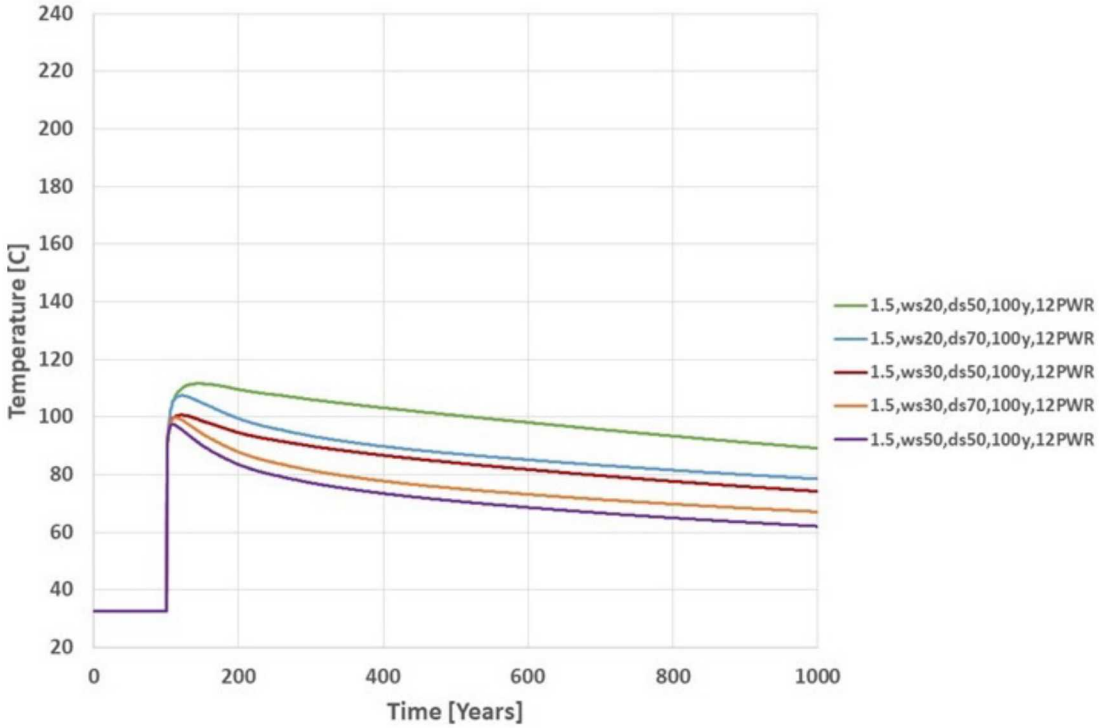

Figure A-10. Predicted drift wall temperature for storage time of 100 years: 12 PWR with buffer thermal conductivity of 1.5 W/m K.

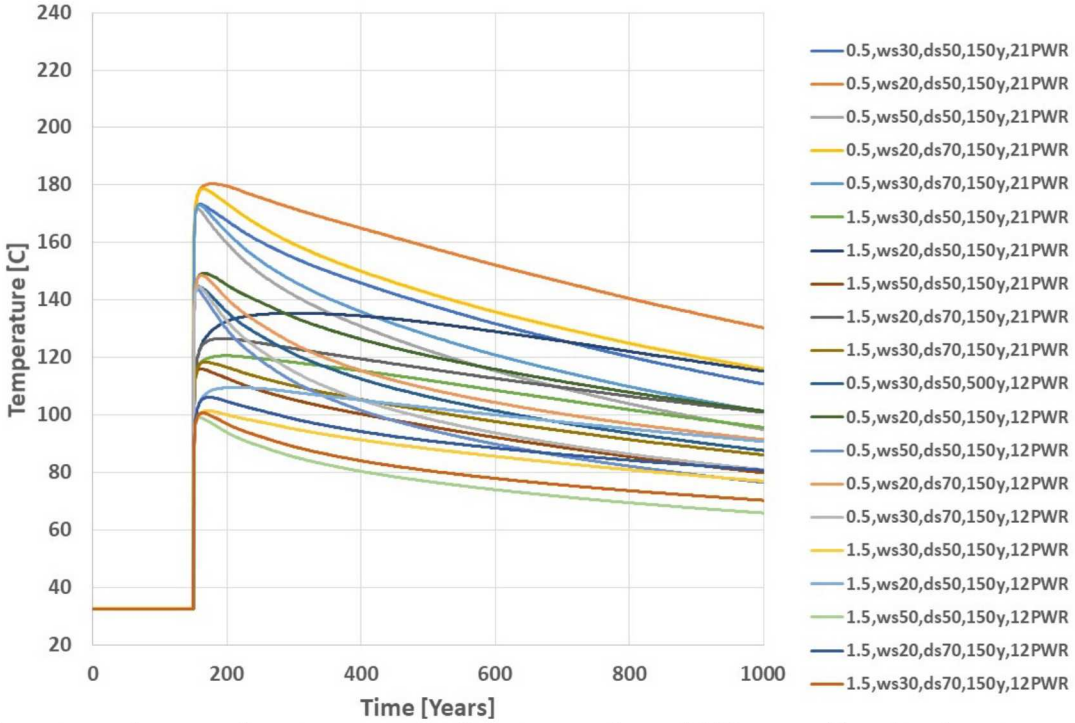

Figure A-11. Predicted waste package surface temperature for storage time of 150 years. Results show temperature plots for various parameters.

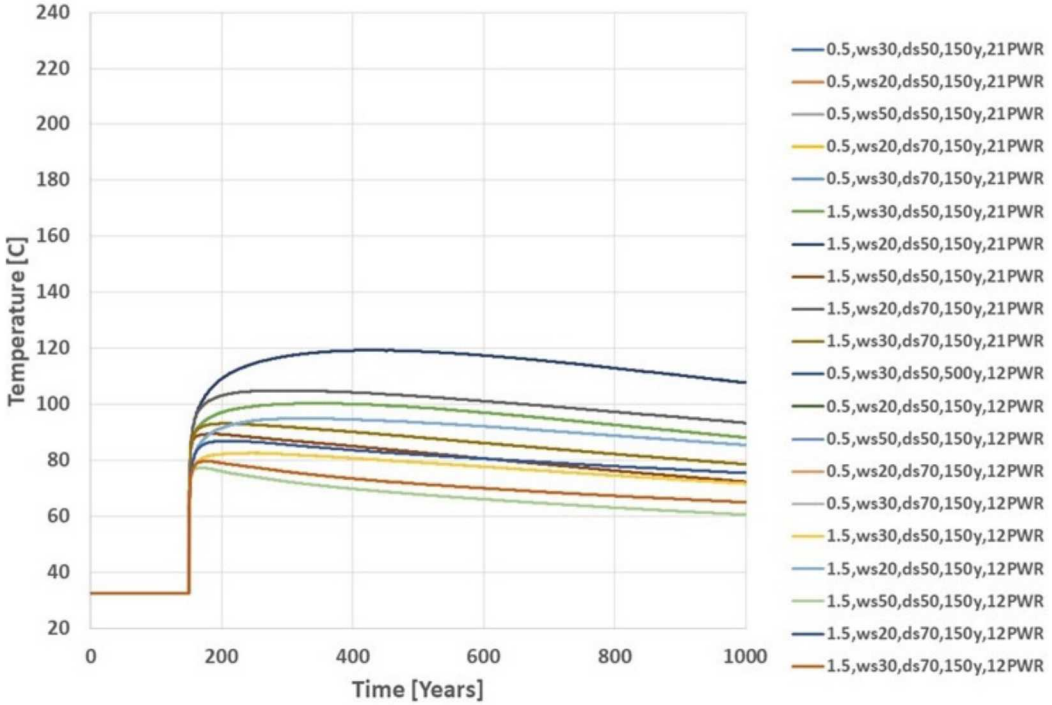

Figure A-12. Predicted drift wall temperature for storage time of 150 years. Results show temperature plots for various parameters.

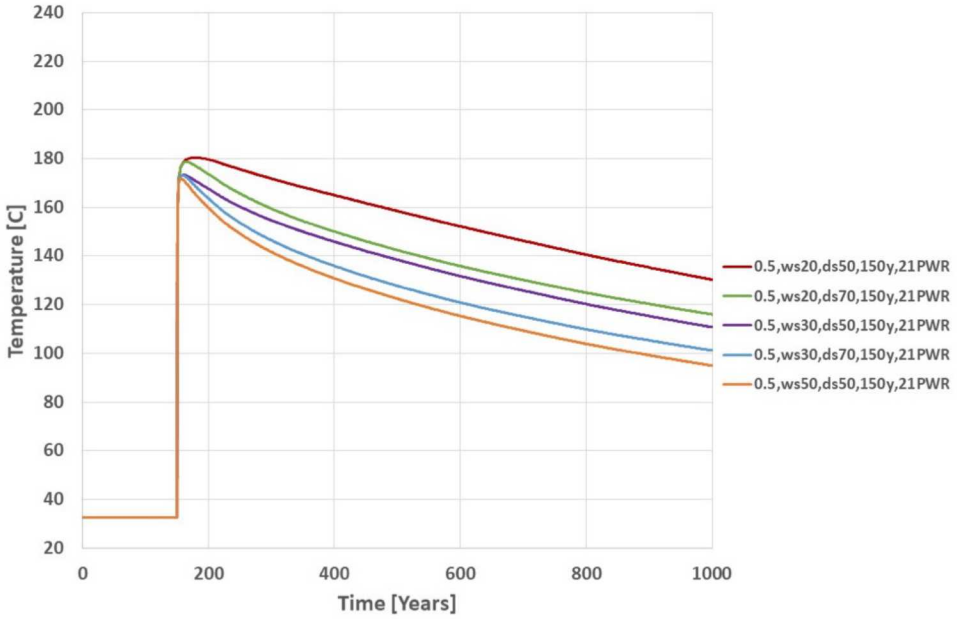

Figure A-13. Predicted waste package surface temperature for storage time of 150 years: 21 PWR with buffer thermal conductivity of 0.5 W/m K.

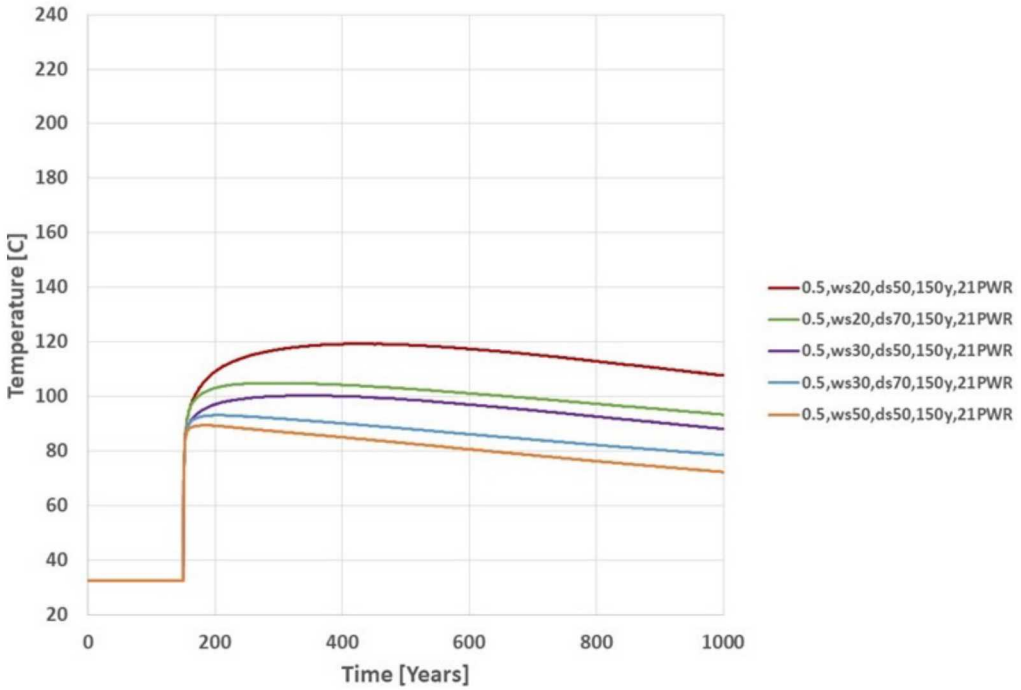

Figure A-14. Predicted drift wall temperature for storage time of 150 years: 21 PWR with buffer thermal conductivity of 0.5 W/m K

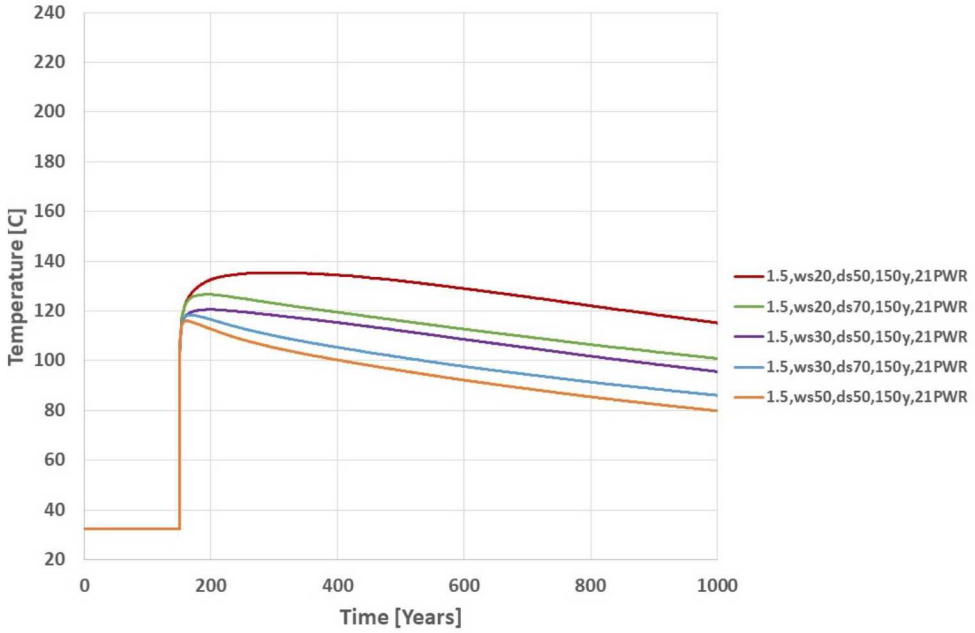

Figure A-15. Predicted waste package surface temperature for storage time of 150 years: 21 PWR with buffer thermal conductivity of 1.5 W/m K.

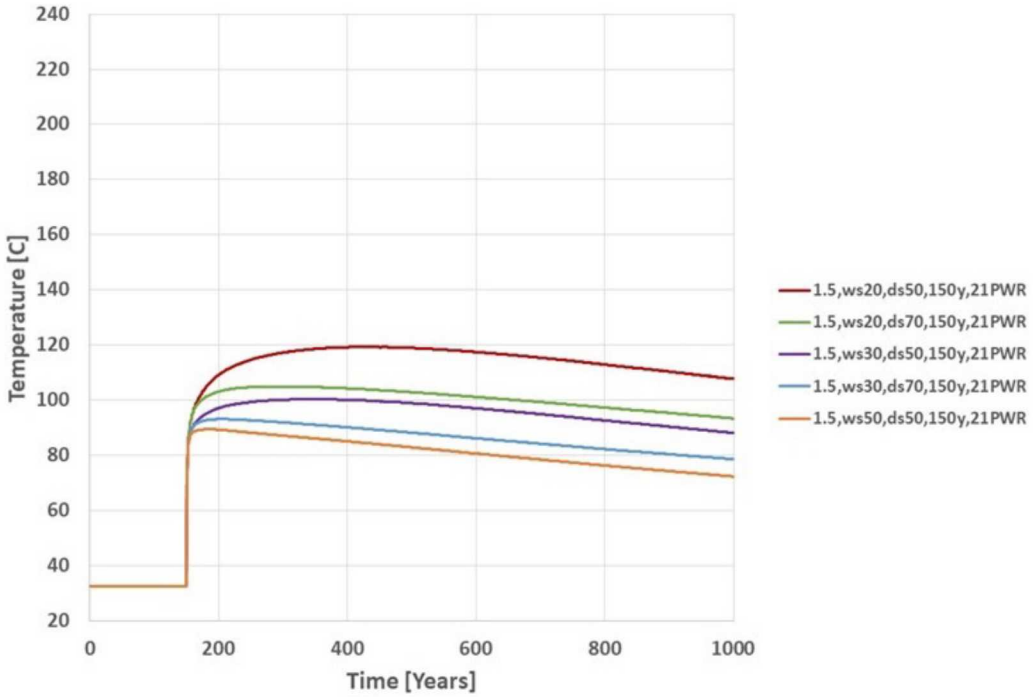

Figure A-16. Predicted drift wall temperature for storage time of 150 years: 21 PWR with buffer thermal conductivity of 1.5 W/m K

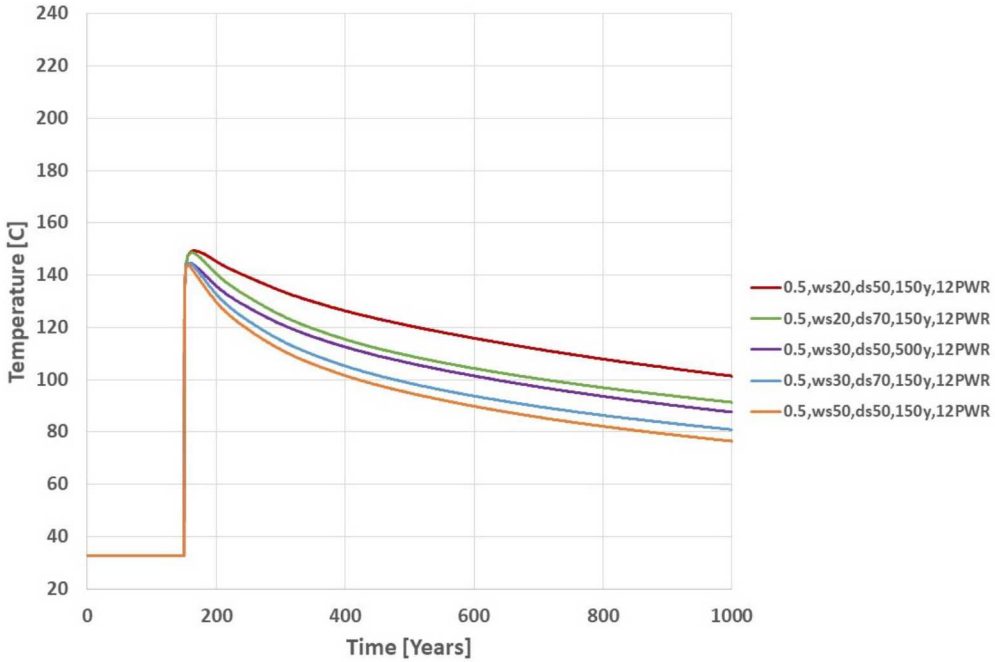

Figure A-17. Predicted waste package surface temperature for storage time of 150 years: 12 PWR with buffer thermal conductivity of 0.5 W/m K.

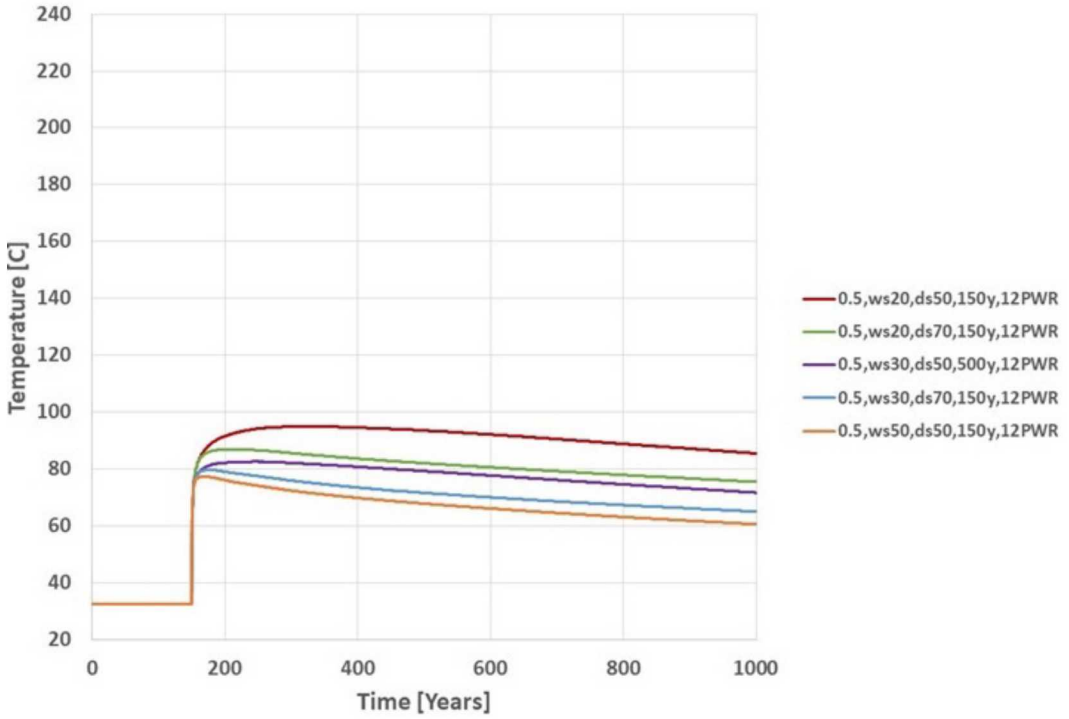

Figure A-18. Predicted drift wall temperature for storage time of 150 years: 12 PWR with buffer thermal conductivity of 0.5 W/m K

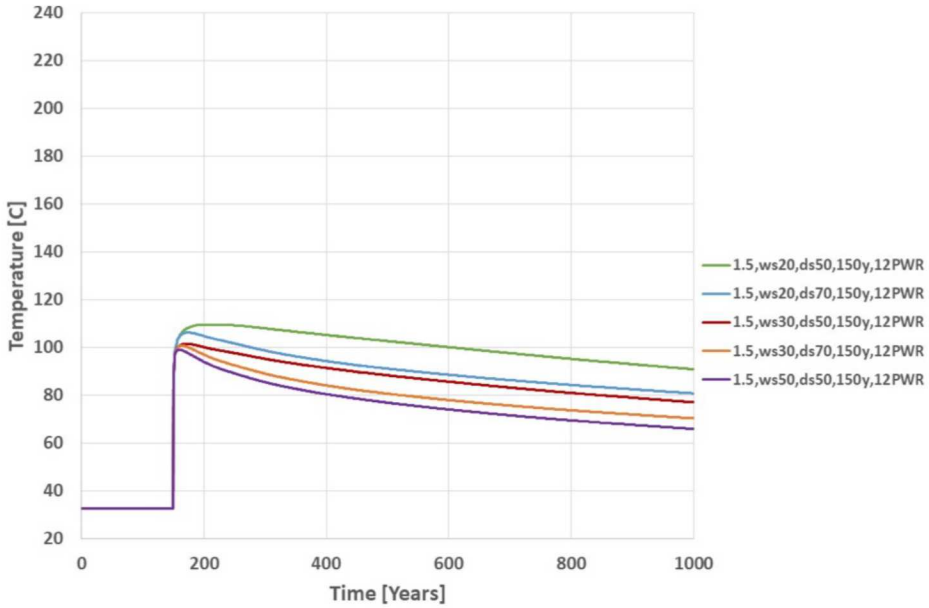

Figure A-19. Predicted waste package surface temperature for storage time of 150 years: 12 PWR with buffer thermal conductivity of 1.5 W/m K.

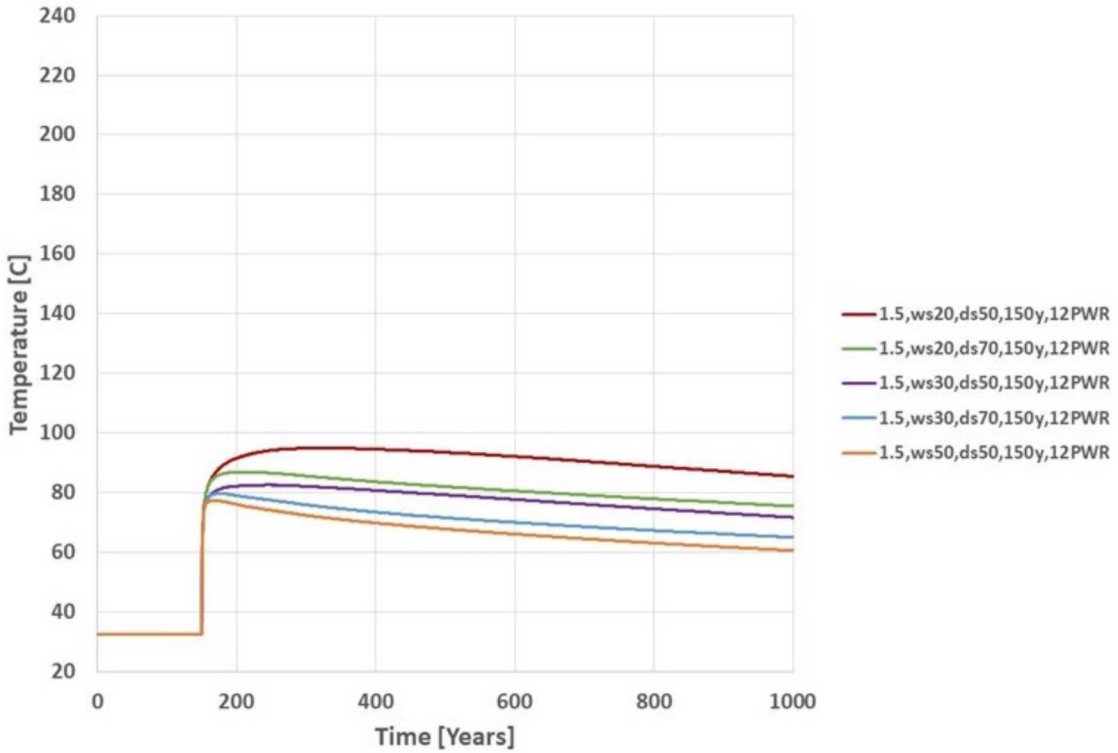

Figure A-20. Predicted drift wall temperature for storage time of 150 years: 12 PWR with buffer thermal conductivity of 1.5 W/m K.

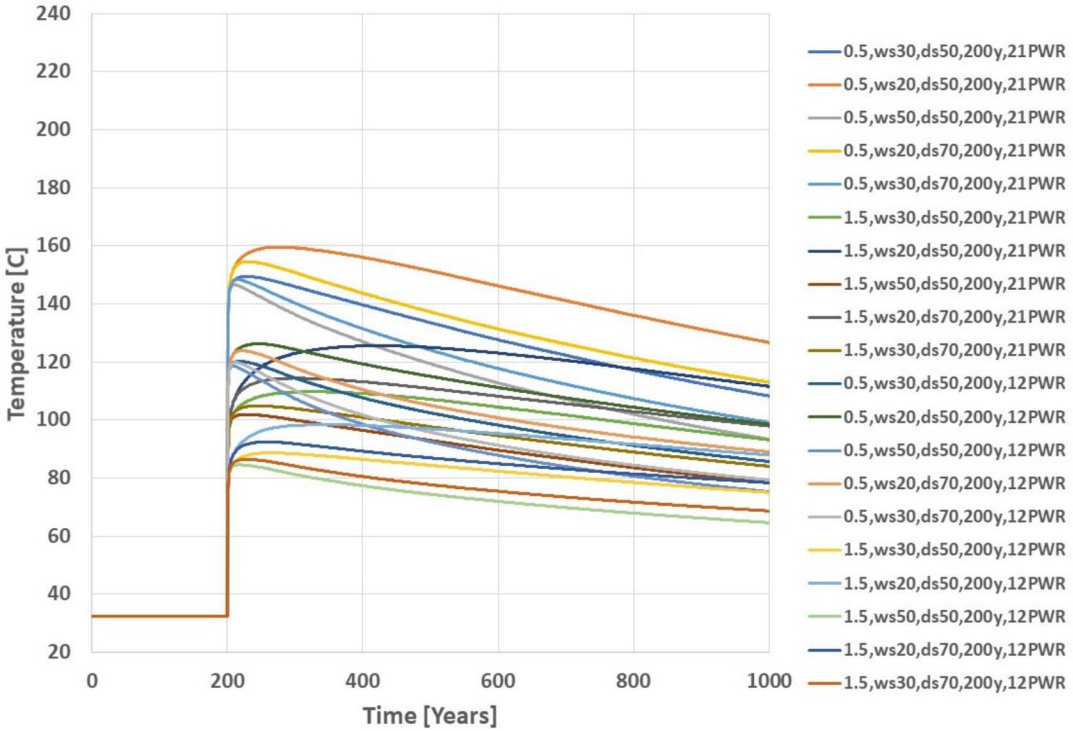

Figure 21. Predicted waste package surface temperature for storage time of 200 years. Results show temperature plots for various parameters.

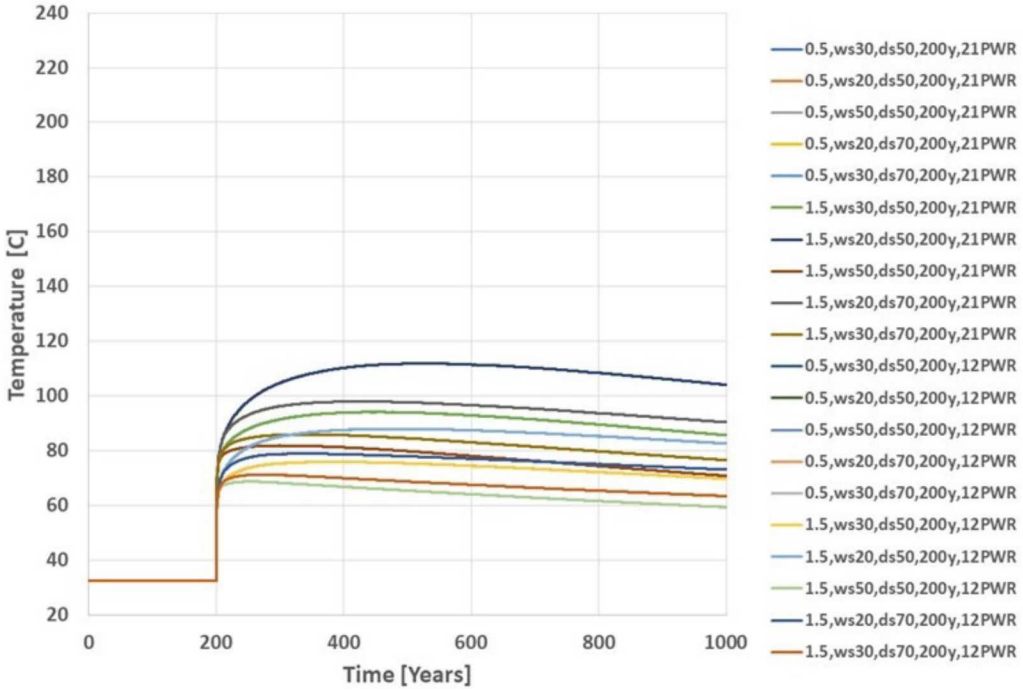

Figure A-22. Predicted waste package surface temperature for storage time of 200 years. Results show temperature plots for various parameters.

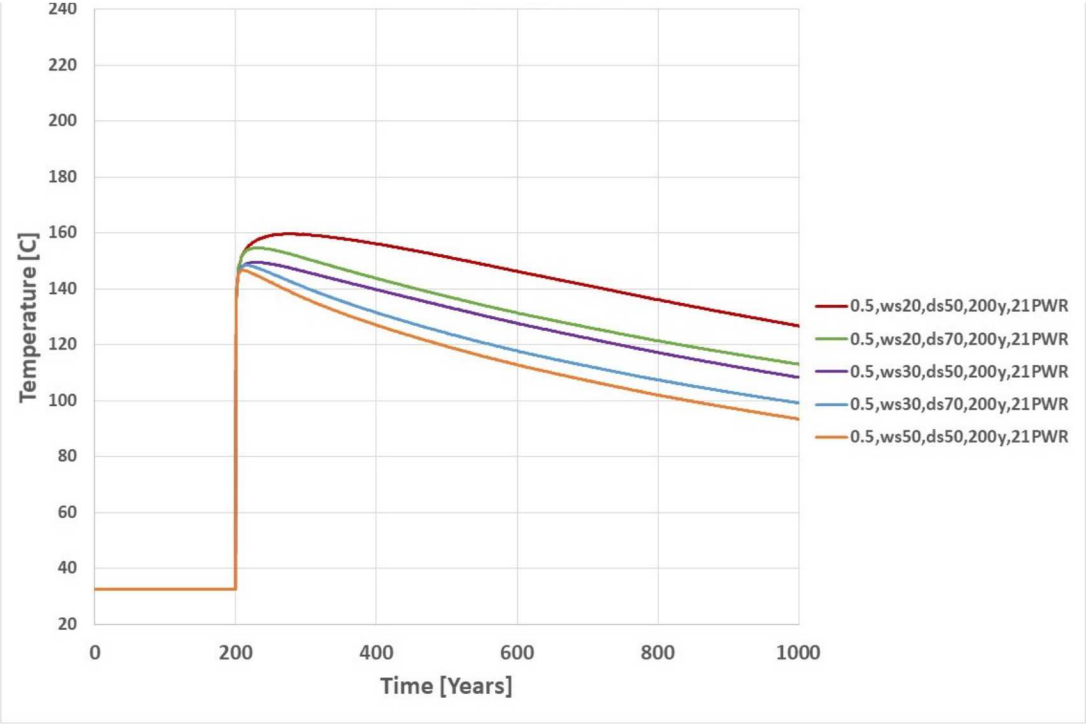

Figure A-23. Predicted waste package surface temperature for storage time of 200 years: 21 PWR with buffer thermal conductivity of 0.5 W/m K.

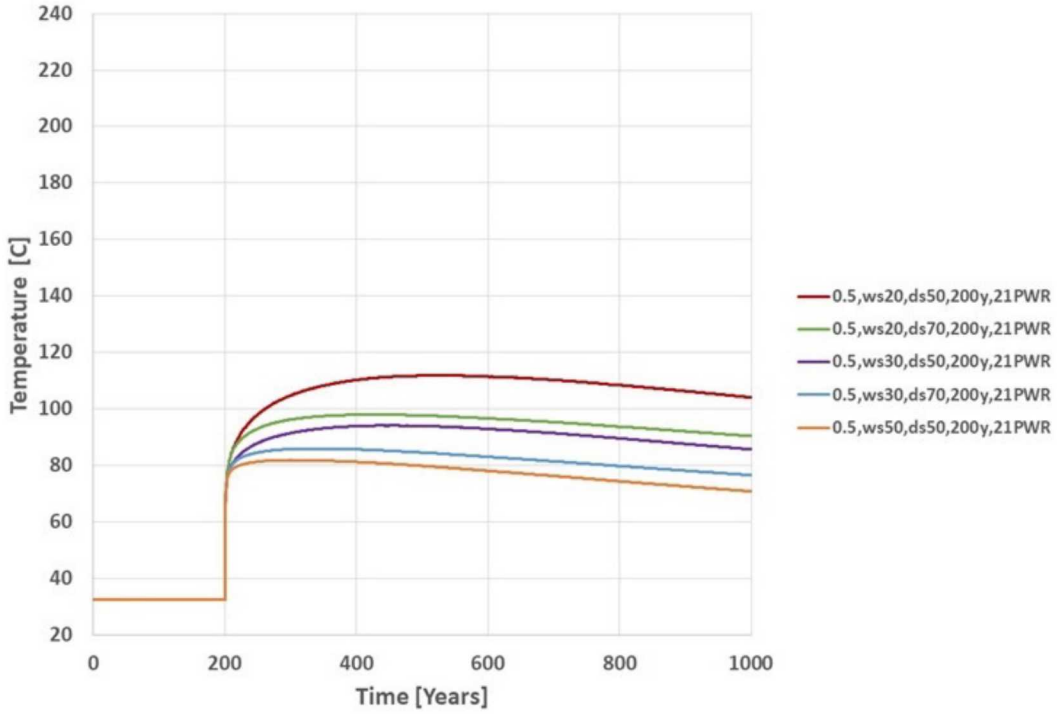

Figure A-24. Predicted drift wall temperature for storage time of 200 years: 21 PWR with buffer thermal conductivity of 0.5 W/m K.

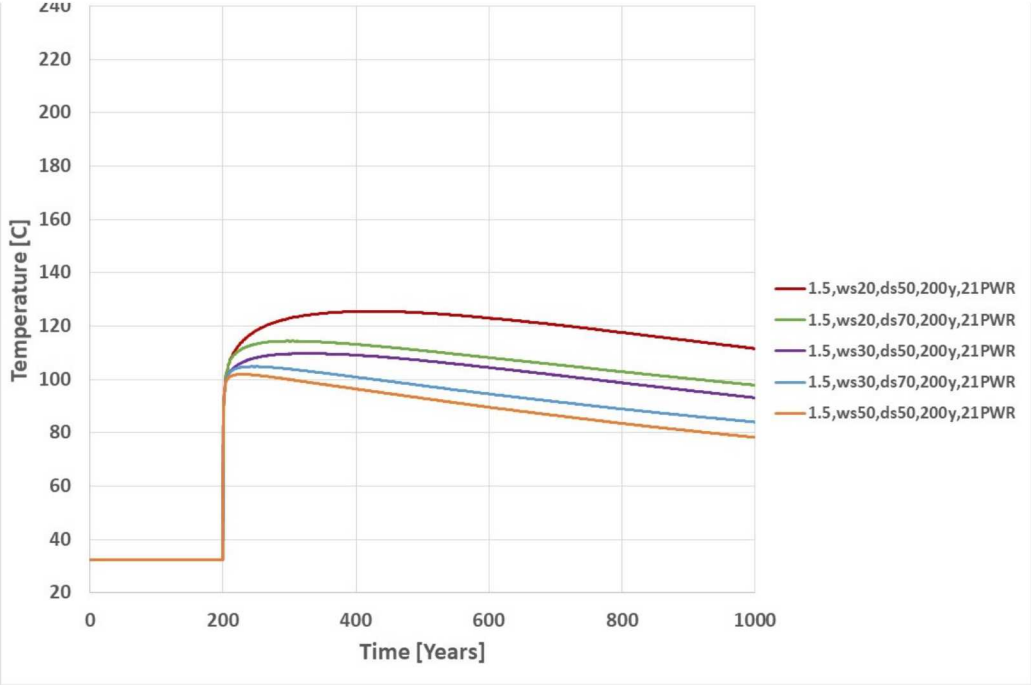

Figure A-25. Predicted waste package surface temperature for storage time of 200 years: 21 PWR with buffer thermal conductivity of 1.5 W/m K.

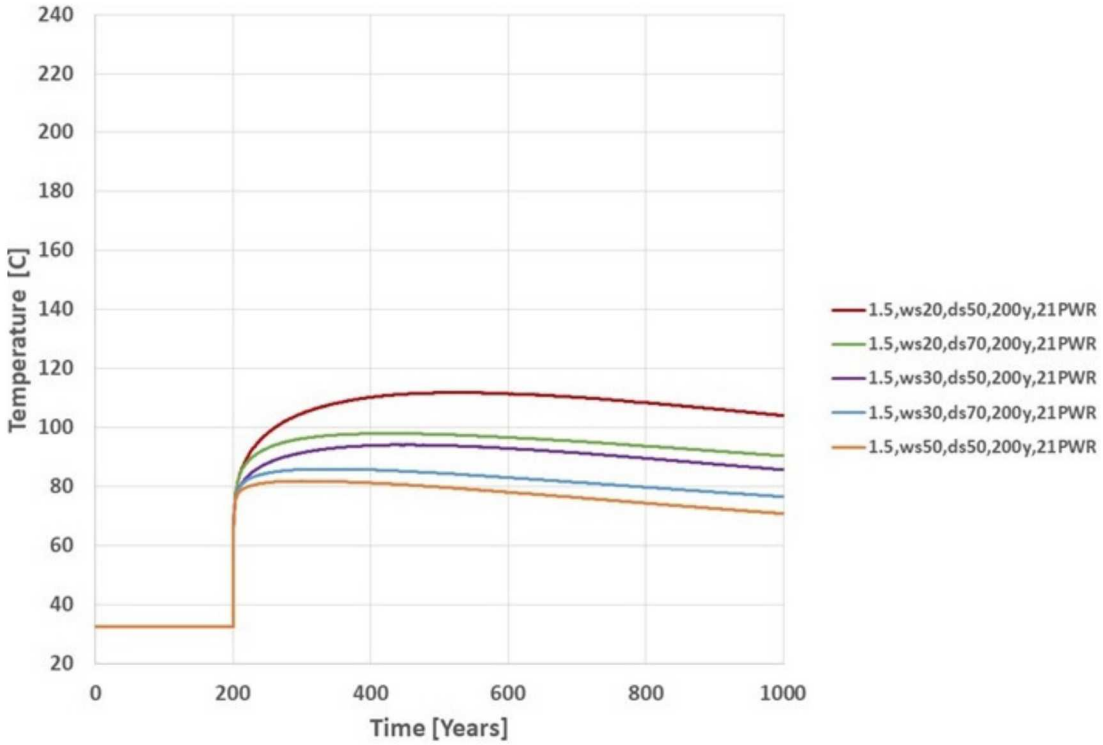

Figure A-26. Predicted waste package surface temperature for storage time of 200 years: 21 PWR with buffer thermal conductivity of 1.5 W/m K.

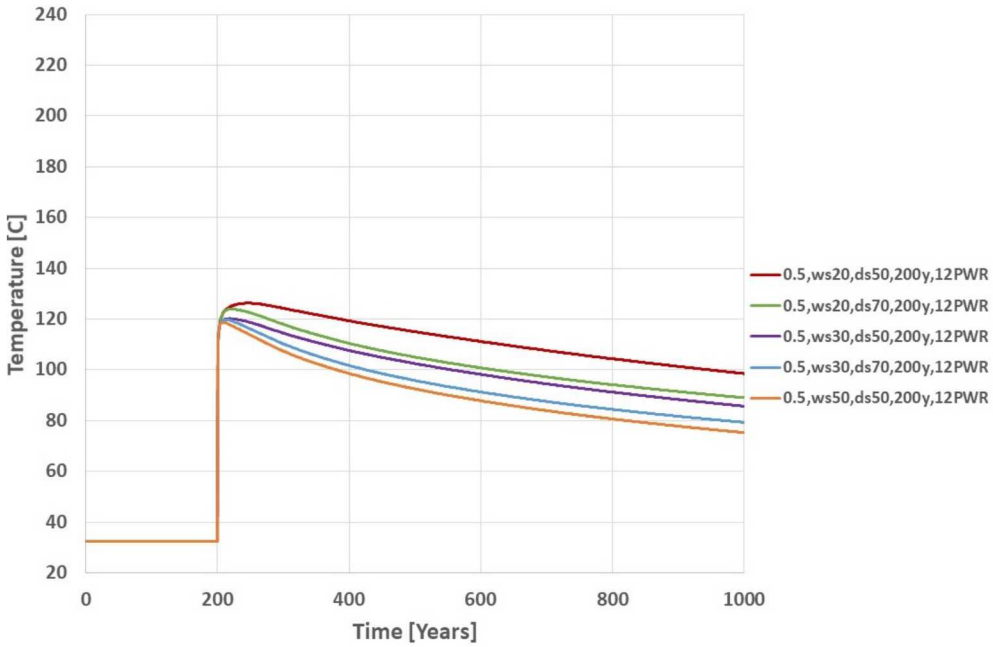

Figure A-27. Predicted waste package surface temperature for storage time of 200 years: 12 PWR with buffer thermal conductivity of 0.5 W/m K.

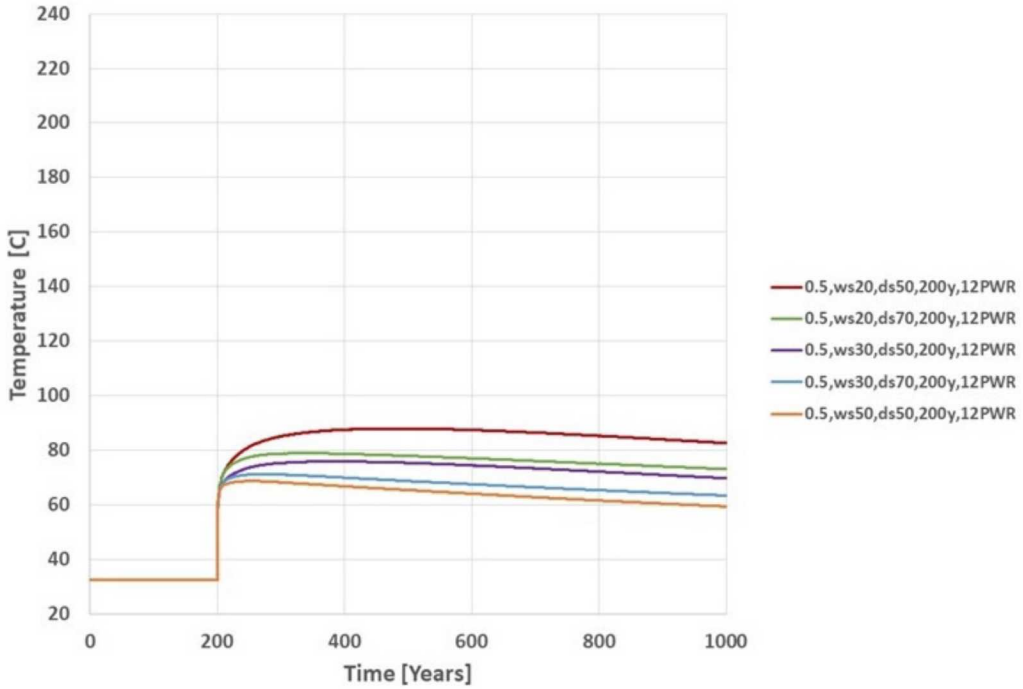
240
220
200
180
160
140
120
100
80
60
40
20
Temperature [C]
0
200
400
600
800
1000
Time [Years]
0.5,ws20,ds50,200y,12PWR
0.5,ws20,ds70,200y,12PWR
0.5,ws30,ds50,200y,12PWR
0.5,ws30,ds70,200y,12PWR
0.5,ws50,ds50,200y,12PWR

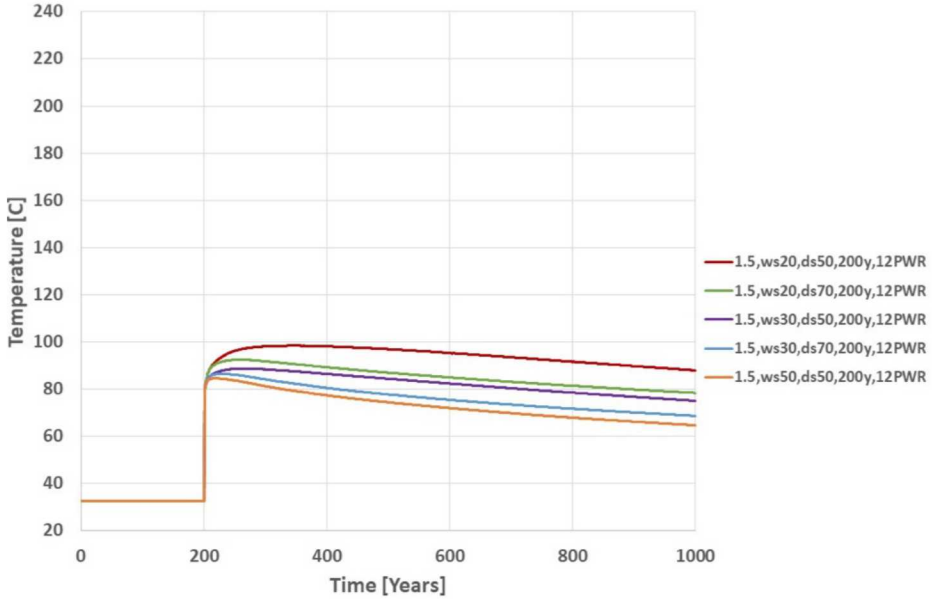

Figure A-29. Predicted waste package surface temperature for storage time of 200 years: 12 PWR with buffer thermal conductivity of 1.5 W/m K.

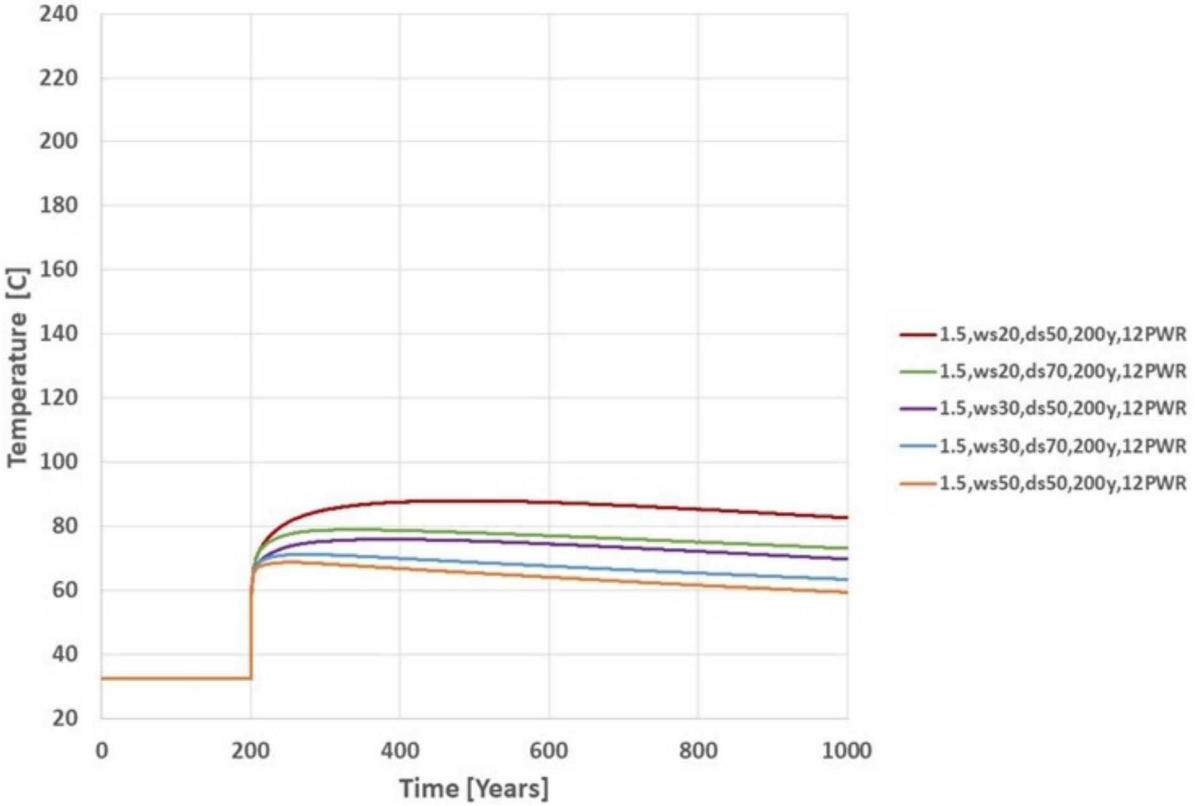

Figure A-30. Predicted waste package surface temperature for storage time of 200 years: 12 PWR with buffer thermal conductivity of 1.5 W

Appendix B Water Chemistry IEBS-1 and IEBS-2

IEBS-1 UNFILTERED

Lab ID	Sample Date	Al	B	Ba	Br	Ca	Cl^-	Cr	F^-	Fe	K	Li	Mg	Mn	Na	NO_3^-	PO_4^{3-}	Si	SiO_2	SO_4^{2-}	Sr	Ti	Zn	TDS	Cation	Anion	Balance
		ppm	ppm	ppm	ppm	ppm	ppm	ppm	ppm	ppm	ppm	ppm	ppm	ppm	ppm	ppm	ppm	ppm	ppm	ppm	ppm	ppm	ppm	ppm	ppm	ppm	
IEBS-1-1 UF	11/22/2017	5.01	4.45	0.07	<0.1	2.23	31.94	0.01	6.69	0.79	2.19	0.05	0.38	<0.006	150.31	<0.1	<0.1	263.31	563.48	201.87	0.02	0.01	<0.104	969	14	6	0.42
IEBS-1-2 UF	11/30/2017	2.94	4.62	0.05	<0.1	1.54	19.92	<0.006	6.37	0.37	2.40	0.05	0.37	<0.006	130.46	<0.1	<0.1	221.33	473.65	199.87	0.01	<0.004	<0.104	843	12	5	0.38
IEBS-1-3 UF	12/7/2017	2.46	4.15	0.04	<0.1	1.29	18.27	<0.006	5.87	0.16	1.81	0.04	0.28	<0.006	124.16	<0.1	<0.1	191.7	410.20	182.39	0.01	<0.004	<0.104	751	11	5	0.38
IEBS-1-4 UF	12/14/2017	2.47	3.95	0.05	<0.1	1.33	18.47	0.01	6.21	0.68	1.61	0.03	<0.02	<0.006	120.74	<0.1	<0.1	294.70	630.66	172.72	0.01	<0.004	<0.104	959	13	5	0.48
IEBS-1-5 UF	12/20/2017	2.59	3.75	0.07	<0.1	0.87	17.88	<0.006	5.78	0.28	1.54	0.03	0.12	<0.006	115.98	<0.1	<0.1	303.02	648.46	182.78	0.01	<0.004	<0.104	980	13	5	0.46
IEBS-1-6 UF	1/5/2018	0.70	2.21	0.11	<0.1	1.67	11.78	0.01	3.27	3.94	<1.122	0.10	0.18	0.01	120.14	<0.1	<0.1	156.72	335.37	98.65	0.01	<0.004	<0.104	578	10	3	0.56

IEBS-1 FILTERED

Lab ID	Sample Date	Al	B	Ba	Ca	Cr	Fe	K	Li	Mg	Mn	Na	Si	SiO_2	Sr	Ti	Zn	TDS	Cation	Anion	Balance
		ppm	ppm	ppm	ppm	ppm	ppm	ppm	ppm	ppm	ppm	ppm	ppm	ppm	ppm	ppm	ppm	ppm	ppm	ppm	
IEBS-1-1 F	11/22/2017	4.65	4.51	0.19	1.89	0.01	0.66	2.35	0.04	0.10	<0.006	156.71	259.45	555.23	0.03	<0.004	<0.104	726	14	0	0.97
IEBS-1-2 F	11/30/2017	2.90	4.35	0.06	1.08	<0.006	0.70	1.97	0.04	<0.02	<0.006	130.81	310.90	665.33	0.01	<0.004	<0.104	807	14	0	0.97
IEBS-1-3 F	12/7/2017	2.60	4.19	0.07	0.92	<0.006	1.71	1.85	0.04	0.09	<0.006	127.94	319.37	683.46	0.01	<0.004	<0.104	823	14	0	0.97
IEBS-1-4 F	12/14/2017	2.63	4.03	0.03	0.86	<0.006	0.21	1.95	0.03	<0.02	<0.006	126.17	310.52	664.52	0.01	<0.004	<0.104	800	14	0	0.97
IEBS-1-5 F	12/20/2017	2.71	3.71	0.06	1.00	<0.006	0.45	1.55	0.03	<0.02	<0.006	119.35	325.59	696.77	0.01	<0.004	<0.104	826	14	0	0.98
IEBS-1-6 F	1/5/2018	0.65	1.99	0.12	1.42	0.01	3.87	<1.122	0.10	0.08	<0.006	122.93	167.30	358.02	0.01	<0.004	<0.104	489	10	0	0.98

IEBS-2 UNFILTERED

Lab ID	Sample Date	Al	B	Ba	Br	Ca	Cl^-	Cr	F^-	Fe	K	Li	Mg	Mn	Na	NO_3^-	PO_4^{3-}	Si	SiO_2	SO_4^{2-}	Sr	Ti	Zn	TDS	Cation	Anion	Balance
		ppm	ppm	ppm	ppm	ppm	ppm	ppm	ppm	ppm	ppm	ppm	ppm	ppm	ppm	ppm	ppm	ppm	ppm	ppm	ppm	ppm	ppm	ppm	ppm	ppm	
IEBS-2-1 UF	3/15/2018	3.21	3.76	0.09	0.21	1.86	23.16	0.01	8.50	0.51	1.68	0.05	0.04	<0.006	128.08	0.56	0.17	316.94	678.26	347.49	0.02	<0.004	<0.104	1198	14	9	0.24
IEBS-2-2 UF	3/22/2018	3.23	3.38	0.08	0.14	2.30	17.33	0.01	5.89	0.43	2.12	0.06	0.30	<0.006	109.71	0.43	0.12	256.43	548.76	242.91	0.02	0.01	<0.104	937	12	6	0.32
IEBS-2-3 UF	3/29/2018	2.65	3.04	0.16	0.16	0.76	15.78	0.01	5.27	0.37	1.64	0.06	<0.02	<0.006	106.63	0.53	0.09	222.10	629.41	197.02	0.01	<0.004	<0.104	964	12	5	0.43
IEBS-2-4 UF	4/5/2018	2.65	2.92	0.08	0.13	0.97	15.69	<0.006	5.71	0.27	1.74	0.05	<0.02	<0.006	105.83	0.20	0.07	305.08	652.86	205.86	0.01	<0.004	<0.104	995	13	5	0.42
IEBS-2-5 UF	4/12/2018	2.59	2.75	0.11	0.13	1.27	15.69	<0.006	6.13	0.87	1.62	0.05	0.14	<0.006	103.29	0.31	0.20	295.38	632.11	207.91	0.01	0.01	<0.104	975	12	5	0.41
IEBS-2-6 UF	4/19/2018	2.61	2.58	0.08	0.19	1.55	15.51	<0.006	6.41	0.20	1.38	0.05	0.14	<0.006	97.69	0.78	0.10	287.69	615.65	196.82	0.01	<0.004	<0.104	942	12	5	0.41
IEBS-2-7 UF	4/20/2018	38.84	1.92	0.48	<0.1	7.12	12.41	0.03	4.54	19.27	2.14	0.14	11.84	0.12	113.08	0.21	0.28	284.97	609.84	143.12	0.16	0.20	0.11	966	19	4	0.67

IEBS-2 FILTERED

Lab ID	Sample Date	Al	B	Ba	Ca	Cr	Fe	K	Li	Mg	Mn	Na	Si	SiO_2	Sr	Ti	Zn	TDS	Cation	Anion	Balance
		ppm	ppm	ppm	ppm	ppm	ppm	ppm	ppm	ppm	ppm	ppm	ppm	ppm	ppm	ppm	ppm	ppm	ppm	ppm	
IEBS-2-1 F	3/15/2018	3.04	3.88	0.06	1.67	0.01	0.35	1.98	0.05	<0.02	<0.006	129.33	321.28	687.55	0.02	<0.004	<0.104	828	14	0	0.97
IEBS-2-2 F	3/22/2018	0.81	1.32	0.34	101.77	<0.006	0.12	100.51	0.25	<0.02	<0.006	1859.73	24.22	51.82	0.53	<0.004	<0.104	2117	89	0	1.00
IEBS-2-2 F (rerun)	3/22/2018	0.78	1.13	0.33	106.57	<0.006	<0.036	104.29	0.25	<0.02	<0.006	1943.18	23.91	51.16	0.53	<0.004	<0.104	2208	93	0	1.00
IEBS-2-3 F	3/29/2018	1.63	3.59	6.16	0.72	<0.006	0.28	3.56	0.06	0.08	<0.006	119.63	227.26	448.57	0.03	<0.004	1.41	586	11	0	0.97
IEBS-2-3 F (rerun)	3/29/2018	1.71	3.64	4.77	0.78	0.01	0.21	2.72	0.05	0.07	<0.006	128.78	209.61	475.30	0.03	<0.004	1.41	619	12	0	0.97
IEBS-2-4 F	4/5/2018	2.55	2.85	0.05	1.24	<0.006	0.15	1.71	0.06	0.07	<0.006	107.87	281.38	602.16	0.01	<0.004	<0.104	719	12	0	0.98
IEBS-2-5 F	4/12/2018	2.63	2.73	0.11	1.19	0.01	0.49	2.09	0.05	0.08	<0.006	104.99	291.42	623.63	0.01	<0.004	<0.104	738	12	0	0.98
IEBS-2-6 F	4/19/2018	2.57	2.60	0.09	0.75	0.01	0.73	1.66	0.05	<0.02	<0.006	101.49	299.68	641.32	0.01	<0.004	<0.104	751	12	0	0.98
IEBS-2-7 F	4/20/2018	0.50	1.89	0.09	0.23	0.01	0.52	<1.122	0.12	0.03	<0.006	96.44	207.15	443.29	0.00	<0.004	<0.104	543	9	0	0.98

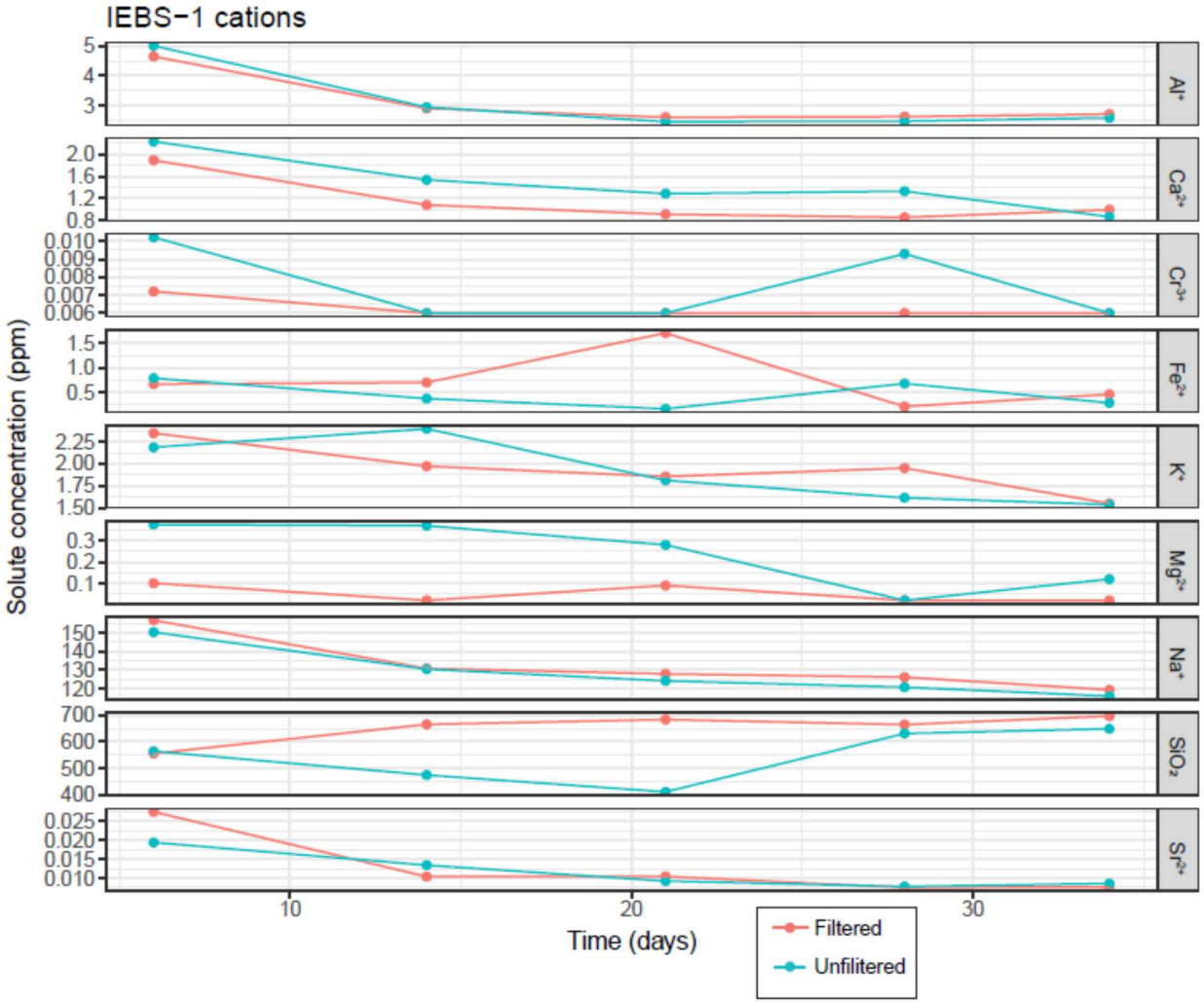
IEBS−1 cations
Solute concentration (ppm)
Al³⁺
Ca²⁺
Cr³⁺
Fe²⁺
K⁺
Mg²⁺
Na⁺
SiO₂
Sr²⁺
Time (days)
Filtered
Unfiltered

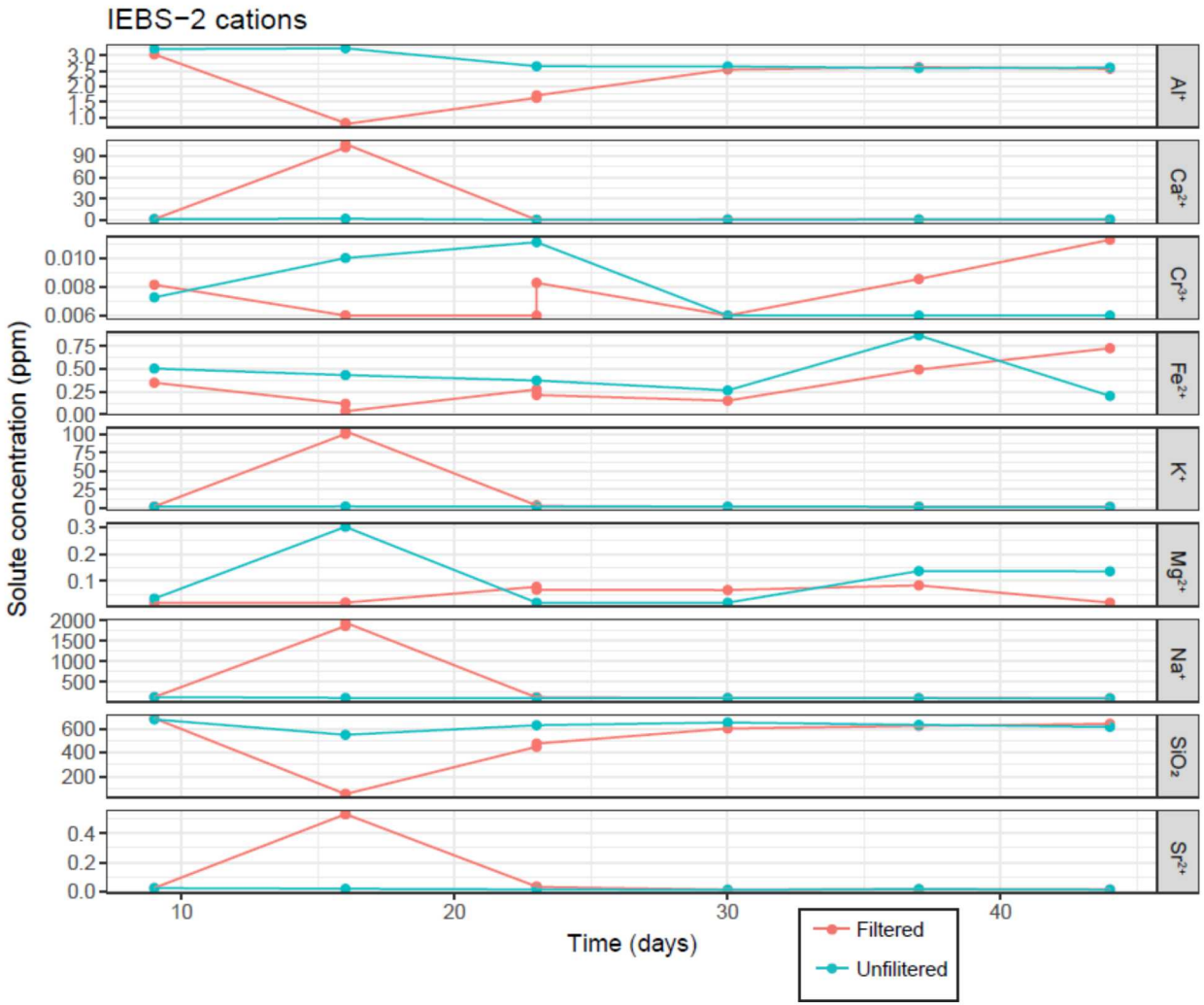
IEBS−2 cations
Solute concentration (ppm)
Al+
Ca2+
Cr2+
Fe2+
K+
Mg2+
Na+
SiO2
Sr2+
Time (days)
Filtered
Unfilitered

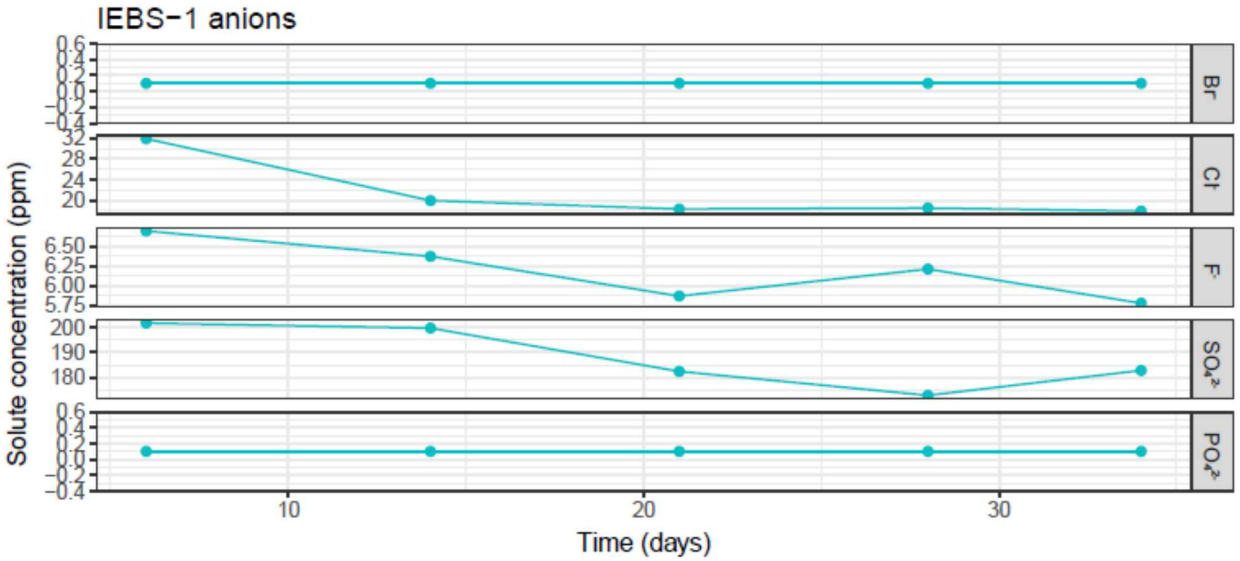
IEBS−1 anions
Solute concentration (ppm)
Br⁻
Cl⁻
F⁻
SO4²⁻
PO4³⁻
Time (days)

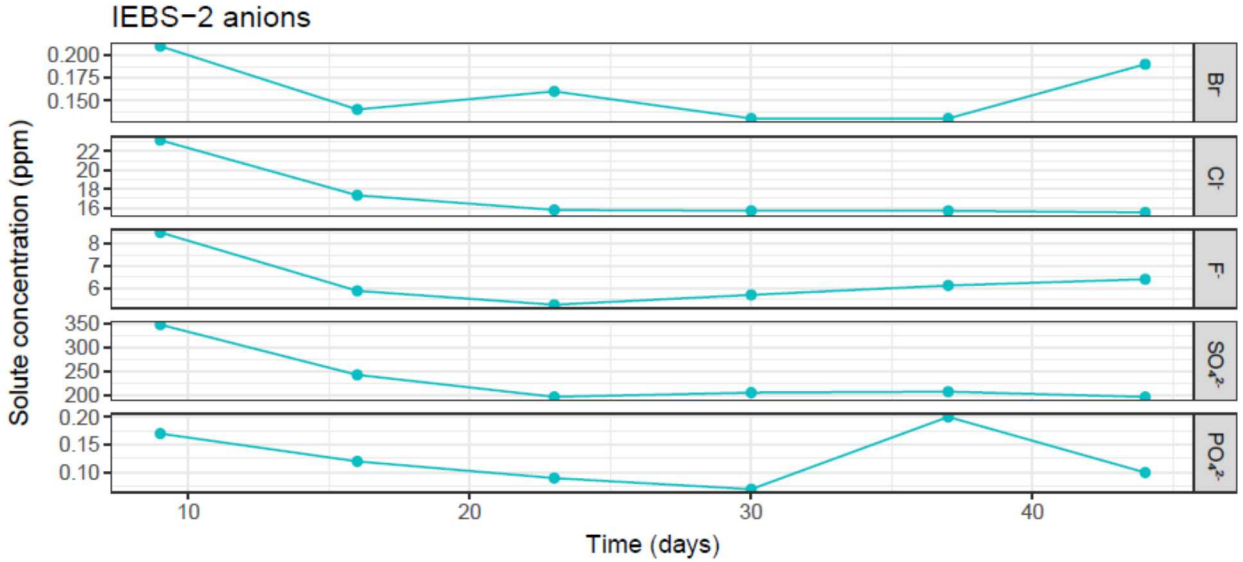
IEBS−2 anions
Solute concentration (ppm)
Br⁻
Cl⁻
F⁻
SO4²⁻
PO4³⁻
Time (days)

Appendix C Electron Microprobe Data IEBS-1 and IEBS-2

Table C-1: EMP standards and oxide detection limits for silicate analyses

Element	Standard Material	Minimum Detection Limit[a]
Mg	Synthetic Phlogopite	0.02
F	Synthetic Phlogopite	0.11
Na	Albite (Amelia, NC, U.S.A, Rutherford Mine)	0.02
Al	Labradorite (Chihuahua, Mexico)	0.02
Si	Labradorite (Chihuahua, Mexico)	0.02
Ca	Labradorite (Chihuahua, Mexico)	0.01
Cl	Tugtupite (Greenland)	0.01
K	Adularia (St. Gotthard, Switzerland)	0.01
Ti	Titanite glass (Penn State)	0.02
Cr	Synthetic Magnesio-chromite	0.04
Mn	Rhodonite (unknown locality)	0.02
Fe	Augite (unknown locality)	0.02
Ni	Synthetic Liebenbergite	0.06
Zn	Gahnite	0.05

[a] Minimum Detection Limit (MDL) values for oxides of respective elements

IEBS-1															
Clinoptilolite	**SiO_2**	**TiO_2**	**Al_2O_3**	**Cr_2O_3**	**FeO**	**NiO**	**MnO**	**MgO**	**CaO**	**Na_2O**	**K_2O**	**Cl**	**F**	**O=F&Cl**	**TOTAL**
IEBS-1 Area 1 Shard	70.70	0.01	11.28	0.00	0.10	0.00	0.01	0.10	1.98	1.89	0.39	0.01	0.02	-0.01	86.47
IEBS-1 Area 3 Shard	62.94	0.01	12.29	0.00	0.09	0.00	0.01	0.13	1.83	3.07	0.45	0.00	0.03	-0.01	80.83
IEBS-1 Area 3 Shard	70.38	0.01	11.82	0.00	0.08	0.01	0.03	0.10	1.88	2.17	0.40	0.00	0.05	-0.02	86.87
IEBS-1 Area 3 Shard	64.94	0.00	11.35	0.00	0.11	0.00	0.04	0.13	1.77	3.34	0.29	0.00	0.02	-0.01	81.96
IEBS-1 Area 4 shard	61.11	0.00	12.28	0.00	0.10	0.00	0.02	0.11	2.03	2.29	0.48	0.00	0.00	0.00	78.42
AVERAGE	**66.02**	**0.00**	**11.80**	**0.00**	**0.10**	**0.00**	**0.02**	**0.11**	**1.90**	**2.55**	**0.40**	**0.00**	**0.03**	**-0.01**	**82.91**
Std. Dev.	**4.35**	**0.00**	**0.48**	**0.00**	**0.01**	**0.01**	**0.01**	**0.01**	**0.11**	**0.62**	**0.08**	**0.00**	**0.02**	**0.01**	**3.66**
	18 oxygen atoms per formula unit (sum excludes F & Cl)														
	Si	**Ti**	**Al**	**Cr**	**Fe**	**Ni**	**Mn**	**Mg**	**Ca**	**Na**	**K**	**Cl**	**F**		**Sum**
IEBS-1 Area 1 Shard	7.676	0.001	1.443	0.000	0.009	0.000	0.000	0.016	0.231	0.397	0.054	0.001	0.008		9.827
IEBS-1 Area 3 Shard	7.399	0.000	1.703	0.000	0.009	0.000	0.001	0.023	0.231	0.700	0.068	0.000	0.012		10.133

IEBS-1 Area 3 Shard	7.619	0.001	1.508	0.000	0.007	0.001	0.002	0.016	0.218	0.455	0.055	0.000	0.018		9.882
IEBS-1 Area 3 Shard	7.513	0.000	1.548	0.000	0.010	0.000	0.004	0.022	0.219	0.748	0.042	0.000	0.009		10.108
IEBS-1 Area 4 shard	7.388	0.000	1.749	0.000	0.010	0.000	0.002	0.019	0.263	0.538	0.074	0.001	0.000		10.043
AVERAGE	**7.52**	**0.00**	**1.59**	**0.00**	**0.01**	**0.00**	**0.00**	**0.02**	**0.23**	**0.57**	**0.06**	**0.00**	**0.01**		**10.00**
Std. Dev.	**0.13**	**0.00**	**0.13**	**0.00**	**0.00**	**0.00**	**0.00**	**0.00**	**0.02**	**0.15**	**0.01**	**0.00**	**0.01**		**0.14**
Chlorite	**SiO_2**	**TiO_2**	**Al_2O_3**	**Cr_2O_3**	**FeO**	**NiO**	**MnO**	**MgO**	**CaO**	**Na_2O**	**K_2O**	**Cl**	**F**	**O=F&Cl**	**TOTAL**
IEBS-1 Area 1 Chlorite	34.60	1.58	16.65	0.00	22.61	0.00	0.60	7.11	0.01	0.16	9.24	0.09	0.72	-0.32	92.64
IEBS-1 Area 3 chlorite	36.26	1.86	16.32	0.00	22.18	0.00	0.57	8.04	0.00	0.17	9.53	0.07	0.80	-0.35	95.00
IEBS-1 Area 4 chlorite	34.40	4.52	14.13	0.00	24.58	0.00	0.28	7.82	0.00	0.41	8.85	0.22	0.54	-0.28	95.21
AVERAGE	**35.09**	**2.65**	**15.70**	**0.00**	**23.12**	**0.00**	**0.48**	**7.66**	**0.01**	**0.25**	**9.21**	**0.13**	**0.69**	**-0.32**	**94.29**
Std. Dev.	**1.02**	**1.62**	**1.37**	**0.00**	**1.28**	**0.00**	**0.18**	**0.49**	**0.00**	**0.14**	**0.34**	**0.08**	**0.14**	**0.04**	**1.43**
	11 oxygen atoms per formula unit (sum excludes F & Cl)														
	Si	**Ti**	**Al**	**Cr**	**Fe**	**Ni**	**Mn**	**Mg**	**Ca**	**Na**	**K**	**Cl**	**F**		**Sum**
IEBS-1 Area 1 Chlorite	2.777	0.095	1.575	0.000	1.517	0.000	0.040	0.850	0.001	0.025	0.946	0.012	0.182		7.826
IEBS-1 Area 3 chlorite	2.768	0.107	1.469	0.000	1.416	0.000	0.037	0.915	0.000	0.025	0.928	0.009	0.193		7.665
IEBS-1 Area 4 chlorite	2.721	0.269	1.317	0.000	1.626	0.000	0.019	0.922	0.000	0.063	0.893	0.029	0.135		7.830
AVERAGE	**2.76**	**0.16**	**1.45**	**0.00**	**1.52**	**0.00**	**0.03**	**0.90**	**0.00**	**0.04**	**0.92**	**0.02**	**0.17**		**7.77**
Std. Dev.	**0.03**	**0.10**	**0.13**	**0.00**	**0.10**	**0.00**	**0.01**	**0.04**	**0.00**	**0.02**	**0.03**	**0.01**	**0.03**		**0.09**
Unknown zeolite pseudomorph	**SiO_2**	**TiO_2**	**Al_2O_3**	**Cr_2O_3**	**FeO**	**NiO**	**MnO**	**MgO**	**CaO**	**Na_2O**	**K_2O**	**Cl**	**F**	**O=F&Cl**	**TOTAL**
IEBS-1 Area 2 Analcime?	46.76	0.13	13.44	0.00	18.93	0.00	0.14	5.24	0.70	2.98	0.22	0.03	0.12	-0.06	88.58
IEBS-1 Area 6 analcime?	42.38	0.09	11.97	0.00	26.47	0.08	0.20	5.83	1.27	6.03	0.26	0.02	0.00	0.00	94.58
AVERAGE	**44.57**	**0.11**	**12.71**	**0.00**	**22.70**	**0.04**	**0.17**	**5.53**	**0.99**	**4.50**	**0.24**	**0.02**	**0.06**	**-0.03**	**91.58**
Std. Dev.	**3.10**	**0.03**	**1.04**	**0.00**	**5.33**	**0.05**	**0.04**	**0.42**	**0.40**	**2.15**	**0.03**	**0.01**	**0.08**	**0.04**	**4.25**
	6 oxygen atoms per formula unit (sum excludes F & Cl)														
	Si	**Ti**	**Al**	**Cr**	**Fe**	**Ni**	**Mn**	**Mg**	**Ca**	**Na**	**K**	**Cl**	**F**		**Sum**
IEBS-1 Area 2 Analcime?	1.935	0.004	0.655	0.000	0.655	0.000	0.005	0.323	0.031	0.239	0.011	0.002	0.015		3.859
IEBS-1 Area 6 analcime?	1.760	0.003	0.586	0.000	0.919	0.003	0.007	0.361	0.057	0.485	0.014	0.001	0.000		4.194
AVERAGE	**1.85**	**0.00**	**0.62**	**0.00**	**0.79**	**0.00**	**0.01**	**0.34**	**0.04**	**0.36**	**0.01**	**0.00**	**0.01**		**4.03**
Std. Dev.	**0.12**	**0.00**	**0.05**	**0.00**	**0.19**	**0.00**	**0.00**	**0.03**	**0.02**	**0.17**	**0.00**	**0.00**	**0.01**		**0.24**
Clay Matrix	**SiO_2**	**TiO_2**	**Al_2O_3**	**Cr_2O_3**	**FeO**	**NiO**	**MnO**	**MgO**	**CaO**	**Na_2O**	**K_2O**	**Cl**	**F**	**O=F&Cl**	**TOTAL**
IEBS-1 Area 4 Matrix	61.55	0.11	21.61	0.00	3.99	0.00	0.01	1.91	0.54	1.11	0.28	0.02	0.20	-0.09	91.14
IEBS-1 Area 4 matrix	59.35	0.12	22.31	0.00	4.17	0.01	0.01	1.90	0.14	0.99	0.27	0.02	0.28	-0.12	89.29

IEBS-1 Area 1 Matrix	59.55	0.12	22.16	0.00	3.93	0.01	0.02	2.08	0.42	1.15	0.27	0.02	0.21	-0.09	89.74
AVERAGE	**60.15**	**0.12**	**22.03**	**0.00**	**4.03**	**0.01**	**0.01**	**1.97**	**0.37**	**1.08**	**0.27**	**0.02**	**0.23**	**-0.10**	**90.06**
Std. Dev.	**1.22**	**0.01**	**0.37**	**0.00**	**0.13**	**0.01**	**0.00**	**0.10**	**0.20**	**0.09**	**0.01**	**0.00**	**0.05**	**0.02**	**0.96**
	12 oxygen atoms per formula unit (sum excludes F & Cl)														
	Si	**Ti**	**Al**	**Cr**	**Fe**	**Ni**	**Mn**	**Mg**	**Ca**	**Na**	**K**	**Cl**	**F**		**Sum**
IEBS-1 Area 4 Matrix	4.341	0.006	1.796	0	0.235	0	6E-04	0.201	0.041	0.152	0.025	0.002	0.045		6.80
IEBS-1 Area 4 matrix	4.268	0.006	1.891	0	0.251	6E-04	6E-04	0.204	0.011	0.138	0.025	0.002	0.064		6.80
IEBS-1 Area 1 Matrix	4.271	0.006	1.873	0	0.236	6E-04	0.001	0.222	0.032	0.16	0.025	0.002	0.048		6.83
AVERAGE	**4.29**	**0.01**	**1.85**	**0.00**	**0.24**	**0.00**	**0.00**	**0.21**	**0.03**	**0.15**	**0.02**	**0.00**	**0.05**		**6.81**
Std. Dev.	**0.04**	**0.00**	**0.05**	**0.00**	**0.01**	**0.00**	**0.00**	**0.01**	**0.02**	**0.01**	**0.00**	**0.00**	**0.01**		**0.02**
Stilpnomelane	**SiO_2**	**TiO_2**	**Al_2O_3**	**Cr_2O_3**	**FeO**	**NiO**	**MnO**	**MgO**	**CaO**	**Na_2O**	**K_2O**	**Cl**	**F**	**O=F&Cl**	**TOTAL**
IEBS-1 Area 5 stil?	33.81	0.02	12.03	0.00	24.99	0.01	0.11	1.31	0.58	1.84	0.08	0.13	0.00	-0.03	74.90
IEBS-1 Area 5 stil?	32.93	0.01	12.39	0.00	25.73	0.02	0.12	1.23	0.75	1.96	0.06	0.09	0.02	-0.03	75.29
IEBS-1 Area 5 stil?	31.76	0.03	11.14	0.01	21.30	0.00	0.11	1.28	0.34	2.02	0.08	0.16	0.05	-0.05	68.21
IEBS-1 Area 5 stil?	43.61	0.09	15.21	0.01	25.60	0.00	0.11	2.00	1.09	2.45	0.15	0.01	0.16	-0.07	90.32
IEBS-1 Area 6 stil?	34.02	0.01	11.09	0.01	24.29	0.00	0.10	2.12	0.48	1.59	0.02	0.10	0.00	-0.02	73.85
IEBS-1 Area 6 stil?	35.03	0.02	12.55	0.00	26.48	0.00	0.10	1.94	0.46	1.78	0.03	0.09	0.05	-0.04	78.49
IEBS-1 Area 6 stil?	32.95	0.02	11.79	0.01	26.36	0.02	0.10	1.59	0.44	1.57	0.04	0.14	0.01	-0.03	75.02
IEBS-1 Area 6 stil?	45.21	0.06	17.01	0.01	22.68	0.00	0.10	1.84	0.96	4.45	0.30	0.02	0.07	-0.03	92.64
AVERAGE	**36.17**	**0.03**	**12.90**	**0.01**	**24.68**	**0.01**	**0.11**	**1.66**	**0.64**	**2.21**	**0.10**	**0.09**	**0.04**	**-0.04**	**78.59**
Std. Dev.	**5.20**	**0.03**	**2.10**	**0.00**	**1.84**	**0.01**	**0.01**	**0.36**	**0.27**	**0.95**	**0.09**	**0.05**	**0.05**	**0.02**	**8.47**
	28 oxygen atoms per formula unit (sum excludes F & Cl)														
	Si	**Ti**	**Al**	**Cr**	**Fe**	**Ni**	**Mn**	**Mg**	**Ca**	**Na**	**K**	**Cl**	**F**		**Sum**
IEBS-1 Area 5 stil?	8.281	0.003	3.472	0.000	5.120	0.002	0.022	0.478	0.151	0.875	0.026	0.052	0.000		18.431
IEBS-1 Area 5 stil?	8.089	0.002	3.586	0.000	5.286	0.004	0.025	0.451	0.196	0.935	0.019	0.036	0.018		18.593
IEBS-1 Area 5 stil?	8.434	0.005	3.486	0.001	4.730	0.000	0.024	0.506	0.096	1.042	0.026	0.070	0.038		18.351
IEBS-1 Area 5 stil?	8.577	0.013	3.526	0.001	4.211	0.000	0.018	0.586	0.229	0.934	0.037	0.005	0.098		18.131
IEBS-1 Area 6 stil?	8.406	0.002	3.230	0.002	5.020	0.000	0.022	0.781	0.128	0.762	0.008	0.042	0.000		18.361
IEBS-1 Area 6 stil?	8.198	0.003	3.462	0.000	5.183	0.001	0.019	0.677	0.114	0.809	0.010	0.037	0.040		18.477
IEBS-1 Area 6 stil?	8.141	0.004	3.434	0.002	5.448	0.003	0.021	0.586	0.116	0.754	0.012	0.059	0.005		18.520
IEBS-1 Area 6 stil?	8.558	0.009	3.794	0.001	3.591	0.000	0.016	0.518	0.194	1.632	0.073	0.007	0.039		18.388
AVERAGE	**8.34**	**0.01**	**3.50**	**0.00**	**4.82**	**0.00**	**0.02**	**0.57**	**0.15**	**0.97**	**0.03**	**0.04**	**0.03**		**18.41**

Std. Dev.	**0.19**	**0.00**	**0.16**	**0.00**	**0.63**	**0.00**	**0.00**	**0.11**	**0.05**	**0.29**	**0.02**	**0.02**	**0.03**		**0.14**

IEBS-2															
C(A)SH (Zeophyllite, tobermorite?)	**SiO_2**	**TiO_2**	**Al_2O_3**	**Cr_2O_3**	**FeO**	**NiO**	**MnO**	**MgO**	**CaO**	**Na_2O**	**K_2O**	**Cl**	**F**	**O=F&Cl**	**TOTAL**
IEBS-2 Area 1 zeolite?	12.11	0.01	1.65	0.00	0.76	0.00	0.06	0.08	46.27	0.28	0.03	0.03	0.69	-0.30	61.28
IEBS-2 Area 1 zeolite?	9.79	0.01	1.88	0.00	0.82	0.00	0.06	0.09	48.20	0.31	0.02	0.02	0.54	-0.23	61.20
IEBS-2 Area 1 zeolite?	7.45	0.01	1.07	0.00	0.66	0.00	0.07	0.08	41.74	0.55	0.02	0.02	0.22	-0.10	51.66
IEBS-2 Area 1 zeolite?	7.27	0.01	1.74	0.00	0.64	0.00	0.08	0.06	42.03	0.38	0.02	0.03	0.57	-0.25	52.26
IEBS-2 Area 1-2 zeolite?	10.13	0.00	1.80	0.00	0.70	0.01	0.04	0.13	48.64	0.43	0.02	0.03	0.94	-0.40	61.93
IEBS-2 Area 1-2 zeolite?	9.33	0.00	1.25	0.00	0.58	0.01	0.05	0.08	48.25	0.49	0.03	0.03	1.24	-0.53	60.11
IEBS-2 Area 1-2 zeolite?	10.45	0.00	3.37	0.00	0.66	0.00	0.03	0.12	43.09	0.74	0.04	0.04	0.80	-0.35	58.52
AVERAGE	**9.50**	**0.01**	**1.82**	**0.00**	**0.69**	**0.00**	**0.05**	**0.09**	**45.46**	**0.45**	**0.03**	**0.03**	**0.71**	**-0.31**	**58.14**
Std. Dev.	**1.70**	**0.00**	**0.74**	**0.00**	**0.08**	**0.00**	**0.02**	**0.02**	**3.09**	**0.16**	**0.01**	**0.01**	**0.32**	**0.14**	**4.36**
	12 oxygen atoms per formula unit (sum excludes F & Cl)														
	Si	**Ti**	**Al**	**Cr**	**Fe**	**Ni**	**Mn**	**Mg**	**Ca**	**Na**	**K**	**Cl**	**F**		**Sum**
IEBS-2 Area 1 zeolite?	1.815	0.001	0.291	0.000	0.095	0.000	0.008	0.018	7.431	0.081	0.006	0.008	0.327		9.747
IEBS-2 Area 1 zeolite?	1.516	0.001	0.343	0.000	0.106	0.000	0.008	0.021	7.998	0.093	0.004	0.005	0.264		10.090
IEBS-2 Area 1 zeolite?	1.407	0.001	0.238	0.000	0.104	0.000	0.011	0.023	8.447	0.201	0.005	0.006	0.131		10.438
IEBS-2 Area 1 zeolite?	1.330	0.001	0.375	0.000	0.098	0.000	0.012	0.016	8.239	0.135	0.005	0.009	0.330		10.212
IEBS-2 Area 1-2 zeolite?	1.523	0.000	0.319	0.000	0.088	0.001	0.005	0.029	7.834	0.125	0.004	0.008	0.447		9.928
IEBS-2 Area 1-2 zeolite?	1.441	0.000	0.228	0.000	0.075	0.001	0.007	0.018	7.985	0.147	0.006	0.008	0.606		9.908
IEBS-2 Area 1-2 zeolite?	1.626	0.000	0.618	0.000	0.086	0.000	0.004	0.028	7.184	0.223	0.008	0.011	0.394		9.776
AVERAGE	**1.52**	**0.00**	**0.34**	**0.00**	**0.09**	**0.00**	**0.01**	**0.02**	**7.87**	**0.14**	**0.01**	**0.01**	**0.36**		**10.01**
Std. Dev.	**0.16**	**0.00**	**0.13**	**0.00**	**0.01**	**0.00**	**0.00**	**0.00**	**0.44**	**0.05**	**0.00**	**0.00**	**0.15**		**0.25**
Plagioclase	**SiO_2**	**TiO_2**	**Al_2O_3**	**Cr_2O_3**	**FeO**	**NiO**	**MnO**	**MgO**	**CaO**	**Na_2O**	**K_2O**	**Cl**	**F**	**O=F&Cl**	**TOTAL**
IEBS-2 Area 1 feldspar	62.07	0.00	22.72	0.00	0.24	0.02	0.00	0.00	4.91	7.69	0.91	0.00	0.02	-0.01	98.57
	8 oxygen atoms per formula unit (sum excludes F & Cl)														
	Si	**Ti**	**Al**	**Cr**	**Fe**	**Ni**	**Mn**	**Mg**	**Ca**	**Na**	**K**	**Cl**	**F**		**Sum**
IEBS-2 Area 1 feldspar	2.792	0.000	1.205	0.000	0.009	0.001	0.000	0.000	0.237	0.671	0.052	0.000	0.003		4.967
Clay Matrix	**SiO_2**	**TiO_2**	**Al_2O_3**	**Cr_2O_3**	**FeO**	**NiO**	**MnO**	**MgO**	**CaO**	**Na_2O**	**K_2O**	**Cl**	**F**	**O=F&Cl**	**TOTAL**
IEBS-2 Area 1 matrix	58.94	0.14	21.33	0.00	6.81	0.00	0.04	2.23	0.24	1.56	0.26	0.01	0.21	-0.09	91.56

IEBS-2 Area 3 matrix	59.02	0.12	21.19	0.00	5.06	0.01	0.01	1.75	0.32	1.04	0.29	0.01	0.23	-0.10	88.85
IEBS-2 Area 1-2 matrix	58.13	0.12	21.06	0.00	4.10	0.00	0.01	1.94	0.18	1.19	0.34	0.01	0.24	-0.10	87.10
IEBS-2 Area 4 matrix	60.06	0.11	22.16	0.00	4.60	0.00	0.01	1.82	0.29	0.93	0.26	0.01	0.19	-0.08	90.27
AVERAGE	**59.04**	**0.13**	**21.43**	**0.00**	**5.14**	**0.00**	**0.02**	**1.94**	**0.26**	**1.18**	**0.29**	**0.01**	**0.22**	**-0.09**	**89.44**
Std. Dev.	**0.79**	**0.01**	**0.50**	**0.00**	**1.17**	**0.01**	**0.02**	**0.21**	**0.06**	**0.27**	**0.04**	**0.00**	**0.02**	**0.01**	**1.92**
	12 oxygen atoms per formula unit (sum excludes F & Cl)														
	Si	**Ti**	**Al**	**Cr**	**Fe**	**Ni**	**Mn**	**Mg**	**Ca**	**Na**	**K**	**Cl**	**F**		**Sum**
IEBS-2 Area 1 matrix	4.223	0.008	1.801	0.000	0.408	0.000	0.002	0.238	0.018	0.217	0.024	0.001	0.048		6.940
IEBS-2 Area 3 matrix	4.297	0.007	1.818	0.000	0.308	0.001	0.001	0.190	0.025	0.147	0.027	0.001	0.053		6.820
IEBS-2 Area 1-2 matrix	4.297	0.007	1.835	0.000	0.253	0.000	0.001	0.214	0.014	0.171	0.032	0.001	0.056		6.823
IEBS-2 Area 4 matrix	4.289	0.006	1.865	0.000	0.275	0.000	0.001	0.194	0.022	0.129	0.024	0.001	0.043		6.804
AVERAGE	**4.28**	**0.01**	**1.83**	**0.00**	**0.31**	**0.00**	**0.00**	**0.21**	**0.02**	**0.17**	**0.03**	**0.00**	**0.05**	**#DIV/0!**	**6.85**
Std. Dev.	**0.04**	**0.00**	**0.03**	**0.00**	**0.07**	**0.00**	**0.00**	**0.02**	**0.00**	**0.04**	**0.00**	**0.00**	**0.01**	**#DIV/0!**	**0.06**
Shard (Clinoptilolite?)	**SiO_2**	**TiO_2**	**Al_2O_3**	**Cr_2O_3**	**FeO**	**NiO**	**MnO**	**MgO**	**CaO**	**Na_2O**	**K_2O**	**Cl**	**F**	**O=F&Cl**	**TOTAL**
IEBS-2 Area 1-2 shard	71.66	0.01	12.01	0.00	0.20	0.01	0.04	0.13	2.33	1.60	0.10	0.00	0.00	0.00	88.08
IEBS-2 Area 1-2 shard	71.59	0.00	11.64	0.00	0.18	0.01	0.04	0.15	1.53	2.27	0.24	0.00	0.00	0.00	87.64
IEBS-2 Area 1-2 shard	69.62	0.00	11.55	0.00	0.22	0.00	0.03	0.13	1.85	1.40	0.11	0.00	0.02	-0.01	84.92
IEBS-2 Area 1 shard	68.13	0.00	10.28	0.00	0.15	0.00	0.02	0.07	2.22	1.88	0.17	0.00	0.00	0.00	82.92
IEBS-2 Area 1-2- shard	59.92	0.00	9.27	0.00	0.24	0.00	0.01	0.12	1.20	1.91	0.17	0.11	0.01	-0.03	72.97
IEBS-2 Area 3 shard	61.68	0.00	9.37	0.00	0.23	0.00	0.02	0.15	2.49	1.67	0.07	0.00	0.09	-0.04	75.69
IEBS-2 Area 4 shard	64.31	0.00	7.16	0.00	0.15	0.00	0.02	0.15	1.69	1.90	0.13	0.00	0.00	0.00	75.52
AVERAGE	**66.70**	**0.00**	**10.18**	**0.00**	**0.20**	**0.00**	**0.03**	**0.13**	**1.90**	**1.80**	**0.14**	**0.02**	**0.02**	**-0.01**	**81.10**
Std. Dev.	**4.76**	**0.00**	**1.73**	**0.00**	**0.04**	**0.00**	**0.01**	**0.03**	**0.47**	**0.28**	**0.06**	**0.04**	**0.03**	**0.02**	**6.27**
	18 oxygen atoms per formula unit (sum excludes F & Cl)														
	Si	**Ti**	**Al**	**Cr**	**Fe**	**Ni**	**Mn**	**Mg**	**Ca**	**Na**	**K**	**Cl**	**F**		**Sum**
IEBS-2 Area 1-2 shard	7.629	0.001	1.507	0.000	0.018	0.000	0.003	0.021	0.266	0.329	0.013	0.000	0.000		9.788
IEBS-2 Area 1-2 shard	7.663	0.000	1.469	0.000	0.016	0.000	0.003	0.023	0.175	0.471	0.032	0.001	0.000		9.854
IEBS-2 Area 1-2 shard	7.666	0.000	1.498	0.000	0.021	0.000	0.003	0.022	0.218	0.299	0.016	0.001	0.007		9.742
IEBS-2 Area 1 shard	7.713	0.000	1.371	0.000	0.015	0.000	0.002	0.012	0.269	0.412	0.025	0.001	0.000		9.820
IEBS-2 Area 1-2- shard	7.711	0.000	1.406	0.000	0.026	0.000	0.001	0.023	0.166	0.475	0.029	0.025	0.004		9.838
IEBS-2 Area 3 shard	7.673	0.000	1.373	0.000	0.023	0.000	0.003	0.028	0.332	0.402	0.012	0.000	0.035		9.847
IEBS-2 Area 4 shard	7.962	0.000	1.045	0.000	0.015	0.000	0.003	0.027	0.224	0.457	0.020	0.000	0.002		9.754
AVERAGE	**7.72**	**0.00**	**1.38**	**0.00**	**0.02**	**0.00**	**0.00**	**0.02**	**0.24**	**0.41**	**0.02**	**0.00**	**0.01**		**9.81**

Std. Dev.	**0.11**	**0.00**	**0.16**	**0.00**	**0.00**	**0.00**	**0.00**	**0.01**	**0.06**	**0.07**	**0.01**	**0.01**	**0.01**		**0.05**
Stilpnomelane	**SiO_2**	**TiO_2**	**Al_2O_3**	**Cr_2O_3**	**FeO**	**NiO**	**MnO**	**MgO**	**CaO**	**Na_2O**	**K_2O**	**Cl**	**F**	**O=F&Cl**	**TOTAL**
IEBS-2 Area 2 Stilp?	34.60	0.00	11.14	0.00	31.40	0.01	0.09	1.27	5.85	2.51	0.03	0.15	0.06	-0.06	87.05
IEBS-2 Area 3 stilp?	41.95	0.05	16.08	0.01	29.64	0.02	0.14	1.68	0.76	2.98	0.14	0.07	0.00	-0.02	93.53
IEBS-2 Area 3 stilp?	36.58	0.02	15.09	0.01	27.74	0.02	0.13	1.73	0.59	2.41	0.16	0.09	0.01	-0.03	84.56
IEBS-2 Area 3 stilp?	38.07	0.02	15.82	0.00	30.21	0.01	0.15	1.54	0.78	3.57	0.15	0.06	0.11	-0.06	90.38
AVERAGE	**37.80**	**0.02**	**14.53**	**0.01**	**29.75**	**0.02**	**0.13**	**1.55**	**1.99**	**2.87**	**0.12**	**0.09**	**0.04**	**-0.04**	**88.88**
Std. Dev.	**3.11**	**0.02**	**2.30**	**0.01**	**1.53**	**0.01**	**0.03**	**0.21**	**2.57**	**0.53**	**0.06**	**0.04**	**0.05**	**0.02**	**3.91**
	18 oxygen atoms per formula unit (sum excludes F & Cl)														
	Si	**Ti**	**Al**	**Cr**	**Fe**	**Ni**	**Mn**	**Mg**	**Ca**	**Na**	**K**	**Cl**	**F**		**Sum**
IEBS-2 Area 2 Stilp?	7.671	0.000	2.911	0.000	5.822	0.002	0.017	0.420	1.390	1.079	0.008	0.056	0.042		19.38
IEBS-2 Area 3 stilp?	8.171	0.007	3.691	0.002	4.828	0.003	0.023	0.488	0.159	1.125	0.035	0.023	0.000		18.56
IEBS-2 Area 3 stilp?	7.938	0.003	3.859	0.002	5.034	0.003	0.024	0.560	0.137	1.014	0.044	0.033	0.007		18.65
IEBS-2 Area 3 stilp?	7.799	0.003	3.820	0.000	5.176	0.002	0.026	0.470	0.171	1.418	0.039	0.021	0.071		18.95
AVERAGE	**7.89**	**0.00**	**3.57**	**0.00**	**5.21**	**0.00**	**0.02**	**0.48**	**0.46**	**1.16**	**0.03**	**0.03**	**0.03**		**18.88**
Std. Dev.	**0.21**	**0.00**	**0.45**	**0.00**	**0.43**	**0.00**	**0.00**	**0.06**	**0.62**	**0.18**	**0.02**	**0.02**	**0.03**		**0.37**

IEBS-2 Steel															
Fe-saponite	**SiO_2**	**TiO_2**	**Al_2O_3**	**Cr_2O_3**	**FeO**	**NiO**	**MnO**	**MgO**	**CaO**	**Na_2O**	**K_2O**	**Cl**	**F**	**O=F&Cl**	**TOTAL**
IEBS-2 Steel Area 1 Fe sap	41.79	0.03	16.85	0.17	29.86	0.24	0.29	1.52	0.89	3.86	0.06	0.01	0.01	-0.01	95.58
IEBS-2 Steel Area 1 Fe sap	43.70	0.06	16.35	0.15	27.16	0.23	0.25	1.57	0.92	3.24	0.07	0.02	0.00	-0.01	93.73
IEBS-2 Steel Area 1 Fe sap	41.41	0.04	17.17	0.18	29.27	0.23	0.24	1.50	0.85	3.60	0.08	0.02	0.00	0.00	94.60
IEBS-2 Steel Area 1 Fe sap	35.41	0.02	15.74	0.33	34.11	0.29	0.33	1.20	0.45	2.58	0.08	0.01	0.03	-0.02	90.57
IEBS-2 Steel Area 4 Fe sap	41.10	0.03	16.11	0.23	27.33	0.40	0.22	1.58	0.14	4.19	0.17	0.08	0.08	-0.05	91.59
IEBS-2 Steel Area 4 Fe sap	33.77	0.03	15.05	0.22	25.55	0.25	0.26	1.46	0.08	5.65	0.10	0.09	0.06	-0.04	82.52
AVERAGE	**39.53**	**0.04**	**16.21**	**0.21**	**28.88**	**0.27**	**0.27**	**1.47**	**0.56**	**3.86**	**0.09**	**0.04**	**0.03**	**-0.02**	**91.43**
Std. Dev.	**3.97**	**0.01**	**0.77**	**0.07**	**3.00**	**0.07**	**0.04**	**0.14**	**0.39**	**1.04**	**0.04**	**0.04**	**0.03**	**0.02**	**4.75**

	12 oxygen atoms per formula unit (sum excludes F & Cl)														
	Si	**Ti**	**Al**	**Cr**	**Fe**	**Ni**	**Mn**	**Mg**	**Ca**	**Na**	**K**	**Cl**	**F**		**Sum**
IEBS-2 Steel Area 1 Fe sap	3.434	0.002	1.632	0.011	2.052	0.016	0.020	0.186	0.079	0.614	0.006	0.002	0.002		8.053
IEBS-2 Steel Area 1 Fe sap	3.587	0.004	1.581	0.010	1.864	0.015	0.018	0.192	0.081	0.516	0.008	0.002	0.001		7.876
IEBS-2 Steel Area 1 Fe sap	3.426	0.003	1.675	0.012	2.025	0.015	0.017	0.186	0.075	0.578	0.008	0.002	0.000		8.021
IEBS-2 Steel Area 1 Fe sap	3.196	0.001	1.674	0.024	2.575	0.021	0.025	0.162	0.044	0.452	0.010	0.001	0.009		8.185
IEBS-2 Steel Area 4 Fe sap	3.497	0.002	1.615	0.015	1.945	0.027	0.016	0.200	0.013	0.691	0.019	0.012	0.020		8.041
IEBS-2 Steel Area 4 Fe sap	3.267	0.002	1.716	0.017	2.067	0.019	0.021	0.210	0.008	1.060	0.012	0.015	0.018		8.401
AVERAGE	**3.40**	**0.00**	**1.65**	**0.01**	**2.09**	**0.02**	**0.02**	**0.19**	**0.05**	**0.65**	**0.01**	**0.01**	**0.01**		**8.10**
Std. Dev.	**0.15**	**0.00**	**0.05**	**0.01**	**0.25**	**0.00**	**0.00**	**0.02**	**0.03**	**0.22**	**0.00**	**0.01**	**0.01**		**0.18**

Chlorite?	**SiO_2**	**TiO_2**	**Al_2O_3**	**Cr_2O_3**	**FeO**	**NiO**	**MnO**	**MgO**	**CaO**	**Na_2O**	**K_2O**	**Cl**	**F**	**O=F&Cl**	**TOTAL**
IEBS-2 Steel Area 3 chl?	46.02	0.10	21.84	0.12	5.98	0.10	0.06	1.57	0.19	2.29	0.35	0.01	0.23	-0.10	78.63
IEBS-2 Steel Area 3 chl?	62.39	0.12	21.12	0.07	6.69	0.11	0.01	1.97	0.22	1.42	0.43	0.01	0.17	-0.08	94.58
AVERAGE	**54.20**	**0.11**	**21.48**	**0.09**	**6.33**	**0.11**	**0.04**	**1.77**	**0.21**	**1.85**	**0.39**	**0.01**	**0.20**	**-0.09**	**86.60**
Std. Dev.	**11.58**	**0.01**	**0.51**	**0.03**	**0.51**	**0.01**	**0.04**	**0.28**	**0.03**	**0.62**	**0.06**	**0.00**	**0.04**	**0.02**	**11.27**

	11 oxygen atoms per formula unit (sum excludes F & Cl)														
	Si	**Ti**	**Al**	**Cr**	**Fe**	**Ni**	**Mn**	**Mg**	**Ca**	**Na**	**K**	**Cl**	**F**		**Sum**
IEBS-2 Steel Area 3 chl?	3.570	0.006	1.997	0.007	0.388	0.006	0.004	0.182	0.016	0.344	0.035	0.001	0.056		6.56
IEBS-2 Steel Area 3 chl?	3.957	0.006	1.579	0.004	0.355	0.006	0.001	0.186	0.015	0.175	0.035	0.001	0.034		6.32
AVERAGE	**3.76**	**0.01**	**1.79**	**0.01**	**0.37**	**0.01**	**0.00**	**0.18**	**0.02**	**0.26**	**0.03**	**0.00**	**0.05**		**6.44**
Std. Dev.	**0.27**	**0.00**	**0.30**	**0.00**	**0.02**	**0.00**	**0.00**	**0.00**	**0.00**	**0.12**	**0.00**	**0.00**	**0.02**		**0.17**

Appendix D SEM Images

IEBS-1

SEM Images

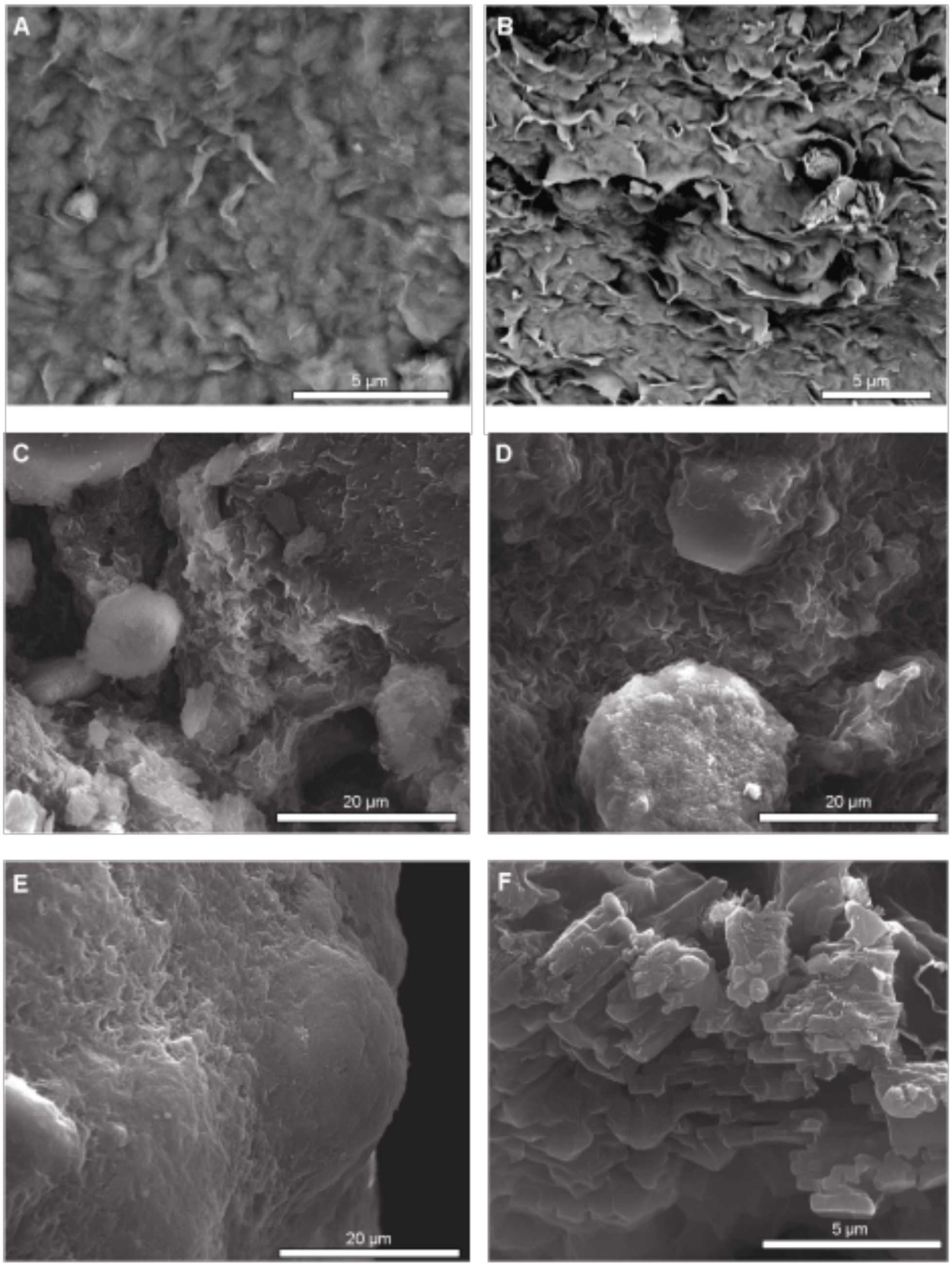

Figure D-1. IEBS-1 secondary electron images. [A] Montmorillonite transitioning to smectite. [C, D, E] SEM images of C(A)SH crystals in the smectite matrix. [F] Albite crystals, note that these albite crystals are corroding.

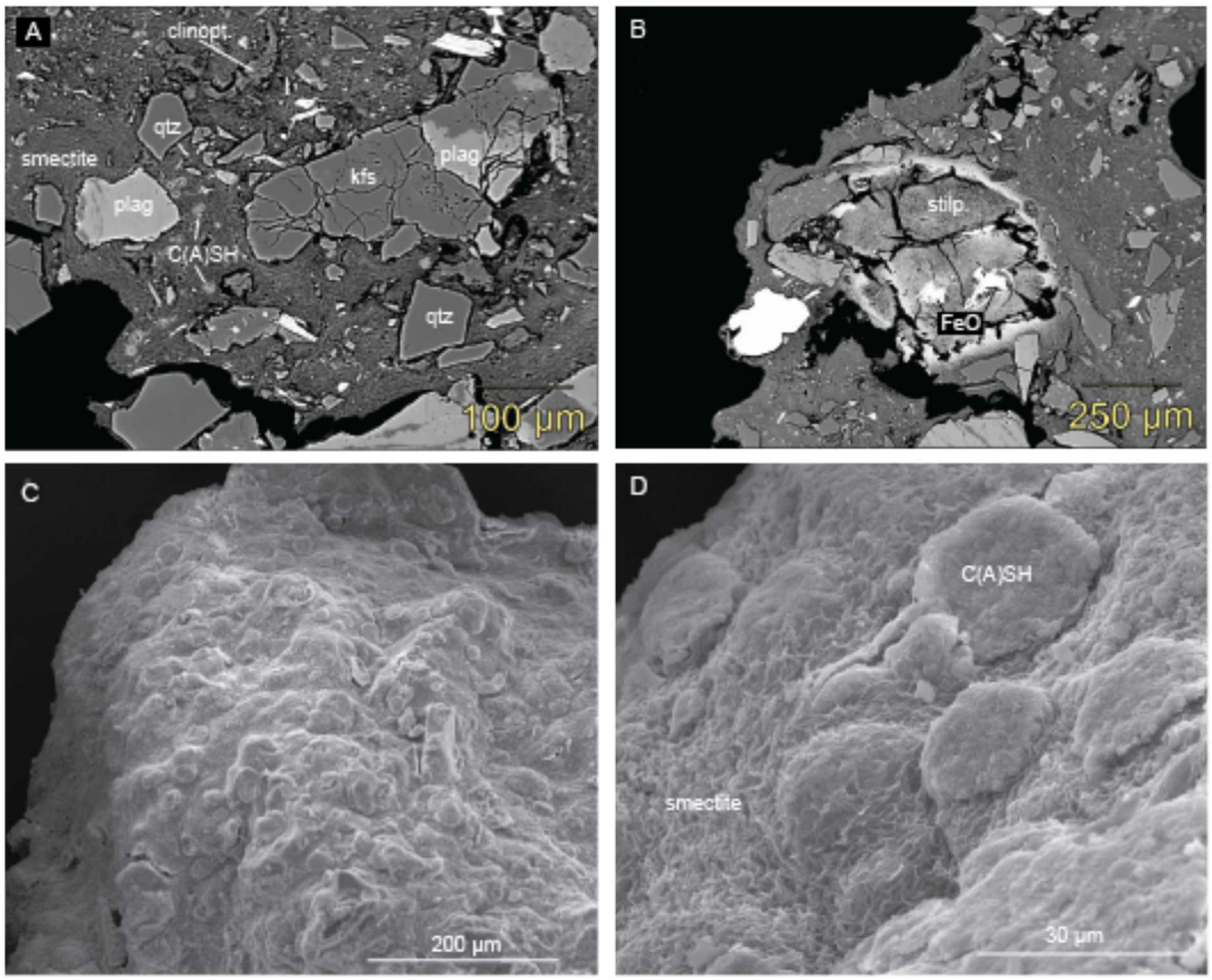

Figure D-2. IEBS-1. [A] BSE image of an IEBS-1 thin section showing feldspar, quartz, C(A)SH minerals, and glass shards in a smectite matrix. [B] Stilpnomelane growth around a grain of FeO (buffer material) in a smectite matrix. [C] Secondary electron image of C(A)SH mineral growth in smectite. [D] Zoomed in view of area [C]. Abbreviations: C(A)SH, calcium (aluminum) silicate hydrate; clinopt, clinoptilolite; kfs, K-feldspar; plag, plagioclase; qtz, quartz.

IEBS-2

SEM Images

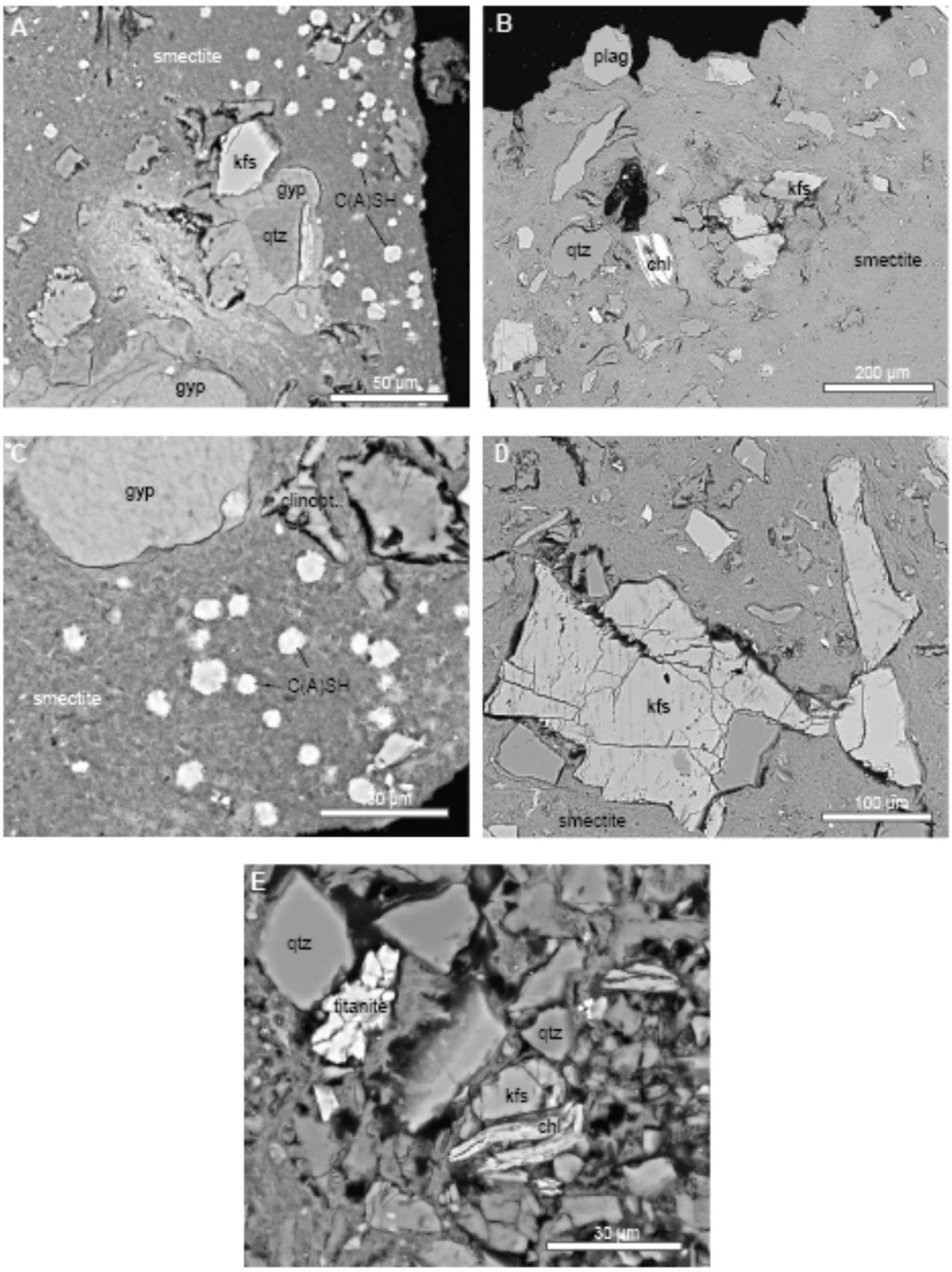

Figure D-3. IEBS-2. Backscattered electron images from IEBS-2 (thin section). Labelled minerals were identified with EDS. [A–D] Feldspar, quartz, and gypsum in the fine-grained clay matrix [A, C] White spherical minerals are C(A)SH minerals. [E] Grimsel Granodiorite fragment composed of feldspars, quartz, chlorite, and accessory minerals (e.g., titanite). Abbreviations: C(A)SH, calcium (aluminum) silicate hydrate; chl, chlorite; gyp, gypsum; kfs, K-feldspar; plag, plagioclase; qtz, quartz.

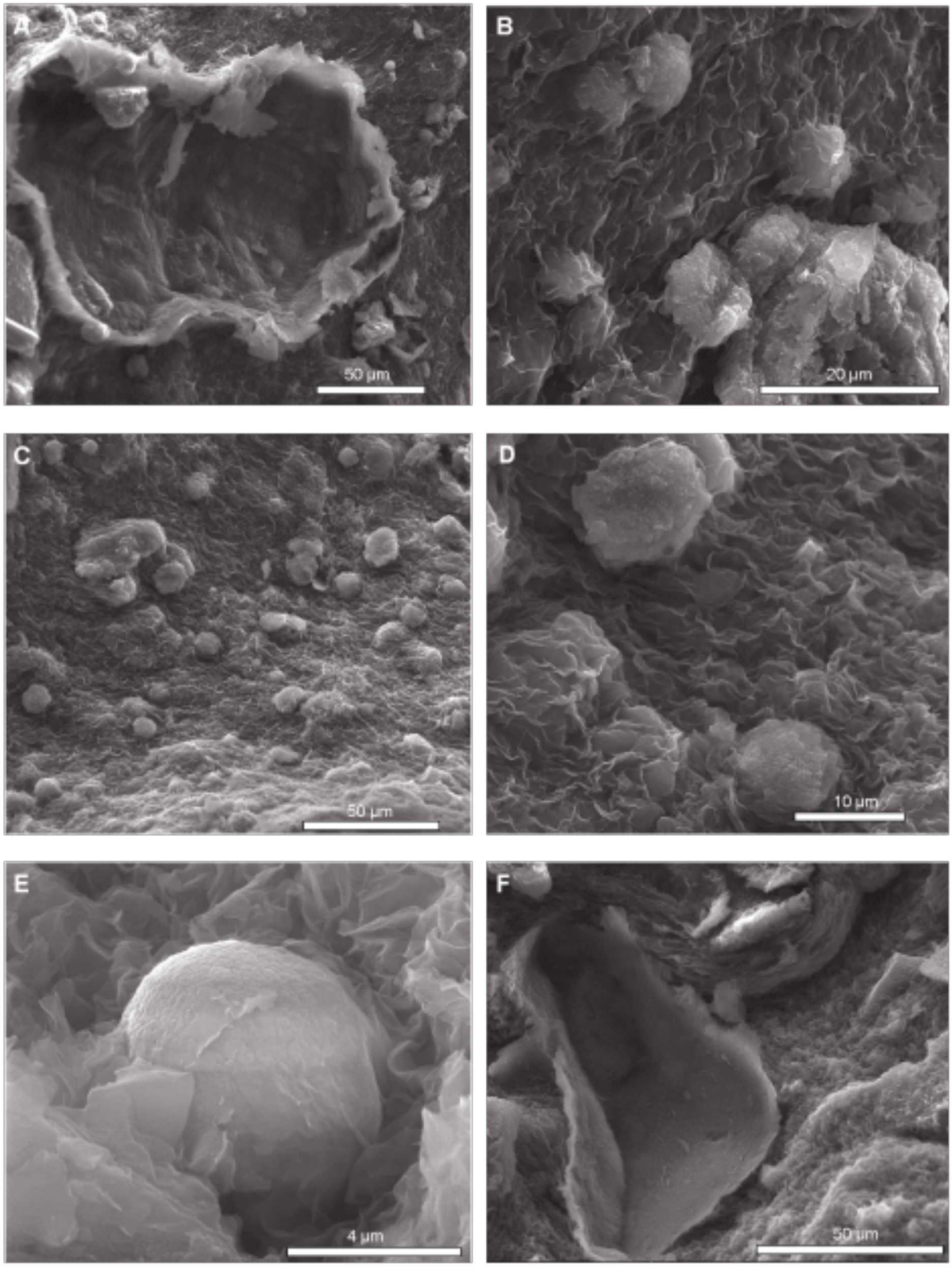

Figure D-4. IEBS-2 secondary electron images. [A, F] Chlorite fragment from original host granodiorite. [B, C, D] Juvenile-to-mature C(A)SH crystals embedded in smectite matrix. [E] C(A)SH crystal embedded in smectite.

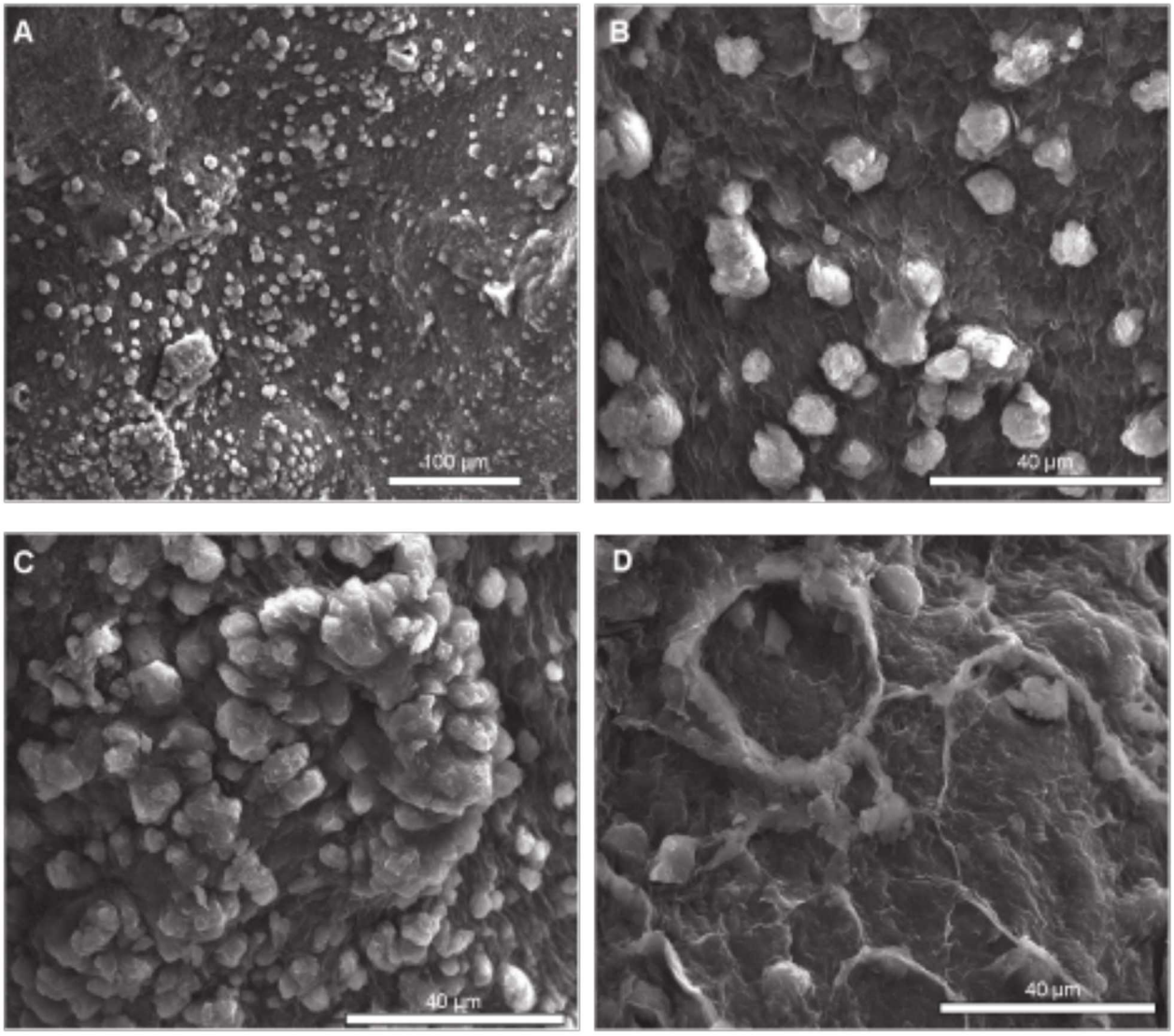

Figure D-5. IEBS-2. [A, B, C] Secondary electron images of gypsum crystals embedded in smectite matrix and [D] mixed phases of C(A)SH crystals and secondary feldspars.

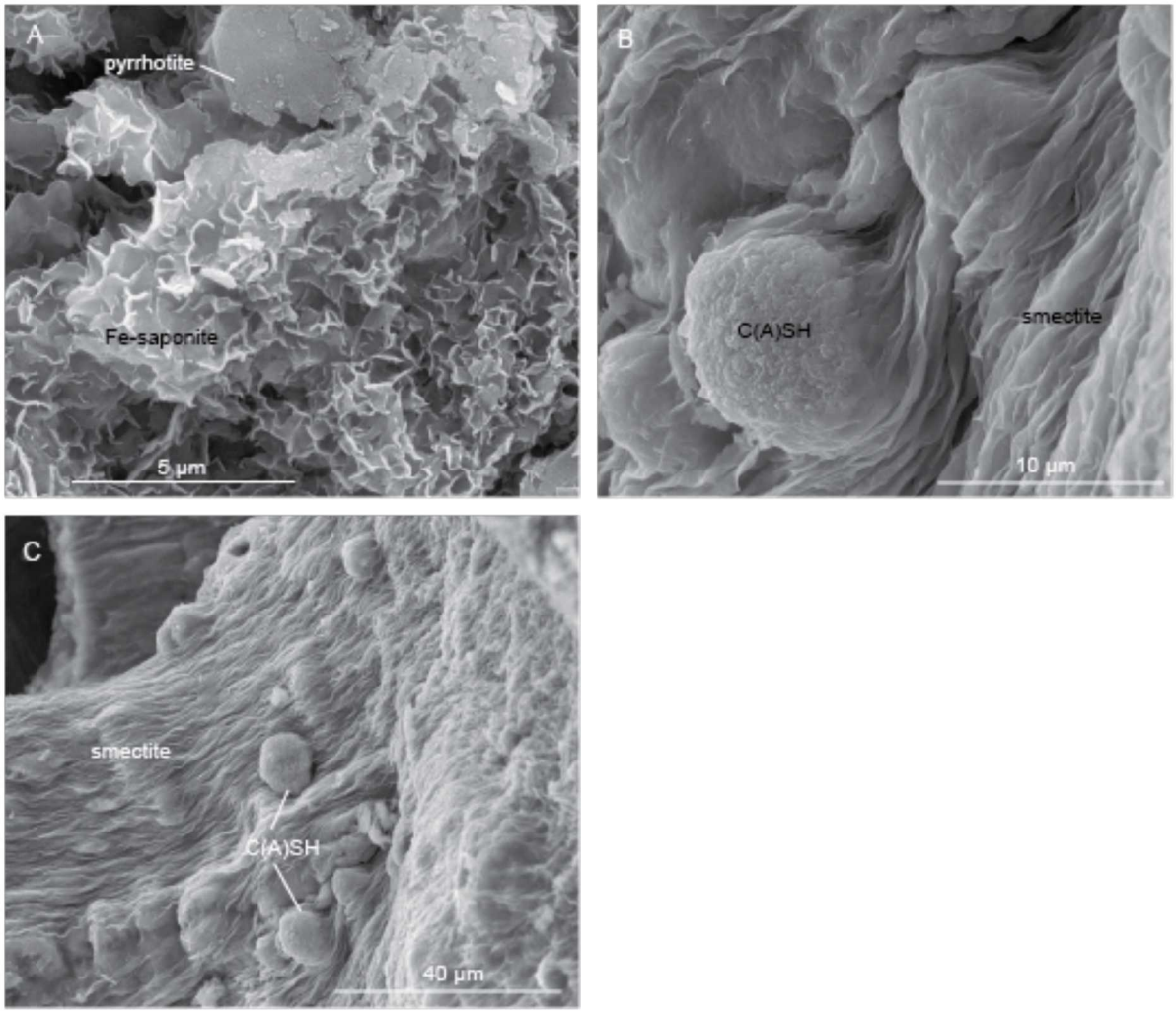

Figure D-6. Secondary electron images of IEBS-2 reaction products. [A] Fe-saponite and pyrrhotite that likely formed at the interface of the 316 SS and the Wyoming bentonite. [B, C] C(A)SH minerals embedded in smectite.